

Assessment of Myocardial Fibre Structure in Hypertrophic Cardiomyopathy with Magnetic Resonance Diffusion Tensor Imaging

Dr Rina Ariga
BSc (Hons), MB BS, MRCP

Exeter College

Division of Cardiovascular Medicine
Radcliffe Department of Medicine

Thesis submitted for the degree of
Doctor of Philosophy

Trinity Term 2018

ACKNOWLEDGEMENTS

It has been a great privilege to be supervised by Prof Hugh Watkins, Prof Stefan Neubauer and Prof Matt Robson. I have received outstanding guidance, support and advice, and I am sincerely grateful for their mentorship.

Thank you to all my colleagues at OCMR from 2012-2018 for their enthusiasm, stimulation and friendship. I worked most closely with Dr Liz Tunnicliffe and I am grateful for her physics expertise and encouragement.

I was fortunate to develop a collaboration with Prof Blanca Rodriguez and her Computational Cardiovascular Science group, and I am indebted to her for providing me with extra funding. I also thank the British Heart Foundation for funding my 3-year Clinical Research Training Fellowship for this project.

A very special thank you to my husband, Prof Sanjay Manohar for his generous and invaluable help both intellectually and emotionally. Sanjay has patiently taught me how to code in MATLAB to handle these complex data, for which I am truly grateful.

Finally, I thank my children Alexander and Benjamin Manohar for their love and patience during my long hours of work.

DECLARATION

I declare that the work presented in this thesis is my own, except where otherwise indicated.

Dr Elizabeth Tunnicliffe implemented and validated the DT-CMR sequence and post-processing pipeline used in Chapters 3-5. Prof Sanjay Manohar wrote the code for voxel-wise DT-CMR analysis, transforming DT-CMR parameters to normalised LV co-ordinates and visualising the tensor used in Chapters 3-5. Prof Sanjay Manohar, Dr Lei Clifton (*Centre for Statistics in Medicine*) and Prof Martin Farrall advised on statistical methods (Chapters 3-6, Chapters 4-5 and Chapter 6 respectively).

The work presented in Chapter 6 has been published in Frontiers in Physiology with a joint first authorship for Dr Aurore Lyon and me. We have contributed equally to this specific work. Dr Aurore Lyon developed and performed the computational methods: ECG signal processing, computational modelling, feature extraction, dimensionality reduction and clustering analysis.

MANUSCRIPTS ARISING FROM THIS WORK

1. **Ariga R**, Tunnicliffe EM, Manohar SG, Mahmod M, Raman B, Piechnik SK, Francis JM, Robson MD, Neubauer S and Watkins H.
   Identification of Myocardial Disarray in Patients With Hypertrophic Cardiomyopathy and Ventricular Arrhythmias.
   Journal of the American College of Cardiology. 2019 May 73(20): 2493-2502.

2. *Lyon A, ***Ariga R**, Mincholé A, Mahmod M, Ormondroyd E, Laguna P, de Freitas N, Neubauer S, Watkins H, Rodriguez B.
   Distinct ECG phenotypes identified in hypertrophic cardiomyopathy using machine learning associate with arrhythmic risk markers.
   Frontiers in physiology. 2018 Mar 9:213.
   joint first author

3. Minchole A, Zacur E, **Ariga R**, Grau V, Rodriguez B.
   MRI-based computational torso/biventricular multiscale models to investigate the impact of anatomical variability on the ECG.
   Under review Frontiers in physiology. 2019

4. Lyon A, Bueno-Orovio A, Zacur E, **Ariga R**, Grau V, Neubauer S, Watkins H, Rodriguez B, Mincholé A.
   ECG phenotypes in hypertrophic cardiomyopathy caused by distinct mechanisms: apico-basal repolarization gradients versus Purkinje-myocardial coupling abnormalities. Insights from a high-performance simulation study informed by cardiac magnetic resonance.
   Europace. 2018 Nov; 20 (suppl_3): iii102-iii112.

5. Zacur E, Minchole A, Villard B, Carapella V, **Ariga R**, Rodriguez B and Grau V.
   MRI-Based Heart and Torso Personalization for Computer Modeling and Simulation of Cardiac Electrophysiology.
   Imaging for Patient-Customized Simulations and Systems for Point-of-Care Ultrasound. Springer, Cham (2017) 61-70.

6. Tunnicliffe EM, Scott AD, Ferreira P, **Ariga R**, McGill LA, Nielles-Vallespin S, Neubauer S, Pennell DJ, Robson MD, Firmin DN.
   Intercentre reproducibility of cardiac apparent diffusion coefficient and fractional anisotropy in healthy volunteers.
   Journal of Cardiovascular Magnetic Resonance. 2014 Dec 16(1):31.

PRIZES AWARDED FOR THIS WORK

1. Young Investigator Award winner 2018
   British Society for Cardiovascular Magnetic Resonance (BSCMR, Edinburgh)

2. Winner 2nd Prize 2018
   Royal Society of Medicine Cardiology Section President's Prize (RSM, London)

3. Winner Clinical Science Prize 2018
   Innovation in Inherited Cardiovascular Conditions Symposium (UCL, London)

4. Winner Best Poster Prize 2018
   Association for Inherited Cardiovascular Conditions (AICC, London)

5. 1st Prize and the People's Choice winner 2018
   3 Minute Thesis competition (Exeter College, Oxford)

6. Young Investigator Award winner 2015
   National Institute for Health Research Oxford Biomedical Research Centre (BRC, Oxford)

7. Young Investigator Award winner 2015 (for Dr Aurore Lyon - joint work in Chapter 6)
   Computing in Cardiology (CinC, Nice, France)

ABBREVIATIONS

ABPRE	abnormal blood pressure response to exercise
ADC	apparent diffusion coefficient
BPM	beats per minute
CMR	cardiovascular magnetic resonance
DT-CMR	diffusion tensor cardiac magnetic resonance
ECG	electrocardiogram
ECV	extracellular volume
EPI	echo planar imaging
FA	fractional anisotropy
G+LVH-	genotype positive HCM with normal left ventricular wall thickness
HA	helix angle
HCM	hypertrophic cardiomyopathy
ICD	implantable cardioverter-defibrillator
IVIM	intravoxel incoherent motion
LGE	late gadolinium enhancement
LAD	left axis deviation
LV	left ventricular
LVH	left ventricular hypertrophy
LVOT	left ventricular outflow tract
MRI	magnetic resonance imaging
MYBPC3	myosin-binding protein C

MYH7	beta-myosin heavy chain
NSVT	non-sustained ventricular tachycardia
NYHA	New York Heart Association
PEFA	pacing-induced electrogram fractionation analysis
RF	radiofrequency
ROI	region of interest
RV	right ventricular
SCD	sudden cardiac death
SA	sheetlet angle
SNR	signal-to-noise ratio
STE	stimulated echo
STEAM	stimulated echo acquisition mode
TNNI3	troponin I

THESIS ABSTRACT

Myocardial disarray is a likely focus for fatal ventricular arrhythmia in hypertrophic cardiomyopathy (HCM). Measuring the extent of this disarray could provide a better and more mechanistic marker of arrhythmic sudden cardiac death (SCD). Disarray may be inferred by using diffusion tensor cardiac magnetic resonance (DT-CMR), a novel non-invasive imaging technique which allows tissue microstructure to be assessed in vivo – something previously only possible in post-mortem specimens. DT-CMR probes the underlying myocardial architecture by characterising the three-dimensional process of water molecule diffusion as it is impeded by myocytes and interstitium. Thus, diffusion imaging surpasses the usual limits imposed by image resolution.

Disarray together with other structural and ionic HCM defects are likely to cause irregularities in myocardial depolarisation and repolarisation to produce an abnormal electrocardiogram (ECG). Computational techniques such as machine learning could objectively learn from and make predictions on HCM ECG morphology, to identify distinct phenotypes within this heterogenous disease. The overall aim of this thesis was to characterise the underlying HCM substrate using in vivo DT-CMR imaging and machine learning of high-fidelity digital ECGs.

Diastolic fractional anisotropy (FA), a parameter calculated from the diffusion tensor, was established as a marker of coherent myocyte alignment which demonstrated a mid-wall ring of high FA in healthy controls, corresponding to circumferentially-aligned mid-wall myocytes. In HCM, this ring was disrupted by reduced FA, despite the presence of normal helix angles

which represents preserved transmural helical arrangement of myocytes. These findings are in concordance with published histology demonstrating that firstly, disarray and fibrosis invade circumferentially-aligned mid-wall myocytes at the interventricular insertion points and hypertrophied segment. And that secondly, the average myocyte orientation within the septal mid-wall remains circumferential despite disarray.

FA was reduced in HCM compared to controls. Reduced FA in HCM was due to disarray and fibrosis. Markers of fibrosis, late gadolinium enhancement (LGE) and extracellular volume imaging, were both significant predictors of FA, in line with fibrosis contributing to low FA. Yet FA adjusted for fibrosis remained reduced in HCM, suggesting that low FA is likely to represent disarray after accounting for fibrosis. Reduced FA was associated with ventricular arrhythmia in HCM, even after correcting for fibrosis and hypertrophy.

Phenotyping using machine learning of ECG morphology revealed four distinct HCM phenotypes. One phenotypic group with primary T wave inversion not secondary to QRS abnormalities had increased risk scores for SCD and increased extent of coexisting septal and apical hypertrophy compared to the other phenotypes.

In conclusion, DT-CMR can reveal the microarchitecture of the beating left ventricle. I propose that diastolic FA is the first in vivo marker of disarray. Computational ECG phenotyping captures abnormal anatomical and ionic mechanisms and provides insights into HCM heterogeneity. Both techniques may provide independent risk factors as current clinical risk predictors do not capture the underlying pathophysiology intrinsically linked to arrhythmic risk in HCM.

CONTENTS

CHAPTER 1. INTRODUCTION 1

1.1. HYPERTROPHIC CARDIOMYOPATHY (HCM) 1

1.1.1. Risk stratification for sudden cardiac death (SCD) 4

1.1.1.1. 2011 United States guidelines versus 2003 European guidelines 5

1.1.1.2. 2014 ESC guidelines 6

1.1.1.3. Limitations of current US and European HCM ICD guidelines 7

1.1.1.4. Other potential risk factors 7

1.1.2. Mechanism of sudden cardiac death in HCM 8

1.1.3. Histology of HCM 9

1.1.4. Hypertrophy as the substrate for ventricular arrhythmia 10

1.1.5. Fibrosis as the substrate for ventricular arrhythmia 11

1.1.6. Disarray as the substrate for ventricular arrhythmia 12

1.2. DIFFUSION TENSOR CARDIAC MAGNETIC RESONANCE (DT-CMR) 13

1.2.1. Diffusion 13

1.2.2. The diffusion tensor 14

1.2.3. The Eigensystem 16

1.2.4. Scalar measures derived from DTI 16

1.2.4.1. Apparent diffusion coefficient (ADC) 17

1.2.4.2. Fractional anisotropy (FA) 17

1.2.5. Tensor Orientation 18

1.2.5.1. Primary eigenvector: myocyte long axis 18

1.2.5.2. Secondary and tertiary eigenvectors: myolaminar sheetlets 20

1.2.1. Mechanism of Diffusion Imaging 21

1.2.2. Diffusion weighting using the b-value 23

1.2.3. Development of in vivo DT-CMR 24

1.2.3.1. Spin echo sequence 24

1.2.3.2. Stimulated Echo Sequence 25

1.2.3.3. Strain effects using stimulated echo 26
1.2.3.4. Number of diffusion-encoding gradient directions 29
1.2.3.5. Optimal b-value 29
1.2.3.6. Number of signal averages 31
1.2.3.7. Noise 31
1.2.4. Limitations of in vivo DT-CMR using stimulated echo 32
1.3. ELECTROCARDIOGRAPHIC PHENOTYPING OF HCM 33
1.3.1.1. Heartbeat classification, feature extraction and dimensionality reduction 34
1.3.1.2. Clustering analysis for patient stratification 36
1.4. STUDY AIMS AND HYPOTHESES 37
CHAPTER 2. METHODS 38
2.1. OVERVIEW 38
2.1.1. Inclusion criteria 38
2.1.2. Exclusion criteria 39
2.2. CLINICAL ASSESSMENT 39
2.3. ELECTROCARDIOGRAPHIC MEASUREMENTS 40
2.3.1. 12-lead resting ECG 40
2.3.2. 12-lead ambulatory Holter ECG 40
2.4. DIFFUSION TENSOR CARDIAC MAGNETIC RESONANCE (DT-CMR) ACQUISITION 41
2.5. DT-CMR SEQUENCE VALIDATION AND REPRODUCIBILITY 44
2.5.1. Phantom validation of DT-CMR sequence 44
2.5.2. Inter-centre reproducibility in healthy volunteers 44
2.6. DT-CMR PRACTICALITIES 47
2.6.1.1. Poor Breath Holding 47
2.6.1.2. Arrhythmia 48
2.6.1.3. Bradycardia 48
2.7. DT-CMR POST-PROCESSING 49
2.7.1. DT-CMR segmentation 49
2.7.2. Rejection of corrupted images 50

2.7.3. Image registration *51*

2.7.4. Diffusion tensor calculation *51*

2.7.5. Transformation of DT-CMR parameters to normalised LV co-ordinates *54*

2.7.6. Tensor visualisation *55*

2.8. CARDIOVASCULAR MAGNETIC RESONANCE (CMR) IMAGING 56

2.8.1. Cine imaging *56*

2.8.2. Late gadolinium enhancement (LGE) imaging *58*

2.8.3. Extracellular volume (ECV) imaging *58*

2.9. CLINICAL DATA COLLECTION 60

2.10. STATISTICAL ANALYSIS 61

CHAPTER 3. DIFFUSION TENSOR CARDIAC MAGNETIC RESONANCE IN HEALTHY CONTROLS 63

3.1. INTRODUCTION 63

3.1.1. Normal left ventricular myoarchitecture *65*

3.1.2. Expected FA in the healthy left ventricle *69*

3.1.3. Previous DT-CMR studies in healthy controls *70*

3.1.4. Hypotheses and aims *72*

3.2. METHODS 73

3.3. RESULTS 73

3.3.1. DT-CMR maps – qualitative assessment *73*

3.3.2. Slice level analysis of DT-CMR parameters *75*

3.3.3. Apical slice: reduced measurement accuracy *76*

3.3.4. Mid slice: consistent and reproducible parameters *78*

3.3.4.1. Segmental analysis of mid slice at diastole 80

3.3.5. Basal slice: FA significantly lower than mid slice in diastole *83*

3.4. DISCUSSION 86

3.4.1. Concordance with previous DT-CMR studies *86*

3.4.2. Reduced quality of DT-CMR from the base and apical slice *86*

3.4.3. Segmental variation of FA estimates from the mid slice *87*

3.4.4. Limitations *88*

3.4.4.1. Whole heart coverage 88

3.4.4.2. SNR 88

3.4.4.3. Microvascular perfusion 89

3.4.5. Conclusion *89*

CHAPTER 4. DIFFUSION TENSOR CARDIAC MAGNETIC RESONANCE IN HYPERTROPHIC CARDIOMYOPATHY 91

4.1. INTRODUCTION 91

4.1.1. HCM myoarchitecture *92*

4.1.1.1. Disarray predominantly located in the mesocardium of hypertrophied segments 92

4.1.1.2. Heterogeneity in disarray extent 94

4.1.1.3. Heterogeneity in myocyte orientations 94

4.1.1.4. Heterogeneity in myocyte size 96

4.1.2. DT-CMR in HCM *96*

4.1.3. Hypotheses and aims *97*

4.2. METHODS 98

4.3. RESULTS 98

4.3.1. Study group characteristics *98*

4.3.2. Group analysis of DT-CMR parameters across slice and segment *100*

4.3.2.1. SNR 104

4.3.3. Mid-ventricular DT-CMR maps in HCM – qualitative assessment *104*

4.3.4. Diastolic FA in the mid-ventricular slice *105*

4.3.5. Relationship between FA and clinical features *109*

4.3.6. Inter-observer reproducibility of FA in HCM *109*

4.3.7. Diffusion tensor visualisation *111*

4.4. DISCUSSION 112

4.4.1. SNR *112*

4.4.2. Concordance with other in vivo DT-CMR studies *113*

4.4.3. Concordance with histology *114*

4.4.4. Limitations *115*

4.5. CONCLUSION 116

CHAPTER 5. PREDICTING THE RISK OF VENTRICULAR ARRHYTHMIA IN HYPERTROPHIC CARDIOMYOPATHY USING MULTIPARAMETRIC CARDIAC MAGNETIC RESONANCE 117

5.1. INTRODUCTION 117

5.1.1. Extracellular matrix *117*

5.1.2. Cross myocyte laminar sheetlets *118*

5.1.3. Myocardial fibrosis *121*

5.1.4. Fibrosis affects DT-CMR *121*

5.2. METHODS 124

5.3. RESULTS 124

5.3.1. Diffusion Tensor CMR maps *124*

5.3.2. Diffusion Tensor CMR parameters in HCM and controls *125*

5.3.3. Relationship of Fractional Anisotropy with LGE and extracellular volume *127*

5.3.4. Relationship between Fractional Anisotropy and ventricular arrhythmia in HCM *128*

5.4. DISCUSSION 132

5.4.1. Detecting the anatomic substrate for arrhythmia in HCM *132*

5.4.2. Sheetlet angle *133*

5.4.3. Limitations *134*

CHAPTER 6. IDENTIFYING DISTINCT ECG PHENOTYPES USING A MACHINE LEARNING APPROACH IN HYPERTROPHIC CARDIOMYOPATHY 136

6.1. INTRODUCTION 136

6.2. METHODS 138

6.2.1. Holter ECG pre-processing *138*

6.2.2. Extraction of QRS and T wave biomarkers *140*

6.2.3. Hermite transform *141*

6.2.4. Feature selection and dimensionality reduction for clustering *143*

6.3. RESULTS 145

6.3.1. Study population characteristics *145*

6.3.2. Clustering using QRS morphology only *148*

6.3.3. Combined clustering with QRS morphology and T wave biomarkers identifies four HCM phenotypes *152*

6.3.4. Differences between the four HCM phenotypes in HCM Risk-SCD score, ventricular arrhythmia events and LV hypertrophy *156*

6.3.5. Repeat combined QRS and T wave clustering with the exclusion of gene positive HCM with normal wall thickness (G+LVH-) *157*

6.4. DISCUSSION 158

6.4.1. QRS morphology *159*

6.4.2. T wave inversion *160*

6.4.3. Low risk phenotypes *162*

6.4.4. Clinical implications *163*

6.4.5. Limitations *164*

6.5. CONCLUSIONS 165

CHAPTER 7. CONCLUSIONS AND FUTURE DIRECTIONS 166

7.1. DT-CMR 166

7.2. ECG PHENOTYPING 168

7.3. CONCLUSION 170

REFERENCES 171

CHAPTER 1. **INTRODUCTION**

1.1. Hypertrophic Cardiomyopathy (HCM)

Hypertrophic cardiomyopathy (HCM) is an autosomal dominant disease commonly caused by sarcomere gene mutations (Seidman and Seidman, 2001). It is the most common inherited cardiac condition and has remained a challenge due to the extreme heterogeneity in its clinical course and its phenotypic expression (Olivotto et al., 2012). HCM is the leading cause of sudden cardiac death (SCD) in young people yet the majority of patients remain asymptomatic (Maron et al., 2000b). Some patients have profound exercise limitation and progress to end stage heart failure requiring heart transplantation (Melacini et al., 2010). While others develop atrial fibrillation, increasing the risk of stroke and thromboembolic complications (Guttmann et al., 2014). However, there are no definitive methods to distinguish who will remain well and who will be devastated by disease complications.

The extent and distribution of characteristic pathological HCM features such as left ventricular hypertrophy (LVH; Figure 1.1), myocyte disarray, interstitial fibrosis and microvascular ischaemia, are equally variable and sometimes absent due to incomplete and age-related penetrance (Michels et al., 2009). HCM is clinically diagnosed by the presence of unexplained left ventricular hypertrophy on cardiac imaging such as echocardiography or cardiovascular magnetic resonance (CMR; Figure 1.2). Unexplained LVH is defined as wall thickness of ≥15mm or ≥13mm with a family history, in the absence of abnormal loading conditions (such as hypertension or aortic stenosis), infiltrative or storage disorders (Authors/Task Force et al.,

2014). These patients usually present in response to symptoms or in asymptomatic individuals, because of family screening, a systolic murmur or an abnormal electrocardiogram (ECG). Rarely, SCD is the presenting manifestation of HCM (Maron et al., 2000a).



Figure 1.1 Macroscopic findings of hypertrophic cardiomyopathy
Ventricular short-axis section from a 22-year old male with HCM who died suddenly demonstrating the classic appearance of severe asymmetrical septal hypertrophy. The anteroseptum measures 40 mm (normal left ventricular wall thickness 7-12 mm) with a "whorled" appearance of the myocardium, white foci of scarring, and prominent trabeculae and papillary muscles (*www.thoracickey.com*).

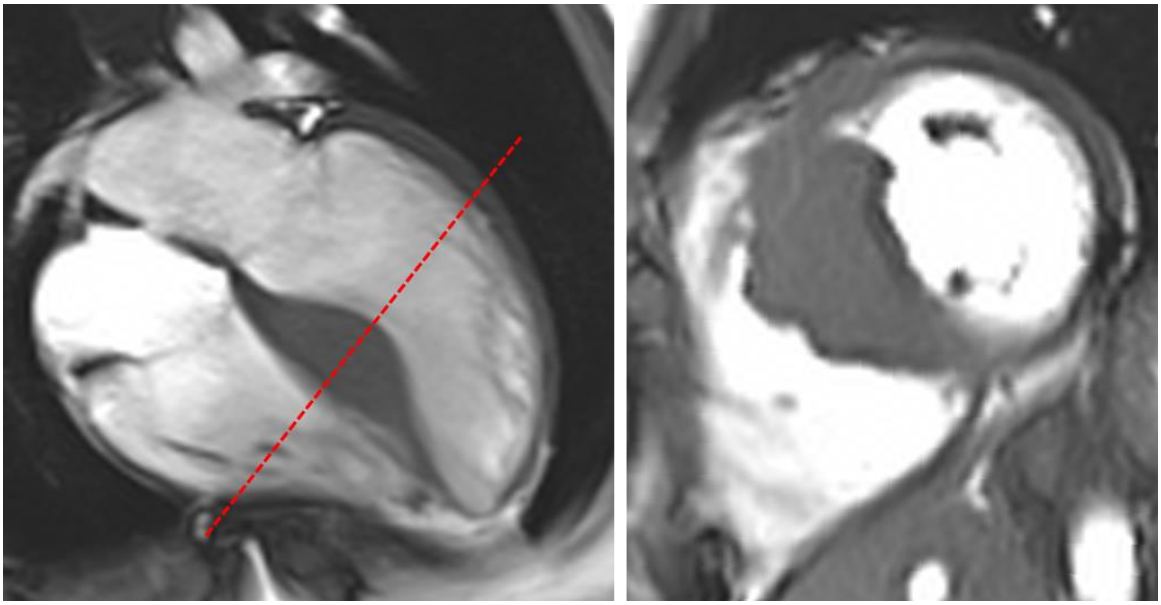


Figure 1.2 Cardiovascular Magnetic Resonance imaging in HCM
End-diastolic horizontal long-axis (left) and mid-ventricular short-axis (right) views in a 27-year old female with HCM demonstrating moderate asymmetrical septal hypertrophy. The anteroseptum measures 27 mm (normal 7-12 mm). Red line denotes position of short-axis cut.

Implantable cardioverter-defibrillators (ICD) are effective in aborting SCD but at the expense of ICD complications (inappropriate shocks, pneumothorax, haematoma, infection, displacement, lead fracture), life-time requirement for generator changes, quality of life restrictions and the psychological burden imposed by ICDs (Maron et al., 2007). A meta-analysis of 2190 HCM patients with a 3.7 year follow-up reported inappropriate ICD shocks and complications of 4.8% per year and 3.4% per year respectively, while the appropriate ICD intervention rate was 3.3% per year (Schinkel et al., 2012).

The overall incidence of SCD in HCM is less than 1% per year. Thus, the challenge is to distinguish this sub-population and reduce unnecessary ICD implantation. Although the risk of SCD is relatively low, HCM is a common disease and SCD in HCM is frequently highlighted

worldwide due to its tragic and unpredictable yet preventable occurrence in young fit athletes (Maron et al., 1996). The original prevalence of HCM was estimated at 1 in 500 (Maron et al., 1995) but may be closer to 1 in 200 with the advent of contemporary genetic testing and imaging which are detecting more individuals with a subclinical phenotype (Semsarian et al., 2015).

1.1.1. Risk stratification for sudden cardiac death (SCD)

ICD implantation is strongly warranted in HCM following a cardiac arrest for secondary prevention as the risk of SCD is around 11% per year (Priori et al., 2001). However, ICDs for primary prevention of SCD is challenging due to the uncertainty of which HCM patients are at greatest risk. Current primary prevention risk stratification uses non-invasive clinical risk factors based on previous observational and retrospective cohort studies which have become incorporated into expert consensus guidelines (Elliott et al., 2000). The five conventional risk factors for SCD include non-sustained ventricular tachycardia on Holter monitoring (NSVT), unexplained syncope, family history of SCD in a first-degree relative, massive left ventricular hypertrophy (LVH ≥30 mm) and abnormal blood pressure response to exercise (ABPRE; only relevant in patients <40 years). Many patients with an absence of SCD risk factors have an excellent prognosis with a normal life expectancy (Kofflard et al., 2003) and, yet SCD does still occur in this so-called low risk group (Elliott et al., 2000, O'Mahony et al., 2013). Conversely, risk can be overestimated leading to inappropriate ICD implantation.

1.1.1.1. 2011 United States guidelines versus 2003 European guidelines

Historically, the United States (2011 ACC/AHA (Gersh et al., 2011)) and European (2003 ESC (Maron et al., 2003)) guidelines have disagreed on the number of risk factors for primary prevention ICD recommendations. The Europeans recommended ICD implantation with ≥1 risk factor due to the relatively low predictive value of these predictors individually. In the US, ICD implantation is recommended with a single risk factor of unexplained syncope, family history of SCD in a first-degree relative or LVH ≥30 mm. This is due to the significant proportion of ICD interventions which occur in patients with just one risk factor (Maron et al., 2007). NSVT and ABPRE were only considered a significant risk factor if observed in conjunction with another risk factor or risk modifier (Figure 1.3). Risk modifiers include significant left ventricular outflow tract obstruction (LVOTO), significant late gadolinium enhancement (LGE) on CMR, apical aneurysm and specific high risk genetic mutations such as multiple mutations (Maron et al., 2012a) and Troponin T (Gimeno et al., 2009).

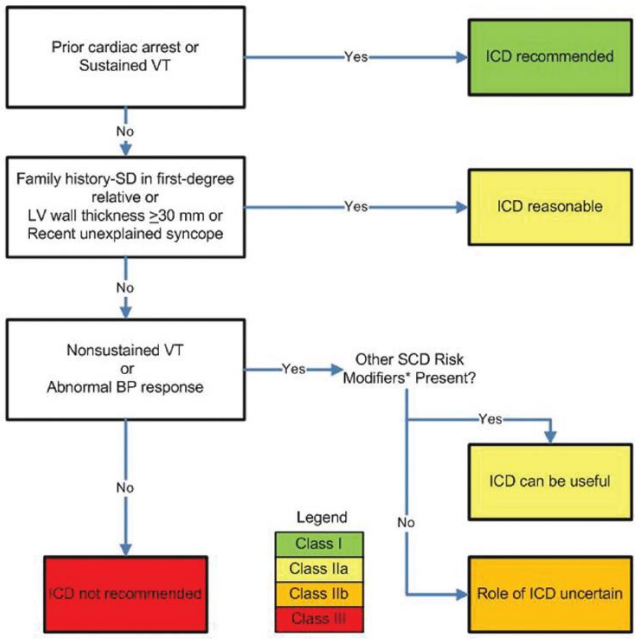


Figure 1.3 2011 ACC/AHA guidelines for ICD implantation in HCM (Gersh et al., 2011)

1.1.1.2. **2014 ESC guidelines**

However, evidence for these risk factors have come from patients with severe symptoms preferentially seen at tertiary centres which distorts the clinical picture. Further problems include continuous variables (LVH and LVOTO) treated as binary, the varying definition of family history of SCD across studies, and risk factors having lower predictive value with advancing age (Maron et al., 2012b). The 2014 ESC HCM Risk-SCD score tries to address this by using a model equation for the first 4 conventional risk factors in addition to age, left atrial diameter and maximal LVOT gradient (O'Mahony et al., 2014) (Figure 1.4).

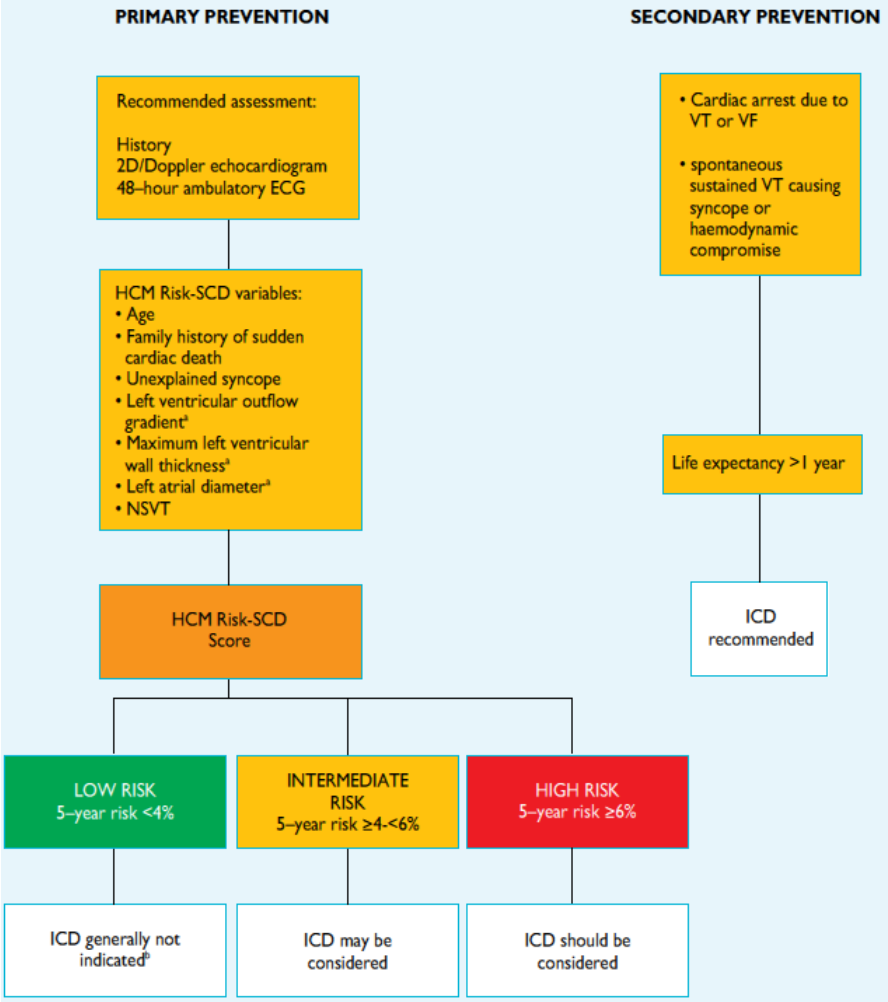


Figure 1.4 2014 ESC guidelines for ICD implantation in HCM (Authors/Task Force et al., 2014)

1.1.1.3. **Limitations of current US and European HCM ICD guidelines**

Current SCD risk stratification using 2011 ACC/AHA or 2014 ESC criteria (Gersh et al., 2011, Authors/Task Force et al., 2014) still lack the high sensitivity and specificity needed to accurately predict this low yet devastating complication (Maron et al., 2015, O'Mahony et al., 2013). Maron et al. re-tested the utility of the 2014 ESC HCM Risk-SCD score in a retrospective cohort of 1629 patients and found that only 4 of 35 sudden death events met criteria for ICD implantation based on these criteria. This is not an unexpected finding. HCM patients with ≤1 ACC/AHA risk factor greatly outnumber the high-risk patient group with ≥2 ACC/AHA risk factors. Thus, most sudden deaths occur in the "low risk" group even though individually they have the lowest risk of SCD. A similar result was found when the ACC/AHA criteria were also validated using an independent dataset (O'Mahony et al., 2013). O'Mahony et al. found that the area under the curve for receiver operating characteristic curves for the ACC/AHA criteria were 0.61 at 1 year and 0.63 at 5 years. Both guidelines are based on clinical features alone. There is no direct assessment of the underlying pathophysiology leading to sudden death.

1.1.1.4. **Other potential risk factors**

Potential risk factors which are not included in current guidelines include QRS fragmentation on ECG (Femenía et al., 2013, Kang et al., 2014), mid-ventricular obstruction (Minami et al., 2011, Efthimiadis et al., 2013), myocardial ischaemia (Maron et al., 1986, Basso et al., 2000, Maron et al., 2009, Petersen et al., 2007, Sorajja et al., 2003) and invasive pacing-induced electrogram fractionation analysis (PEFA) (Saumarez et al., 2008). PEFA are multiple discrete and delayed potentials created from unidirectional block and delay as a result disarray.

Although this technique is currently the closest in vivo marker of disarray, it is invasive and therefore not without risk. It is also limited by right ventricular (RV) measurements rather than LV and despite reporting improved risk assessment compared to conventional risk markers, 4 patients (31%) with negative PEFA died suddenly.

1.1.2. Mechanism of sudden cardiac death in HCM

Stored electrograms in HCM patients treated with an appropriate ICD therapy have shown that SCD is caused by ventricular tachycardia or fibrillation (Maron et al., 2000c). However, the annual rate of appropriate ICD discharge is only 11% even in those with a secondary prevention ICD following successful resuscitation from cardiac arrest (Maron et al., 2000c). This highly unpredictable nature of SCD suggests that a convergence of triggers (known to include myocardial ischaemia (Basso et al., 2000), abnormal baroreflex control (Thomson et al., 1998), LVOT obstruction (Elliott et al., 2006) or conduction disturbance (Nicod et al., 1988)) at a particular critical time onto a pro-arrhythmogenic substrate is required to induce a malignant arrhythmia.

The anatomical substrate is most likely to be disarray and/or fibrosis which has been found to be more extensive in those HCM patients who die suddenly (Varnava et al., 2001b, Shirani et al., 2000). However, disarray may be of greater importance as evidenced by patients with troponin T mutations who have a high risk of SCD. These patients have widespread disarray yet minimal LVH and fibrosis (Varnava et al., 2001a). Measuring the extent of disarray could provide a better and more mechanistic marker of arrhythmic sudden death, were disarray not solely a post mortem finding.

1.1.3. Histology of HCM

In 1958, Donald Teare, a forensic pathologist in London, was the first to bring together the disease characteristics recognised for many centuries (asymmetrical LVH, myocyte disarray, LV outflow tract obstruction, familial disease, premature sudden death); into the modern description of HCM (Teare, 1958). He described the bizarre and disorganised arrangement of the muscle bundles in the ventricular septum as the salient pathological feature of HCM.

Myocardial disorganisation occurs at three levels:

i) At low power light microscopy, large muscle bundles cross each other in a herring-bone pattern, interspersed with tracts of connective tissue.

ii) At high power light microscopy, hypertrophied misshapen myocytes with distinct nuclear changes have disorganised cell to cell arrangement. Cells are arranged obliquely or perpendicularly to each other around a focus of collagen in characteristic pinwheel or herringbone pattern (Figure 1.5).

iii) At ultrastructural (electron microscopy) and histochemical analysis, individual myocytes show myofibrillar disorganisation and fragmentation and irregular side-to-side connections between myocytes (Noorden et al., 1971, Ferrans et al., 1972). Type IV collagen (non-fibrillar collagen), a normal component of the basement membrane, forms thickened patches around the myocyte and localises to regions of replacement fibrosis (Watanabe et al., 1998).

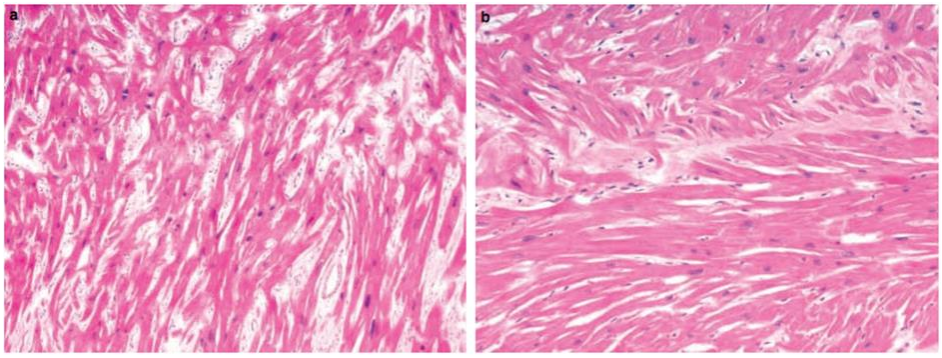


Figure 1.5 Histology of myocyte disarray
Myocyte disarray in HCM is characterised by hypertrophied misshapen myocytes arranged obliquely and perpendicularly around foci of interstitial collagen in a pinwheel (left) or herringbone pattern (right) (Hughes, 2004).

Myocyte disarray is the disorganisation at the cellular level. It remains the gold standard for a histological diagnosis of HCM and can be focal, juxtaposed beside normal myocardium or widespread. Although LVH and fibrosis are often described separately, disarray is in fact a collective term which encompasses myocyte hypertrophy causing deformed myocytes, myocyte disorientation causing uncharacteristic alignments, and increased interstitial fibrosis which contributes to further distortions of myocardial architecture. Therefore, the pro-arrhythmic features of these individual abnormalities are likely to act in synergy.

1.1.4. Hypertrophy as the substrate for ventricular arrhythmia

Myocyte hypertrophy causes prolongation of the action potential due to altered expression of ion channels and calcium handling proteins as seen in HCM myocytes (Coppini et al., 2012) as well as hypertrophied cells in terminally failing hearts (Beuckelmann et al., 1992). Ranolazine, which is known to reduce arrhythmia (Scirica et al., 2007), partially reversed these cellular abnormalities and thereby indirectly suggesting that these cellular changes may be

pro-arrhythmic. Furthermore, ranolazine was associated with reduced premature ventricular complex burden in a randomised controlled trial in HCM (Olivotto et al., 2018).

Gross LVH requires an increase in myocardial oxygen demand predisposing to ischaemia which leads to electrical instability (Maron et al., 2009). Furthermore, LVH may in part be driven by increased interstitial fibrosis rather than myocyte hypertrophy per se, since fibrosis has a significant albeit weak correlation with LV mass and wall thickness in HCM (Varnava et al., 2000).

1.1.5. Fibrosis as the substrate for ventricular arrhythmia

Fibrosis can cause conduction delay via abnormal zig-zag conduction (De Bakker et al., 1993) and fractionated extracellular electrograms (De Bakker et al., 1996) leading to block and re-entry in chronic myocardial infarction and dilated cardiomyopathy respectively. However, the role of fibrosis in HCM causing re-entry is based primarily on the association of monomorphic ventricular tachycardia (VT) in patients with apical aneurysms. Extensive transmural fibrosis in the scarred rim of apical aneurysms is the substrate for re-entry based on initiation and termination by programmed electrical stimulation (Alfonso et al., 1989), and entrainment mapping (Rodriguez et al., 1997, Mantica et al., 1997, Lim et al., 2009). Similarly end-stage HCM characterised by cavity dilatation, impaired systolic function and thinned myocardium with extensive transmural fibrosis, also has an increased incidence of SCD of 11% per year (Harris et al., 2006, Kawarai et al., 2011). NSVT is a risk factor for SCD (Adabag et al., 2005, Monserrat et al., 2003) and appears to occur more commonly in HCM patients with LGE, a marker of focal fibrosis (Adabag et al., 2008).

1.1.6. Disarray as the substrate for ventricular arrhythmia

Disarray is thought to promote arrhythmogenesis by causing heterogeneity in the normally rapid and orderly conduction of the cardiac action potential through the ventricle. Variability in size, shape and alignments of disarrayed myocytes together with fibrosis causes differences in conduction velocities and refractory periods, thus providing conditions for re-entry and arrhythmogenesis (Saumarez et al., 1992). Arrhythmias are also promoted in areas of disarray which contain myocytes with abnormal gap junctions (responsible for electrical conduction) dispersed over the cell surface rather than confined to intercalated discs located at the ends of myocytes (Sepp et al., 1996, Masuda et al., 2005). Conduction is slower in side-to-side connections (across myocyte width) versus end-to-end (along myocyte length) due to the increased number of gap junctions traversed for the same distance. Thus, disarray may delineate the anatomical substrate for re-entrant arrhythmia specific to HCM.

1.2. Diffusion tensor cardiac magnetic resonance (DT-CMR)

Diffusion tensor cardiac magnetic resonance (DT-CMR) is a novel imaging technique which infers myocardial structure at a microscopic scale by measuring molecular diffusion.

1.2.1. Diffusion

Standard magnetic resonance imaging (MRI) assumes that protons are either stationary or in bulk flow within blood. In reality, water molecules within tissues at room temperature are self-propelled by thermal energy in a process called molecular diffusion (Figure 1.6). Diffusion describes the random motion of particles arising from collisions between particles which was discovered by Robert Brown (Brownian motion) and later developed by Albert Einstein. Einstein deduced that the mean-squared molecular displacement was related to diffusion time and the diffusion coefficient which is based on the size of the molecule, viscosity of surroundings and temperature. Thus DT-CMR is based on the random displacement of water molecules which is used to probe tissue structure at a microscopic scale.

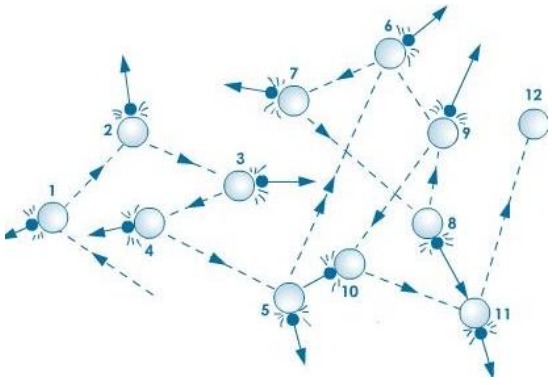


Figure 1.6 Molecular diffusion
Random walk of diffusing particles was first discovered in 1827 by Botanist Robert Brown who observed the motion of pollen grains under a microscope.

1.2.2. The diffusion tensor

The diffusion tensor, first proposed for use in MRI by Peter Basser in 1994 (Basser et al., 1994), describes the 3D shape of water diffusion within an imaging voxel. The diffusion tensor model assumes a Gaussian (normal distribution) model. When molecules are free to diffuse, the displacements form a Gaussian distribution, where zero is the peak, and the probability of diffusing a given distance is the same in all directions. Free (Gaussian) diffusion in one dimension forms a bell curve and in 3D forms a sphere (Figure 1.7). However, in biological tissue, water molecule diffusion is not free but constrained at the cellular level by 3 main mechanisms (Le Bihan, 2014):

- Restriction – water is restricted intracellularly by impermeable cell membranes and thus diffusion forms the cell geometry
- Barriers – water may escape across permeable cell membranes however this diffusion is slow as it moves from intracellular to extracellular and vice versa.
- Hindrance – water in the extracellular space is impeded by cell membranes and has to navigate obstacles to form a tortuous pathway.

The diffusion tensor consists of the diffusion rates in each combination of x, y, z orthogonal (mutually perpendicular) directions and is given by a 3 x 3 matrix of numbers which are symmetrical when diffusion is assumed to be Gaussian. Thus, the tensor only contains 6 independent elements (even though there are 9 elements, diffusion along *xy* direction is the same as *yx* direction) and can be estimated by 6 diffusion-weighted images and one baseline non-diffusion-weighted image (Figure 1.8).

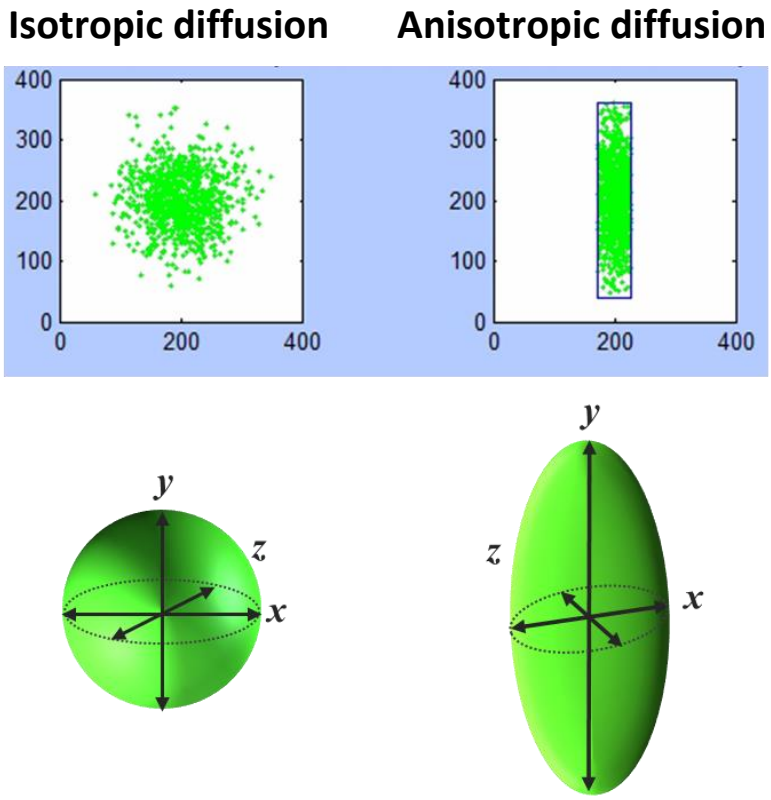


Figure 1.7 The diffusion tensor ellipsoid
The diffusion tensor describes diffusion of water molecules in three dimensions. Without barriers, water motion is random and equal in all directions, which can be represented as a sphere using the diffusion tensor. Cell membranes act as barriers restricting water motion in certain directions, which the diffusion tensor represents as an ellipsoid. *Top panel: simulated diffusion experiments, courtesy of Dr Joanne Bates, IBME, Oxford.*

$$\begin{bmatrix} D_{xx} & D_{xy} & D_{xz} \\ D_{yx} & D_{yy} & D_{yz} \\ D_{xz} & D_{yz} & D_{zz} \end{bmatrix}$$

Figure 1.8 The diffusion tensor matrix
The diffusion tensor is a 3 x 3 symmetrical matrix which characterises the displacement in three dimensions with 6 distinct elements.

1.2.3. The Eigensystem

The lengths and orientations of the three major orthogonal axes of the tensor are described by 3 positive eigenvalues (λ; a scalar quantity having only magnitude, not direction and represents the squared distance diffused within a given time) and 3 eigenvectors (ε; an eigenvector has both size and direction) (Figure 1.9). The primary eigenvalue λ_1 is the longest (direction of fastest diffusion), the secondary eigenvalue λ_2 is intermediate, and the tertiary eigenvalue λ_3 is the shortest (direction of slowest diffusion). λ_1 is significantly larger than the other two eigenvalues. Therefore, the estimation of the primary eigenvalue λ_1 is comparatively robust to λ_2 and λ_3 which is challenging to reliably sort from each other.

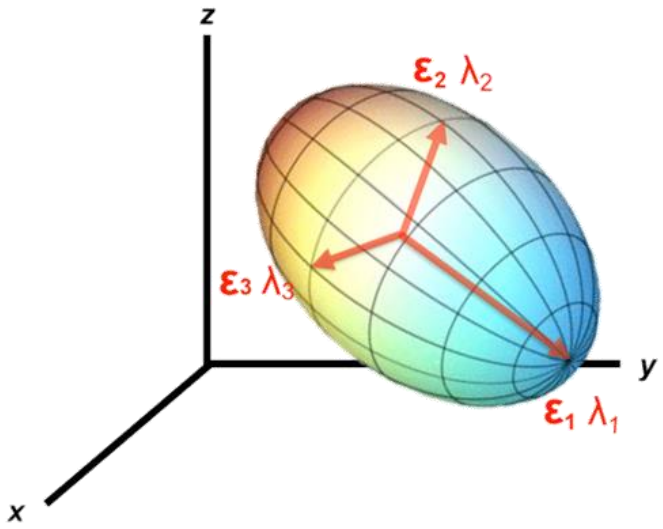


Figure 1.9 The Eigensystem
The tensor ellipsoid is described by 3 orientations, (ε_1, ε_2 and ε_3) the eigenvectors with corresponding lengths (λ_1, λ_2 and λ_3), the eigenvalues (*www.mriquestions.com).*

1.2.4. Scalar measures derived from DTI

Several quantitative parameters can be derived from the tensor to describe the 3D ellipsoid as a single number. These numbers can then be plotted at each voxel location to create a parametric map which relates to diffusion.

1.2.4.1. **Apparent diffusion coefficient (ADC)**

Apparent diffusion coefficient (ADC; mm^2/s) is the average of the tensor's eigenvalues (also referred to as the mean diffusivity) and characterises the overall magnitude of diffusion in an imaging voxel (Le Bihan et al., 2001):

$$\mathrm{ADC} = \frac{\lambda_1 + \lambda_2 + \lambda_3}{3}$$

"Apparent" is used to describe the diffusion coefficient to account for partial volume averaging, perfusion and measurement error. High ADC signal denotes fast diffusion (and is affected by both water content and cellular constraints. For example, in the brain, ADC is reduced in acute stroke due to cytotoxic oedema. Conversely, ADC is increased in established cerebral infarcts due to loss of membrane integrity.

1.2.4.2. **Fractional anisotropy (FA)**

Anisotropy comes from the Greek *an* = not; *iso* = the same; *tropic* = turn i.e. not the same in all directions. Tensor anisotropy measures are ratios of the eigenvalues and quantifies the shape of the diffusion. Fractional anisotropy (FA) is most commonly used, which measures the fraction of the diffusion that is anisotropic i.e. the difference of the tensor ellipsoid's shape from that of a perfect sphere. FA is the normalised variance of the eigenvalues:

$$\mathrm{FA} = \sqrt{\frac{3}{2}}\sqrt{\frac{(\lambda_1 - \lambda)^2 + (\lambda_2 - \lambda)^2 + (\lambda_3 - \lambda)^2}{\lambda_1{}^2 + \lambda_2{}^2 + \lambda_3{}^2}}$$

where λ = ADC. Both ADC and FA are independent of orientation which is known as being rotationally invariant. Without barriers, water motion is random and equal in all directions (perfect isotropy), which can be represented as a sphere using the diffusion tensor and has

FA of zero. Diffusion in just one single linear direction (perfect anisotropy) has FA of 1 (Figure 1.10).

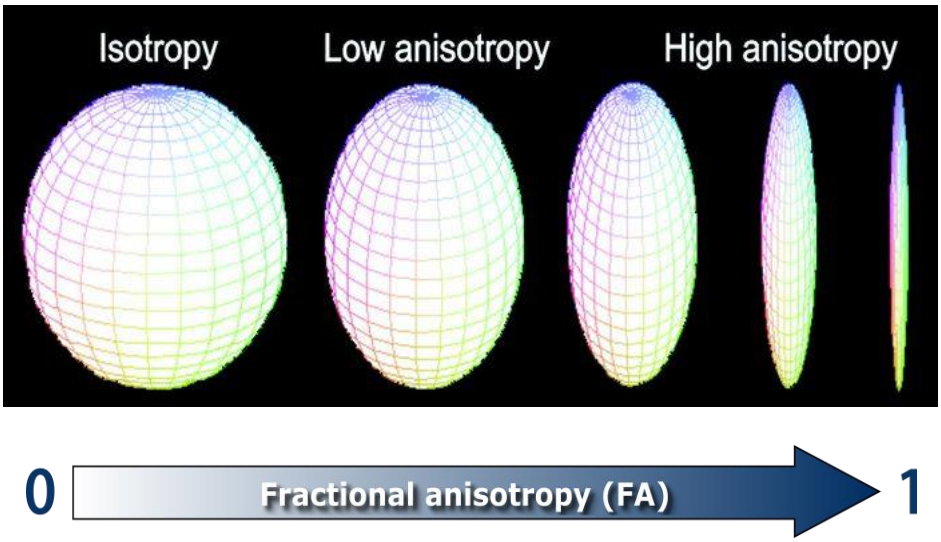


Figure 1.10 Fractional anisotropy
Free diffusion is spherical and symmetrical in nature (isotropic). Anisotropic diffusion is shown increasing from left to right. Fractional anisotropy is the extent to which diffusion is not spherically symmetric (Nagy et al., 2005).

1.2.5. Tensor Orientation

Although the scalar measures of ADC and FA are rotationally invariant, the tensor itself contains directional information to probe structural orientation in vivo.

1.2.5.1. **Primary eigenvector: myocyte long axis**

The primary eigenvector ε_1 is the dominant (fastest) diffusion direction which coincides with the myocyte long axis and defines the fibre orientation (Reese et al., 1995). The angle between the primary eigenvector and the short-axis (circumferential) ventricular plane is the helix angle and corresponds to the transmural helical arrangement of myocytes, first reported by Pettigrew (Pettigrew, 1864) and later quantified by Streeter (Streeter et al., 1969).

Extensive validation against histology in several species has shown high concordance of the helix angle obtained from DT-CMR with the classical counter-clockwise rotation of myocytes from a left-handed helix in the epicardium, circumferential in the mid-wall, to a right-handed helix in the endocardium (Hsu et al., 1998, Scollan et al., 1998, Holmes et al., 2000). However, due to signal averaging and the spatial resolution of DT-CMR, the mid-wall plateau from circumferentially-orientated myocytes on histology was not seen with imaging (Figure 1.11) (Reese et al., 1995).

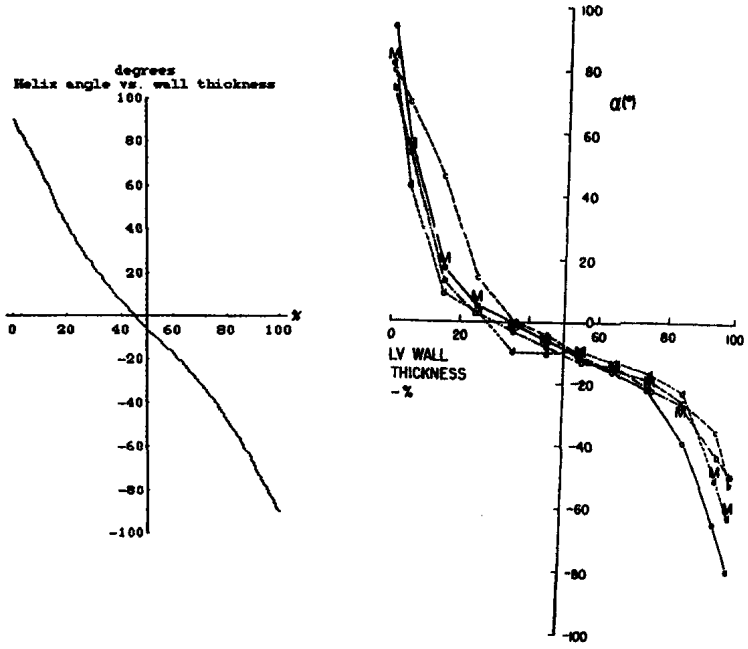


Figure 1.11 Helix angle from DT-CMR and histology data
Helix angle from endocardium to epicardium from ex-vivo DT-CMR (left) (Reese et al., 1995) is comparable to Streeter's histological assessment (right) (Streeter et al., 1969).

More recently, primary eigenvector data have been reconstructed into "tracts" to provide visually stunning diffusion derived myocyte tractography (Figure 1.12). However, this streamlines eigenvectors rather than providing true anatomical features (Teh et al., 2016), it requires high signal-to-noise-ratio (SNR) and increased number of diffusion directions for accurate results.

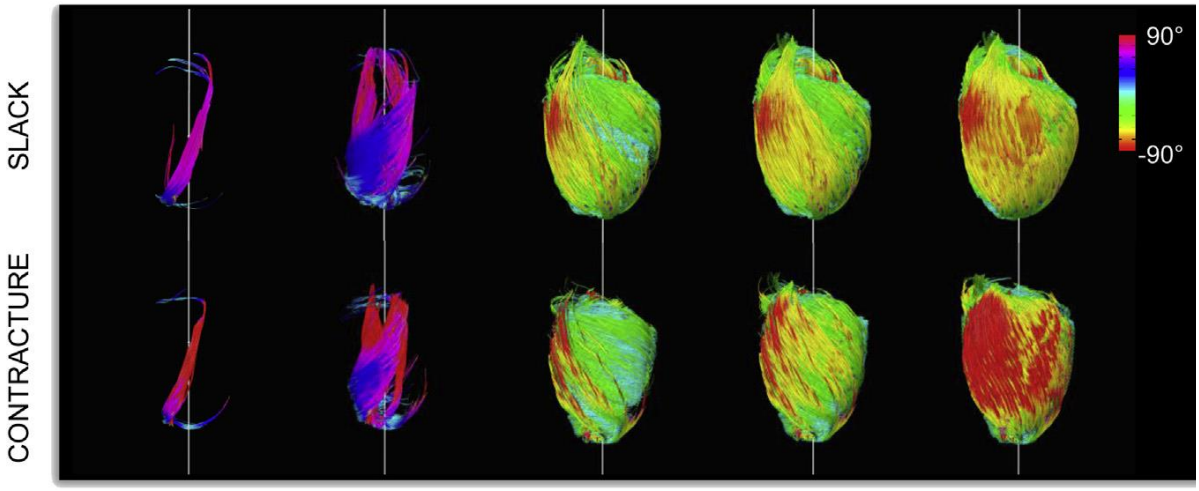


Figure 1.12 Tractography
3D tracking of the primary eigenvector in slack (top) and contractured (bottom) states in ex vivo rat hearts, showing the progression from right to left helical fibres from the endocardium (left) to epicardium (right). Tracts are colour coded by helix angle where negative and positive angles correspond to left handed and right handed fibres respectively (Lohezic et al., 2014).

1.2.5.2. **Secondary and tertiary eigenvectors: myolaminar sheetlets**

The secondary ε_2 and tertiary ε_3 eigenvectors also show systematic orientations and correspond to the secondary structure of myocytes arranged in laminar "sheetlets" and their separation by cleft-like spaces "sheetlet-normal" direction respectively (Scollan et al., 1998, Tseng et al., 2003). The secondary eigenvector is predominantly in the transmural (radial) direction. The tertiary eigenvector is orthogonal to the primary and secondary eigenvectors. Sheetlets have a bimodal distribution of 2 sheetlet-populations with sheetlet angles of opposing polarity (Figure 1.13) (Harrington et al., 2005). These sheetlet populations move relative to each other to cause LV thickening and thus have changing sheetlet-intersection angles (the deviation between sheetlet populations with opposing polarity) (Figure 1.14).

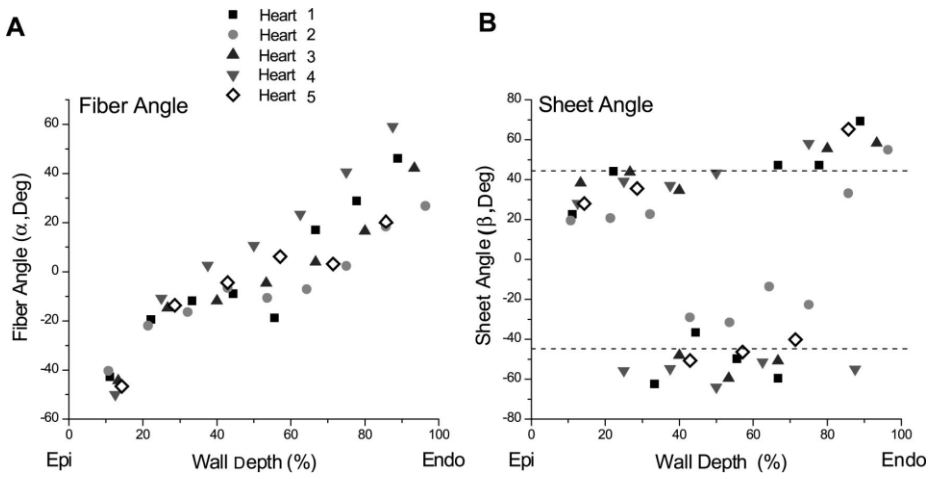


Figure 1.13 Helix angle and sheetlet angle
Transmural distribution of helix angles, α (A) and sheetlet angles, β (B) in the lateral wall from 5 ex vivo sheep hearts measured at histology. Sheetlet angles were centred around 2 "families" approximately +45˚ in the epicardium and endocardium and -45˚in the midwall (Harrington et al., 2005).

1.2.1. Mechanism of Diffusion Imaging

Instead of using a homogenous magnetic field, diffusion imaging sensitises MRI to diffusion by linearly varying homogeneity using 2 strong magnetic field gradient pulses in a particular direction (Stejskal and Tanner, 1965). Protons in water molecules precess proportionally to magnet field strength but in the presence of a magnetic field gradient, the MRI resonant frequency varies along the direction of the gradient. With the first "diffusion winding" gradient pulse, precession occurs at different rates resulting in dispersion of dephasing. A second "diffusion unwinding" gradient pulse of the same magnitude is applied in the opposite direction to rephase the spins. This rephasing will not be perfect for protons that have diffused during the time between gradient pulses and therefore the signal remains dephased (lost or attenuated), creating darker voxels i.e. the faster the diffusion in the direction of the diffusion gradient, the darker the image. DT-CMR is an inherently low SNR technique due to diffusion signal attenuation and short T2 relaxation times of heart tissue.

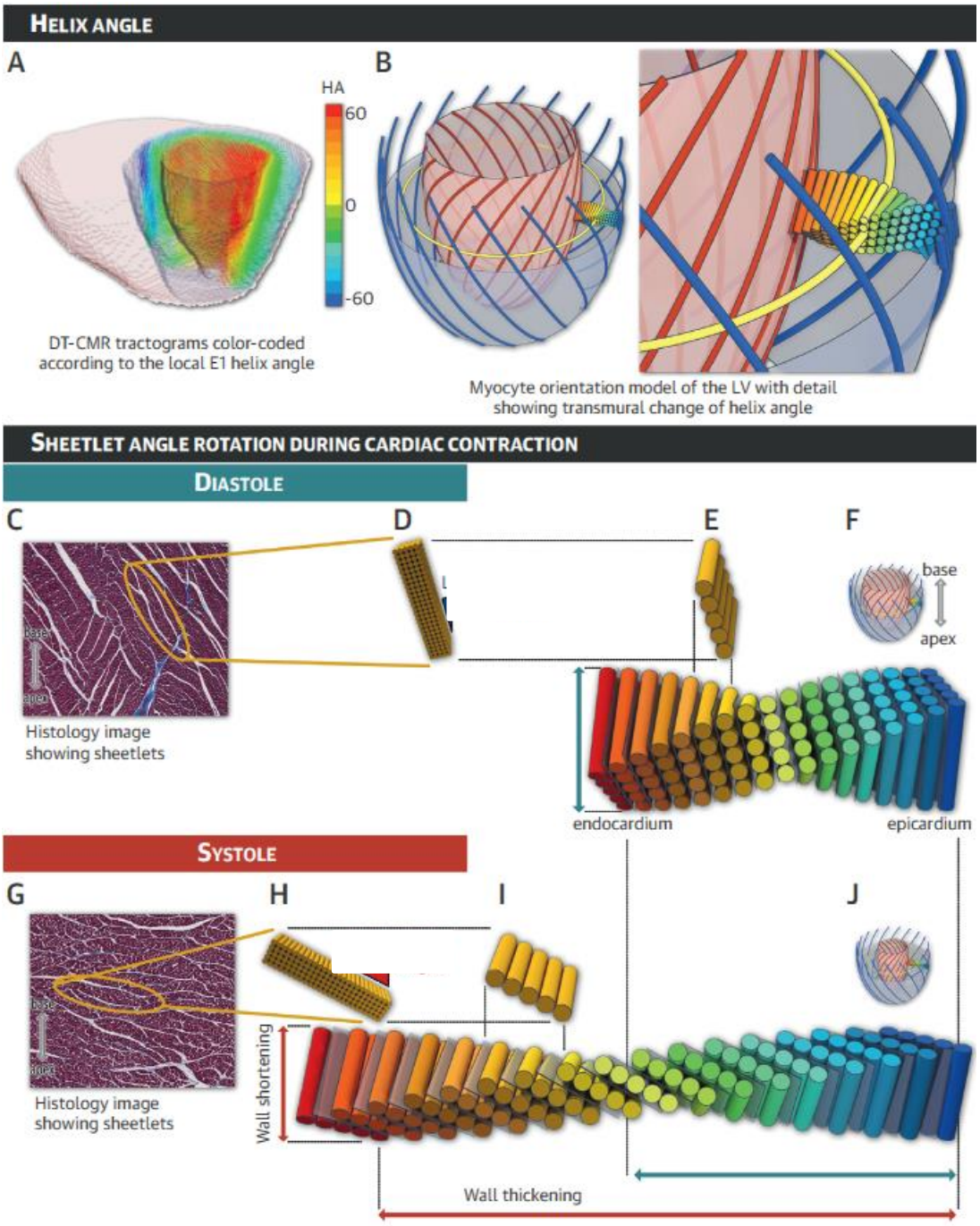


Figure 1.14 Myolaminar sheet dynamics

(A) Tractography from ex vivo DT-CMR depicting the primary eigenvector (ε1) direction color-coded by helix angle (HA). (B) Diagram of the helical structure of myocytes. Sheetlet angle (SA) rotation during cardiac contraction is depicted during diastole (C to F) and systole (G to J). Histology sections from the mid-myocardium cut perpendicular to the local cardiomyocytes acquired from relaxed (C) and contracted (G) ex vivo heart samples. The yellow ellipse surrounds a single sheetlet composed of closely packed cardiomyocytes bounded by the pale cracks of shear layers. Sheetlets vary from a relatively vertical orientation in diastole (D) to a relatively horizontal orientation in systole (H). See Online Video http://jaccjacc.acc.org/video/2016/3598_VID1.mp4 (Nielles-Vallespin et al., 2017).

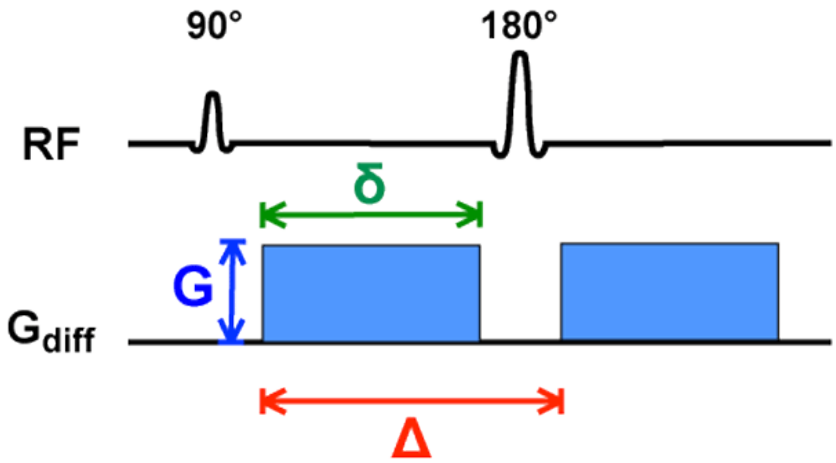


Figure 1.15 Stejskal-Tanner pulsed gradient spin echo diffusion sequence
Diffusion weighted images are produced by applying 2 strong gradient pulses of amplitude (G) and duration (δ), separated by time interval (Δ); $b = \gamma^2 G^2 \delta^2 (\Delta - \delta/3)$, where b is a measure of diffusion-weighting and γ is the gyromagnetic ratio. Protons which have diffused during the time between gradient pulses have signal loss and appear darker (*www.mriquestions.com).*

1.2.2. Diffusion weighting using the b-value

Two MR signals are needed to quantify diffusion:

- Baseline signal without diffusion sensitive gradients
- Diffusion attenuated signal using a diffusion-sensitising gradient

These two signals are obtained using different b-values; a low b-value close to 0 (b_{ref}) and a high b-value (b_{main}). The b-value, named after Dennis LeBihan, the father of modern diffusion imaging, is a measure of diffusion-weighting. The larger the b-value, the greater the diffusion effects. Large b-values are achieved by increasing the gradient amplitude and duration and widening the time interval between paired gradient pulses (Figure 1.15). The b-value combine these physical factors into a single parameter and is measured in s/mm^2 (Le Bihan et al., 1986).

1.2.3. Development of in vivo DT-CMR

Although diffusion tensor imaging is widely used in the brain, in vivo DT-CMR is technically more challenging with prohibitively long acquisition times. Thus DT-CMR has largely been used ex vivo. For example high quality whole heart DT-CMR datasets of the ex vivo rat heart are often acquired overnight with acquisition times in excess of 15 hours (McClymont et al., 2017b). In vivo methods require the following:

- Sensitivity to microscopic motion of water molecules - by "freezing" macroscopic cardiac and respiratory motion which are several orders of magnitude larger. ECG-gating ensures that diffusion measures are obtained at identical points in the cardiac cycle. Respiratory motion is minimised by instructed breath holding. Synchronised breathing (Tseng et al., 1999) and navigator approaches (Reese et al., 1995) have also been used.
- High SNR images – for reliable tensor calculation by using sufficiently high b-values to provide good contrast between the reference and diffusion-weighted images

1.2.3.1. Spin echo sequence

The Stejskal-Tanner diffusion sequence uses spin echo with echo planar imaging (EPI) readout (Figure 1.15) (Stejskal and Tanner, 1965). Spin echo is generated by two successive radiofrequency (RF) pulses. EPI is an acquisition mode which allows the acquisition of individual MR slices in a time frame of 50-100 ms thus minimising the effects of patient motion. This standard spin echo method is unsuitable for in vivo cardiac imaging as strong

diffusion gradients at different points within the same cardiac cycle results in gross cardiac motion artefacts.

1.2.3.2. **Stimulated Echo Sequence**

While spin echo arises from two RF pulses, a stimulated echo occurs from the action of 3 or more RF pulses. The stimulated echo acquisition mode (STEAM) thus splits the refocusing 180° RF pulse into two 90° pulses. The timing of the stimulated echo (STE) depends on the spacing of the 3 RF pulses. If the first two pulses are separated by time TE/2, the peak of the STE will occur precisely at TE/2 after the third RF pulse. The mixing time, TM is the interval between the second and third pulses, during which the magnetisation is "stored" along the z-axis and does not undergo T2 decay. Thus, the echo time, TE for the sequence is defined by TE/2 +TE/2. The first winding and second unwinding diffusion encoding gradients are applied with the same polarity (monopolar) at the same point in two adjacent cardiac cycles when the heart has the same position and velocity (Figure 1.16). STEAM with an EPI readout produced the first in vivo diffusion weighted images in the human heart in 1994 (Edelman et al., 1994). The resulting diffusion time is long which permits the use of smaller diffusion gradients which are less sensitive to cardiac motion but at the expense of increased loss of SNR. Longer diffusion time also produces enhanced tissue characterisation as water molecules have longer to diffuse through myocardial structures which may provide better insight into the underlying architecture.

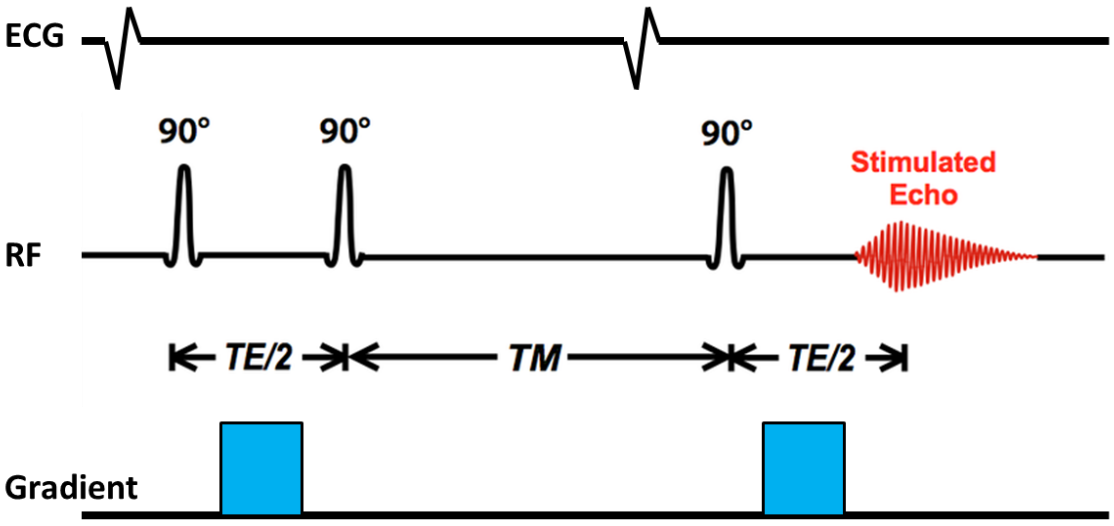


Figure 1.16 Stimulated Echo Acquisition Mode (STEAM)
Winding and unwinding diffusion gradients of the same amplitude and duration are applied at identical points in two consecutive cardiac cycles. The diffusion sensitising period is equivalent to the mixing time, TM which is equal to the subject's RR interval (*www.mriquestions.com).*

1.2.3.3. **Strain effects using stimulated echo**

STEAM sequences make use of the cyclical nature of cardiac motion, but this makes them sensitive to myocardial strain. Strain effects of STEAM were initially described in experiments using a gelatine phantom deformed by a plunger during the diffusion time which then relaxed before the rewinding gradient was applied (Reese et al., 1996). Diffusion signal losses were increased along the direction of compression (negative strain) which led to artificially increased ADC, while diffusion signal losses were reduced in the direction perpendicular to compression (positive strain) resulting in reduced ADC. However, gelatine is an isotropic material and therefore comparisons with anisotropic myocardium were reported to be erroneous as wall thickening in systole is primarily produced by sheetlet reorientation with only limited contribution from myocytes shortening (Nielles-Vallespin et al., 2017).

Sweet spot imaging has been used to overcome strain effects (Tseng et al., 1999). The “sweet-spots” are two points in the cardiac cycle when the time spent in positive (diastole) and negative (systole) strain are balanced and therefore the net effect of strain on diffusion is zero. However, this results in increased motion artefacts as the myocardium is actively moving during the sweet spot. Furthermore, analysing strain data to calculate the sweet-spot timings are time consuming during an in vivo scan. An alternative would be to correct diffusion using accurate 3D strain data although this would be at the expense of prolonged scan duration, increased data processing time and increased chance of systematic error.

In vivo DT-CMR using STEAM with and without strain correction via 3D tagging in 10 healthy controls demonstrated that strain correction was required when acquired at systole or diastole , except for FA acquired in diastole which was unchanged by strain correction (Figure 1.17) (Stoeck et al., 2014). This phenomenon can be observed from the time curves of strain, ADC and FA obtained from earlier work using gelatine phantoms (Figure 1.18) (Tseng et al., 1999). However, the impact of strain correction on helix angle and sheetlet angle in diastole was small. Conversely, ADC increased in systole and decreased in diastole as predicted by the gelatine experiments. There were also large differences in systolic sheetlet angles. Thus, diastolic FA is the only reliable DT-CMR invariant suitable for investigation using STEAM without strain correction.

		systole		diastole	
		w/o correction	with correction	w/o correction	with correction
ADC [10^{-4} mm²/s]	base	8.6±1.2*	9.5±1.3	8.5±1.0*	8.2±1.0†
	medial	8.8±1.4*	10.1±1.8	9.2±1.1*	8.7±1.1†
	apex	9.6±0.8*	11.2±1.2	10.1±1.1*	9.4±0.9†
FA	base	0.52±0.03*	0.61±0.02	0.61±0.05	0.61±0.04
	medial	0.52±0.05*	0.60±0.03	0.61±0.04	0.61±0.04
	apex	0.48±0.02*	0.55±±0.02	0.57±0.03	0.57±0.03†

* indicates statistical significance (p-value<0.05) between uncorrected and corrected data and
†indicates statistical significance between systole and diastole.

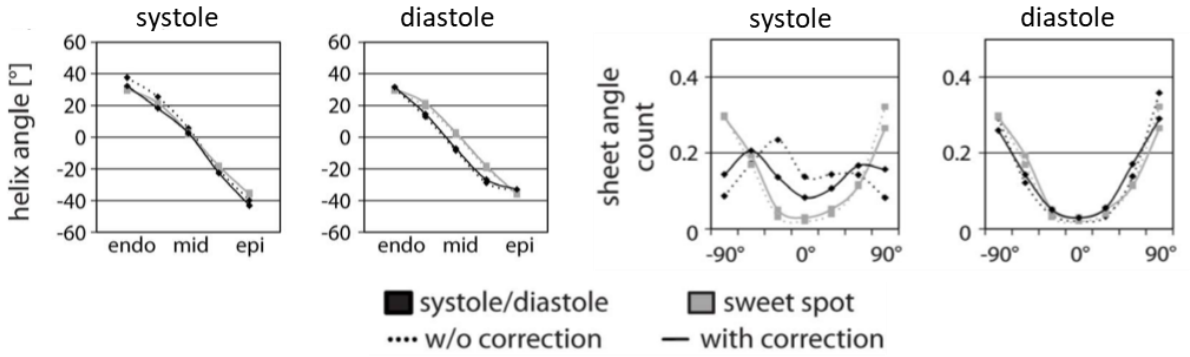


Figure 1.17 Diffusivity, fractional anisotropy, helix angles and sheetlet angles with and without strain correction

Significant differences are seen with and without strain correction in ADC, systolic FA, helix and sheetlet angles. Albeit differences were small in helix angle and diastolic sheetlet angle. Importantly, diastole FA remained unaffected by strain correction (Stoeck et al., 2014).

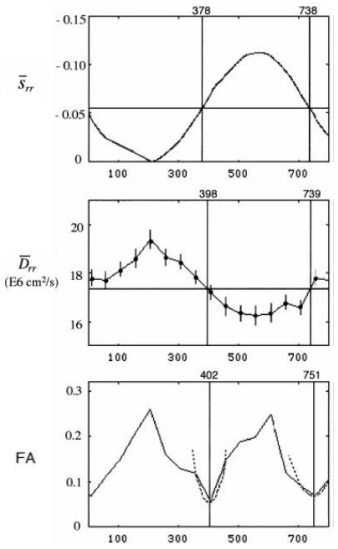


Figure 1.18 Time curves of radial strain, diffusion and FA in a gel phantom

Time is referenced to the ECG R-wave. Sweet spot locations, indicated by vertical lines, are defined by the intersections of the time curves with horizontal lines representing net strain is zero (top panel) or diffusivity measured in the absence of strain (true diffusion). The sweet spots predicted by strain agree with those determined on the diffusion curves and correspond with times of minimum FA (Tseng et al., 1999).

1.2.3.4. **Number of diffusion-encoding gradient directions**

Most in vivo cardiac studies use the minimum of 6 diffusion directions to calculate the diffusion tensor. However, tensor estimation accuracy improves with increasing number of diffusion directions but at the expense of increased scan duration. For example, brain DTI uses 32-64 directions while the exquisite DTI tractography of white matter tracts are generated using 256 diffusion directions (Figure 1.19). However, neuronal axons are highly anisotropic (closely linear) which require a greater number of directions to characterise as most directions will be close to zero. In comparison, myocytes are more isotropic and therefore 6 directions may be acceptable.

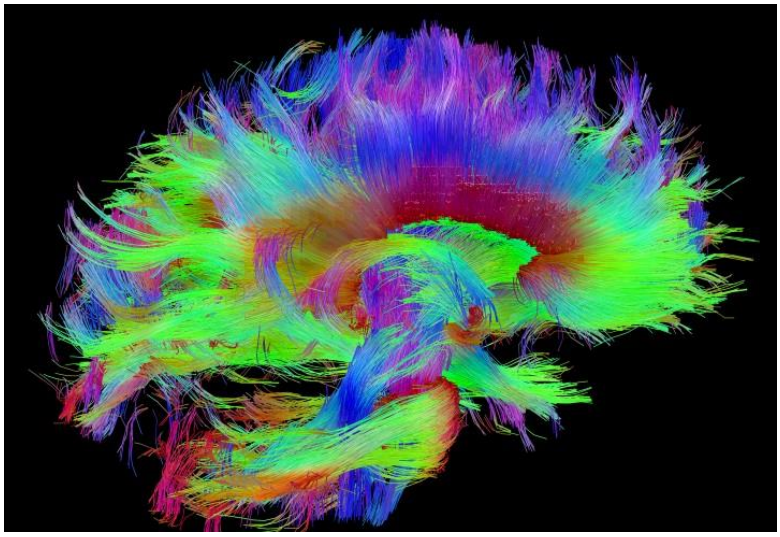


Figure 1.19 White matter tractography
From the connectome scanner dataset (*www.humanconnectomeproject.org*).

1.2.3.5. **Optimal b-value**

The b value is determined by gradient amplitude, duration and interval between gradient. Thus b-value is dependent on the subject's heart rate as the RR interval will define the interval between gradients. The gradient strength of the scanner often limits increasing the b-value.

However, increased b-values results in decreased SNR. Optimal diffusion weighting in the brain is around 900-1000 s/mm^2. However most in vivo cardiac studies have used values between 300-500 s/mm^2 (Edelman et al., 1994, Reese et al., 1995, Reese et al., 1996, Tseng et al., 1999, Dou et al., 2002, Dou et al., 2003, Wu et al., 2006, Tseng et al., 2006, Wu et al., 2009). Recent work from the Royal Brompton report 750 s/mm^2 as optimal for cardiac diffusion in combination with b_{ref} 150 s/mm^2 (Scott et al., 2015). Diffusion weighting of the reference image minimised the signal loss caused by intravoxel incoherent motion (IVIM) other than diffusion such as microvascular perfusion (Le Bihan et al., 1988), but in turn this requires higher b_{main} than previous in vivo cardiac studies to ensure a sufficient difference in signal intensity. ADC and FA are no longer comparable to previous studies once there is a change in b-values (Figure 1.20).

IVIM assumes that the capillary network has a random organisation and therefore causes a rapid “pseudo-diffusion” attenuation of signal from blood perfusion which is up to three orders of magnitude greater than “true” diffusion. This can be observed as a deviation from the Gaussian model at lower b-values (Figure 1.20). The signal also deviates at high b-values. The Gaussian model which is used in diffusion tensor calculations, assumes a single diffusion compartment (known as a mono-exponential diffusion tensor model). However, biological tissue deviates from Gaussian behaviour due to hindered and restricted diffusion from intracellular and extracellular microstructure. A number of models have been proposed to describe this non-Gaussian behaviour including diffusion kurtosis, bi-exponential and multi-compartmental (with fast and slow components) models (McClymont et al., 2017a).

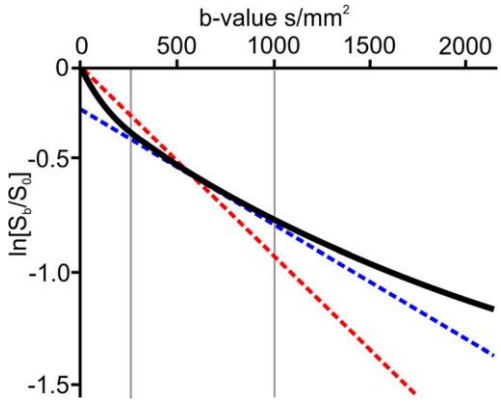


Figure 1.20 Diffusion signal decay as a function of b-value in the myocardium
The solid black line is the diffusion signal decay which is multi-exponential due the complexity of diffusion within biological tissue. For low b-values the signal from intra voxel incoherent motion causes rapid decay of signal up to ~200 s/mm^2. For higher b-values the decay also deviates. ADC calculated at different b-values will have different values. For example the red line denotes the signal at b=0 s/mm^2 and b=500 s/mm^2 which will produce a different ADC compared to the blue line which is the signal at b=300 s/mm^2 and b=1000 s/mm^2 (Froeling et al., 2014).

1.2.3.6. **Number of signal averages**

Signal averages are repeated acquisitions of the same frame used to generate sufficient SNR for diffusion tensor calculation. 8 signal averages are deemed optimal in the brain (Jones et al., 1999). Tensor accuracy once again increases with increasing number of signal averages but at the expense of longer scan duration and the increased risk of registration of artefacts between averages.

1.2.3.7. **Noise**

Noise strongly affects the accuracy of the tensor and thus derived parameters such as FA depend on SNR (McClymont et al., 2017b). Low SNR causes eigenvalue repulsion causing an overestimation of the primary eigenvalue and FA, and an underestimation of tertiary eigenvalue (Jones and Basser, 2004). For example, if diffusion is isotropic, the eigenvalues are

equal. However, in the presence of noise, the primary eigenvalue increases while the tertiary eigenvalue decreases from their true value, creating apparent anisotropy. This effect is most evident at low b-values.

1.2.4. Limitations of in vivo DT-CMR using stimulated echo

Specific limitations of stimulated echo DT-CMR include:

- Long scan duration – at least 8 averages are acquired due to low SNR
- Long breath-hold – acquisitions require 6 diffusion directions and a reference image
- Impossible in arrhythmia – heart needs to be the same shape at the second diffusion encoding
- Consistent breath-holding – heart needs to be in the same position at the second diffusion encoding
- Low spatial resolution – large voxels are needed to generate adequate signal due to low SNR
- Need for strain correction except for diastolic FA
- EPI images susceptible to distortion – by B_0 inhomogeneity

1.3. Electrocardiographic phenotyping of HCM

The ECG is altered in most patients with HCM because of structural (disarray, hypertrophy, fibrosis (Watkins et al., 2011)), electrophysiological (ion channel remodelling) and chemical (altered calcium handling (Ashrafian et al., 2011)) abnormalities. These affect the conductive properties of the heart, resulting in slow propagation (Saumarez, 1994) and prolonged repolarisation (Passini et al., 2016), with likely pro-arrhythmic effects. The ECG is an important tool in the clinical diagnosis of HCM. However, reliable ECG risk markers are still not available despite the ECG being a likely correlate to aspects of the underlying disease processes.

Previous studies have attempted to investigate ECG abnormalities in HCM by visually describing pathological Q waves, wide QRS, prolonged QT interval and inverted T waves from paper ECGs (Savage et al., 1978, Lakdawala et al., 2011). This however has not yielded reliable risk markers (Sherrid et al., 2009, Maron et al., 1983). The relation of ECG abnormalities and the presence of hypertrophy and LGE by CMR have been assessed in small cohorts of around 100 patients with inconclusive results. Dumont et al. (2006) found that conduction abnormalities and abnormal Q waves were associated with septal hypertrophy and LGE in a population of 102 HCM patients. While no such association was found in a later study of 56 HCM patients in Japan (Satoh et al., 2009).

All the studies thus far, have categorised ECG abnormalities visually from paper printouts of only one or two heartbeats from 12 leads. Manual interpretation by experts is time-consuming, prone to observer variability and does not objectively capture the subtle shape diversities of ECG complexes. Computational analysis of digital ECG recordings is automated,

consistent and can make sense of such multivariate datasets in ways that are impossible for the human eye to process due to volume and complexity (Obermeyer and Emanuel, 2016).

Machine learning in ECG analysis can automatically learn data structure and make predictions. This learning can either be supervised or unsupervised. In supervised learning, algorithms are trained to learn data relationships and are then tested on unknown data. In unsupervised learning, algorithms learn data structure independently. These techniques make fewer assumptions by selecting discriminatory features from the whole ECG which could provide tools for phenotyping the heterogeneous HCM population.

1.3.1.1. **Heartbeat classification, feature extraction and dimensionality reduction**

Normal sinus heartbeat detection is a well-developed machine learnt classification based on established databases (Moody and Mark, 2001). These classification techniques require quantitative descriptions of the heartbeat using a feature vector (multi-dimensional vector of numerical features). One heartbeat is composed of a p wave, QRS complex and T wave which represent different electrical events within the cardiac cycle across 12 different leads. Traditionally, the ECG waveform has been described by standard features such as slopes, amplitudes and time intervals (Maron et al., 1983). Even when obtained from digital signals, these discrete features are prone to delineation errors. However, computational approaches now exist to model the ECG using mathematical transforms such as the Hermite transform, to allow morphological assessment rather than extracting discrete features from the raw data (Laguna et al., 1996). Both standard and morphological features can be combined to

characterise the ECG signal, which can be computed over several leads to produce a single feature vector (De Chazal et al., 2004).

When there are low numbers of training datasets, a large number of extracted features may cause overfitting. Thus, techniques such as dimensionality reduction and feature selection are used to reduce features and improve algorithm performance. Dimensionality reduction reduces the number of random variables under consideration using principal component analysis (Nasiri et al., 2009) or linear discriminant analysis (Kumar and Kumaraswamy, 2012) (Figure 1.21).

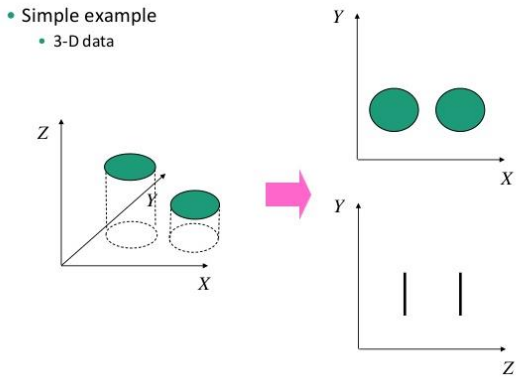


Figure 1.21 Dimensionality reduction
A simple example of how three-dimensional data can be reduced to one dimension.

Feature selection selects only a small subset of the most significant features in the classification (Figure 1.22). Robust features are needed to ensure high performance in classification algorithms, which require good quality signal pre-processing for accurate delineation and filtration of noise. Surrogates of features obtained from mathematical transforms have been shown to reduce the effect of delineation errors (Llamedo and Martínez, 2011).

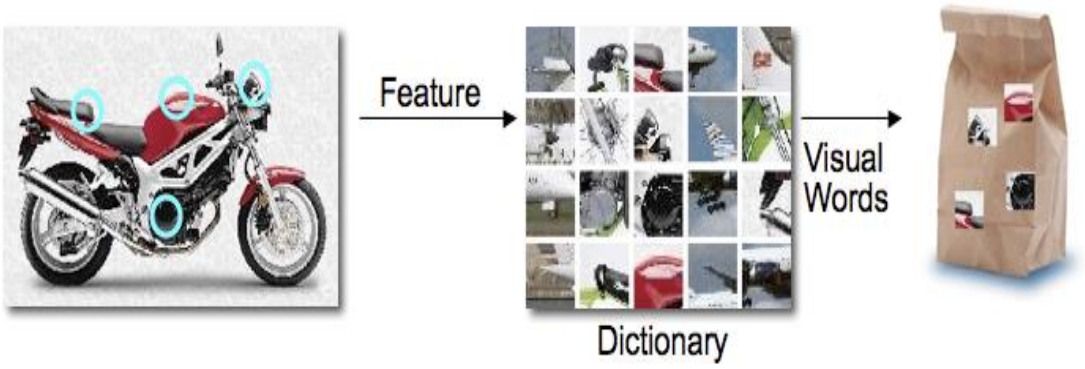


Figure 1.22 Feature extraction
An example of how a motorcycle can be identified by 4 features.

1.3.1.2. **Clustering analysis for patient stratification**

Many studies assess the ability of machine learning methods to distinguish between health and disease or between different diseases. However, computational techniques have the potential to go beyond binary classification which doctors with expert knowledge already do well. Clustering algorithms could be adapted to assess heterogeneity within HCM populations (Figure 1.23). These groups would then need to be interrogated to highlight which biomarkers were significant in distinguishing between groups, thus providing insight into the structure of HCM populations that may be previously unknown. However such algorithms are only predictive and do not give causal information.

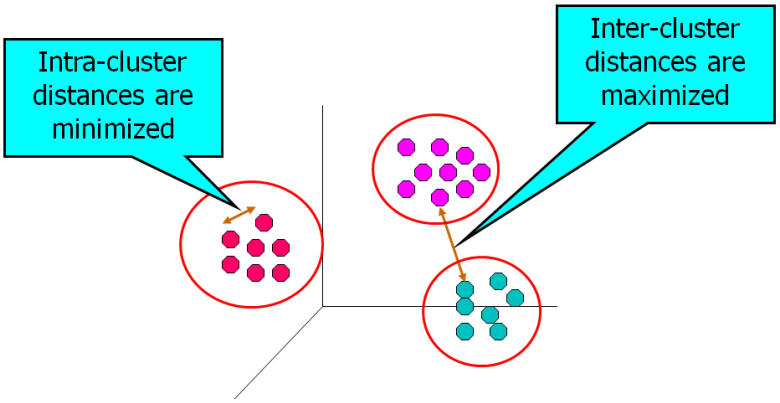


Figure 1.23 Clustering analysis
A method to find groups of objects such that objects in a group are similar or related to one another but different from or unrelated to object in other groups.

1.4. Study aims and hypotheses

1. To assess diastolic FA as a non-invasive biomarker of myocardial architecture.
2. I hypothesised that FA would be reduced in HCM compared to healthy controls due to disarray and fibrosis.
3. I hypothesised that low FA in HCM represents the anatomical substrate for electrical instability and therefore examined the relationship between low FA and ventricular arrhythmia in HCM patients.
4. I hypothesised that ECG morphology encodes underlying HCM disease processes, which could be used to characterise disease heterogeneity. My aim was to identify distinct HCM phenotypes based on ECG computational analysis and describe these groups by clinical risk factors and anatomical differences using CMR imaging.

CHAPTER 2. **METHODS**

2.1. **Overview**

This single-centre prospective study was approved by the National Research Ethics Committee (REC ref 12/LO/1979) and informed written consent was obtained from each participant. HCM patients were recruited from the University of Oxford Inherited Cardiac Conditions clinic, John Radcliffe Hospital, UK. Healthy volunteers were identified from poster advertisements across the University of Oxford and University of Oxford NHS Foundation Trust. For Chapters 3-5, 30 healthy controls and 50 HCM patients were recruited. For Chapter 6, an additional 8 healthy controls and 35 HCM patients (including 9 genotype positive, hypertrophy negative individuals and 19 patients with ICDs) were recruited.

2.1.1. Inclusion criteria

- Aged 18 years or above
- Willing to participate in a research study on a voluntary basis

Healthy controls

- Asymptomatic, no medical history, not taking medications, non-smoker
- Normal physical examination and 12-lead ECG

HCM

- Pathogenic sarcomeric gene mutations (in myosin-binding protein C, MYBPC3; beta-myosin heavy chain, MYH7; troponin I, TNNI3) and LVH ≥13mm or, in the absence of an identified mutation, LVH ≥15mm in the absence of another cause for LVH

HCM gene mutation positive, but no LVH (G+LVH-)

- Pathogenic sarcomeric gene mutations (as above) and LV wall thickness ≤12mm

2.1.2. Exclusion criteria

- Current smoker or a history of smoking in the past 10 years
- History of hypertension, diabetes, atrial fibrillation, coronary artery disease, or valvular heart disease
- HCM phenocopies
- Body mass index ≥35 kg/m^2
- Healthy controls: family history of cardiomyopathy or sudden cardiac death
- HCM patients with ICD: paced rhythm

For participants undergoing CMR:

- Any contraindications to MR scanning (metal implants, pacemakers, claustrophobia, previous head or eye surgery)
- History to suspect pregnancy, a positive pregnancy test or breastfeeding
- Impaired renal function (eGFR <30 ml/min/m^2)

2.2. Clinical Assessment

History and physical examination were performed which included height, weight and blood pressure measurements. Bloods were taken to measure haematocrit.

2.3. Electrocardiographic measurements

2.3.1. 12-lead resting ECG

A 12-lead resting digital ECG was acquired either by me (with 10 years of clinical experience) or a senior cardiac research nurse according to the 2007 AHA/ACC guidelines on ECG Part 1 (Burdick 8500, Glasgow, UK) (Macfarlane et al., 1990). The Burdick recording was 10 seconds with 12 leads recording simultaneously. The sampling rate was 8000 Hz. Automated measurements of ECG axes, amplitudes and intervals were obtained for both global and single-leads from the Burdick ECG XML files. Q waves were considered pathological if they were >30 ms in duration and > 1/3 of the R wave in depth in two or more contiguous leads (I, II, V1-6). Abnormal T wave axis deviation was classified as <-15° to ≥-180° or >105° to ≤180°. T wave inversion was defined as T wave amplitude ≤−0.1 mV and giant T wave inversion ≤−1.0 mV in two or more contiguous leads in V3-6.

2.3.2. 12-lead ambulatory Holter ECG

All participants also underwent 12-lead ambulatory digital Holter monitoring (sampling frequency 1,000 Hz, H12+, Mortara Instrument, Milwaukee, WI, USA) for 24 hours after the CMR scan. Participants were advised not to restrict their daily activities during the recording. These ECG recordings were not assessed clinically but were analysed by Dr Aurore Lyon, Research Fellow in the Computational Cardiovascular Science Group, Department of Computer Science, University of Oxford. The group has a strong focus on Computational Cardiac Electrophysiology with expertise in ECG signal processing and computational modelling and simulation. These methods are described in Chapter 6.

2.4. Diffusion Tensor Cardiac Magnetic Resonance (DT-CMR) acquisition

DT-CMR was performed using an ECG-gated monopolar stimulated echo acquisition mode (STEAM) single-shot echo planar imaging sequence at 3 tesla (TIM Trio, Siemens) with anterior and posterior 16-channel cardiac array coils of which all 32 elements were used in each image. The STEAM sequence diffusion encoded over one cardiac cycle as previously described (Figure 2.1) (Reese et al., 1995, Nielles-Vallespin et al., 2013, Tunnicliffe et al., 2014). Sequence parameters were: fat saturation, TR = 2 RR intervals, TE = 22 ms, BW = 2442 Hz/pixel, GRAPPA parallel imaging acceleration factor of 2, FOV = 360 x 135 mm, acquisition matrix = 128 x 48 pixels, spatial resolution = 2.8 x 2.8 x 8 mm^3, interpolated to 1.4 x 1.4 x 8 mm^3.

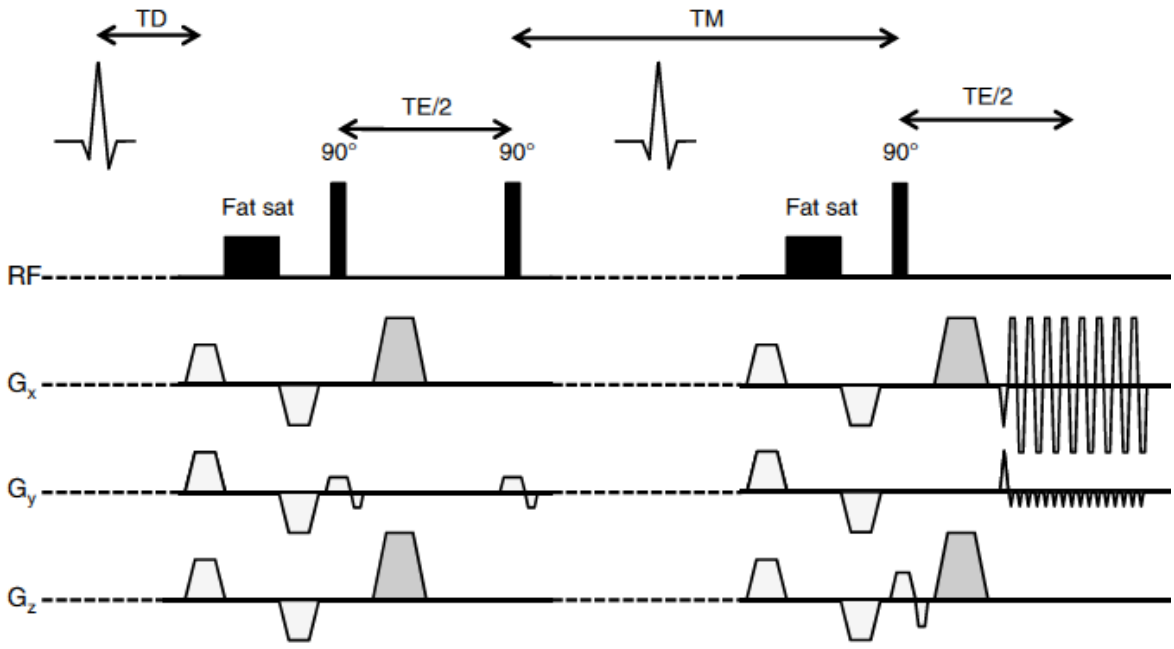


Figure 2.1 The STEAM DT-CMR sequence used

The diffusion weighting gradients were fixed in magnitude and duration, therefore the b-values depended on the subject's RR interval during scanning. For example, a heart rate of 60 beats per minute (bpm) yielded a b-value of 350 s/mm^2, while a heart rate of 45 bpm, increased the b-value to 467 s/mm^2. Spoilers were used in the reference image to avoid unwanted magnetisation to ensure equal T1- and T2-weighting in all images, which yielded a b-value of 15 s/mm^2 with a heart rate of 60 bpm. Diffusion-encoding gradients negated the need for spoilers in the diffusion-weighted images.

Standard cardiac localisers were obtained to determine the short axis orientation and cardiac cine to determine end diastole and peak systole. Subject-specific second-order shimming was performed to minimise the main magnetic field inhomogeneities using an adjustment volume covering the whole left ventricle.

Three ventricular short-axis slices (base, mid and apical) were acquired during the diastolic and systolic pause. The mid ventricular slice was defined as the first slice from the mitral annulus to contain papillary muscles. The basal and apical slice was acquired as either the next or the second contiguous slice from the mid depending on the LV length to ensure adequate coverage of the LV using 3 slices. Care was taken to avoid the LV outflow in systole on the basal slice and to avoid LV tapering towards the apex in the apical slice. Tagging was used to track the slice location between diastolic and systolic acquisitions so that the tissue imaged was the same. Linear tags separated by 16 mm were used in the 2- and 4-chamber long-axis views. The displacement of the linear tag was manually tracked from the diastolic to the systolic phase.

Each acquisition was an 18-heartbeat breath-hold including reference image (b=15 s/mm^2) and 6 diffusion-encoding directions (b=350 s/mm^2, for heart rate of 60 bpm):

- 2 heartbeats: phase correction lines
- 2 heartbeats: external GRAPPA reference lines
- 2 heartbeats: b=15 s/mm^2 reference image
- 12 heartbeats: b=350 s/mm^2; 6 diffusion encoding directions

This was repeated to obtain a minimum of 8 averages (Figure 2.2). Images affected by breathing motion or ectopy were repeated. Total acquisition time was approximately 10 minutes per slice which consisted of a minimum of 8 breath-holds of 15-20 seconds duration with recovery time between breath-holds.

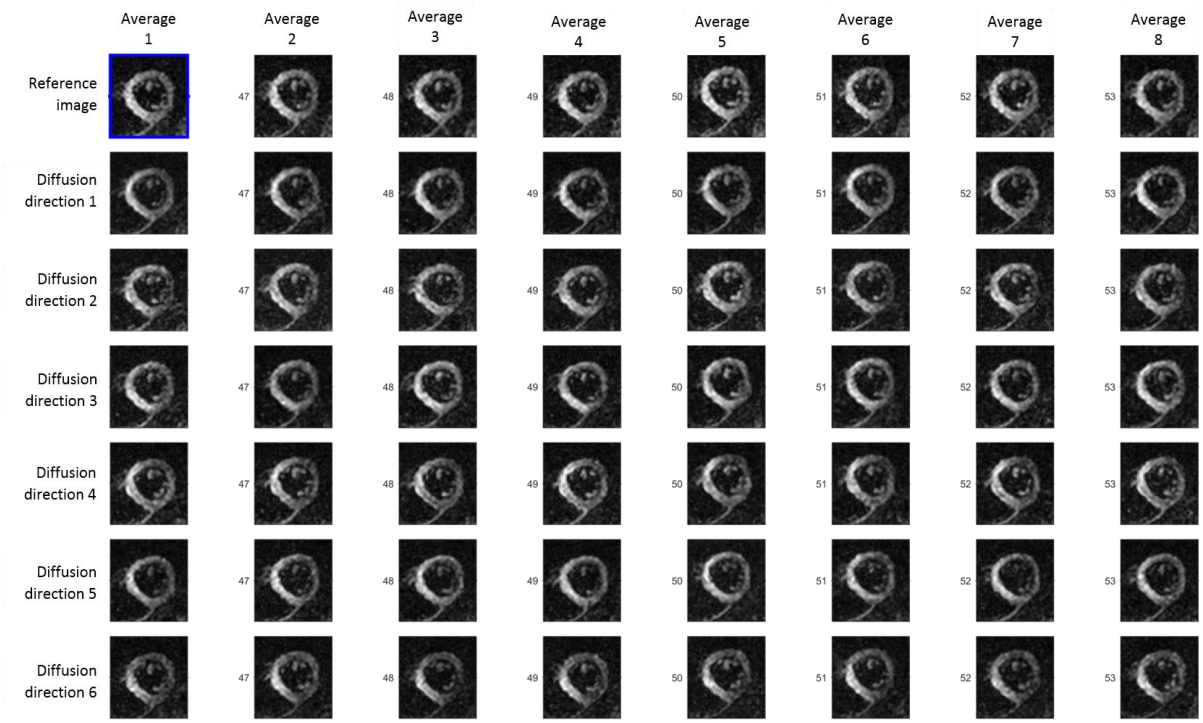


Figure 2.2 DT-CMR acquisition
Each DT-CMR acquisition consists of a reference image and 6 diffusion encoding directions which are repeated to obtain a minimum of 8 averages.

2.5. DT-CMR sequence validation and reproducibility

2.5.1. Phantom validation of DT-CMR sequence

In order to validate the accuracy with which our DT-CMR STEAM sequence measured ADC, we imaged four alkane phantoms (Sigma Aldrich, Gillingham, UK) with a range of diffusivities (Tunnicliffe et al., 2014). Good agreement was seen between the measured diffusivity and expected values from the literature (Table 2.1) (Tofts et al., 2000). We were the first group to demonstrate the accuracy of DT-CMR using STEAM in phantoms with known diffusivities.

Table 2.1 Phantom validation of DT-CMR STEAM sequence
MR parameters, expected diffusivities and measured diffusivities of four alkane phantoms, mean ± standard deviation (Tunnicliffe et al., 2014).

	T1 (ms)	**T2** (ms)	**ADC** ($x10^{-3}$ mm^2/s)	
			Literature value at 19.3°C (Tofts et al., 2000)	**STEAM EPI**
Undecane	1331	204	0.994	0.999
Dodecane	1160	163	0.770	0.794
Tridecane	999	173	0.623	0.670
Pentadecane	751	178	0.395	0.419

2.5.2. Inter-centre reproducibility in healthy volunteers

Although intra-centre reproducibility of DT-CMR parameters have been demonstrated in both healthy controls (Nielles-Vallespin et al., 2013) and HCM patients (McGill et al., 2012), FA and ADC values are inconsistent across centres (Figure 2.3 and Table 2.2). DT-CMR is not standardised due to the use of different magnet field strengths, b-values, time points in the cardiac cycle, voxel size, post-processing techniques, all of which affect quantitative DT-CMR parameters. Therefore we assessed inter-centre reproducibility of these diffusion measures in collaboration with Professor Dudley Pennell, Dr David Firmin and colleagues at the Royal

Brompton Hospital, Imperial College, London using well-matched sequences and processing (Tunnicliffe et al., 2014).

A single mid-ventricular short-axis slice was imaged in ten healthy volunteers at our centre (Centre O) and the within 7 days at Royal Brompton Hospital, Imperial College, London (Centre B) where the stimulated echo diffusion EPI sequence had been independently implemented on a 3T Skyra scanner (Siemens). Our ADC and FA values were higher than their previously reported values (Nielles-Vallespin et al., 2013, McGill et al., 2012). Previous publications had not accounted for the small diffusion weighting of the b_{ref} gradient from spoiler gradients which when included showed good agreement with our work (Nielles-Vallespin et al., 2014). Initial analysis showed a bias in both ADC and FA between the centres which was due to a difference in ROIs. Centre B drew extended into the full epicardium while centre O excluded the epicardial border. Once similar ROIs were used, we were the first collaborative group to show reproducibility of ADC and FA in 10 healthy controls scanned at two centres (Figure 2.4).

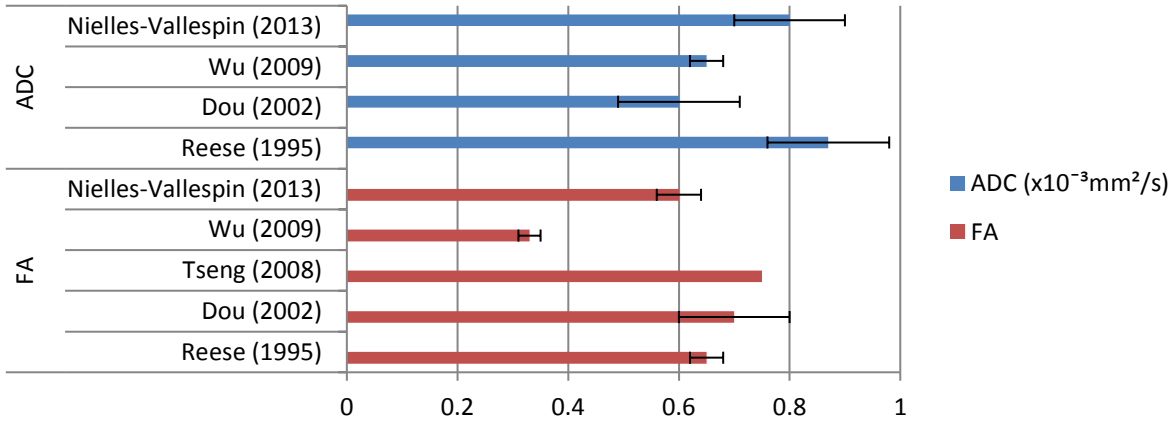


Figure 2.3 Comparison of previously published ADC and FA values in healthy controls

Table 2.2 Comparison of previously published ADC and FA values
ADC and FA mean ± standard deviation using DT-CMR STEAM sequences in controls, HCM and myocardial infarction (MI) (Tunnicliffe et al., 2014).

REFERENCE	Field strength (T)	Voxel size (mm^3)	ADC ($x10^{-3}$ mm^2/s) **Healthy controls**	ADC Disease (% change)	FA **Healthy controls**	FA Disease (% change)	Notes
(Reese et al., 1995)	1.5	3x3x9	0.87±0.11	-	0.65±0.03	-	Systole
(Dou et al., 2002)	1.5	4x4x12	0.60±0.11	-	0.7±0.1	-	Systole
(Tseng et al., 2006) **HCM**	1.5	3x3x3	-	-	0.78/0.75	0.72/0.56 (-22%)	Free wall/ Septum
(Wu et al., 2009) **Acute MI**	1.5	1.9x1.9x8	0.65±0.03	0.92 (+46%)	0.33±0.02	0.25 (-26%)	Systole
Chronic MI				0.74 (+17%)		0.27 (-21%)	Systole
(Nielles-Vallespin et al., 2013)	3.0	2.9x2.9x8	0.8±0.1	-	0.60±0.04	-	Systole
(McGill et al., 2012) **HCM**	3.0	2.9x2.9x8	-	0.73 (-9%)	-	0.62 (+3%)	Systole
(Tunnicliffe et al., 2014)	3.0	2.9x2.9x8	1.10±0.06	-	0.41±0.04	-	Systole
			1.20±0.09	-	0.54±0.03	-	Diastole

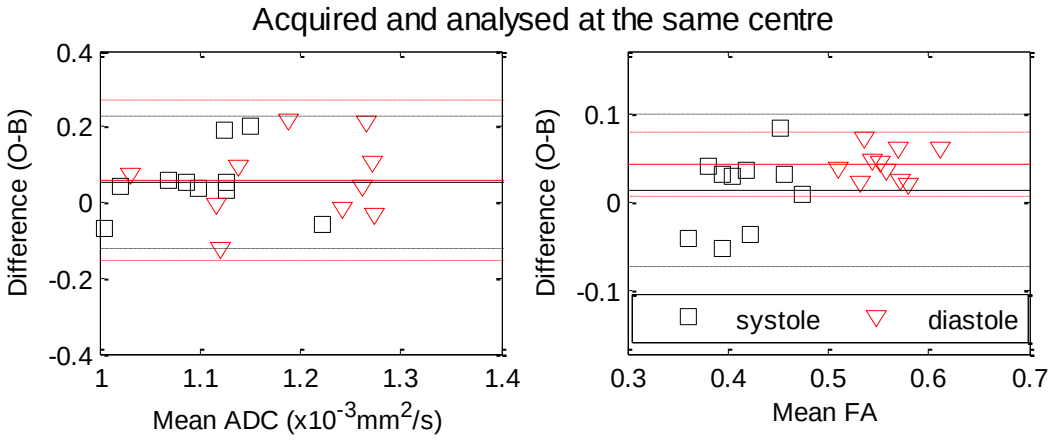


Figure 2.4 Bland-Altman plots to compare ADC and FA obtained by each centre independently
(Tunnicliffe et al., 2014)

2.6. DT-CMR practicalities

The following observations during scanning prompted protocol adjustments.

2.6.1.1. Poor Breath Holding

Due to the 18-heartbeat breath hold, some participants were unable to hold their breath for the full acquisition (Figure 2.5, Figure 2.6). Therefore, the order of diffusion directions was cycled with each repeat acquisition to ensure that any impact of poor breath-holding in the final direction was spread equally across all directions.

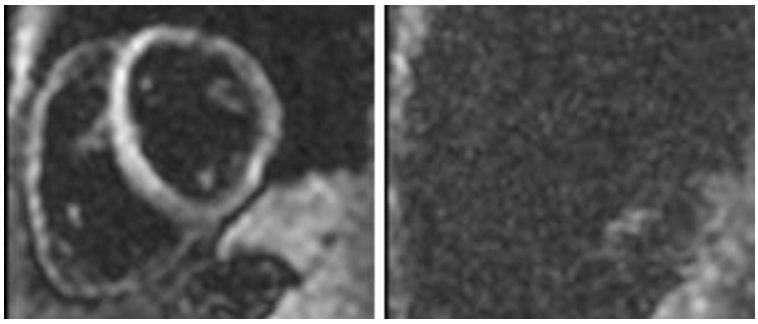


Figure 2.5 DT-CMR artefact due to breathing

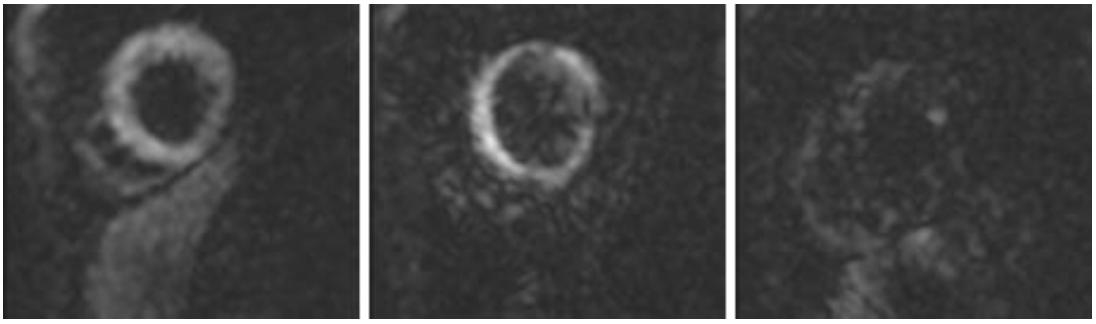


Figure 2.6 DT-CMR artefact due to gradual loss of breath-holding

2.6.1.2. **Arrhythmia**

Poor image quality was obtained during bi or trigeminy, sinus arrhythmia (Figure 2.7) and frequent ectopy. This was most likely due to subtle changes in ventricular filling between the two diffusion gradients resulting in the heart being at a slightly different position by the second diffusion encoding gradient and thus signal loss occurs. Additional averages were acquired for occasional ectopy; however, the scan was abandoned if arrhythmia persisted. For example, one patient had to return another day after starting beta-blockers (medication was started for clinical symptoms due to frequent ectopy and bigeminy).

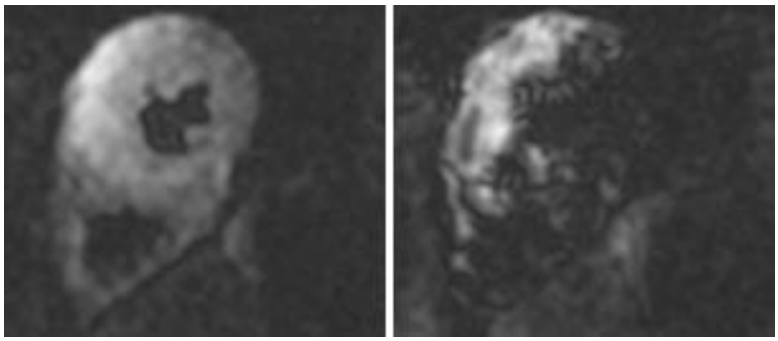


Figure 2.7 DT-CMR artefact due to marked sinus arrhythmia

2.6.1.3. **Bradycardia**

Poor quality data was obtained with heart rates <50 bpm (Figure 2.8). This was attributed to T1 decay during the mixing time.

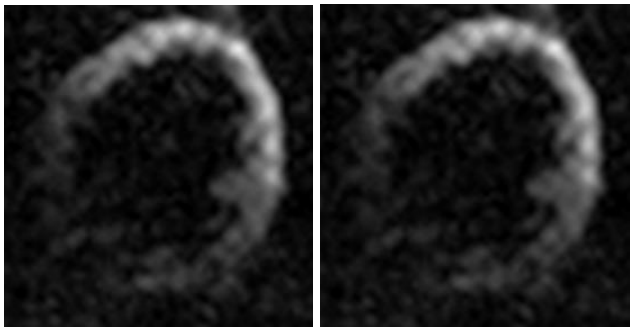


Figure 2.8 DT-CMR artefact due to bradycardia

2.7. DT-CMR post-processing

Post-processing was performed by a single observer (me) who was blinded to clinical data using custom-built software developed in house using MATLAB (Mathworks, MA, USA) as previously described (Tunnicliffe et al., 2014). Developments to the post-processing protocol are described.

2.7.1. DT-CMR segmentation

Epicardial and endocardial region of interest (ROI), and anterior interventricular insertion point were manually segmented on a single reference diffusion image per slice and phase. Segmentation was originally performed in MATLAB however the contouring tools were suboptimal for accurate delineation. Therefore, the protocol was modified to use cmr42© (Circle Cardiovascular Imaging, Calgary, Canada). All images were re-segmented and contours were then imported to MATLAB. Due to the limited spatial resolution of DT-CMR, segmentation was performed in conjunction with the corresponding cine slice to improve recognition of trabeculae (Figure 2.9). Left ventricular endocardial trabeculae, right

ventricular endocardium of the interventricular septum and papillary muscles were excluded from ROIs to avoid partial volume effects. Importantly, there are no partial volume effects from the blood pool as the stimulated echo diffusion preparation completely suppresses the free blood signal because of its motion, as well as any signal from fat (because of the its short T1). The mid-ventricular slice was divided into six segments based on the 16-segment LV model for analysis using the anterior insertion point as reference (Figure 2.14).

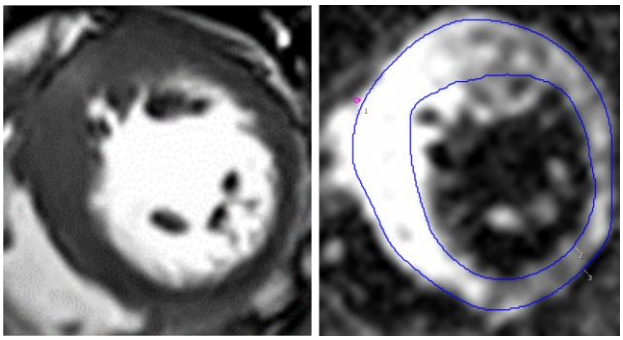


Figure 2.9 Manual segmentation of the first DT-CMR reference image
Manual segmentation of epicardial and endocardial borders were performed on a single DT-CMR reference image (right) per slice and the averages underwent rigid co-registration. Segmentation was performed alongside the corresponding cine slice (left) to ensure recognition of trabeculae.

2.7.2. Rejection of corrupted images

Diffusion images were visually inspected and corrupted frames were rejected (Figure 2.10). Corrupted frames were defined as partial or complete absence of the myocardium. This feature was implemented during protocol adjustments to avoid discarding the whole acquisition of reference and 6 directions when only select frames were degraded.

2.7.3. Image registration

A minimum of six averages per direction in each slice/phase set underwent rigid co-registration to the first reference image using a single-step discrete Fourier transform method to correct for variation in cardiac position between breath-holds (Guizar-Sicairos et al., 2008).

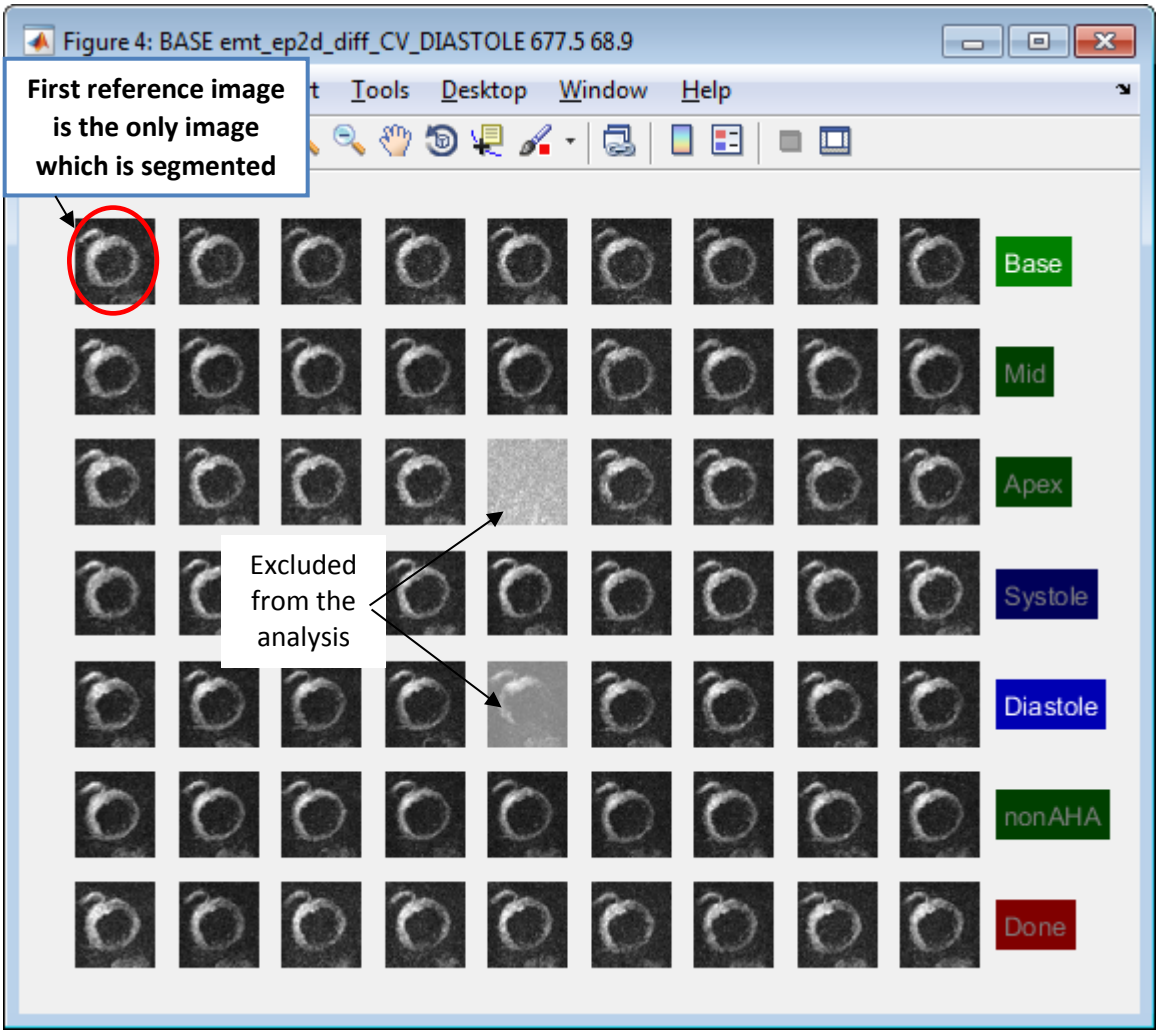


Figure 2.10 Manual rejection of corrupted DT-CMR images
Corrupted frames were defined as partial or complete absence of the myocardium.

2.7.4. Diffusion tensor calculation

The timestamp on each image was used to calculate the correct b-value based on the subject's heart rate. Six diffusion maps were calculated for each average, one for each diffusion

direction. The b-value in the reference image (which was non-zero due to the spoilers) was subtracted from the b-value of the diffusion-weighted image when calculating the diffusion maps. 48 maps (six directions and eight averages) per slice/phase was used to determine the diffusion tensor at each voxel using the H-matrix based method of Kingsley (Kingsley, 2006). The eigenvalues and eigenvectors were derived from the diffusion tensor which were used to calculate apparent diffusion coefficient (ADC; see page 17), fractional anisotropy (FA; see page 17), helix angle (HA), sheetlet angle (SA) and signal-to-noise ratio (SNR) voxel-wise. Voxels with negative eigenvalues, which violate the assumption that the tensor is positive definite, were excluded from the analysis. All parameters except HA were averaged across each segment and across the whole slice. HA was defined as the angle subtended by the projection of the primary eigenvector onto the tangential plane (circumferential-longitudinal) and the short-axis plane (circumferential-radial; Figure 2.11).

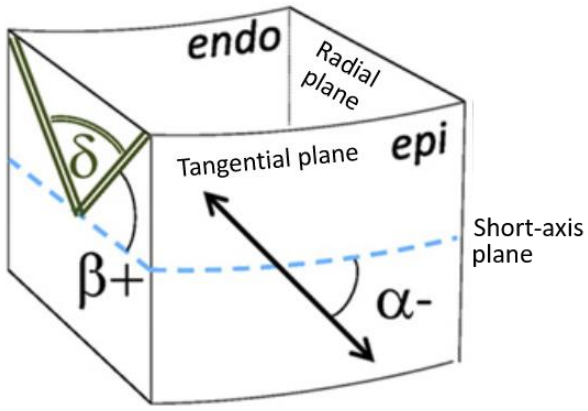


Figure 2.11 Fibre and sheetlet angle definitions
Excised tissue block. Black arrow indicates the epicardial fibre orientation. Double green lines indicate the transmural sheetlet orientation. The helix angle (α) is the deviation of fibre orientation projected in the tangential plane from the short-axis plane. Negative if fibres point from top-left to bottom right, and positive if fibre point from bottom-left to top-right. The sheetlet angle (β) is the deviation of sheetlets projected in the radial plane from short-axis plane. Positive if sheetlets are in an apico-basal (upward) direction and vice versa. The sheet-intersection angle (δ) is the deviation of opposite sheetlet populations (Hales et al., 2012).

HA was reported as the transmural HA gradient from the linear fit to provide a single transmural value for comparison between groups. 30 radial lines were defined from the centre of the LV to the epicardial border. The helix angles values between the endocardial and epicardial borders were fit to a straight line. The gradient of each linear fit, in degrees per mm, was averaged over all radial profiles to obtain the average radial gradient of the helix per segment and per slice. However, linear fitting assumes that the HA varies proportionally to transmural depth which it does not. In fact, the so-called transmural "layers" of the epicardium, mesocardium and endocardium are defined by the rate of change of angles (gradient) with a reduced gradient in the mesocardium (midwall). Albeit the gradient change is not as pronounced as seen in histology due to DT-CMR resolution and averaging (Figure 2.12). Thus, HA gradient causes smoothing of the data.

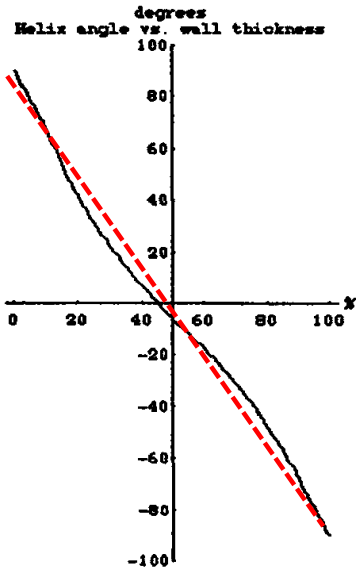


Figure 2.12 Helix angle from DT-CMR and histology data with linear fit for helix angle gradient calculation
Red line represents linear fit for the transmural HA gradient using DT-CMR data (left) from (Reese et al., 1995), which causes data smoothing as the gradient reduces in the midwall.

SA was defined as the angle formed between the projection of the tertiary eigenvector onto the radial-longitudinal plane and the short axis plane, and was positive for sheets rising towards the base from endocardium to epicardium, as previously described (Hales et al., 2012). The set of low b-value reference images for each subject after rigid-body registration was used to produce SNR maps by dividing the mean value of each pixel by the standard deviation of the signal within that pixel (Sodickson et al., 1999). Post-processing and analysis time were approximately 15 minutes per slice for each phase.

2.7.5. Transformation of DT-CMR parameters to normalised LV co-ordinates

360 radial lines were constructed from the centre of the LV to the epicardial border. The first of these lines passed through the anterior interventricular insertion point. For each radial line, the line segment between the endocardial and epicardial borders was divided into 30 equally spaced points, running transmurally. This resulted in a 360 by 30 grid spanning the whole myocardium in polar co-ordinates. For each DT-CMR parameter, the values on this grid were estimated by linear interpolation. This enabled images to be averaged across participants despite variation in LV shape (Figure 3.15, Figure 4.8). For example, a co-ordinate of (0, 15) would consistently measure the midwall of the anterior insertion point across people.

To calculate the epicardial to endocardial pattern of variation in DT-CMR parameters, these images were collapsed across the 360 radii to give a mean transmural trace for each participant. Across participant curves were obtained for each group by taking the mean at each of the 30 points, with error bars calculated as standard error of the mean across participants (Figure 3.14, Figure 4.10).

2.7.6. Tensor visualisation

For one individual participant, the shape of the diffusion tensor in each voxel in a slice can be visualised. For every alternate voxel, an ellipsoid was constructed with stretch factors corresponding to the three eigenvectors of the diffusion tensor, and principal axes aligned to the corresponding eigenvectors. This was achieved using the fanDTasia Toolbox for MATLAB (Barmpoutis et al., 2007). In Figure 4.14 the colours were mapped according to FA. This resulted in a representation in which voxels with very high FA appear as needles, orientated in the direction of maximum diffusion, whereas voxels with zero FA appear as spheres. Thus, the ellipsoid shape indicates the mixture of myocyte orientations within a voxel.

2.8. Cardiovascular Magnetic Resonance (CMR) imaging

CMR imaging was performed at 3 tesla (TIM Trio, Siemens). In chapter 6, 10 HCM patients with ICD at the time of enrolment did not undergo CMR. The previous clinical CMR prior to ICD insertion was evaluated in these patients.

2.8.1. Cine imaging

Cine imaging using a steady state free precession sequence in held end-expiration was acquired in the ventricular horizontal and vertical long-axis, short-axis, and 3-chamber views. Left ventricular (LV) volumes, mass and function were calculated from contiguous parallel short axis slices of 8 mm thickness with an interslice gap of 2 mm covering the entire heart (Karamitsos et al., 2007). LV short axis epicardial and endocardial borders were manually segmented at end diastole and end systole, for determining end diastolic volume (EDV) and end systolic volumes (ESV). End-diastolic maximal LV wall thickness was measured semi-automatically by the centreline method (Buller et al., 1997) according to the standard 16-segment LV model (Schiller et al., 1989) (Figure 2.13, Figure 2.14). 50 chords at equal distances were placed perpendicular to the centreline midway between the endo- and epicardial borders in each slice. Short-axis slices with an incomplete ring of myocardium were excluded from wall thickness analysis. Left atrial diameter was measured antero-posteriorly at end-systole in the 3-chamber left ventricular outflow tract view. Image analysis was performed using cmr42© (Circle Cardiovascular Imaging, Calgary, Canada).

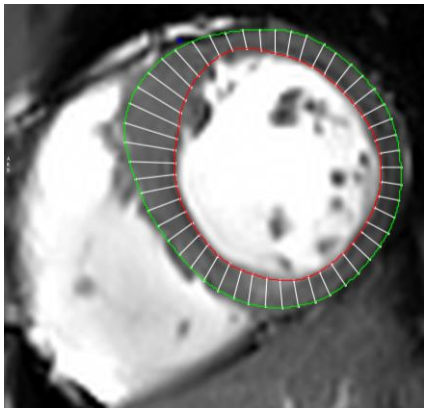


Figure 2.13 Centreline method to measure maximal segmental LV wall thickness
50 chords were defined on all short-axis slices following manual segmentation of epicardial and endocardial borders at end-diastole. Maximal segmental wall thickness was calculated using the 16-segment model with anterior interventricular insertion point as a reference.

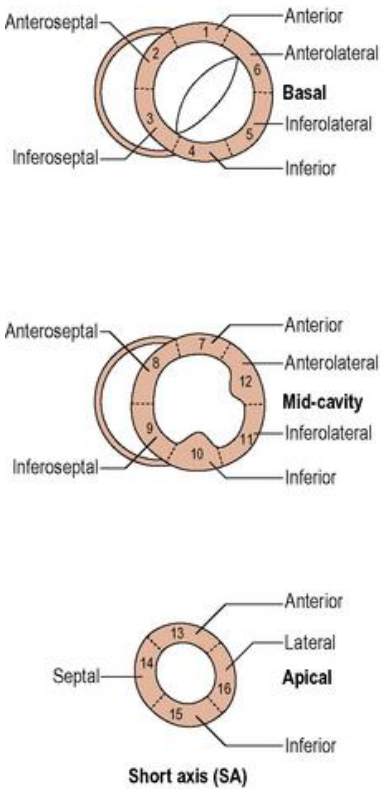


Figure 2.14 The 16-segment left ventricular model
The 16-segment model divides the left ventricle into 16 segments, six each on the basal and mid-ventricular slices and four on the apical slice based on three short-axis images (basal, mid-ventricular, and apical) (Schiller et al., 1989).

2.8.2. Late gadolinium enhancement (LGE) imaging

Late gadolinium enhancement (LGE) imaging was performed in both healthy controls and HCM patients using a T1-weighted phase-sensitive inversion recovery sequence (Kellman et al., 2002). Images were acquired 10 minutes after intravenous administration of gadolinium contrast (Gadoterate meglumine, Dotarem, Guerbet, France; 0.1 mmol/kg body weight), optimised by the Look-Locker sequence (TI scout) to null normal myocardium. LGE images included a contiguous stack of LV short-axis slices and single slices in 2-chamber, 4-chamber and 3-chamber long-axis orientations at the same slice locations as obtained for cine imaging. Spatial resolution was 1.7 x 1.4 x 8 mm^3 with a diastolic trigger delay. LGE was defined as the presence of hyper-enhanced pixels with signal intensities of 5 standard deviations above the mean of normal myocardium in that slice (Maron, 2013) and was quantified using in-house software MC-ROI (IDL v6.1). Epicardial, endocardial borders and a region of normal myocardial were manually segmented. Histological correlation with various LGE quantification methods in HCM patients has shown that 5 SD is the most clinically relevant method for quantifying LGE in HCM (Moravsky et al., 2013).

2.8.3. Extracellular volume (ECV) imaging

T1 mapping was performed at the mid-ventricular short-axis slice (matched to cine and LGE) using the Shortened MOdified Look-Locker Inversion recovery sequence (ShMOLLI) (Piechnik et al., 2010) before and 15 minutes after administration of gadolinium contrast (Dotarem, Guerbet). T1 maps and the R-squared “goodness of fit” maps were reviewed during acquisition to assess image quality and guide re-acquisition of images (if necessary) after

optimisations, such as shim, image sizing and triggering. Epicardial, endocardial borders and a blood ROI (in the LV cavity blood pool avoiding papillary muscles) were manually segmented using custom-built software developed in house (MC-ROI, running on IDL v6.1) (Figure 2.15). Extracellular volume (ECV) was derived from blood haematocrit, native and post-contrast myocardial and blood T1 values calculated per slice and per segment (White et al., 2013). Myocardial ECV was calculated as:

$$Myocardial\ ECV = (1 - haematocrit)\left(\frac{\Delta\ R1myocardium}{\Delta\ R1blood}\right), where\ R1 = \frac{1}{T1}$$

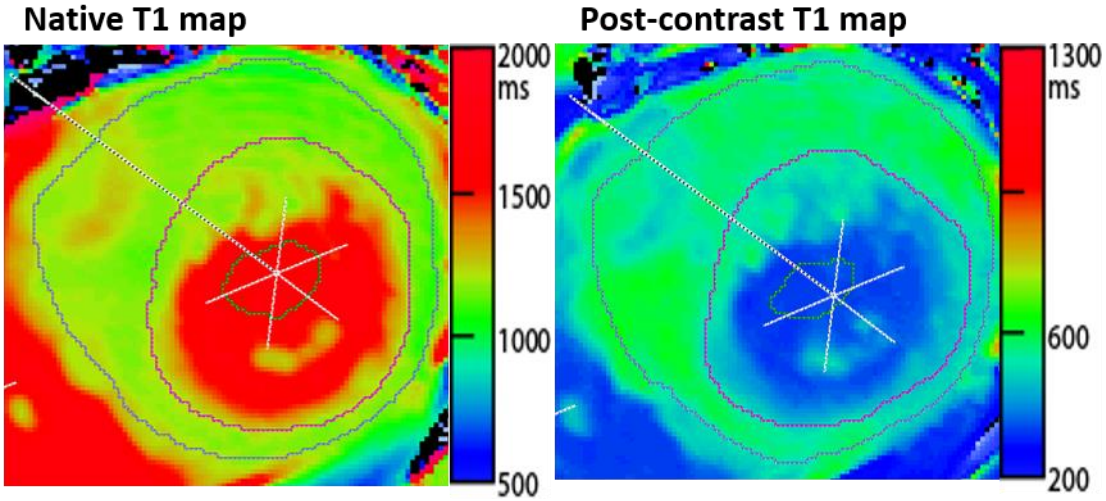


Figure 2.15 Extracellular volume (ECV) from native and post-contrast T1 maps
The extracellular volume fraction was calculated from blood haematocrit, native and post-contrast myocardial and blood T1 values. Epicardial, endocardial borders and a blood region of interest were manually segmented on both T1 maps.

2.9. Clinical data collection

Data from clinical investigations (Holter ECG, exercise testing, echocardiography and genetic testing) performed as part of the patient's routine clinical care were documented including those in the past and at follow-up. Clinical data was collected by Joanne Sellwood, Research Nurse and Rachel Given, Research Data Co-ordinator. All HCM patients underwent ambulatory 3-lead 24-hour Holter ECG monitoring. Ventricular arrhythmia was defined as ≥3 consecutive ventricular beats of ≥120 bpm, in line with the definition used in the ESC HCM guidelines (Authors/Task Force et al., 2014). Stored ECG data and appropriate device therapy was assessed for ventricular arrhythmia in patients with an ICD. The other conventional risk factors were defined as unexplained syncope, ≥1 episode of unexplained syncope; family history of SCD, history of SCD in ≥1 first degree relative ≤40 years old or SCD in a first degree relative with confirmed HCM at any age; massive LVH, LV wall thickness in any myocardial segment of ≥30 mm on end-diastolic short axis CMR images and abnormal exercise blood pressure response, rise in systolic BP <20 mmHg or a fall of >10 mmHg from baseline to peak exercise in patients ≤40 years old.

The risk modifiers were defined as LVOTO, gradient ≥30 mmHg at rest and/or on Valsalva provocation using transthoracic echocardiography (performed as part of routine clinical care); LGE, visual assessment for the presence of LGE and LV apical aneurysm, visual assessment of aneurysm formation with regional scarring on CMR. All HCM patients underwent genetic testing at the Oxford Medical Genetics Laboratories, Oxford University Hospitals NHS Foundation Trust as part of routine clinical care.

The ESC HCM Risk-SCD score was also calculated for each patient to estimate SCD risk at 5 years using disease variables at the time of study recruitment in the following formula (O'Mahony et al., 2014): Probability $_{\text{SCD at 5 years}} = 1 - 0.998^{\exp(\text{Prognostic index})}$, where Prognostic index = [0.15939858 × maximal wall thickness (mm)] − [0.00294271 × maximal wall thickness^2 (mm^2)] + [0.0259082 × left atrial diameter (mm)] + [0.00446131 × maximal (rest/Valsalva) LVOT gradient (mmHg)] + [0.4583082 × family history of SCD] + [0.82639195 × NSVT] + [0.71650361 × unexplained syncope] - [0.01799934 × age at clinical evaluation (years)].

A risk score of ≥6% is classified as high risk and ICD implantation is recommended, 4–6% is intermediate risk and ICD may be considered, and <4% is low risk.

2.10. **Statistical analysis**

Mean ADC and FA of all voxels across slice and segment were plotted across group as histograms to visualise the distribution which were normal. Normality in other variables were checked using the Shapiro-Wilk test. Data were expressed as mean ± standard deviation or median and range. Normally distributed data were compared using Student's t-test or analysis of variance, and non-normally distributed data by Mann-Whitney U-test or Kruskal-Wallis test. Paired t-tests were used to compare the difference between septal and lateral segments within individuals. Repeated measures ANOVA was used to compare segments within healthy controls. Post-hoc pairwise testing with Bonferroni correction for multiple comparisons were used. Categorical data were compared using Chi-square or Fisher's exact test. Circular statistics were used for QRS axis and SA since the angles "wrap" around a circle

(i.e. SA of 90° is equivalent to -90°). This angular data was expressed as circular mean ± circular standard deviation and compared using Watson-Williams F test (Berens 2009).

Segmental DT-CMR parameters were analysed using a linear mixed-effects model and expressed as estimated mean with 95% confidence intervals (Pinheiro and Bates 2000). The mixed model was fitted to account for any within-patient correlation or variation across the six mid-ventricular segments. Fixed effects included slice (base *vs* mid) and segment in Chapter 3 and group (HCM *vs* control) and segment in Chapter 5. Individual subjects were included as random effect. In chapter 3, FA was adjusted for SNR by including segmental SNR as a covariate in the fixed effects part of the model. In chapter 5, FA was adjusted for fibrosis (which is expected to decrease FA (Abdullah, Drakos et al. 2014, Bates, McClymont et al. 2017)) by including segmental LGE (presence/absence) and segmental mean ECV as a covariate in the fixed effects part of the model. All model residuals were normally distributed without transformation of any of the variables. Univariate and multivariable binary logistic regression were used to assess FA as a predictor of ventricular arrhythmia in HCM.

All tests were assumed to be statistically significant when $p<0.05$. Statistical analysis was performed with IBM SPSS Statistics, version 24.0, MATLAB version 2016a (for voxel-wise analysis and circular statistics) and STATA software version 14.2 (for linear mixed-effects model).

CHAPTER 3. DIFFUSION TENSOR CARDIAC MAGNETIC RESONANCE IN HEALTHY CONTROLS

3.1. Introduction

Diffusion tensor cardiac magnetic resonance (DT-CMR) is a novel imaging technique capable of visualising tissue microstructure by exploiting the natural mobility of water molecules as an endogenous contrast mechanism (Garrido et al., 1994). Ex vivo DT-CMR has been extensively validated by histological animal data and shown to correlate with cardiac fibre and sheet orientation (Figure 3.1 and Figure 3.2) (Scollan et al., 1998, Hsu et al., 1998, Holmes et al., 2000, Geerts et al., 2002, Tseng et al., 2003, Kung et al., Hales et al., 2012).

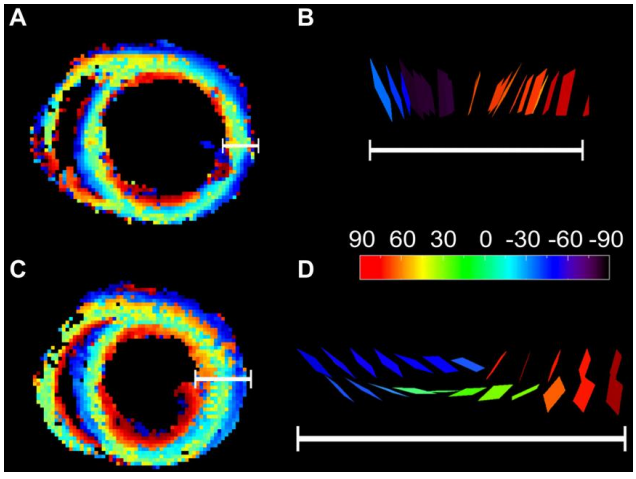


Figure 3.1 Helix angles (left) and sheetlet angles (right) from ex vivo DT-CMR
DT-CMR from the mid slice of a perfused rat heart in slack "diastolic" (top) and contracture "systolic" (bottom) states. White bars represent the location of the sheetlet angle profiles and their spatial extent relative to the ventricular cross-sections on the left. Helix angles are similar in both states but sheetlets are relatively vertical in slack versus horizontal in contracture (Hales et al., 2012).

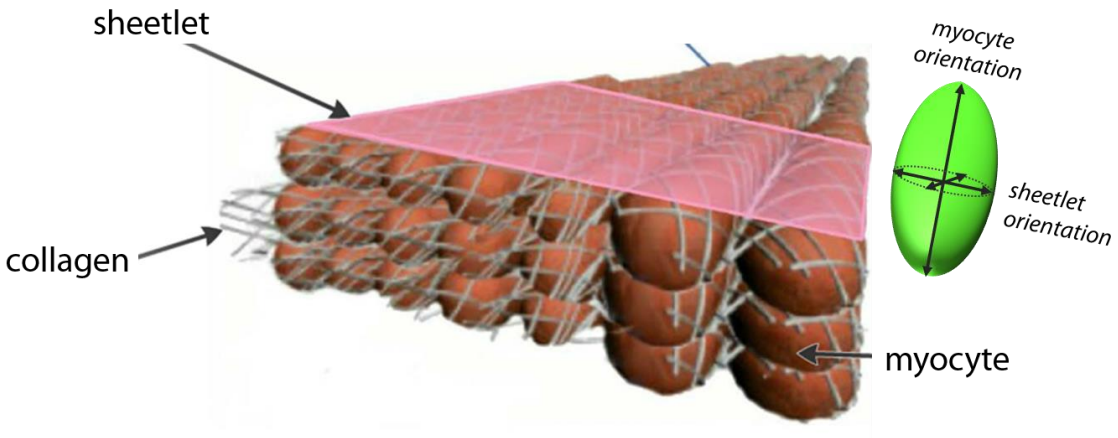


Figure 3.2 Myocyte and sheetlet orientation correspond to the primary and secondary eigenvectors of the diffusion tensor

In vivo DT-CMR was developed more than 20 years ago, yet clinical DT-CMR studies have only recently grown in number. In vivo human studies are technically more challenging (Edelman et al., 1994). It is the difficult to detect molecular motion of water in the presence of a beating heart (µm *vs* mm scale), and acquisition times are prohibitively long due to low signal-to-noise ratio (SNR). Recent advancements in pulse sequence design and MR hardware have now made DT-CMR in humans feasible with relevant spatial resolution and within clinically acceptable acquisition times (Reese et al., 1995, Nielles-Vallespin et al., 2013). However, previous DT-CMR studies have focused on a single mid-ventricular slice. This limits disease assessment such as HCM where hypertrophy can solely localise to basal and apical regions. Little is known about the feasibility of whole heart DT-CMR and the possible heterogeneity of quantitative DT-CMR parameters within the normal LV.

3.1.1. Normal left ventricular myoarchitecture

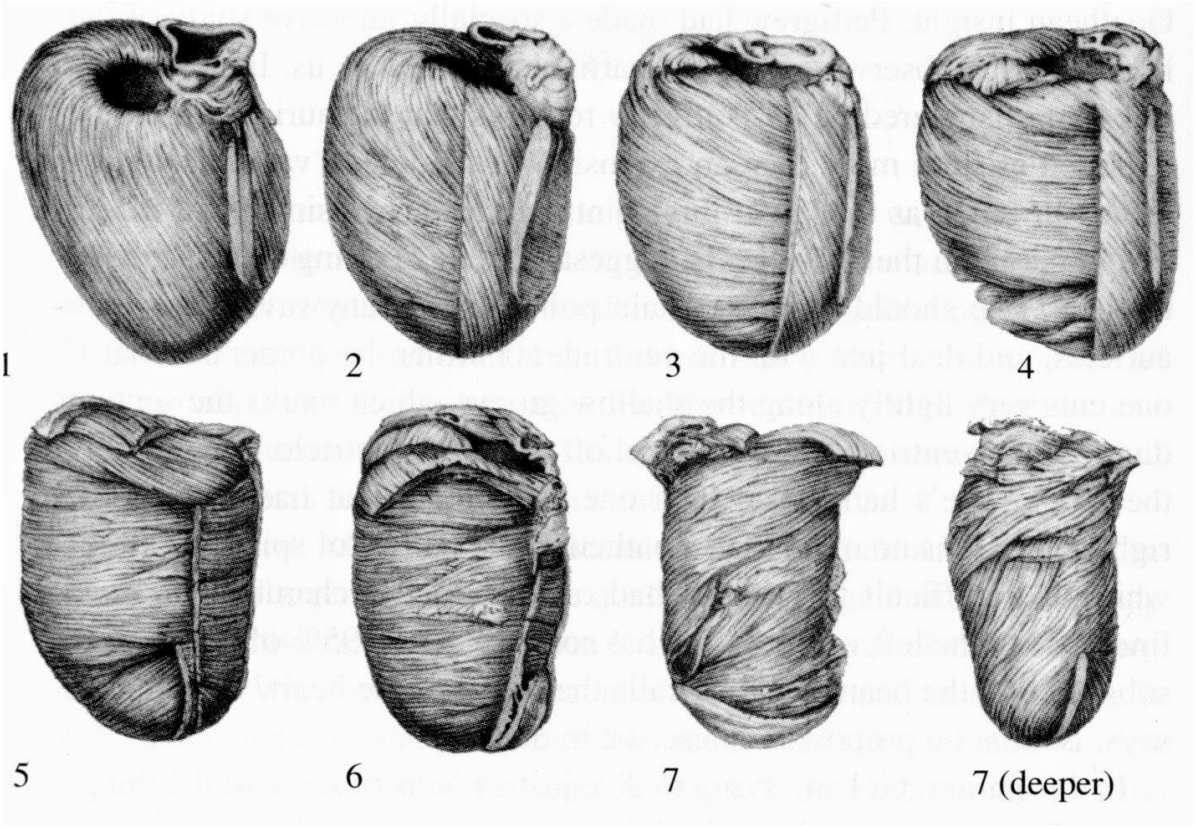


Figure 3.3 Pettigrew's anatomical dissections of the heart
Pettigrew showed that the heart consists of distinct layers of spiralling fibres which he described as "beautiful gradation in direction by which the fibres diverge from an imaginary vertical, and gradually return to it after having intersected each other in all directions" (Pettigrew, 1864).

The LV has a distinct three-dimensional helical arrangement of cells (Figure 3.3) (Pettigrew, 1864). Healthy adult cardiomyocytes are cylindrical and measure approximately 100 µm in length and 10-25 µm in diameter (Olivetti et al., 1996, Opie, 2004, Ho, 2009). Cardiomyocytes join end-to-end to form long fibres which branch and adjoin adjacent myocytes orientated in parallel and in 3-4 myocyte thick layers to form laminar sheets within an extracellular collagen matrix (Figure 3.4) (LeGrice et al., 1995). These so-called "fibres" simply describe the overall

longitudinal orientation of a collection of myocytes which progressively change their orientation transmurally from a left-handed helix in the epicardium, circumferential in the mesocardium to a right-handed helix in the endocardium (referred to as a negative, close to zero and positive helix angles respectively; Figure 3.5) (Streeter et al., 1969, Greenbaum et al., 1981).

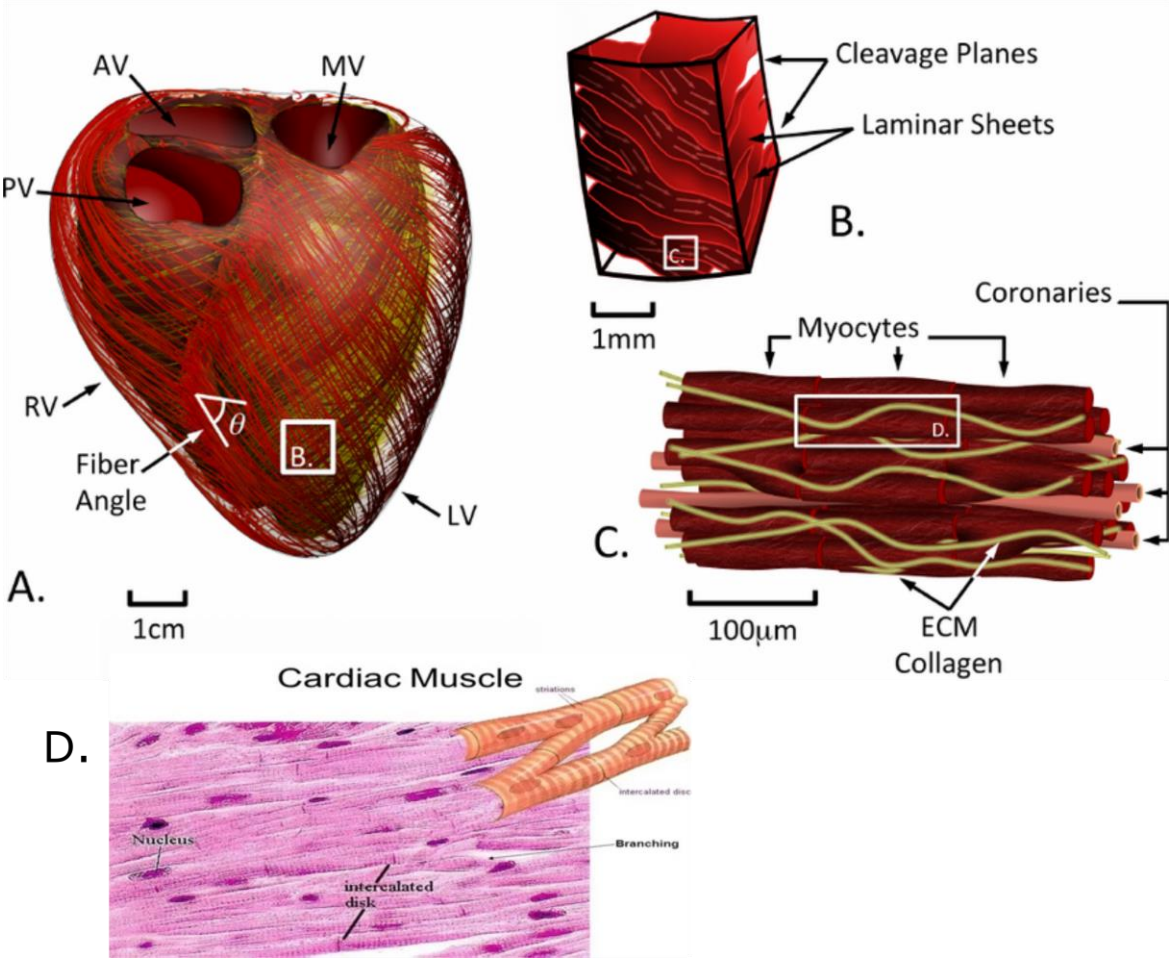


Figure 3.4 Multiscale cardiac anatomy
(A) The heart with streamlines illustrating its fibre architecture. (B) Tissue block illustrating the laminar structure of the heart comprising fibre bundles arranged into sheets separated by cleavage planes. (C) Local structural arrangement of myocytes, coronary capillaries and extracellular matrix collagen. (D) Myocytes branch and connect to each other with intercalated disks. RV, right ventricle; LV, left ventricle; PV, pulmonary valve; AV, aortic valve; MV, mitral valve; ECM, extracellular matrix. Adapted from (Chabiniok et al., 2016).

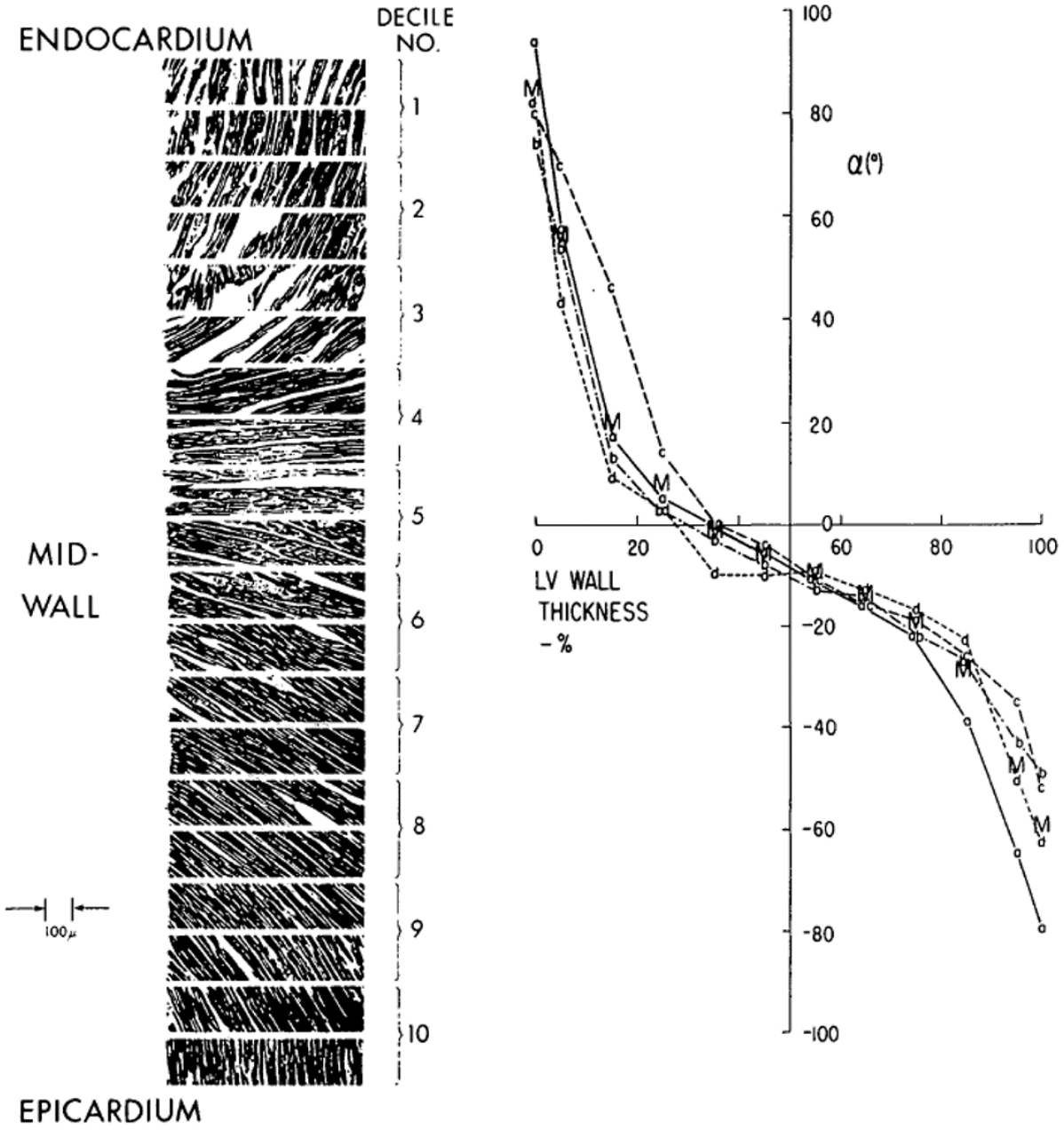


Figure 3.5 Streeter's measurements of transmural progression in fibre angle
Photomicrographs (left) showing fibre angles in successive sections taken from the canine heart parallel to the epicardial plane. Fibre angles measured from four samples in the mid-ventricular short-axis slice in diastole from endocardium (0% wall thickness) to epicardium (Streeter et al., 1969).

These three concentric LV "layers" are defined by their rapid change in myocyte orientation from longitudinal to circular to longitudinal as there are no fibrous partitions between them. 25% of wall thickness is composed of the epicardium (Sanchez-Quintana et al., 1999). In a

small area at the anterior interventricular insertion point, crossing fibres (disarray) are seen epicardially but do not extend into the mesocardium (Greenbaum et al., 1981, Kuribayashi and Roberts, 1992). The mesocardium forms a circular unit comprising of circumferentially-orientated myocytes (Kuribayashi and Roberts, 1992). Mesocardial thickness varies according to location along the LV long-axis. At the mid-ventricle, the mesocardium consists of 53-59% of the LV wall thickness, which thins out apically and basally except at the basal anteroseptum where it thickens to encircle the outflow (Figure 3.6) (Greenbaum et al., 1981). The endocardium is the thinnest layer occupying <20% of the wall thickness, which fuses with longitudinally-directed trabeculae in the apical third of the ventricle.

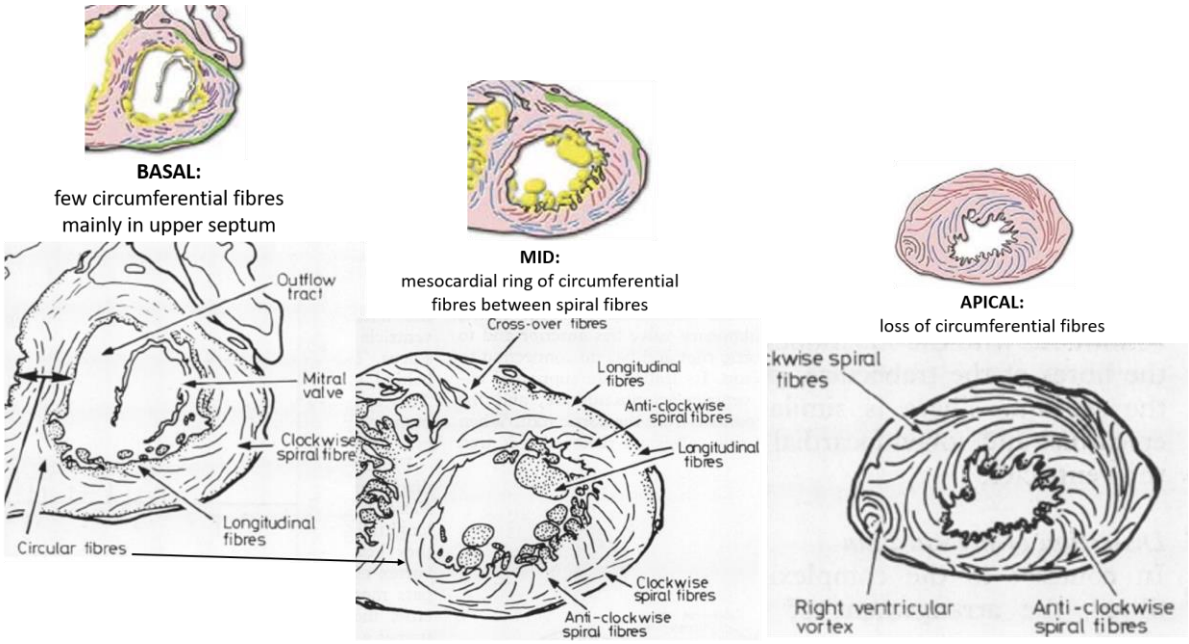


Figure 3.6 LV architecture of the basal, mid and apical short-axis ventricular sections
Top colour panel: longitudinal fibres of the subepicardial layer are in green (top left and top middle) and longitudinal fibres in the subendocardial layer in yellow (top left and top middle) (Greenbaum et al., 1981, Anderson et al., 2005).

3.1.2. Expected FA in the healthy left ventricle

Fractional anisotropy (FA), calculated from the diffusion tensor, quantifies the directionality of diffusion within an imaging voxel, from 0 – random motion (perfect isotropy), to 1 – diffusion in a single linear direction (perfect anisotropy). We expect that FA will be high in voxels with coherent myocyte alignment, such as the mesocardium where myocytes align circumferentially (single orientation). Conversely, we expect FA will be lower in the epicardium and endocardium where myocyte alignments change rapidly towards a left- or right-handed helix respectively (multiple orientations) (Figure 3.7 and Figure 3.8). I propose that FA is a measure of the underlying cell alignment within a voxel.

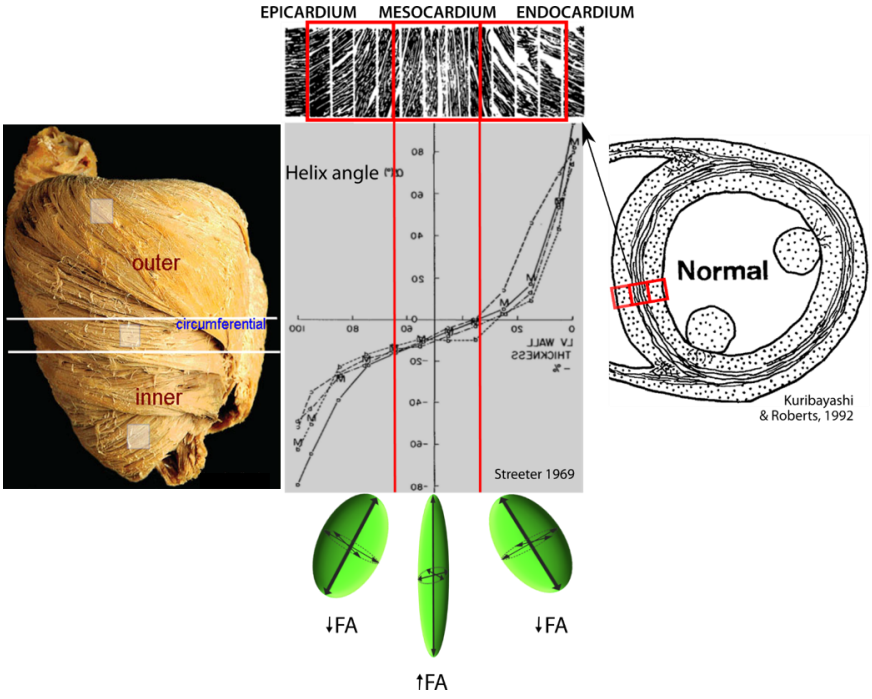


Figure 3.7 The proposed transmural heterogeneity of fractional anisotropy
Fractional anisotropy (FA), calculated from the diffusion tensor, infers the underlying cell alignment in an imaging voxel. The in-plane spatial resolution of DT-CMR (2.8 x 2.8 mm) allows 3 pixels on average across the LV wall in short-axis. FA is expected to be high in the mesocardium where myocytes align circumferentially (single orientation) compared to the epicardium and endocardium where myocyte alignments change rapidly towards a left- or right-handed helix respectively (multiple orientations) as shown by the classical distribution of helix angles in histology (Streeter et al., 1969, Kuribayashi and Roberts, 1992).

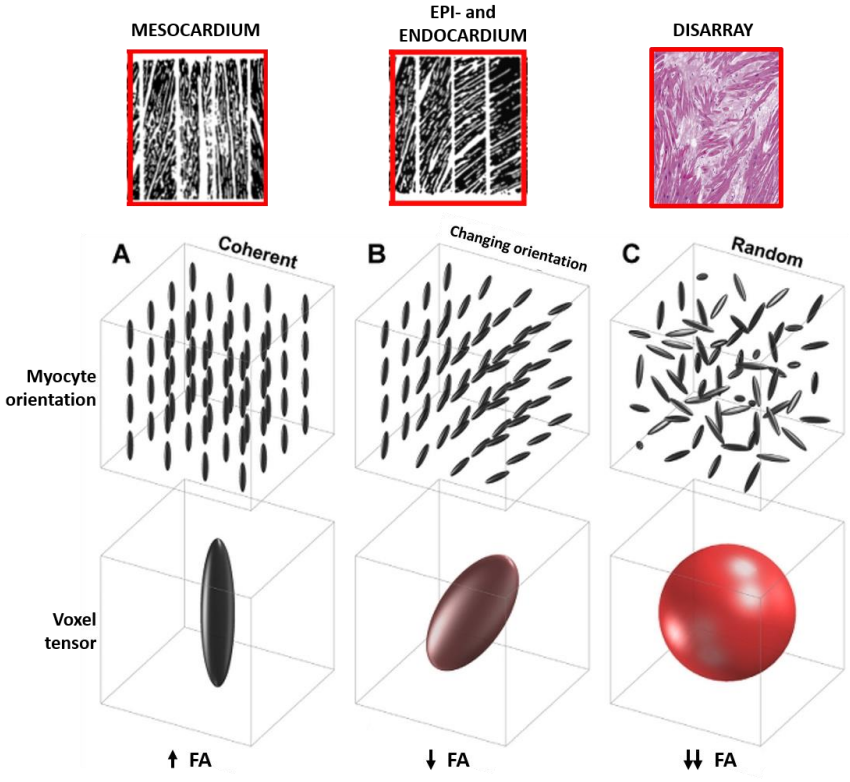


Figure 3.8 The proposed effect of myocyte orientation on fractional anisotropy
Each imaging voxel (2.8 × 2.8 × 8 mm^3) quantifies water molecule diffusion as its motion is impeded by several million myocytes and the surrounding interstitium. (A) Coherently aligned myocytes with a circumferential orientation as seen in the mesocardium will result in high FA. (B) myocytes which are progressively changing their orientation from vertical to horizontal as seen in the epi- and endocardium will have a lower FA. (C) Disorganised myocytes such as disarray in HCM will have a further reduction in FA. Adapted from (Szczepankiewicz et al., 2015).

3.1.3. Previous DT-CMR studies in healthy controls

We have previously demonstrated intercentre reproducibility of DT-CMR using stimulated echo in 10 healthy controls with a single mid-ventricular slice at both cardiac phases (Tunnicliffe et al., 2014). Using the same protocol, our London collaborators reported no slice differences between 3 contiguous mid-ventricular slices (slice gap 4 mm) in 43 controls which they subsequently analysed as 4 segments (anterior, septal, inferior and lateral) averaged

across all three slices. They found increased diastolic FA in the septum, anterior and inferior walls compared to the lateral (McGill et al., 2015b). While systolic FA was only greater in the anterior and inferior walls compared to the lateral. There was no association of diastolic or systolic FA with an individual's anthropometrics (age, gender, LV end-diastolic volume, LV mass, body surface area and ejection fraction).

The same group optimised their imaging protocol following investigation into the effects of SNR and microvascular perfusion on DT-CMR, and adopted higher b-values of 150 s/mm^2 and 750 s/mm^2 (compared to 15 s/mm^2 and 350 s/mm^2) (Scott et al., 2015, Scott et al., 2016). Using this optimised protocol, they acquired a single mid-ventricular slice in 20 controls which they subsequently analysed as 4 segments and 3 equal transmural layers (epi-, meso-, endocardium) (McGill et al., 2015a). Unfortunately, this acquisition protocol change precludes direct comparability with our data as DT-CMR parameters are heavily influenced by b-values. Furthermore, they only acquired systolic DT-CMR data which is confounded by cardiac strain (Tseng et al., 1999). Whereas FA calculated from diastolic DT-CMR data is robust to strain effects and does not require laborious strain correction (Stoeck et al., 2014). Nevertheless, they reported transmural and regional heterogeneity in FA at systole (McGill et al., 2015a). FA was higher in the mesocardium than the endocardium and epicardium. Septal FA was higher than lateral wall FA. They also showed a relative reduction in the rate of change in the helix angle within the mesocardium, in keeping with Streeter's histological data. However, they found heterogeneity in SNR with greatest SNR in the mesocardium transmurally and the septum regionally. They tested whether increased FA could be the result of increased SNR by using higher resolution. SNR reduces at higher resolution which in fact

increased FA in areas of low SNR in the lateral and inferior walls. But there was little difference in transmural FA between the standard and high-resolution scans.

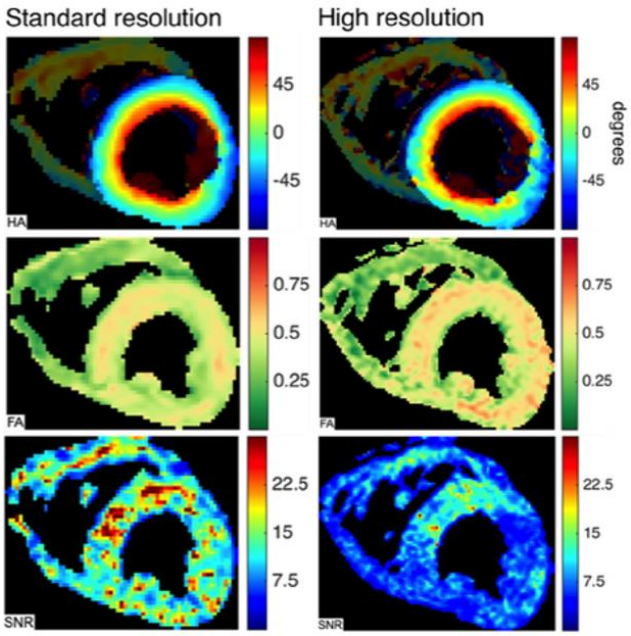


Figure 3.9 Standard and high-resolution DT-CMR maps
SNR (bottom row) is lower at high-resolution (right) compared to standard (left) yet the increased mesocardial FA (middle row) persists despite the reduction in SNR. Decreased SNR in the inferior and lateral wall cause FA to increase. No difference in transmural helical angles (top row) (McGill et al., 2015a).

3.1.4. Hypotheses and aims

We hypothesised that diastolic FA, a marker of myocyte alignment coherency within an imaging voxel, will have both transmural heterogeneity and slice heterogeneity. We propose that FA will be higher in the mesocardium compared to the epi- and endocardium due to the single circumferential orientation of myocytes in the mesocardium. FA will be reduced basally and apically compared to the mid-ventricular slice due to the thinning of the mesocardium. The aims of this work in healthy controls were to assess the ability of in vivo DT-CMR to probe the normal heterogeneity of LV myoarchitecture and assess the feasibility of DT-CMR in the whole LV.

3.2. Methods

30 healthy controls (46 ± 16 years, 70% male) underwent DT-CMR of 3 short-axis ventricular slices in diastole and systole. See Chapter 2 - Methods for full description.

3.3. Results

3.3.1. DT-CMR maps – qualitative assessment

Figure 3.10 and are typical example of images and colourised post-processed maps obtained by DT-CMR at diastole and systole respectively with corresponding illustrations of histological findings (Greenbaum et al., 1981, Anderson et al., 2005). The helix angle maps have the expected transmural progression in all three slices including the longitudinal fibres (helix angles close to ±90° in magenta pink) in the LV and RV subendocardium (trabeculae), papillary muscles and LV epicardium. Care was taken to exclude the subendocardium and subepicardium from ROIs to avoid partial volume effects. Diastolic FA maps demonstrated an almost complete mesocardial ring of high FA (yellow/red) in the mid-ventricular slice consistent with corresponding helix angle maps and classical descriptions of circumferentially-aligned mesocardial myocytes in histology. This mesocardial ring of high FA was less well-defined in the diastolic basal and apical slice consistent with histological descriptions of mesocardial thinning (Figure 3.6). ADC and FA were reduced in systole compared to diastole. The sheetlet population were more vertically aligned in diastole and horizontally aligned in systole (angles with respect to the short-axis plane).

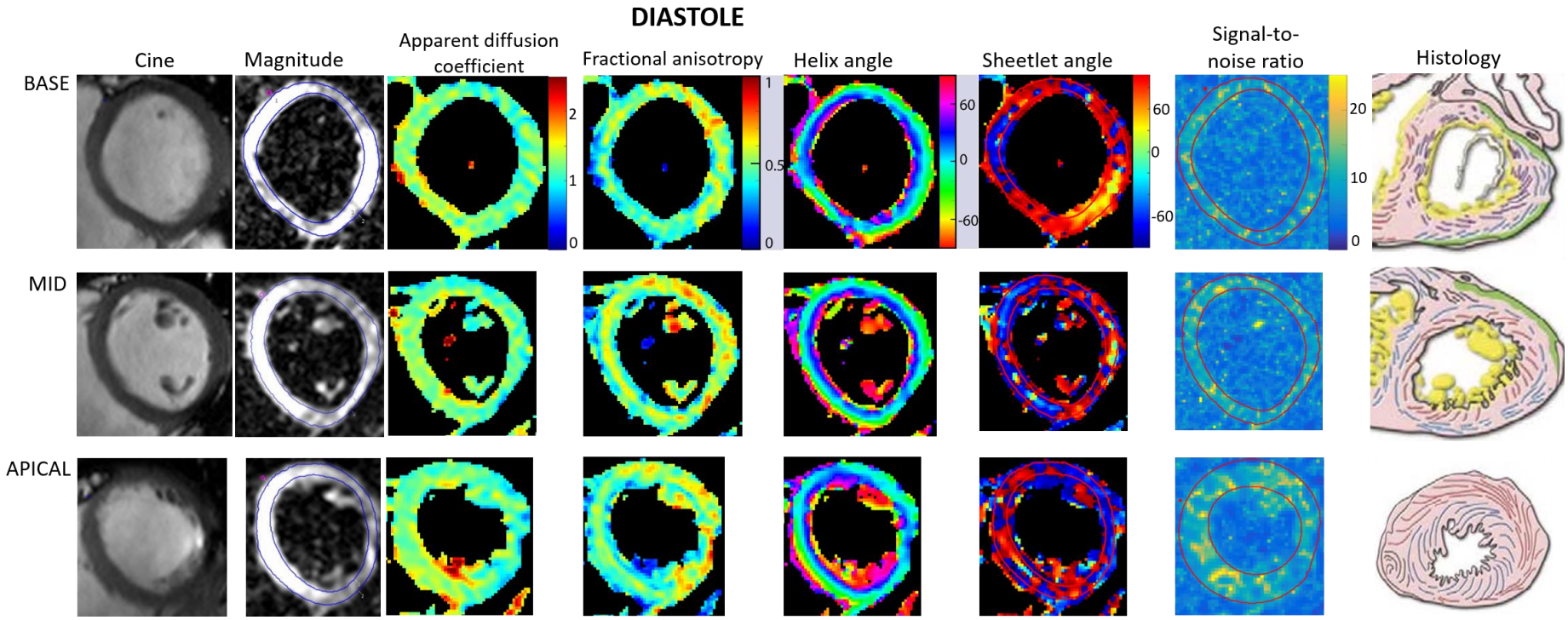


Figure 3.10 Diastolic DT-CMR images and ADC, FA, helix and sheetlet angle maps

The mid-ventricular slice in diastole showed an almost complete mesocardial ring of high fractional anisotropy (yellow/red) while this is less prominent in the base and apical slice. All three slices showed the normal transmural progression of helix angles. The representation of histological findings of (Greenbaum et al., 1981) from sections through the LV corresponded to the helix angle patterns. The longitudinal subepicardial layer (green) on histology matched the area where helix angles are close to 90° (red) while the longitudinal subendocardial layer (yellow) on histology matched the area where helix angles are close to -90° (magenta pink). The sheetlet angles were predominantly vertically orientated with high angles with respect to the short-axis plane. Histology representation reproduced from (Anderson et al., 2005).

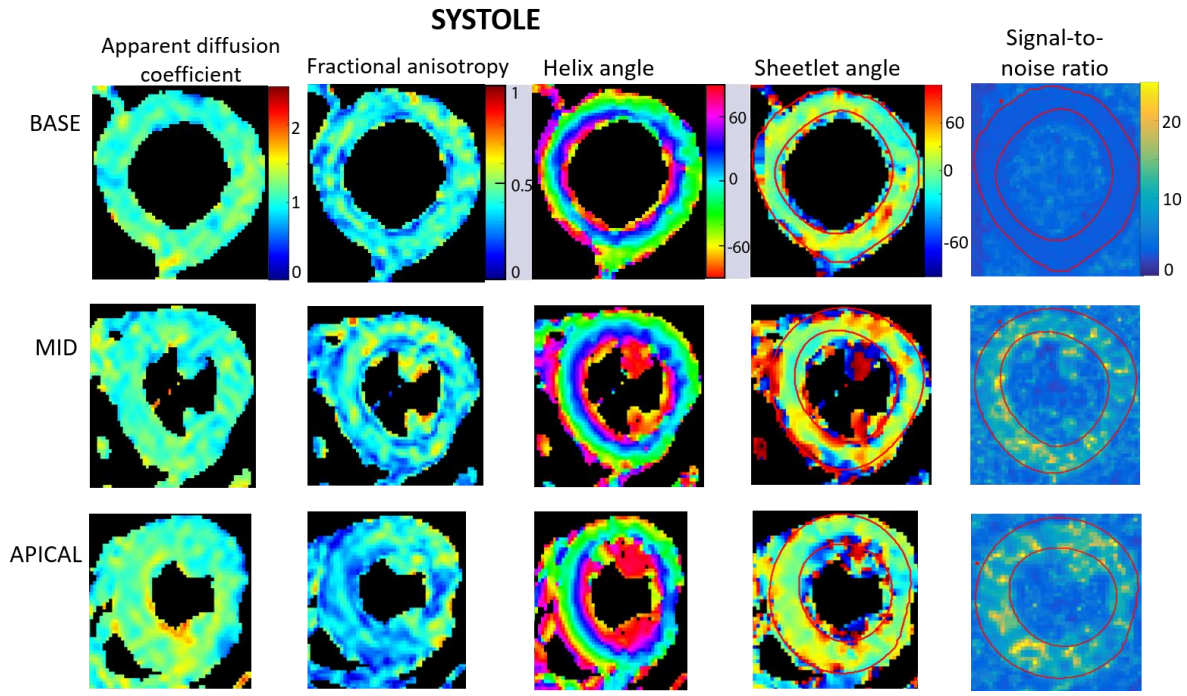


Figure 3.11 Systolic DT-CMR images and ADC, FA, helix and sheetlet angle maps
ADC and FA were lower in systole compared to diastole. Normal transmural progression of helix angles. The sheetlet angles were predominantly horizontally orientated with low angles with respect to the short-axis plane. Very poor SNR in the basal slice.

3.3.2. Slice level analysis of DT-CMR parameters

DT-CMR parameters from both cardiac phases obtained from the basal and mid slices of healthy controls are shown in Table 3.1. No slice differences were detected in FA, ADC or helix angle gradient at systole, yet differences in FA and helix angle gradient were present at diastole. This discrepancy is likely to reflect strain effects on diffusion which are most prominent at peak systole (Stoeck et al., 2014, Ferreira et al., 2018). FA, unlike ADC and angular measures, is the only DT-CMR parameter to be robust to strain when acquired at diastole and therefore further analysis was focused on FA from diastolic data.

Table 3.1 DT-CMR parameters by slice in healthy controls.
[mean ± standard deviation; FA, fractional anisotropy; ADC, apparent diffusion coefficient; HA, helix angle; SNR, signal to noise ratio]

	Base	**Mid**	**p value**
DIASTOLIC (trigger time 685 ± 50 ms)			
FA	0.49 ± 0.03	0.52 ± 0.03	**0.00002**
ADC, $x10^{-3}$ mm^2/s	1.31 ± 0.13	1.26 ± 0.12	0.11
HA gradient, °/mm	6 ± 3	9 ± 3	**0.007**
SNR estimate	8.7 ± 2.0	10.4 ± 2.6	**0.002**
SYSTOLIC (trigger time 367 ± 27 ms)			
FA	0.40 ± 0.06	0.41 ± 0.06	0.33
ADC, $x10^{-3}$ mm^2/s	1.23 ± 0.22	1.18 ± 0.15	0.31
HA gradient, °/mm	10 ± 3	10 ± 2	0.47
SNR estimate	7.0 ± 3.6	9.9 ± 2.6	**0.01**

3.3.3. Apical slice: reduced measurement accuracy

Although apical slice acquisition was attempted in all participants, these images where typically poor quality due to inconsistent breath-holding towards the end of the scan (Figure 3.12) and were unobtainable in 4 controls due to tiring. Furthermore, the apical slice was particularly prone to error due to low spatial resolution of DT-CMR (slice thickness 8mm) which amplifies partial volume effects as the LV tapers towards the apex (Figure 3.13). To avoid major partial volume effects particularly in those with a short LV, the next contiguous slice from the mid-ventricular slice was used despite the slice including papillary muscles and therefore were not truly apical but rather apically positioned mid-ventricular slices. Each of

these factors reduce accuracy and precision therefore apical slices were not used in statistical analysis. Diastolic apical parameters: FA 0.48 ± 0.04, ADC 1.36 ± 0.16 x10^{-3} mm^2/s, SNR 9.6 ± 2.3. Systolic apical parameters: FA 0.36 ± 0.05, ADC 1.30 ± 0.18 x10^{-3} mm^2/s, SNR 11.8 ± 2.7.

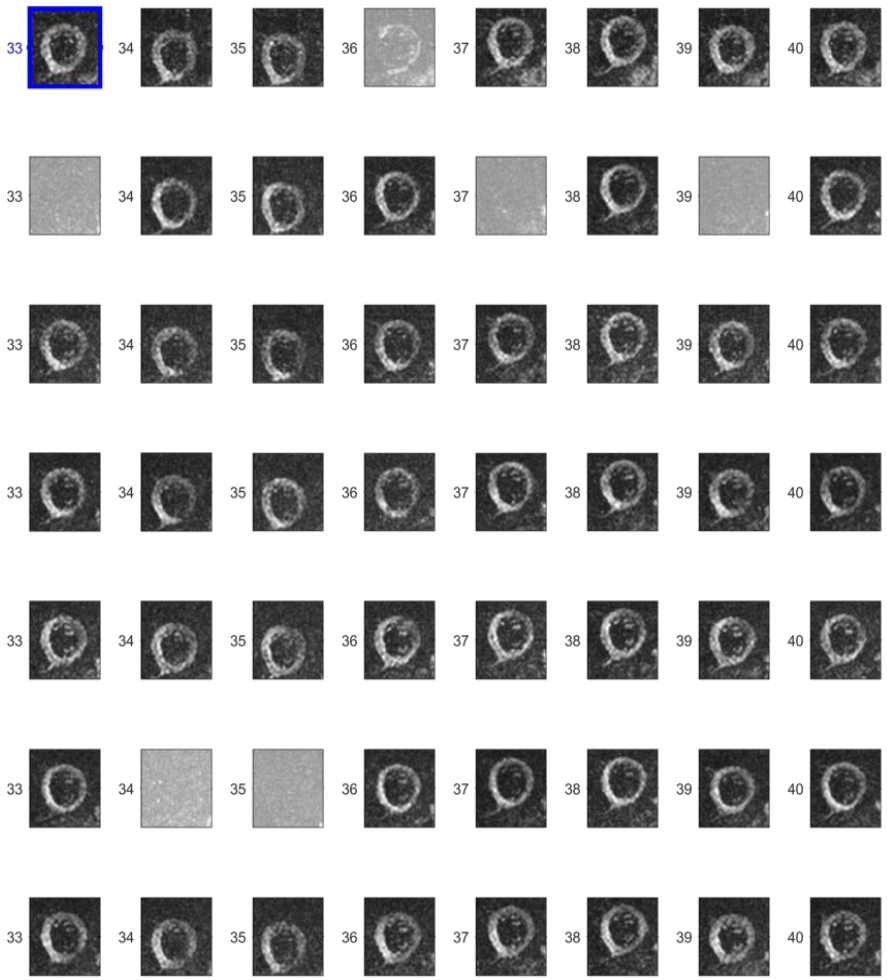


Figure 3.12 Poor quality data from the apical slice due to inconsistent breath-holding at the end of the scan
The minimum of 6 averages was not achieved in the first diffusion direction and therefore this data was not used. Further repeats were not possible as patient was tiring.

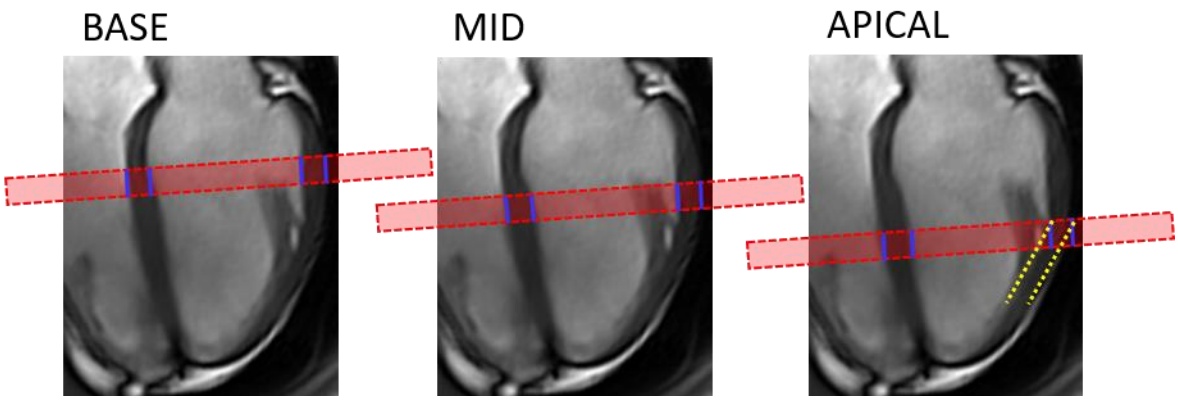


Figure 3.13 Slice position of the diastolic DT-CMR short-axis ventricular slices
Long axis view of the left ventricle (left) with the position of the short-axis slices (red line). The apical slice is prone to partial volume effects as the conical geometry of the left ventricle tapers towards the apex (yellow dashed line). Therefore, in a DT-CMR voxel with an 8mm slice thickness, the endocardium will overlie the epicardium causing inaccurate measurements.

3.3.4. Mid slice: consistent and reproducible parameters

Table 3.2 Intercentre reproducibility reference values for mid-ventricular slice
Apparent diffusion coefficient and fractional anisotropy in healthy volunteers. Centre O refers to our unit (Tunnicliffe et al., 2014).

	Systolic			Diastolic		
	ADC ($\times 10^{-3}$ mm^2/s)	FA	HA grad (°/mm)	ADC ($\times 10^{-3}$ mm^2/s)	FA	HA grad (°/mm)
Centre B	1.06 ± 0.06	0.41 ± 0.05	−8.7 ± 1.4	1.17 ± 0.14	0.54 ± 0.04	−10.1 ± 0.9
Centre O	1.13 ± 0.13	0.40 ± 0.07	−9.0 ± 1.4	1.26 ± 0.16	0.55 ± 0.03	−10.2 ± 0.8

DT-CMR measures from the mid-ventricular slice in both phases were consistent (1 SD) with those previously reported in the mid slice between imaging centres (Table 3.2) (Tunnicliffe et al., 2014). The mean diastolic helix angles plotted transmurally demonstrated the reduction in the rate of angle change (helix angle gradient) at the mesocardium (Figure 3.14B, red line) which is found at histology (Figure 3.5) and corresponded to increased FA. However, this reduction in helix angle gradient was only modest when mean helix angle of all voxel across

the whole slice were averaged in all individuals. This may be due to individual and segmental variability in addition to the effect of interpolation across a relatively large pixel size (interpolation 1.4 x 1.4 mm across imaging pixel 2.8 x 2.8 mm). As a result, transmural FA differences between the epicardium, mesocardium and endocardium were assessed qualitatively rather than quantitively as DT-CMR currently lacks the precision to adequately divide the layers defined by the rate of helix angle change (Figure 3.14A). Visual assessment of FA was made using mean FA of all voxels in the mid slice averaged across all controls and mapped to normalised LV wall. The mesocardium was the largest layer, followed by the epicardium and then the endocardium (Figure 3.15) as described in histology.

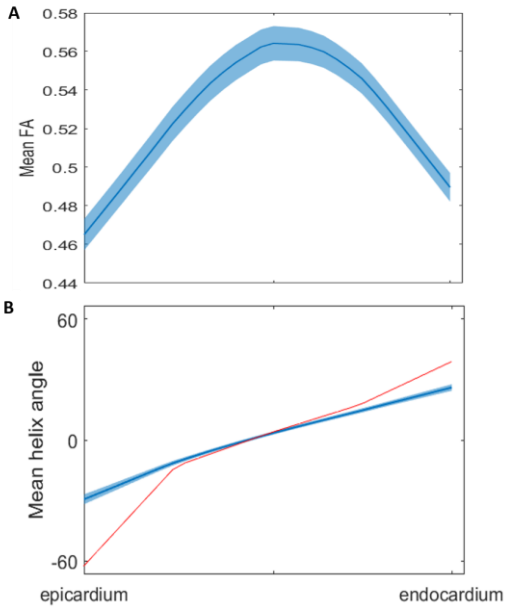


Figure 3.14 Mean diastolic FA and helix angle from epi- to endocardium in mid slice
Mean diastolic FA (A) and helix angle (B) of all mid-ventricular voxels across controls plotted transmurally. There is a steady rise and fall in FA from epicardium to endocardium which peaks at the mid-point (mesocardium). There is a subtle reduction in the transmural helix angle gradient which defines the mesocardial layer (best seen in an individual chord, red line depicts the helix angle from one subject in a single anteroseptal chord) and corresponds to increase in FA. [mean ± standard error]

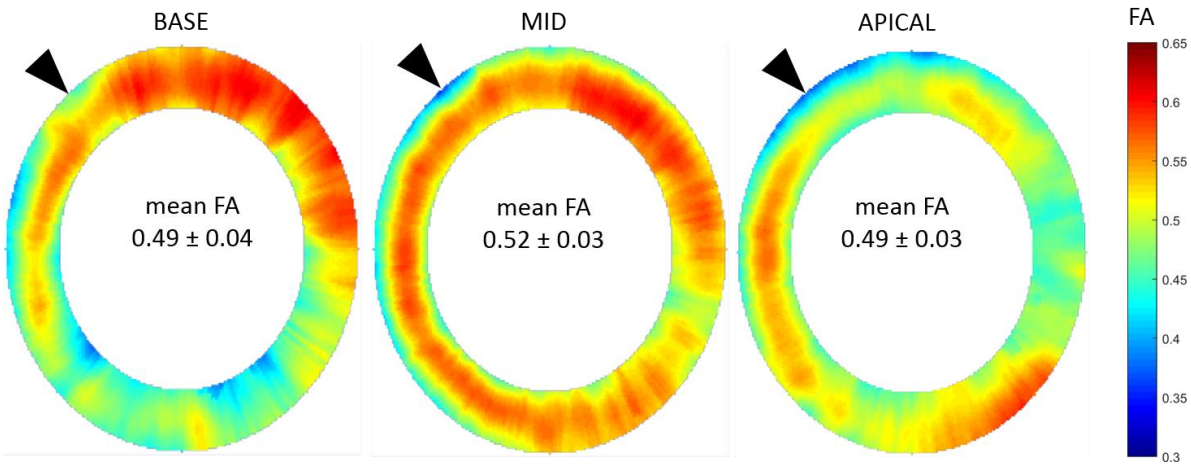


Figure 3.15 Slice mean FA across all controls mapped to normalised LV co-ordinates
There is an almost complete mesocardial ring of high FA in the mid slice which was less prominent in the basal and apical slice. Low FA in the mid slice-inferolateral segment corresponds to the location of spatial distortion due to the sensitivity of EPI to inhomogeneities in the static B_0 magnetic field.
[Black arrowhead denotes anterior interventricular insertion point; mean ± standard deviation; FA, fractional anisotropy]

3.3.4.1. **Segmental analysis of mid slice at diastole**

Quantitative segmental analysis of the mid slice showed a significant difference in diastolic FA between the segments (repeated measures ANOVA $p<0.05$; Table 3.3, Figure 3.16). This was driven by anterolateral FA which was significantly higher than anteroseptal FA ($p<0.05$ Bonferroni-corrected for multiple comparisons). Qualitative analysis from mapping mean FA across all controls to a normalised transmural LV wall (Figure 3.15) revealed that the increase in FA anterolaterally was almost transmural while the decrease in anteroseptal FA was localised to the epicardium at the anterior insertion point. There was also a transmural decrease in FA inferolaterally and all these changes were seen in the basal slice too. The decreased FA at the anterior insertion point is in keeping with the cross-over fibres between the right ventricle and LV described histologically. The lateral and inferior walls typically had patchy heterogenous patterns of FA on individual FA maps compared to the confluent

mesocardial band of high FA seen anteriorly and septally (Figure 3.10). Despite heterogeneity in the FA map, the corresponding helix angle maps showed normal transmural progression throughout the LV, suggesting that lateral FA findings are likely to be driven by technical factors affecting the tensor measurement rather than the underlying myoarchitecture (helix angle relies only on the 1st eigenvector compared to FA which is calculated from 3 eigenvalues).

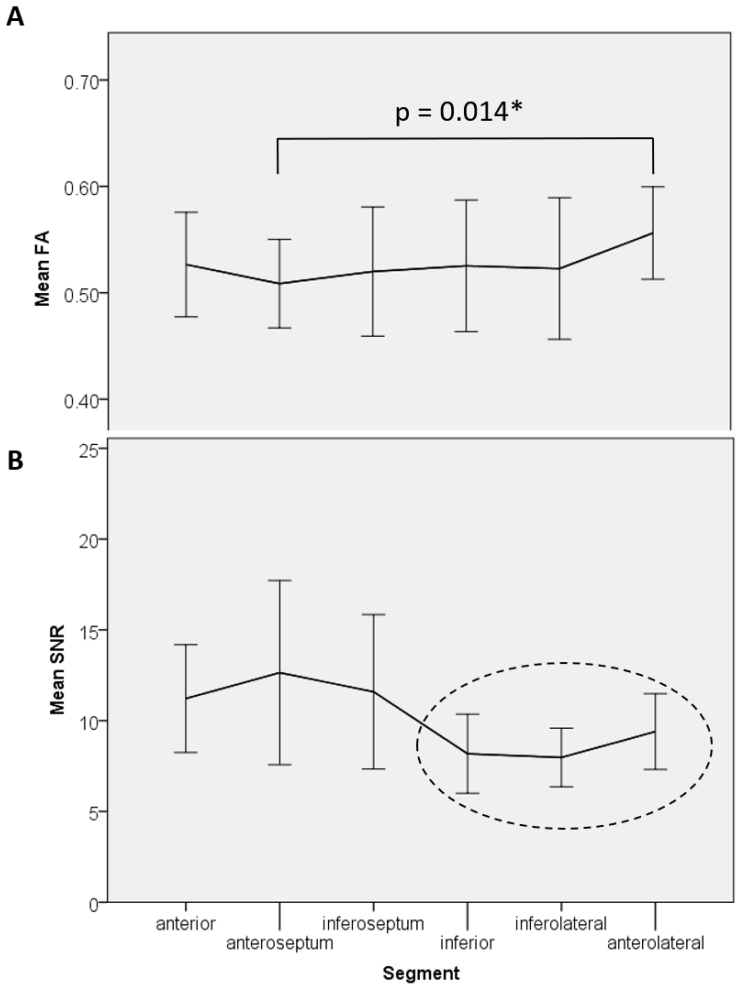


Figure 3.16 Segmental variation of fractional anisotropy (A) and SNR (B) in the mid-ventricular slice

Anterolateral FA was significantly higher than anteroseptal (post hoc p=0.014). Inferior and lateral SNR was significantly lower than anterior and septal SNR (all post hoc p<0.005). [Mean ± SD; repeated measures ANOVA post hoc p values are Bonferroni-corrected for multiple comparisons]

Table 3.3 Diastolic mid-ventricular DT-CMR parameters by segment in healthy controls
[mean ± standard deviation; [a] anteroseptum *vs* anterolateral, [b] inferoseptum *vs* anterolateral, [c] anterior *vs* inferior and inferolateral, [d]anteroseptum *vs* inferior, inferolateral, anterolateral, [e] inferoseptum *vs* inferior and inferolateral, p<0.05 on repeated measures ANOVA post hoc pairwise comparisons Bonferroni-corrected; FA, fractional anisotropy; ADC, apparent diffusion coefficient; HA, helix angle; SNR, signal to noise ratio]

	Anterior	**Anteroseptum**	**Inferoseptum**	**Inferior**	**Inferolateral**	**Anterolateral**	**p value** (Repeated measures ANOVA)
FA	0.53 ± 0.05	0.51 ± 0.04[a]	0.52 ± 0.06	0.53 ± 0.06	0.52 ± 0.07	0.56 ± 0.04	**0.018**
ADC, $x10^{-3}$ mm^2/s	1.21 ± 0.11	1.26 ± 0.13	1.32 ± 0.19[b]	1.28 ± 0.18	1.23 ± 0.17	1.19 ± 0.10	**0.009**
HA gradient, °/mm	10 ± 3 [c]	9 ± 3 [d]	9 ± 3 [e]	7 ± 2	5 ± 4	8 ± 3	**7×10^{-8}**
SNR estimate	11 ± 3 [c]	13 ± 5 [d]	12 ± 4 [e]	8 ± 2	8 ± 2	9 ± 2	**8×10^{-9}**

There are at least two sources for bias occurring in the lateral wall. Firstly, echo planar imaging (EPI) is known to be sensitive to inhomogeneities in the static B_0 magnetic field which typically causes spatial distortion in the lateral wall (Figure 3.10). Secondly, SNR was significantly lower in the inferior and lateral segments (SNR range 4-12), and higher and more variable in the anterior and septal segments (SNR range 7-25; Table 3.3, Figure 3.16, Figure 3.17). This is due to the combination of proximity of the anterior wall and septum to the surface coil, rapid changes in coil sensitivity and individual LV geometry (McGill et al., 2015a, Scott et al., 2015). Although previous studies have reported SNR bias to overestimate FA, no association was detected between SNR and FA across slice or segments (Spearman's correlation, all $p>0.05$).

3.3.5. Basal slice: FA significantly lower than mid slice in diastole

Mean diastolic FA at the basal slice was <1 SD of the FA mean previously reported by (Tunnicliffe et al., 2014). Our data also shows significantly lower FA in the basal compared to the mid slice, consistent with mesocardial thinning basally (i.e. less coherently-aligned circumferential myocytes) ($p<0.05$; Table 3.1, Figure 3.15).

Segmental variation of DT-CMR parameters across slice was investigated using a linear mixed-effects model. This showed that the reduction in FA between the base and mid slices were driven predominantly by the 3 segments (inferoseptum, inferior and inferolateral, all post hoc $p<0.05$; Figure 3.17), consistent with an absence of mesocardium in these segments except in the anteroseptum. No significant FA difference was detected between slices in the anterior and anteroseptum suggestive that these 2 segments may be comparable to mid slice

reference ranges. However, there is likely to be an SNR bias in basal FA measurements as SNR was significantly lower in these 2 segments (all post hoc p<0.05; Table 3.3, Figure 3.18).

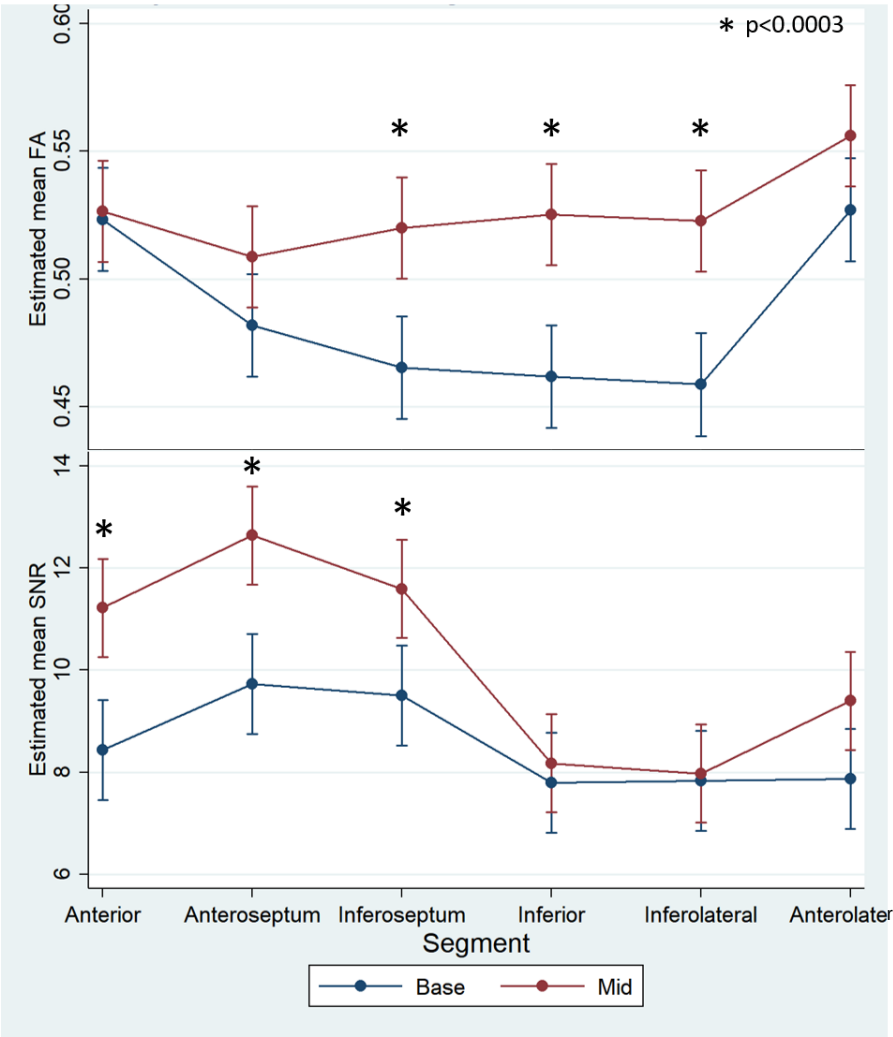


Figure 3.17 Segmental comparison of fractional anisotropy (A) and SNR (B) between the diastolic basal and mid slice

Reduced FA in the basal slice was driven by the inferoseptal, inferior and inferolateral segments (all post hoc p<0.0003). Reduced SNR at the base was seen in the anterior, and septal segments (all post hoc p<0.0003). [estimated mean from mixed model ± 95% confidence intervals; post hoc p values are Bonferroni-corrected for multiple comparisons]

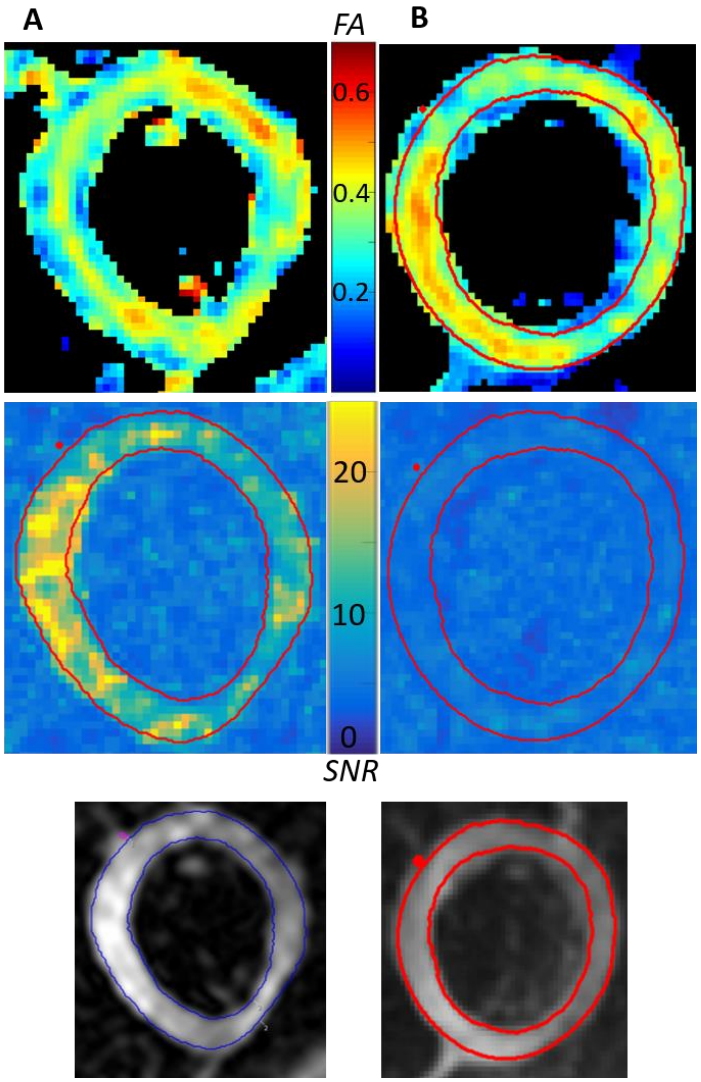


Figure 3.18 Mid (A) and basal (B) diastolic slice comparison of FA and SNR maps
FA maps (top row) from the mid slice have high SNR (middle row) compared to the basal slice with low SNR and the corresponding magnitude diffusion image (bottom row). [FA, fractional anisotropy]

3.4. Discussion

Diastolic DT-CMR provided characterisation of normal myoarchitecture which demonstrated high concordance with histology, without the use of exogenous contrast agents. Despite the relatively coarse spatial resolution of in vivo DT-CMR which was on the scale of millimetres, diastolic FA was sensitive to microscopic structure and was able to image the well-documented circumferential-alignment of myocytes in the mid-wall (Streeter et al., 1969).

3.4.1. Concordance with previous DT-CMR studies

Our quantitative DT-CMR parameters, ADC, FA and HA were comparable with previously reported results using the same imaging protocol measured at two centres (Tunnicliffe et al., 2014). We showed the expected transmural progression on helix angles in all slice and phases. Furthermore, we confirm the sheetlet angle change between diastole and systole as previously described by Ferreira et al. (2014) in accordance to sheetlet re-orientation with contraction (vertical in diastole and relative flattening with respect to the short-axis plane in systole) (Hales et al., 2012). ADC and FA measured in systole were lower than diastole as expected due to strain effects (Reese et al., 1996). Diastolic FA has been shown to be unaffected by strain correction, therefore further analysis was focused on diastolic FA.

3.4.2. Reduced quality of DT-CMR from the base and apical slice

There was significant slice variation in FA. Although the overall pattern of variation matched histological descriptions (mesocardial thinning of the high diastolic FA ring basally and

apically), the quality of DT-CMR from the base and apical slice were reduced. Apical measurements were fraught with inconsistencies from poor breath-holding at the end of a long scan, partial volumes effects due to apical tapering of the LV, and variation in slice position. The basal slice was influenced by significantly lower SNR due to the increased distance of the base of the heart from the surface coil. However, these slices may still prove to be clinically useful for quantifying abnormal shifts in FA if a normal reference range is established and shown to be reproducible. This would enable the assessment of HCM cases which have isolated basal or apical hypertrophy.

3.4.3. Segmental variation of FA estimates from the mid slice

Although DT-CMR parameters have been shown to be highly reproducible in the mid-ventricular slice (Tunnicliffe et al., 2014), we have shown that segmental variation in SNR and spatial distortion also limits the absolute accuracy and precision of FA measurements particularly in the lateral and inferior segments. However, HCM typically affects the anterior and septal segments which fortunately are least affected by such bias errors and therefore provides a method for quantifying abnormalities in disease. Further work into SNR effects are needed to establish the acceptable SNR range for clinical use.

Imaging in the lateral segments could be improved with distortion correction but this needs to be implemented prospectively during acquisition and thus cannot be corrected in these data (Gallichan et al., 2010). Robust distortion correction is essential if FA is to be clinically useful and to allow pixel-by-pixel comparison between diffusion and other CMR modalities

such as T1, ECV mapping and LGE. This will allow fibrosis effects to be dissociated from FA in HCM and provide a marker of disarray.

3.4.4. Limitations

3.4.4.1. Whole heart coverage

We were limited to acquiring three ventricular slices rather than whole heart data due to the long scan duration. Each slice took around 10 minutes and required 8-10, 18-heartbeat breath-holds which was repeated to obtain both cardiac phases. However, whole heart DT-CMR may be feasible if only performed in diastole (since systolic data may not be clinically due to the need for strain-correction), albeit a 1-hour acquisition with reduced quality basally and apically.

3.4.4.2. SNR

SNR effects on FA are complex and may depend on the expected FA of the tissue and the value of b_{main} which varies according to heart rate (Scott et al., 2016). FA has been shown to be invariably overestimated with decreasing SNR (McClymont et al., 2017b). This is thought to be caused by eigenvalue repulsion leading to a negative third eigenvalue. Negative eigenvalues violate the assumption of a positive definite diffusion tensor and are therefore excluded from analysis. However, in our data there was no relationship between SNR and FA suggesting that other factors could also be involved such as motion, beat-to-beat variability, noise or mis-registration artefacts. Future work should focus on using simulated models to

provide range estimates for FA depending on the underlying SNR, expected FA and individual's b_{main}. This will help distinguish whether FA differences are due to disease or fluctuations due to noise.

3.4.4.3. **Microvascular perfusion**

In vivo DT-CMR is affected by microvascular perfusion but since capillaries predominantly align with myocyte orientation it is unlikely to have much impact on the overall FA (Callot et al., 2003, Hsu et al., 2001). Microvascular perfusion effects can be avoided by diffusion weighting the reference image (increase b_0 to 150s/mm^2; our data uses b_0=15s/mm^2) (Scott et al., 2015). However, by increasing $b_{0,}$ the prescribed b_{main} also needs to increase to maximise the signal intensity differences between the main and reference data. Higher diffusion weighting yields greater contrast but at the expense of lowering SNR. Future work is needed to assess the optimal trade-off between suppressing perfusion effects, maximising signal intensity differences and SNR for FA.

3.4.5. Conclusion

Diastolic DT-CMR provided in vivo visualisation and quantification of the essential features of cardiac myoarchitecture as described by histology. This included the expected transmural progression of helix angle, and high mesocardial FA in the mid slice consistent with a well-developed mesocardium of coherently-aligned myocytes which thinned apically and basally. However, the quality of DT-CMR was reduced at the basal and apical slice due to low SNR and

partial volume effects respectively. The mid slice was highly reproducible despite segmental variation in SNR and spatial distortion affecting the lateral and inferior segments.

We have shown that diastolic FA is a marker of coherent myocyte alignment. Normal parallel alignment is lost in HCM, congenital heart disease, and in diseases affected by fibrosis which replaces myocytes with scar tissue. Thus, diastolic FA could be a potential non-contrast imaging marker for the microstructural abnormalities of disarray and fibrosis.

CHAPTER 4. DIFFUSION TENSOR CARDIAC MAGNETIC RESONANCE IN HYPERTROPHIC CARDIOMYOPATHY

4.1. Introduction

The low positive predictive accuracy of SCD risk stratification in HCM is due to the complex unpredictable interplay between histopathological substrate and multiple potential triggers. Nevertheless, triggers ultimately converge on an abnormal substrate to generate arrhythmias leading to SCD and thus, characterisation of the substrate may improve current risk stratification. Disarray is the likely primary arrhythmogenic substrate in HCM since extensive disarray is the hallmark feature of patients who die suddenly particularly in the young (Varnava et al., 2001b). Fibrosis which increases with age, and hypertrophy which has an age-related penetrance, are also pathological features in HCM but may be a reactive secondary process (Varnava et al., 2001b, Charron et al., 1997). Measuring the extent of disarray could potentially guide risk stratification, were disarray not solely a post mortem finding. However, the prevalence and significance of disarray within a low-medium risk HCM population is unknown as post mortem studies have a selection bias for high-risk patients.

4.1.1. HCM myoarchitecture

4.1.1.1. Disarray predominantly located in the mesocardium of hypertrophied segments

Disarray in HCM is characterised by hypertrophied misshapen myocytes with disorganised cell to cell alignment around a focus of collagen. These abnormalities have a patchy distribution with normal myocytes in parallel alignment seen in close proximity to disarray (Figure 4.1) (Varnava et al., 2000). Maximal disarray is confined to the hypertrophied myocardium predominantly in the mesocardium but can occur in focal areas within non-hypertrophied segments particularly in patients who die suddenly (Davies, 1984, Davies and McKenna, 1995). Kuribayashi and Roberts describe disarray as invading the circumferentially-arranged myocytes in the mesocardium, at the interventricular insertion point (IVIP) and hypertrophied segments (Figure 4.2) (Kuribayashi and Roberts, 1992).

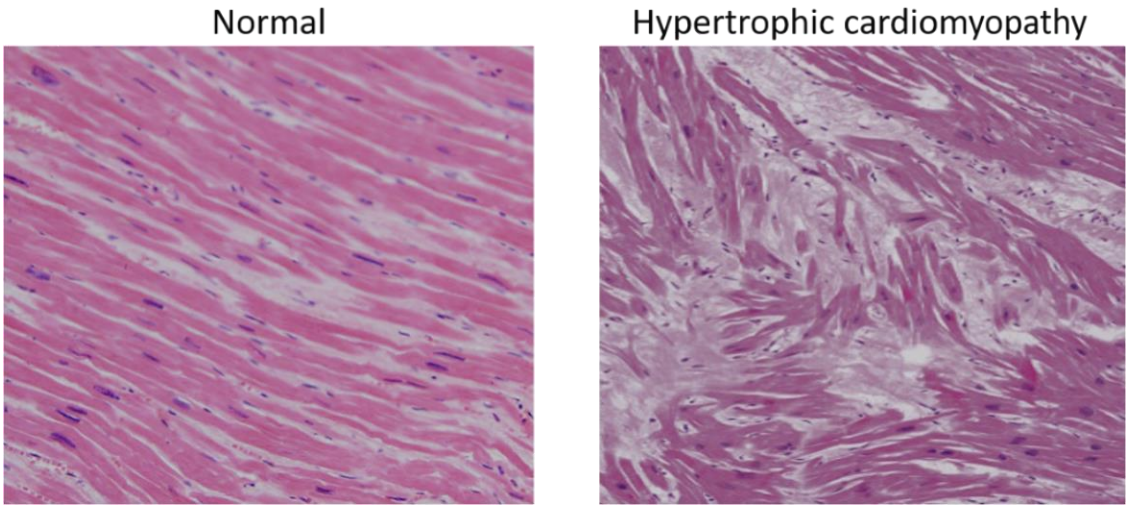


Figure 4.1 Photomicrograph of myocytes from a normal (left) and HCM (right) LV
Normal parallel arrangement of myocytes have been replaced with myocyte disarray and increased connective tissue (Elliott and McKenna, 2004).

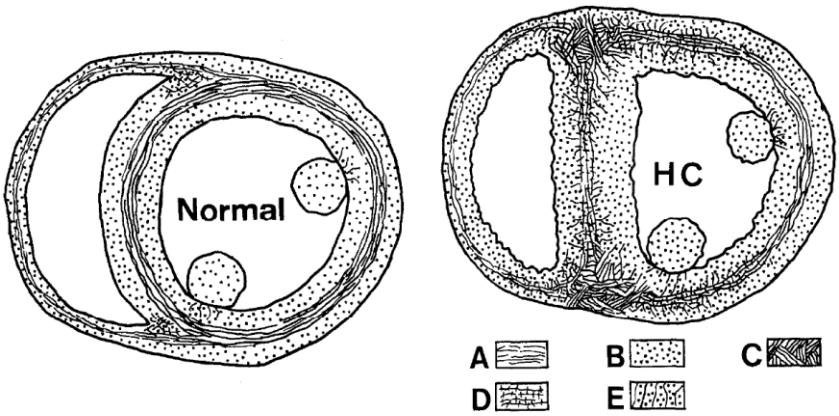


Figure 4.2 Myocardial architecture in the mid-ventricular slice in a normal and HCM heart. A, circumferential fibres; B, longitudinal fibres; C, fascicle disarray that is marked in the interventricular junction (which in controls is confined to the epicardium compared to HCM which invades the mesocardium); D, disarray that is marked adjacent to fascicle disarray but distant to junctional areas; E, disarray in longitudinal fibres, which is in continuity with disarray in mesocardial layer. Disarray in a normal heart is restricted to a small area between the interventricular junction and adjacent to papillary muscles (Kuribayashi and Roberts, 1992).

However disarray is also seen in normal hearts but consists of normal-sized and normal-shaped myocytes which is isolated to the interventricular insertion points without extending into the mesocardium (Kuribayashi and Roberts, 1992). Disarray is also found, although to a lesser extent, in congenital heart disease, dilated cardiomyopathy, hypertension, coronary artery disease and pulmonary hypertension (van der Bel-Kahn, 1977). Histological diagnosis of HCM is now based on the quantitative presence of >10% disarray in conjunction with enlarged myocytes of bizarre shapes and abnormal nuclei, in more than one tissue block from 15-20 samples obtained from multiple segments including several from the septum (Sheppard, 2000). In practice, the majority of HCM demonstrate extensive disarray >20% in several tissue blocks.

4.1.1.2. **Heterogeneity in disarray extent**

The extent of disarray varies from 0-80% (mean 30%) within the septum and lateral wall (Figure 4.3) (Maron et al., 1981a). There is no relationship between extent of disarray and magnitude of LVH despite typically being located within hypertrophied areas (Maron et al., 1992, Varnava et al., 2000). Nor is there an association between disarray and fibrosis or small vessel disease (Varnava et al., 2000). However, young patients who die suddenly show extensive disarray even within the non-hypertrophied free wall (Maron and Roberts, 1979, Varnava et al., 2001b).

4.1.1.3. **Heterogeneity in myocyte orientations**

Interestingly, myocyte orientation within disarray is not randomly distributed. Mesocardial septal samples from HCM have a wide and in some cases, a bimodal distribution of cell orientations but an overall average in the circumferential direction (Figure 4.4). In comparison, myocyte orientation from normal samples peak sharply at the mean orientation angle of zero indicating consistent parallel alignment of cells circumferentially (Whittaker et al., 1989). This is an important finding because it implies that the DT-CMR measure of helix angle alone will not be able identify such disarray since the overall mean angular orientation of myocytes within a mesocardial voxel will coincide with 0˚ as found in controls. FA is likely to be a more robust measure of disarray compared to helix angle because it quantifies the overall variance of cell alignments within a voxel.

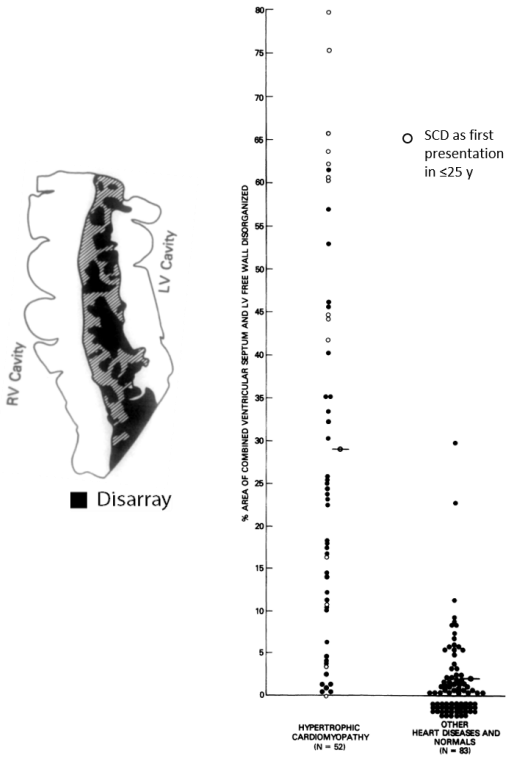


Figure 4.3 Histological map of disarray in a septal section in HCM (left) and percentage area of disarray in HCM and controls (right)
Disarray is extensive in HCM (Maron et al., 1981a).

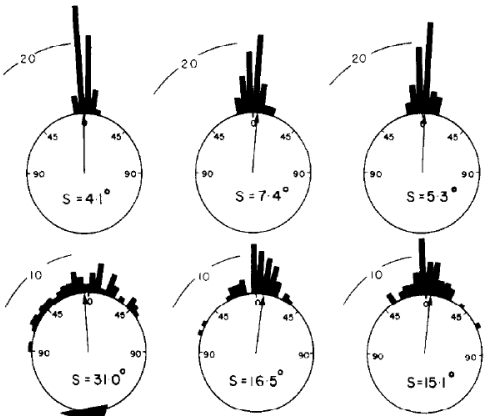


Figure 4.4 Myocyte orientation distributions from 3 normal (top row) and 3 HCM hearts (bottom row)
The mean orientation of mesocardial septal myocytes coincides with 0˚. The angular standard deviation is denoted by S. The circumferential direction of the septum is indicated by the arrow. In normal hearts, the orientation distribution peaked sharply with a narrow distribution. In HCM, the sharp peak was lacking with a wider and sometimes bimodal distribution (Whittaker et al., 1989).

4.1.1.4. **Heterogeneity in myocyte size**

Myocyte hypertrophy in HCM have a wide range of cell diameters 10-70 µm (mean 28 µm; normal 10-25 µm) and irregular shapes (Maron et al., 1974). Normal myocyte cell diameters vary transmurally which decreases from the endocardium to the epicardium (Hoshino et al., 1983). The same distribution is seen in hypertrophied myocytes from hypertensive patients and the non-hypertrophied LV free wall in HCM. However, in HCM, myocytes are maximally hypertrophied in the endocardium and mesocardium of the septum which also coincides with the predominate location of disarray (van der Bel-Kahn, 1977, Kuribayashi and Roberts, 1992) which show maximally hypertrophied myocytes compared to areas without disarray (Unverferth et al., 1987, Hoshino et al., 1983). HCM patients also show increased trabeculation (Petersen et al., 2005, Captur et al., 2014).

4.1.2. DT-CMR in HCM

The diffusion tensor is a rotationally invariant description of water diffusion within an imaging voxel which overcomes the challenge of using two-dimensional histological tissue sections that sometimes give the apparent appearance of disarray to normal myocardium depending on the section plane orientation of a tissue block (Becker and Caruso, 1982). Furthermore, histology of HCM is obtained post mortem, spatial coverage is piecemeal and sample preparation can cause distortion. In contrast, DT-CMR is non-destructive and non-invasive, and therefore has the potential for serial whole heart sampling during life. DT-CMR is a

quantitative method which can be compared in or between patients at different times or in different centres (Tunnicliffe et al., 2014, McGill et al., 2012).

Four human DT-CMR studies using a STEAM sequence have reported on HCM. Fibre disarray was detected in five HCM patients but this initial study was performed during systole at 1.5T field strength (Tseng et al., 2006). A second study at 3T also in systole, demonstrated inter-study reproducibility of DTI measurements in ten HCM patients but found no difference in FA or ADC between HCM and controls (McGill et al., 2012). This group then focused solely on sheetlet angle and demonstrated that HCM patients had impaired sheetlet mobility causing a failure of sheetlets to re-orientate in diastole (Ferreira et al., 2014) which they later validated using ex vivo pig hearts (Nielles-Vallespin et al., 2017).

4.1.3. Hypotheses and aims

We hypothesised that diastolic FA, a marker of myocyte alignment coherency within an imaging voxel, will be reduced due to disarray in HCM patients compared to healthy controls. The aims of this work were to assess the ability of in vivo DT-CMR to probe the LV myoarchitecture in HCM and assess the feasibility of DT-CMR in HCM patients.

4.2. Methods

50 HCM patients (47 ± sd 14 years, 74% male) and 30 age- and gender- matched controls (same controls as Chapter 3; 46 ± 16 y, 70% male) underwent DT-CMR. See Chapter 2 - Methods for full description.

A second blinded operator analysed 10 randomly selected HCM cases. Interobserver reproducibility of FA was assessed by Bland-Altman analysis and paired t-tests were used to determine the statistical significance of any difference.

4.3. Results

4.3.1. Study group characteristics

The study population characteristics are summarised in Table 4.1. HCM patients had increased body mass index, LV wall thickness, mass, ejection fraction and left atrial size. 96% of patients were asymptomatic or mildly symptomatic. Risk for SCD was low (median HCM Risk-SCD score = 2.6%; median total risk factor = 1).

Table 4.1 Clinical and imaging characteristics by group
[mean ± standard deviation unless otherwise indicated]

	HCM (n=50)	**Healthy controls** (n=30)	**p value**
Age, years	47 ± 14	46 ± 16	0.70
Male, n (%)	37 (74)	21 (70)	0.70
Body mass index, kg/m^2	27 ± 4	24 ± 4	**0.003**
Heart rate, beats per minute	57 ± 10	58 ± 11	0.75
Imaging characteristics			
LV end-diastolic volume, ml	154 ± 32	157 ± 37	0.78
LV ejection fraction, %	76 ± 5	68 ± 5	**<0.0001**
LV mass index, g/m^2	74 ± 23	54 ± 12	**<0.0001**
Left atrial diameter, mm	39 ± 7	32 ± 6	**<0.0001**
Maximum LV wall thickness, mm	21 ± 4	11 ± 1	**<0.0001**
ECV	0.32 ± 0.04	0.28 ± 0.03	**0.001**
LGE present, n (%)	22 (44)	0	**-**
LGE, % LV mass	5 ± 7	0	**-**
Clinical characteristics			
NYHA class, n (%)			-
Class I	38 (76)	30 (100)	
Class II	10 (20)	0 (0)	
Class III	2 (4)	0 (0)	
Class IV	0 (0)	0 (0)	
HCM Risk Factors *(Gersh et al., 2011)*			
NSVT	15 (30)		
Unexplained syncope	3 (6)		
Family History SCD	7 (14)		
Massive LVH ≥30mm	0 (0)		
Abnormal exercise BP response	5 (10)		
Total number of risk factors [1, 2, 3], n (%)	24, 3, 0 (48, 6, 0)		
HCM Risk-SCD score (O'Mahony et al., 2014), %; median [range]	2.6 [1.2 - 8.7]		
Genetic mutation, n (%)			-
No pathogenic mutation	20 (40)		
MYBPC3	17 (34)		
MYH7	12 (24)		
TNNI3	1 (2)		

4.3.2. Group analysis of DT-CMR parameters across slice and segment

DT-CMR parameters at diastole from the mid-ventricular and basal slices are shown in Table 4.2. All segments from these slices were analysable in all subjects. No group differences were detected in ADC or helix angle gradient at either slice level. Therefore, further analysis was focused on diastolic FA. There was also no difference in SNR or heart rate between the groups which are potential confounders. The apical slice was unobtainable in 15 subjects (11 HCM patients and 4 controls due to tiring) and was affected by partial volume effects and variation in slice position (Chapter 3), therefore was not assessed. There was no group difference detected in any DT-CMR parameter in systole. Further analysis focused on the diastolic phase due to known strain effects on FA during systole.

Diastolic FA in the mid slice was reduced in HCM compared to controls (mid slice mean 0.49 ± 0.05 *vs* 0.52 ± 0.03, p=0.0005, Table 4.2, Figure 4.5). There was smaller but still significant reduction in FA at the basal slice (p=0.04). To investigate the relationship between group, segment and FA, a linear mixed-effects model was fitted to account for any within-patient correlation or variation across the six segments in a slice. Although FA was globally reduced in HCM, this effect differed significantly across segments in the mid-ventricular slice (interaction p<0.0001) but no segmental difference was detected in the base (Figure 4.6B).

Table 4.2 DT-CMR parameters in diastole by slice
[slice mean ± standard deviation]

	HCM (n=50)	**Healthy controls** (n=30)	**p value**
Heart rate, beats per minute	57 ± 10	58 ± 11	0.75
MID-VENTRICULAR SLICE			
FA	0.49 ± 0.05	0.52 ± 0.03	**0.0005**
ADC, $x10^{-3}$ mm^2/s	1.29 ± 0.10	1.26 ± 0.12	0.15
HA gradient, °/mm	7 ± 1	9 ± 3	0.53
SNR estimate	10.0 ± 2.5	10.4 ± 2.6	0.53
BASAL SLICE			
FA	0.45 ± 0.04	0.49 ± 0.03	**0.04**
ADC, $x10^{-3}$ mm^2/s	1.31 ± 0.12	1.31 ± 0.13	0.97
HA gradient, °/mm	8 ± 2	6 ± 3	0.84
SNR estimate	8.9 ± 2.1	8.7 ± 2.0	0.45

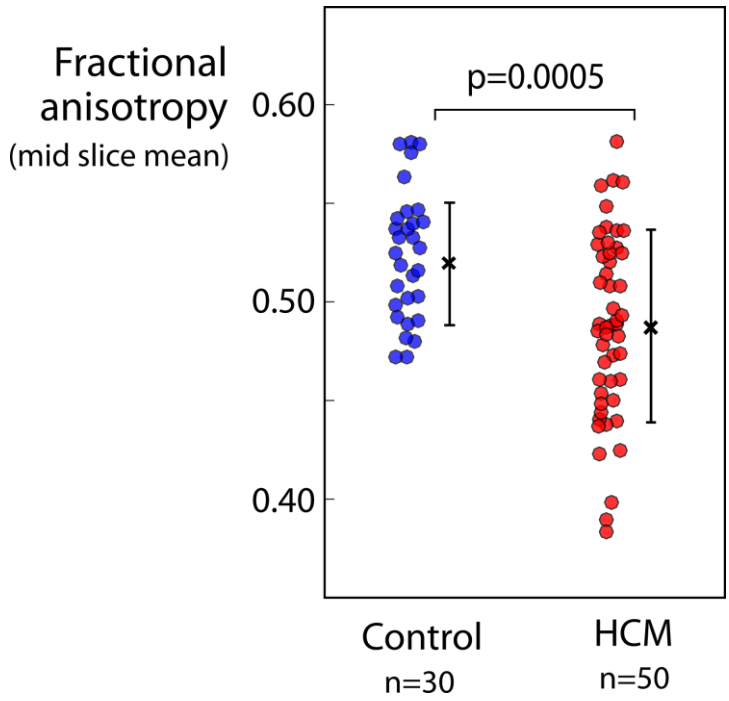


Figure 4.5 Diastolic FA was reduced in HCM compared to controls
The increased standard deviation of FA in HCM demonstrates the heterogeneity within this disease population with considerable overlap with controls. Only a subpopulation of HCM patients show FA below the range for controls.

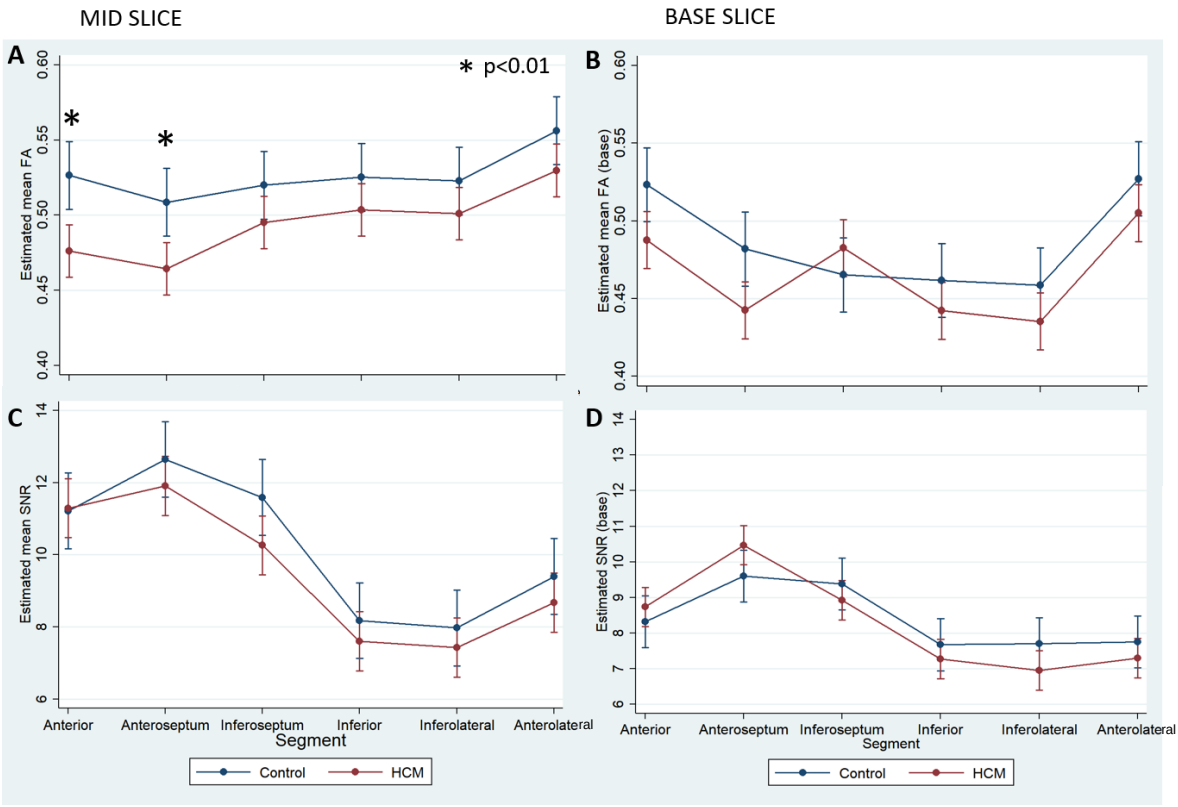


Figure 4.6 Segmental variation by slice and group of FA and SNR

Anterior and anteroseptal FA in the mid-ventricle (A) was significantly lower in HCM compared to controls (post hoc p<0.01). No group differences were detected in FA at the basal slice (B). No group difference was detected in SNR at any segment in both slices (C-D), therefore group differences in FA were unlikely to be confounded by SNR. Low SNR (<10) in the mid-ventricular inferior and lateral segments and basal slice globally (as described in Chapter 3), may impair the detection of FA group differences in these locations [estimated mean ± 95% confidence intervals; post hoc p values are Bonferroni-corrected for multiple comparisons].

4.3.2.1. **SNR**

No group difference was detected in SNR at any segment or slice (Figure 4.6C-D), therefore group differences in FA were unlikely to be confounded by SNR. Furthermore, no difference in FA was found between different reconstruction methods, each with different noise characteristics. This suggests that noise floor effects were not corrupting the data. At SNR >8, ADC had an accuracy within 1% using high quality ex-vivo DTI data in 5 rat hearts (McClymont et al., 2017b). FA, at this SNR however, was systematically overestimated and required SNR of ~50 for accurate estimation. Such high SNR is not currently achievable in the clinical setting. However, if SNR is comparable between groups then group differences in FA overestimation is likely to be a useful measure. Further analysis focused on mid-ventricular data as these had the greatest SNR and are known to be reproducible (Tunnicliffe et al., 2014).

4.3.3. Mid-ventricular DT-CMR maps in HCM – qualitative assessment

Figure 4.7 shows typical DT-CMR maps at diastole and systole in a HCM patient. HA maps showed the expected transmural progression in HCM as controls. Diastolic SA maps had a vertical orientation of sheetlet populations, except in the hypertrophied segment which had horizontally aligned sheetlets. In systole, the sheetlets were all horizontal as controls. Visually, in HCM, the mesocardial ring of high FA (yellow/orange) seen in controls (Figure 3.10) was disrupted by reduced FA in hypertrophied septal segments and insertion points, consistent with the locations of disarray and fibrosis in HCM histology invading the circumferential

mesocardial layer (Kuribayashi and Roberts, 1992). Interestingly, there was no corresponding disruption of helix angle in areas with reduced FA.

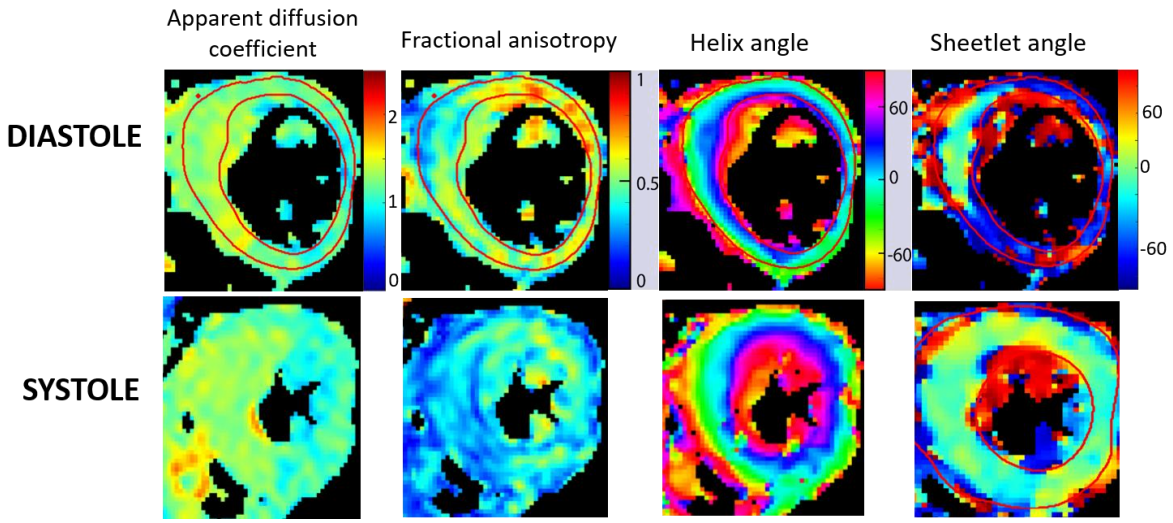


Figure 4.7 DT-CMR maps in an HCM patient from both phases

4.3.4. Diastolic FA in the mid-ventricular slice

Qualitative analysis from mapping mean mid-ventricular FA across all subjects by group to a normalised LV wall (Figure 4.8) revealed that the reduced FA anteriorly and anteroseptally was transmural and localised to the anterior interventricular insertion point. Visually there was also reduced FA transmurally at the presumed inferior interventricular point. However, neither the inferoseptal nor the inferior segment reached statistical significance because the inferior insertion point reduction was less extensive than the anterior and when straddled across two segments, it unlikely to be detected on segmental analysis. ROI analysis at the inferior insertion point is likely to detect this reduction however the definition of insertion

point area is subjective and was therefore not performed. Another reason for low FA to predominate the anterior rather inferior insertion point is that in our HCM cohort, maximum wall thickness was found in the anteroseptum (Figure 4.9) which is likely to show greater disarray than non-hypertrophied areas such as the inferior segment.

Qualitative analysis from plotting mean mid-ventricular SNR across all subjects by group transmurally showed an increase in SNR mesocardially but mesocardial SNR showed no detectable differences between HCM and controls and thus SNR unlikely accounts for the "break" in the mesocardial ring (Figure 4.10).

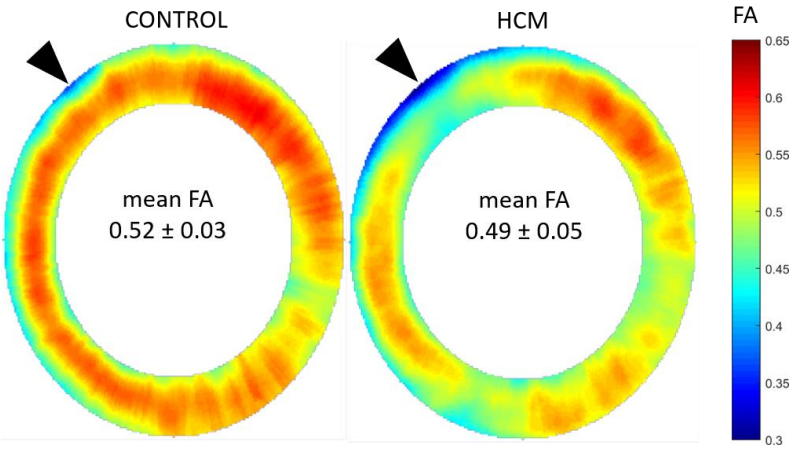


Figure 4.8 Mid-ventricular mean FA across all subjects by group mapped to normalised LV co-ordinates
There is an almost complete mesocardial ring of increased FA in the controls (except inferolaterally due to distortion effects from imaging, see Chapter 3). In HCM this ring is "broken" transmurally at the anterior and inferior interventricular insertion points in keeping with HCM histology. [Black arrowhead denotes anterior interventricular insertion point; mean ± standard deviation]

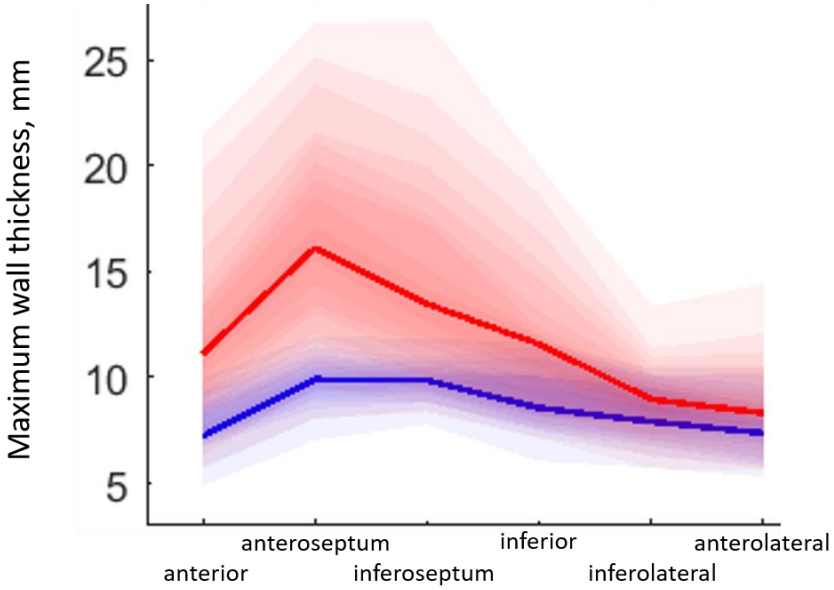


Figure 4.9 Maximum LV wall thickness at end-diastole by mid-ventricular segment
Our HCM cohort predominantly had maximum hypertrophy at the anteroseptum [median with quantiles; red = HCM, blue=controls].

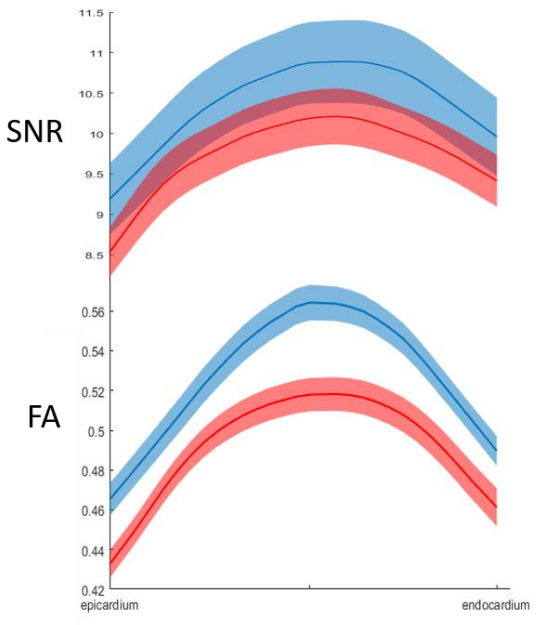


Figure 4.10 Mean diastolic SNR and FA from epi- to endocardium in mid slice in HCM (red) and control (blue)
Mesocardial SNR was increased in both groups but there was no significant difference in SNR between groups to account for the reduced FA in HCM [mean ± standard error].

I previously showed that FA differed significantly across segments (interaction p<0.0001; Figure 4.6). Minimum segmental FA corresponded to the maximally hypertrophied segment in every HCM patient. Within individuals, average segmental FA in HCM was reduced in the maximally hypertrophied segment (either anterior, anteroseptum or inferoseptum) compared to the inferolateral segment (paired T-test 0.44 ± 0.05 *vs* 0.50 ± 0.08, difference 0.06 ± 0.08, p<0.0001; Figure 4.11). In contrast, no such difference was detected in controls between the segment with maximal wall thickness (anteroseptum or inferoseptum) compared to the inferolateral segment (0.51 ± 0.04 *vs* 0.52 ± 0.07, difference 0.01 ± 0.07, p=0.313).

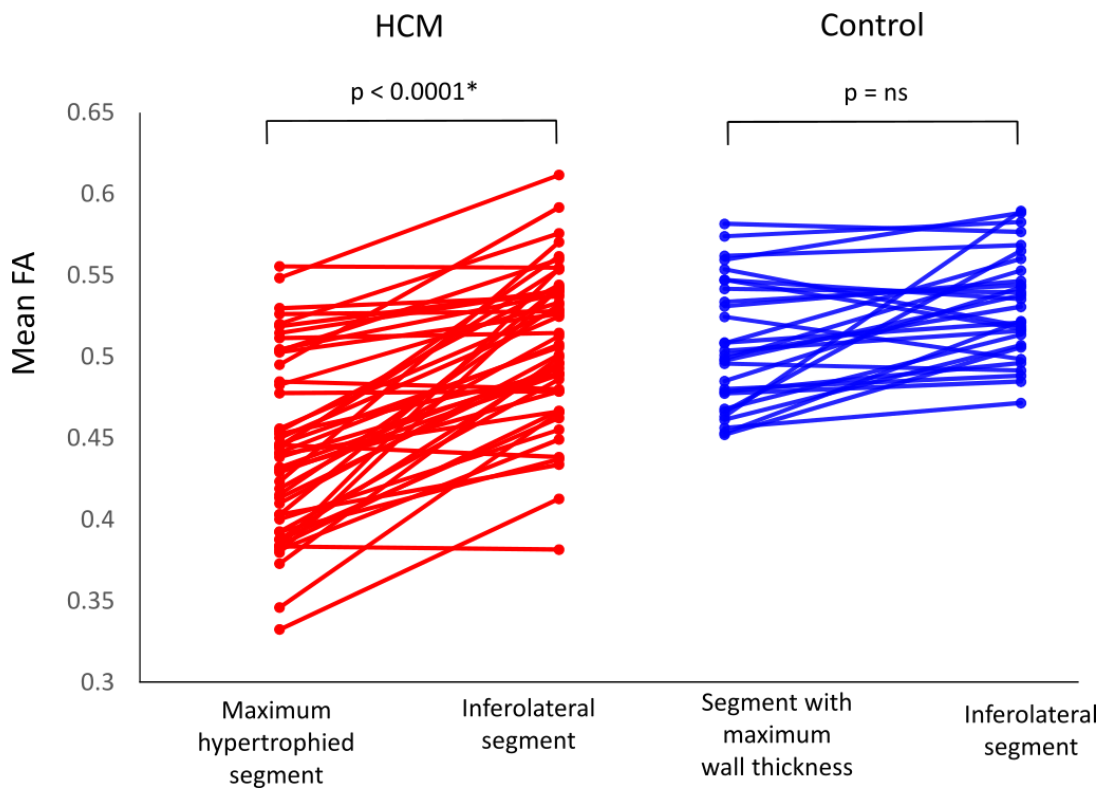


Figure 4.11 Mean FA of the maximally thickened segment had reduced FA compared to the inferolateral segment in HCM

4.3.5. Relationship between FA and clinical features

In controls, no clinical feature was associated with FA which included age, gender, body mass index, heart rate, end-diastolic volume, ejection fraction, mass index, or maximum LV wall thickness (all $p<0.05$). However, in HCM, each year of increasing age was associated with a decrease of 0.01 in FA ($\beta=-0.35$, $p=0.013$), and each unit increase in BMI was associated with a decrease in FA ($\beta=-37.1$, $p=0.08$). This may be a result of increasing fibrosis in older patients (mean age with LGE 50 ± 13years *vs* no LGE 44 ± 14 years, $p=0.03$) (Biernacka and Frangogiannis, 2011) and increased BMI (mean BMI with LGE 28 ± 4 kg/m^2 *vs* no LGE 25 ± 3 kg/m^2, $p=0.01$) (Cavalera et al., 2014), which contributes to FA signal. No other feature was associated with FA in HCM. To examine the relationship between FA, age and BMI in controls and HCM patients, we used logistic regression. The logistic regression model was statistically significant $\chi^2(3)=17.6$, $p=0.001$ and correctly classified 69% of cases. Reduced FA was a significant predictor of HCM despite correcting for age and BMI ($p=0.007$).

4.3.6. Inter-observer reproducibility of FA in HCM

Inter-observer reproducibility of FA in HCM was assessed between two observers. Although reproducibility had been shown previously in controls, this had not yet been tested in HCM. Initial analysis showed a bias due to ROIs. ROIs drawn directly on diffusion images included the full epicardium and endocardial trabeculae which were seen in the subsequent HA maps as ROIs including longitudinal fibres subepicardially and subendocardially. However, when ROIs were repeated alongside cine images (higher resolution than diffusion images) to ensure

adequate exclusion of trabeculae, there was excellent correlation between mid-ventricular slice and segmental FA in HCM (slice r=0.99, segmental anterior r=0.82, anteroseptum r=0.82, inferoseptum r=0.80, inferior r=0.96, inferolateral r=0.93, anterolateral r=0.93; all p<0.05). No statistical difference in FA was detected in any segment or at the slice level (slice difference 0.006). The intra-class coefficient for slice was 0.98 (0.74 to 0.99).

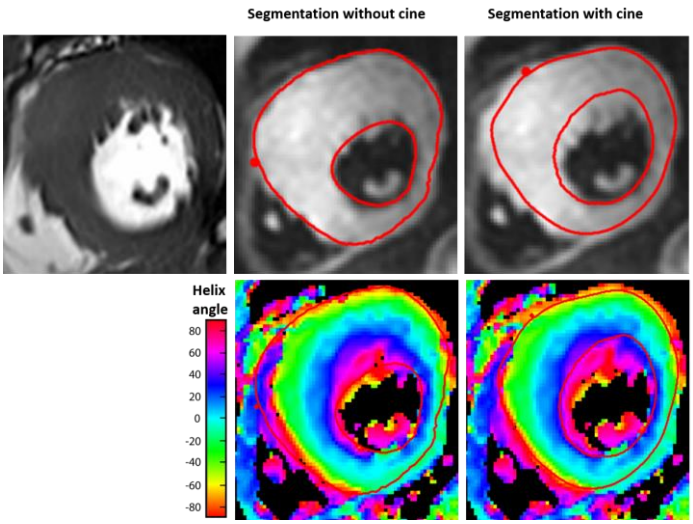


Figure 4.12 Differences between regions of interest by segmenting alongside cine
Segmenting alongside higher resolution cine images ensured adequate exclusion of trabeculae as shown on the helix angle maps.

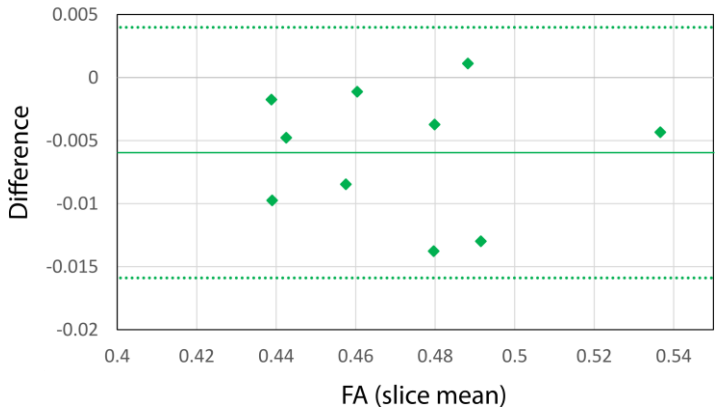


Figure 4.13 Bland-Altman plot showing excellent inter-observer reproducibility of mid-ventricular slice mean FA

4.3.7. Diffusion tensor visualisation

Figure 4.14 shows the 3-dimensional representation of the diffusion tensor for voxels in the mid diastolic slice of a control and HCM patient, colour mapped according to FA. Each ellipsoid represents the mixture of myocyte orientation and interstitium within a voxel. In the control, ellipsoids were thinner/flatter while the HCM patient had globular shaped ellipsoids particularly in the hypertrophied area.

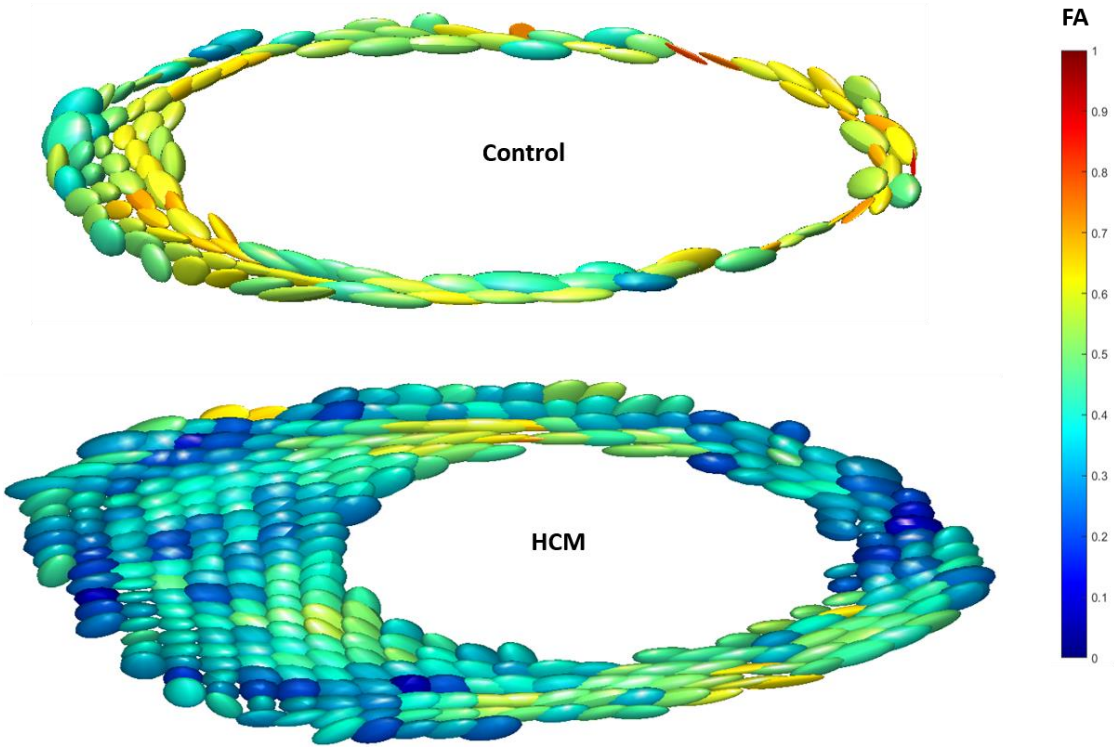


Figure 4.14 Tensor visualisation in the mid diastolic slice of a healthy control and HCM patient
The colours are mapped according to FA. The ellipsoid shape indicates the mixture of myocyte orientations within a voxel. The ellipsoid is orientated in the direction of maximum diffusion.

4.4. Discussion

DT-CMR provided in vivo visualisation and quantification of HCM myocardial architecture which demonstrated high concordance with previously described post-mortem findings (Kuribayashi and Roberts, 1992, Whittaker et al., 1989). The mid-ventricular slice showed excellent inter-observer reproducibility of FA in HCM. FA was reduced in HCM compared to controls, but no difference in helix angle progression was detected between the two groups. There was heterogeneity in FA between HCM patients. Only 34% of patients demonstrated FA values below controls. Reduced FA was associated with increasing age and BMI in HCM which may be confounders for fibrosis. However FA remained reduced in HCM compared to controls even after adjusting for age and BMI.

4.4.1. SNR

As seen Chapter 3, the SNR in HCM patients was also significantly reduced in the basal compared to mid slice. There was transmural heterogeneity in SNR with the greatest SNR in the mesocardium. This increase in SNR in the mesocardium may be due to magnetic susceptibility of myocytes parallel to the magnetic field (Dibb et al., 2015).However, there was no significant difference between SNR in HCM and controls and therefore SNR was unlikely to be the source for FA differences between groups.

4.4.2. Concordance with other in vivo DT-CMR studies

Our diastolic FA results in HCM are consistent with a previous, small study which also reported reduced FA in the septum compared to the free wall in 5 HCM patients using DT-CMR acquired at mid-systole (Tseng et al., 2006). However, more recently McGill *et al*. found no difference in septal FA in 10 HCM, when DT-CMR was acquired from end-systole to end-systole (McGill et al., 2012). We also found no difference in FA at systole. Additionally, more than 10 patients within our cohort had no detectable difference in FA which is likely to represent the significant proportion of HCM patients who have a benign clinical course with no adverse effect to life expectancy (Cecchi et al., 1995). Another factor is that FA measured using a stimulated echo diffusion sequence is affected by cardiac strain which is most marked at peak systole (Stoeck et al., 2014). Although this effect can be corrected by acquiring accurate 3D strain data, it prolongs scan duration, increases data processing time and the chance of systematic error rises (Ferreira et al., 2018). However unlike systole, FA obtained at diastole is unchanged by strain correction thus our FA values have not been adjusted for strain (Stoeck et al., 2014).

We found that diastolic FA in healthy controls did not relate to any clinical factor as did McGill et al (2015b). We also confirm abnormal SA in HCM as previously described (Ferreira et al., 2014, Nielles-Vallespin et al., 2017). In diastole, SA was reduced in HCM compared to controls, i.e. HCM diastolic sheetlet populations were horizontally rather than vertically orientated. While in systole, there was no significant difference in SA between the groups.

4.4.3. Concordance with histology

Our FA maps in controls and HCM corresponded to previous histological findings (Streeter et al., 1969, Kuribayashi and Roberts, 1992). The disruption of the mesocardial ring of high FA in HCM mirrored the findings of Kuribayashi and Roberts in a study of 47 autopsied hearts with HCM (Kuribayashi and Roberts, 1992). They reported destruction of the circular orientation by disarray in 77% at the insertion points, 33% at the septum and 34% at the anterior and inferior walls. In contrast, the circular orientation was intact in 9 out of 10 of the control hearts.

However, our helix angle maps in HCM showed similar transmural angular progression to controls and there was no significant difference in helix angle between the two groups despite finding reduced FA in HCM. Whittaker et al. found similar results in mesocardial septal sections from 12 HCM patients and 6 controls (Whittaker et al., 1989). In controls, myocyte orientation sharply peaked at 0° indicating that they were largely circumferentially aligned in parallel. Although cell orientations were disordered in HCM, rather than a random distribution of angles, the overall mean orientation was also 0°, but there was a wide, sometimes bimodal distribution of myocyte orientations (Figure 4.4). Thus, helix angle at low spatial resolution, is a suboptimal DT-CMR measure of disarray since the overall mean of cell orientations within a voxel converges to the same as a control. FA provides a better marker of disarray since it quantifies the overall variance of cell alignments within a voxel.

4.4.4. Limitations

Only a single mid-ventricular slice has been assessed to ensure consistency of DT-CMR measures with those previously reported as reproducible between imaging centres (Tunnicliffe et al., 2014). This precludes assessment of areas of maximal hypertrophy in basal or apical slices. The apical slice is particularly prone to error as low spatial resolution DT-CMR amplifies partial volume effects as the left ventricle tapers. Furthermore, the transmural myocyte orientation changes with levels: at the base, circumferentially-orientated myocytes are only primarily found in the anteroseptum and disappear towards the apex (Greenbaum et al., 1981). This would reduce FA in the basal and apical slices compared to mid-ventricle, thus standardised reference ranges for slices need to be established (Benson et al., 2008).

We were unable to study patients with severe breathlessness due to the need for repeated long breath-holding in DT-CMR. Participants had to provide consistency in the rate and depth of breath-holding to ensure the myocardium remained in an identical position during diffusion encoding. Furthermore ectopy, which is often seen in HCM, prolonged scan times as optimal diffusion encoding is dependent on a regular RR interval. Shorter scan times are required before DT-CMR can be adopted for routine clinical use in symptomatic patients. This may be achievable with stronger MR gradient systems.

Several HCM patients were unsuitable for this study since we excluded co-morbidities which can cause cardiomyopathies in their own right. This excluded diabetics, hypertensives, atrial fibrillation and obesity. It is likely that phenotypic variability in LVH in HCM is confounded by

changes in loading conditions and these factors may accelerate and exaggerate hypertrophy in the presence of sarcomeric HCM mutations but not impact on the extent of disarray. Future studies should include “real world” patients with co-morbidities to represent HCM in the general population.

4.5. Conclusion

DT-CMR provided in vivo visualisation of HCM myocardial microstructure which demonstrated concordance with previously published post mortem findings. Like healthy controls, the mid-ventricular slice in HCM patients had higher SNR compared to the base. FA was reduced in HCM compared to controls despite normal transmural helix angle progression. Low FA was associated with increasing age and BMI in HCM but not in controls. This association may be attributable to fibrosis as increased age and BMI was associated with increased LGE in HCM. However FA remained reduced in HCM compared to controls even after adjusting for age and BMI, suggesting that FA may be measuring disarray in addition to fibrosis.

CHAPTER 5. PREDICTING THE RISK OF VENTRICULAR ARRHYTHMIA IN HYPERTROPHIC CARDIOMYOPATHY USING MULTIPARAMETRIC CARDIAC MAGNETIC RESONANCE

5.1. Introduction

In addition to disarray, fibrosis is a predominant feature in patients who die suddenly of HCM and both disarray and fibrosis are likely substrates for re-entrant ventricular arrhythmias leading to sudden cardiac death (SCD) (Varnava et al., 2001b, Shirani et al., 2000).

5.1.1. Extracellular matrix

The organisation and function of the myocardium is dependent on the extracellular matrix which is a dynamic environment, continually changing in response to cell signalling. Collagen is the predominant structural component of the extracellular matrix and myocytes exist within a fine network of collagenous connective tissue, of which there are three layers (Figure 5.1) (Caulfield and Borg, 1979).

1. The endomysium surrounds each myocyte connecting them to adjacent myocytes via collagen struts to coordinate the transmission of force and prevent slippage between cells.

2. The perimysium is thicker and surrounds groups of myocytes with three distinct forms: extensive meshwork on laminar sheet surfaces, convoluted fibres connecting adjacent sheets and longitudinal cords which are seen in the subepicardium. They also provide a framework for capillaries. Myocytes within the perimysium produces the “grain” of the ventricle on gross dissection and the so-called “myofibres”.
3. The epimysium surrounds the ventricle and protects against excessive stretch.

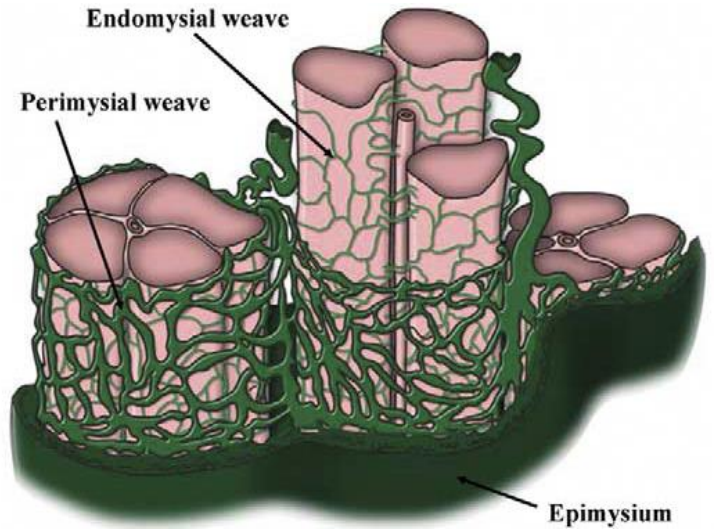


Figure 5.1 The supporting fibrocollagenous network around myocytes
Consists of the endomysial weave surrounding each individual myocyte, the coiled perimysial fibres that group myocytes into “myofibres” and the endomysial around the ventricle (Anderson et al., 2005).

5.1.2. Cross myocyte laminar sheetlets

The perimysium divides the myocardium into laminar sheetlets which are 3-4 myocytes thick and orthogonal to the “myofibre” direction (LeGrice et al., 1995). Myocyte branching and

perimysial fibres connect sheetlets loosely to adjacent sheetlets but visible gaps exist between sheetlets known as cleavage planes. Branches decrease from the epicardium to the mesocardium while the distribution of perimysial collagen is greatest in the mesocardium. However, sheets are not seen in the subepicardium where the perimysium is seen only as longitudinal cords and distinct sheetlet-populations with sheet angles of opposing polarity (positive and negative), meet in the mesocardium and slip across each other using the cleavage planes to cause a change in sheetlet angulation (Harrington et al., 2005, Kung et al.) (Pope et al., 2008).

Laminar sheetlets are responsible for the main component of LV wall thickening which entails the rearrangement of myocytes across the ventricular wall between end diastole to end systole (LeGrice et al., 1995, Spotnitz et al., 1974). During systole, the radial wall thickens by ~25% and the LV shortens by ~50% which cannot simply be accounted for by myocyte shortening of ~15% which only produces ~8% thickening of myocyte diameter. Flattening of sheetlet populations (wall-parallel to short-axis plane) in systolic wall thickening can be likened to the opening of an accordion and flattening of the folds, while in diastole the sheetlets are more vertical (wall-perpendicular) like closing an accordion and bringing the folds together (Hales et al., 2012).

Sheetlet mobility is impaired in HCM and is related to reduced strain. DT-CMR has revealed that sheetlets in HCM appear trapped in a systolic wall-parallel orientation in diastole (Ferreira et al., 2014, Nielles-Vallespin et al., 2017), in keeping with previous histology

showing increased myocyte layers in the hypertrophied septum of HCM patients compared to controls (Unverferth et al., 1987). We have reproduced these findings in Chapter 4, where HCM diastolic sheetlet populations were horizontally rather than vertically orientated. This systolic-like sheetlet orientation in diastole may be the main component of macroscopic wall hypertrophy rather than myocyte hypertrophy alone and may also explain the regional strain abnormalities seen in hypertrophied segments which cannot be explained exclusively by fibrosis (Aletras et al., 2011).

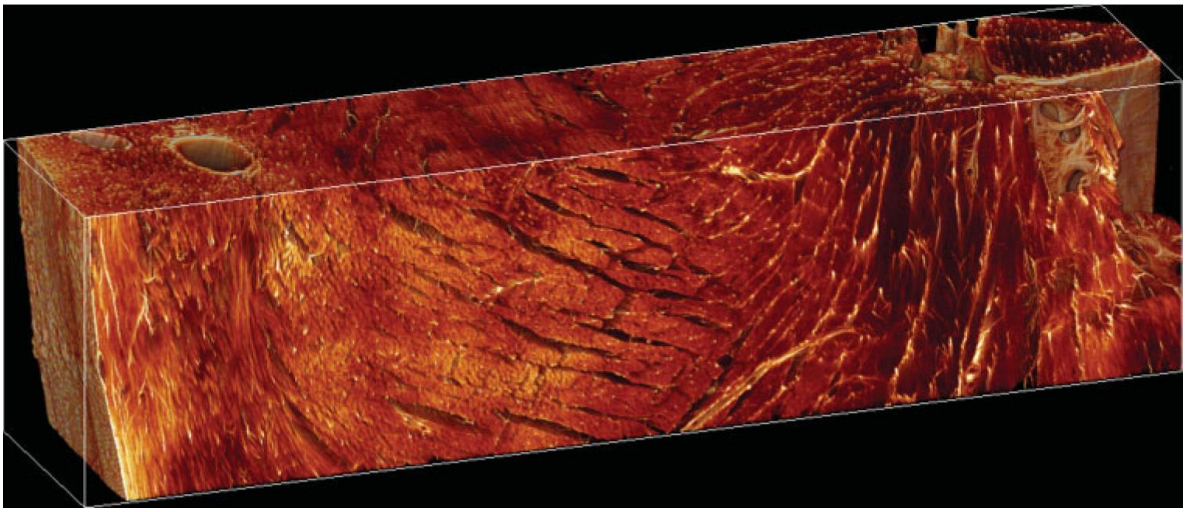


Figure 5.2 Macroscopic view of the three-dimensional organisation of ventricular myocardium
Front face demonstrates the laminar sheet organisation of myocytes and shear layers (cracks) which have gaped at post mortem enhancing visibility. Two sheet populations exist: sheets in the mesocardium are approximately radial while sheets in the epicardium (left) and endocardium (right) are more longitudinal with a chevron pattern. In systole, sheets flatten (wall- parallel to short-axis plane) causing wall thickening, while sheets become more vertical in diastole (wall-perpendicular). Sheet mobility is impaired in HCM; sheets are wall-parallel in diastole i.e. in a systolic orientation which may represent the main factor for macroscopic hypertrophy. Conversely, in DCM, sheets are more wall-perpendicular in systole i.e. in a diastolic orientation leading to wall thinning (extended confocal microscopy (Sands et al., 2005)).

5.1.3. Myocardial fibrosis

Four types of fibrosis are described histologically (Anderson et al., 1979):

1. Microscopic scar is replacement fibrosis not discernible to the naked eye.
2. Interstitial fibrosis is the perimysium encasing groups of myocytes. In severe cases can appear as a honeycomb.
3. Perivascular fibrosis is the perimysium around intramural blood vessels blending with the adventitia.
4. Plexiform fibrosis is a type of interstitial fibrosis unique to disarray which has fine and coarse bands of collagen interlaced between myocytes. Its extent is associated with severity of disarray (Anderson et al., 1979).

Fibrosis is increased universally across the heart in HCM (Unverferth et al., 1987). Fibrosis in the septum is greater than in the non-hypertrophied free wall, while no such variation occurs in normal hearts (Unverferth et al., 1987). Unlike disarray, fibrosis has a weak but significant correlation with LV mass and wall thickness, which also relates to increasing age (Varnava et al., 2000). However no relationship is observed between fibrosis and small vessel disease (Varnava et al., 2000).

5.1.4. Fibrosis affects DT-CMR

Fractional anisotropy (FA), calculated from the diffusion tensor, quantifies the directionality of diffusion, from 0 – random motion (perfect isotropy), to 1 – diffusion in a single linear direction (perfect anisotropy) (Figure 5.3). Thus, FA is expected to be low in voxels with disorganised cell alignments and expanded extracellular space.

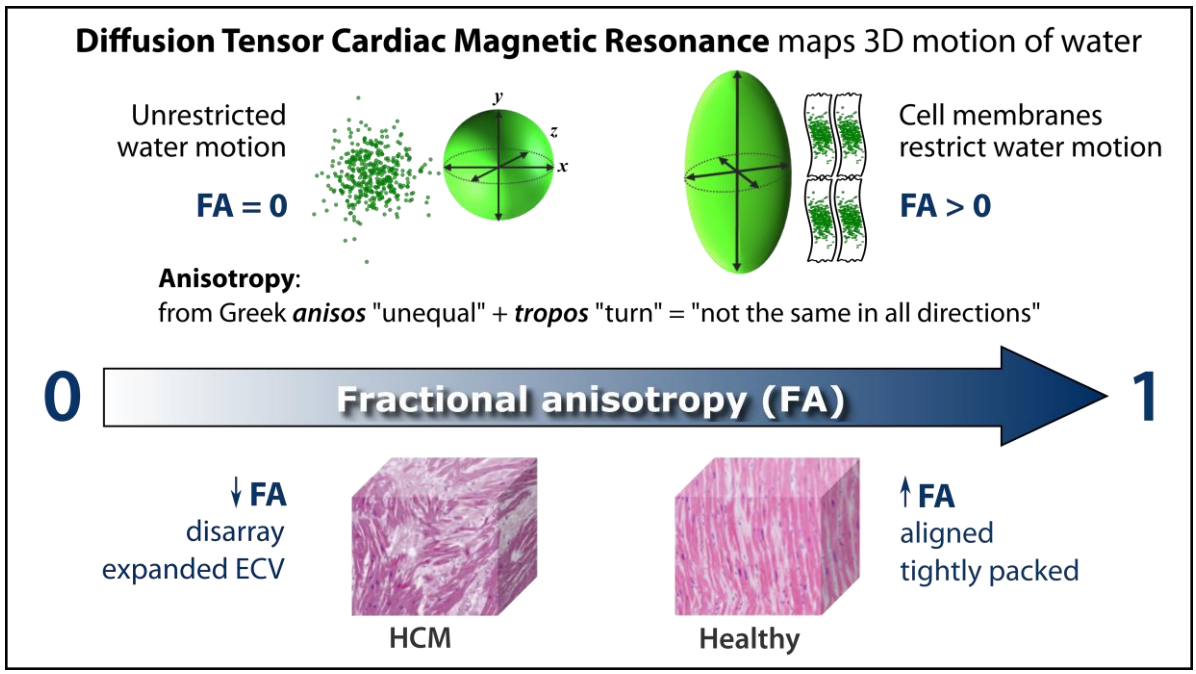


Figure 5.3 Fractional anisotropy (FA) calculated from the diffusion tensor
DT-CMR maps the diffusion of water molecules in three dimensions. FA calculated from the diffusion tensor, quantifies the directionality of water diffusion within each imaging voxel ($2.8 \times 2.8 \times 8 mm^3$) as its motion is impeded by several million myocytes and the surrounding interstitium. Without barriers, water motion is random and equal in all directions, which can be represented as a sphere using the diffusion tensor and has FA of zero (perfect isotropy). Cell membranes act as barriers restricting water motion along the long-axis of myocytes. Thus, FA is expected to be high in voxels with coherently aligned myocytes such as the LV mid-wall where myocytes are consistently aligned circumferentially. Conversely, FA is expected to be low in HCM due to disorganised cell alignments and expanded extracellular volume (ECV).

Post mortem histology has shown that the LV mid-wall contains a band of circumferentially-orientated myocytes (Streeter et al., 1969) which in HCM is infiltrated by disarray and fibrosis, typically at the interventricular junctions and the hypertrophied segments (Figure 4.2) (Kuribayashi and Roberts, 1992). At these regions, FA is expected to be low as water molecules diffuse more isotropically within enlarged myocytes of bizarre shapes and orientations, and within areas of fibrosis.

Fibrosis is known to decrease FA in dilated cardiomyopathy and correlates negatively with histological measurements of collagen, a major component of fibrosis (Abdullah et al., 2014). Therefore, low FA in HCM is likely to reflect a composite measure of both disarray and fibrosis. Late gadolinium enhancement (LGE) correlates with myocardial collagen in HCM but not with disarray (Moon et al., 2004), and thus could potentially be used to separate the fibrosis component of FA to provide an in vivo measure of disarray. However, LGE only represents focal fibrosis rather than the concomitant diffuse fibrosis which is widespread in HCM. In the absence of oedema and infiltration, extracellular volume (ECV) fraction is an excellent quantitative biomarker of diffuse fibrosis (White et al., 2013) but is yet to be histologically validated in HCM.

DT-CMR acquired with stimulated echo measures diffusion throughout the cardiac cycle. Although this allows adequate time to probe microstructure, it is sensitive to cardiac strain. However FA is robust to strain when DT-CMR is acquired from diastole to diastole, unlike other DT-CMR parameters such as apparent diffusion coefficient (ADC; measures magnitude of diffusion) and sheetlet angle (SA) (Stoeck et al., 2014). FA is also invariant under rotation, making it robust to difficulties in aligning hearts of varying shape. Thus, we sought only to assess diastolic FA. We hypothesised that low FA in HCM represents the combination of disarray and fibrosis. Both these histological abnormalities are increased in HCM patients who die suddenly (Shirani et al., 2000, Varnava et al., 2001b). Thus, we also hypothesised that low FA represents the anatomical substrate for electrical instability and therefore examined the relationship between low FA and ventricular arrhythmia in HCM patients.

5.2. Methods

50 HCM patients (47 ± 14y, 74% male) and 30 age- and gender- matched controls (46 ± 16y, 70% male; Table 4.1) underwent DT-CMR (same participants as Chapter 4). Only a single mid-ventricular slice in diastole was analysed. See Chapter 2 - Methods for full description.

5.3. Results

The study population characteristics are summarised in Table 4.1. Median follow-up was 4.4 ± 0.9 years. 15 patients (30%) had non-sustained ventricular tachycardia (NSVT) captured on 24-hour Holter ECG monitoring. No patient had sustained VT. Runs of NSVT ranged from 4-15 beats (median 8) with rates from 125-200 bpm (median 175 bpm). 4 patients (8%) received implantable cardioverter defibrillators (ICD) with no appropriate therapies reported at median follow-up of 4.1 ± 1.0 years since ICD implantation.

5.3.1. Diffusion Tensor CMR maps

Figure 5.4 shows typical images and subsequent FA and HA maps obtained by DT-CMR at diastole with corresponding cine, LGE and ECV maps. HA maps in both HCM and controls showed the expected transmural progression of myocytes from the epicardial left-handed helix to the endocardial right-handed helix. FA maps in controls demonstrated an almost complete mid-wall ring of increased FA (yellow; Figure 5.4A) compared to the epicardium and endocardium. This matched the ring of coherently aligned circumferentially-orientated myocytes revealed on the HA map and in published histology (Streeter et al., 1969). In contrast, this mid-wall ring was disrupted

in HCM at the anterior junction and the hypertrophied anteroseptum (Figure 5.4B-C), and in some cases the ring was absent (Figure 5.4D), again consistent with patterns seen at HCM histology (Figure 5.4E) (Kuribayashi and Roberts, 1992). Areas of profoundly low FA matched the regions of LGE and elevated ECV (Figure 5.4C), in line with fibrosis contributing to low FA, but low FA could not be explained by fibrosis in all cases. In some instances, FA was low in patients without LGE or elevated ECV (Figure 5.4B) and extended beyond areas of fibrosis indicating disarray (Figure 5.4D).

5.3.2. Diffusion Tensor CMR parameters in HCM and controls

Overall diastolic FA, averaged across the slice, was reduced in HCM compared to controls (slice mean 0.49 ± 0.05 *vs* 0.52 ± 0.03, p=0.0005, Figure 5.6A; as seen previously in Chapter 4). SA was reduced in HCM compared to controls, i.e. HCM diastolic sheetlet populations were horizontally rather than vertically orientated (circular mean 5 ± 23° *vs* 84 ± 31°, p<0.0001, Figure 5.5).

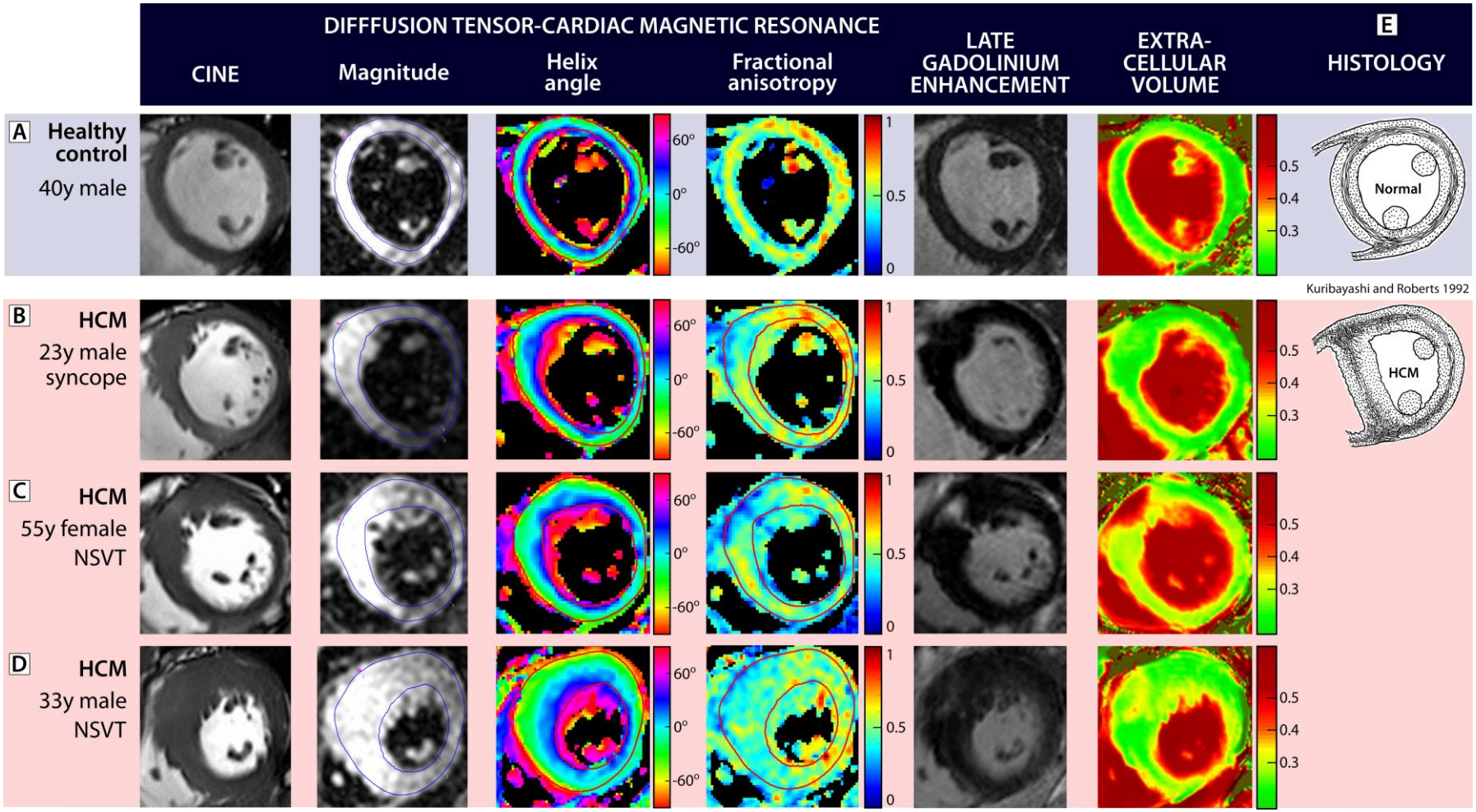


Figure 5.4 Multimodal imaging of disarray using diffusion tensor cardiac magnetic resonance, late gadolinium enhancement and extracellular volume mapping

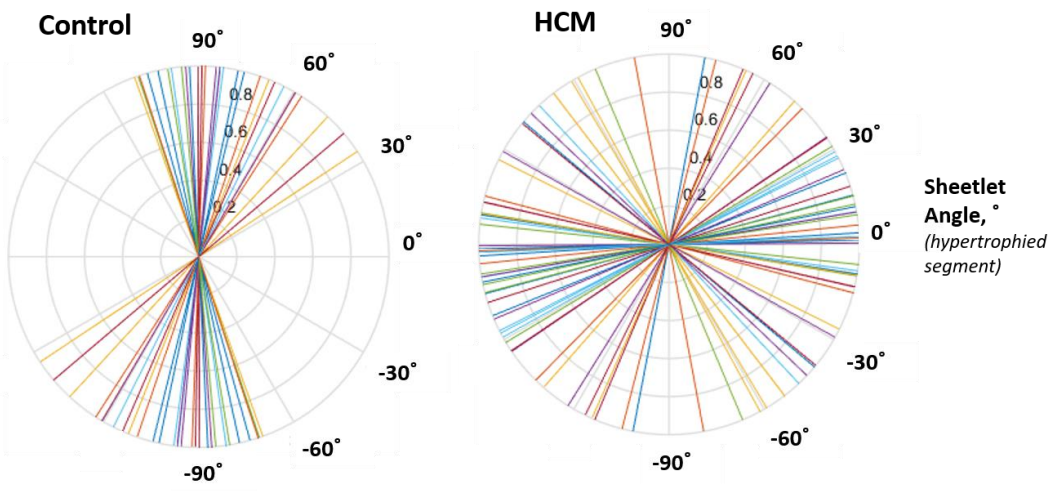


Figure 5.5 Mean sheetlet angle in segment of maximum wall thickness
Diastolic SA averaged (circular mean) across the hypertrophied segment in the mid-ventricular slice. Diastolic HCM sheetlet populations were more horizontally than vertically orientated i.e. there was flattening of sheetlet populations (wall-parallel to short-axis plane) in HCM as seen in systolic wall thickening in controls.

5.3.3. Relationship of Fractional Anisotropy with LGE and extracellular volume

HCM patients with LGE (n=22) had lower FA than those without LGE (slice mean 0.46 ± 0.04 *vs* 0.51 ± 0.04, p=0.00006; Figure 5.6A). To investigate the relationship between FA and fibrosis, we examined per-segment average FA in a linear mixed-effects model with segmental LGE and ECV as covariates. The mixed model was fitted to account for any within-patient correlation or systematic variation across the six mid-ventricular segments. LGE and ECV were significant predictors of FA (segmental linear mixed-effects model, both p<0.001), in keeping with fibrosis contributing to low FA. However, importantly, FA adjusted for LGE and ECV remained reduced in HCM (segmental linear mixed-effects model, estimated marginal means 0.50 [95% CI 0.49 to 0.51] *vs* 0.52 [0.50 to 0.53], p=0.028; Figure 5.6B), consistent with low FA also demonstrating sensitivity to disarray (Figure 5.6C).

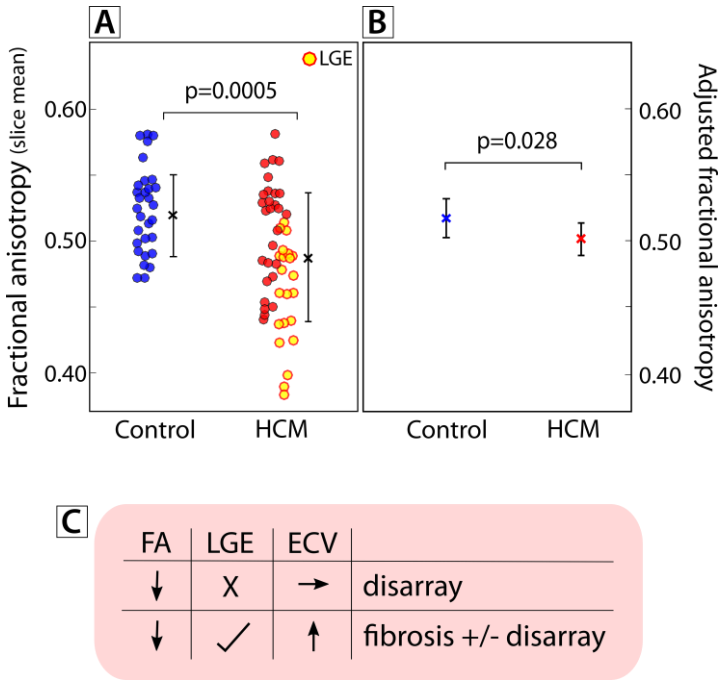


Figure 5.6 Reduced FA in HCM even after adjustment for fibrosis
Diastolic FA, averaged across the mid-ventricular slice, was reduced in HCM compared to healthy controls (A, slice mean ± standard deviation). HCM patients with LGE (n=22; yellow) had lower FA than those without LGE (p<0.001). LGE and ECV were significant predictors of FA (p<0.001), in keeping with fibrosis contributing to low FA. Yet FA adjusted for LGE and ECV remained reduced in HCM (B, linear mixed-effects model estimated marginal means with 95% confidence intervals), consistent with low FA also demonstrating sensitivity to disarray. These results imply that fibrosis (presence of LGE and/or elevated ECV) contributes to low FA (C). However, in the absence of fibrosis, low FA is likely to represent disarray.

5.3.4. Relationship between Fractional Anisotropy and ventricular arrhythmia in HCM

To investigate the relationship between FA and ventricular arrhythmia, we examined FA in the maximally hypertrophied segment as a potential substrate for arrhythmias. The patient characteristics of those with and without ventricular arrhythmias are summarised in Table 5.1 Characteristics of HCM patients with and without ventricular arrhythmia. There were no significant differences between the two groups in demographics or imaging characteristics.

FA was reduced in HCM patients with documented ventricular arrhythmia compared to those without (n=15; segmental mean 0.41 ± 0.03 *vs* 0.46 ± 0.06, p=0.007; Figure 5.7). The lowest FA in any segment of any control was 0.45. Thus, there was no overlap in segmental FA values between controls and HCM patients with NSVT (Figure 5.7). There was only a trend towards increased fibrosis in HCM patients with ventricular arrhythmia compared to those without (LGE, 9 patients *vs* 13, p=0.14; ECV 0.33 ± 0.04 *vs* 0.31 ± 0.04, p=0.058) and no significant difference in hypertrophy (maximum LV wall thickness, 19 mm *vs* 20 mm, p=0.60), suggesting that disarray was the driver for FA difference. No significant difference was detected in SA in HCM patients with and without ventricular arrhythmia (24 ± 33° *vs* 0 ± 30°, p=0.08), despite SA showing marked differences between HCM and controls.

To examine the relationship between FA, fibrosis and maximum wall thickness in patients with and without ventricular arrhythmia, we used logistic regression. FA predicted the odds of a patient having ventricular arrhythmia. A decrease in FA of 0.05 increased the odds of ventricular arrhythmia by 2.5 (95% CI 1.2 to 5.3; p=0.015). This remained significant even after correcting for LGE, ECV and maximum wall thickness by adding them as covariates to the regression model (p=0.036). The significance of FA as predictor of ventricular arrhythmia was unchanged when additionally corrected for age and BMI (p=0.036).

Table 5.1 Characteristics of HCM patients with and without ventricular arrhythmia
[mean ± standard deviation unless otherwise indicated]

	Ventricular arrhythmia (n=15)	**No ventricular arrhythmia** (n=35)	**p value**
Age, years	52 ± 10	44 ± 15	0.054
Male, n (%)	11 (73)	26 (74)	0.94
Body mass index, kg/m^2	27 ± 4	27 ± 4	0.85
Heart rate, bpm	56 ± 10	58 ± 10	0.57
Imaging characteristics			
LV end-diastolic volume, ml	160 ± 33	152 ± 31	0.42
LV ejection fraction, %	77 ± 5	75 ± 6	0.39
LV mass index, g/m^2	78 ± 26	72 ± 22	0.49
LV wall thickness, mm	19 ± 5	20 ± 4	0.60
Left atrial diameter, mm	40 ± 8	39 ± 7	0.52
LGE present, n (%)	9 (60)	13 (37)	0.14
LGE, % LV mass	4 ± 6	4 ± 8	0.56
ECV	0.33 ± 0.04	0.31 ± 0.04	0.058

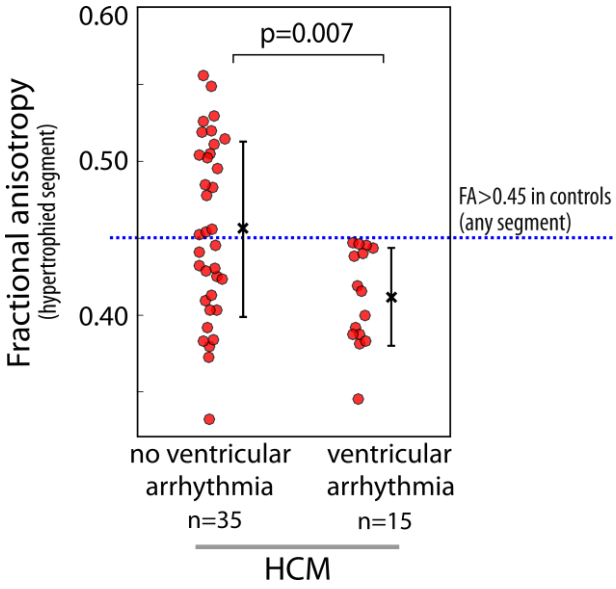


Figure 5.7 Reduced FA in HCM with ventricular arrhythmias
Diastolic FA, measured in the hypertrophied segment, was reduced in HCM with ventricular arrhythmia compared to those without (mean ± standard deviation). Some patients with no apparent ventricular arrhythmia also had low FA, perhaps in part reflecting the low sensitivity of a one-day Holter. Interestingly, the lowest FA in any segment in any control was 0.45. Thus, there was no overlap in segmental FA values between controls and HCM patients with NSVT.

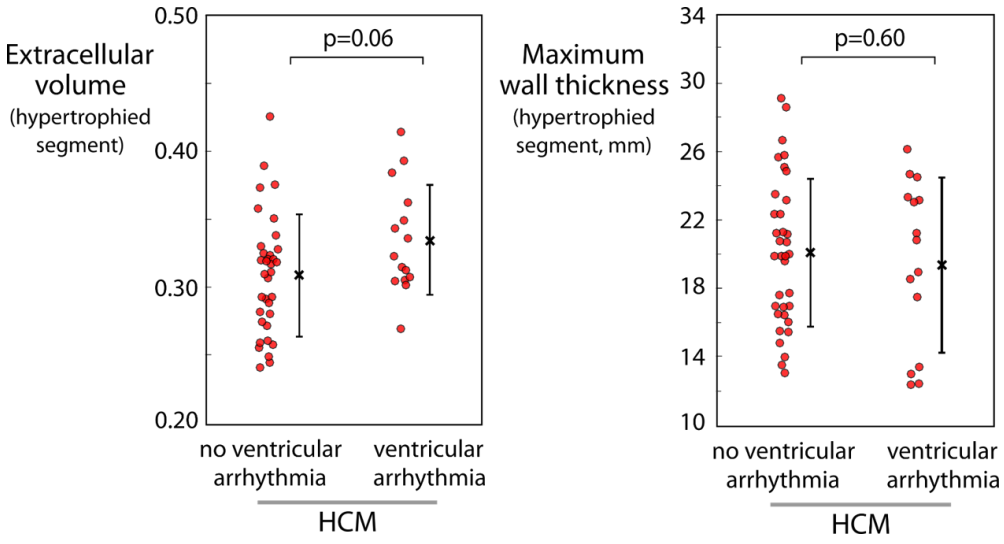


Figure 5.8 A trend to increased ECV but not hypertrophy in HCM with ventricular arrhythmia

5.4. Discussion

Using multimodal CMR, we were able to account for the contribution of fibrosis to FA. FA, adjusted for fibrosis, remained reduced in HCM consistent with low FA demonstrating sensitivity to disarray. We showed that focal reduction of FA in the maximally hypertrophied segment of HCM patients was associated with ventricular arrhythmia. This association of low FA with ventricular arrhythmia persisted even after adjusting for fibrosis and hypertrophy, suggesting that adjusted FA is likely to be measuring disarray and hence may provide a novel, independent risk factor.

5.4.1. Detecting the anatomic substrate for arrhythmia in HCM

Previous studies have suggested that structural disruption such as fibrosis and disarray provide the conditions for re-entrant ventricular arrhythmias which lead to SCD (Saumarez, 1994). LGE has modest correlation to clinical risk factors for SCD (O'Hanlon et al.), suggesting that other factors such as disarray may also be important (Varnava et al., 2001b). It is likely that there is a continuum within the HCM myocardium involving both disarray and fibrosis which increases vulnerability to arrhythmia. This could explain why HCM patients over 35 years of age are not risk-free (Maron et al., 2000a), as fibrosis becomes the predominant post mortem finding in this age group (Varnava et al., 2001b). Interestingly, none of the controls had FA<0.45 in any segment which provided complete separation of controls from HCM patients with ventricular arrhythmia. This may represent a potential FA threshold for arrhythmic risk, if this normal limit persists in larger cohorts.

In our study, a proportion of patients without recorded ventricular arrhythmic events had similarly low FA values to those with ventricular arrhythmias. However, Holter monitoring may underestimate the true burden of ventricular arrhythmia (Musumeci et al., 2011). Continuous monitoring via ICD in HCM has shown a higher prevalence of NSVT than Holter (Francia et al., 2014). NSVT is a recognised marker of arrhythmic potential for precipitating SCD (Syska et al., 2010, McKenna et al., 1981, Maron et al., 1981b), however, most patients with NSVT do not die suddenly, suggesting heterogeneity within this group (Spirito et al., 1994). The underlying structural substrate may be one source of this heterogeneity and future studies will need to assess the relationship between extent, distribution and location of disarray versus fibrosis with SCD or aborted SCD. In practice, using FA as a composite marker of disarray and fibrosis, rather than dissociating the fibrotic component, would be more convenient but may also be clinically useful as both these histological abnormalities are intrinsically linked to arrhythmic risk.

5.4.2. Sheetlet angle

Although diastolic SA was abnormal in HCM, as previously described (Ferreira et al., 2014, Nielles-Vallespin et al., 2017), no significant SA differences were detected in HCM patients with and without ventricular arrhythmia using our protocol. This fixed systolic-like orientation of sheetlets in diastole did not associate with low FA suggesting that two are mutually independent features. Further work is needed to understand why and how sheetlets become less mobile and what their clinical implications are other than the mechanism for wall thickening.

5.4.3. Limitations

The predictive value of FA after adjusting for fibrosis and hypertrophy in ventricular arrhythmias may be slightly lower in a prospective study than our estimate due to over-fitting of multiple variables.

We have excluded RV endocardium, LV endocardial trabeculae and papillary muscles to avoid partial volume effects due to low spatial resolution. However, these structures may act as initiation sites for re-entrant waves during ventricular arrhythmias (Valderrábano et al., 2003). Exclusion of the subendocardium also removes myocardial crypts often associated with HCM, which have demonstrated disarray in adjacent myocardium (Kuribayashi and Roberts, 1992). Both the RV endocardium and the LV endocardial trabeculae are visually increased in our HCM cohort in keeping with findings from (Tseng et al., 2006) which reported increased longitudinal fibres (helix angles towards 90° or -90°) in the septum. We may therefore be underestimating the anatomic substrate for arrhythmia.

Our patients were also relatively low risk as we could not include those with ICDs; thus, in this hypothesis-generating study we could only test for association with predictors of risk rather than events. To document clinical utility of low FA for deciding whom to treat with ICD, we will need to measure its association with hard endpoints such as SCD, aborted SCD and appropriate therapies from ICDs implanted after initial FA measurement. This will need to be tested prospectively in large-scale multicentre studies and registries such as the Hypertrophic Cardiomyopathy Registry (Kramer et al., 2015).

Conclusion

DT-CMR provided in vivo assessment of normal and HCM myocardial microstructure which demonstrated concordance with histology. FA was reduced in HCM compared to controls. Low FA in HCM was associated with ventricular arrhythmia and is likely to represent disarray after accounting for fibrosis. We propose that diastolic FA is the first in vivo marker of disarray and thus a potential independent risk factor in HCM.

CHAPTER 6. IDENTIFYING DISTINCT ECG PHENOTYPES USING A MACHINE LEARNING APPROACH IN HYPERTROPHIC CARDIOMYOPATHY

The work presented in this chapter has been published: "Distinct ECG phenotypes identified in hypertrophic cardiomyopathy using machine learning associate with arrhythmic risk markers" by Lyon, Ariga et al., 2018, Frontiers in Physiology, 2018 Mar 13; 9:213 with a joint first authorship for Dr Aurore Lyon and me. We have contributed equally to this specific work. Dr Aurore Lyon developed and performed the computational methods: ECG signal processing, computational modelling, feature extraction, dimensionality reduction and clustering analysis.

6.1. Introduction

HCM remains a common yet challenging genetic heart muscle disease due to its heterogeneous clinical course (Maron, 2002). Accurate identification of high risk patients with HCM are a clinical priority since ICDs can successfully treat ventricular arrhythmias triggering SCD (Maron et al., 2000c). The use of ICDs has confirmed that ventricular arrhythmia is the precipitating mechanism in SCD. Structural abnormalities induced by HCM – hypertrophy

(Spirito et al., 2000), myocyte disarray (Varnava et al., 2001b) and fibrosis (Adabag et al., 2008) – may act synergistically with ion-channel dysfunction (Coppini et al., 2013) to create an unstable electrical milieu predisposing to arrhythmia. We hypothesised that this electrical instability ought to be reflected by changes in the QRS complex (depolarisation) and T wave (repolarisation). T wave changes can occur when the QRS is normal – a primary repolarisation abnormality or, as a direct result of altered depolarisation – a secondary repolarisation abnormality (where both the QRS and T wave are altered). Despite this biophysical underpinning, the ECG surprisingly does not feature in current risk assessments.

Previous studies have attempted to visually assess the electrophysiological signature of HCM by visually describing pathological Q waves, wide QRS, prolonged QT interval and inverted T waves using paper ECGs (Lakdawala et al., 2011, Savage et al., 1978). However, this approach has not yielded reliable risk markers (Sherrid et al., 2009, Maron et al., 1982), possibly because they do not extract the pertinent information. These discrete clinically interpreted ECG features do not objectively capture the shape diversity of ECG complexes. The combination of machine learning and mathematical modelling provide a set of developed methods that can make sense of multivariate complex datasets and detect differences that might be challenging for the human eye (Obermeyer and Emanuel, 2016). These techniques make fewer assumptions by selecting discriminatory features from the whole ECG data.

In this study, we developed a novel computational analysis of high-fidelity 12-lead digital Holter ECGs using machine learning and mathematical modelling to identify discrete

subgroups of HCM patients. We hypothesised that ECG morphology reflects important aspects of the underlying structural and functional abnormalities and therefore clinical features and markers of arrhythmic risk would differ between the ECG phenotypes.

6.2. Methods

The methods are summarised in Figure 6.1. See Chapter 2 - Methods for full description. The computational methods described below were developed and performed by Dr Aurore Lyon, Department of Computer Science, University of Oxford.

6.2.1. Holter ECG pre-processing

30-minute ECG excerpts were used to analyse the 8 linearly independent leads (I, II, V1-6) with custom-built software using MATLAB (Mathworks, MA, USA). A wavelet based delineator (Martinez et al., 2004) extracted the peaks and boundaries of the ECG waveforms. High frequency noise was removed using a low-pass Butterworth filter with cut-off frequency of 45Hz, baseline drift was removed by a cubic spline method and a notch filter rejected the 50Hz mains power artefact. The first twenty beats with maximal ST segment–T wave (STT) signal-to-noise ratio (ratio between STT peak to peak amplitude and root mean square value of background noise >20Hz) were considered for analysis and were aligned with respect to the QRS complex by Woody's method (Sörnmo and Laguna, 2005). A window of 180ms centred on the mean energy of the QRS and a 500ms window aligned to the STT onset were

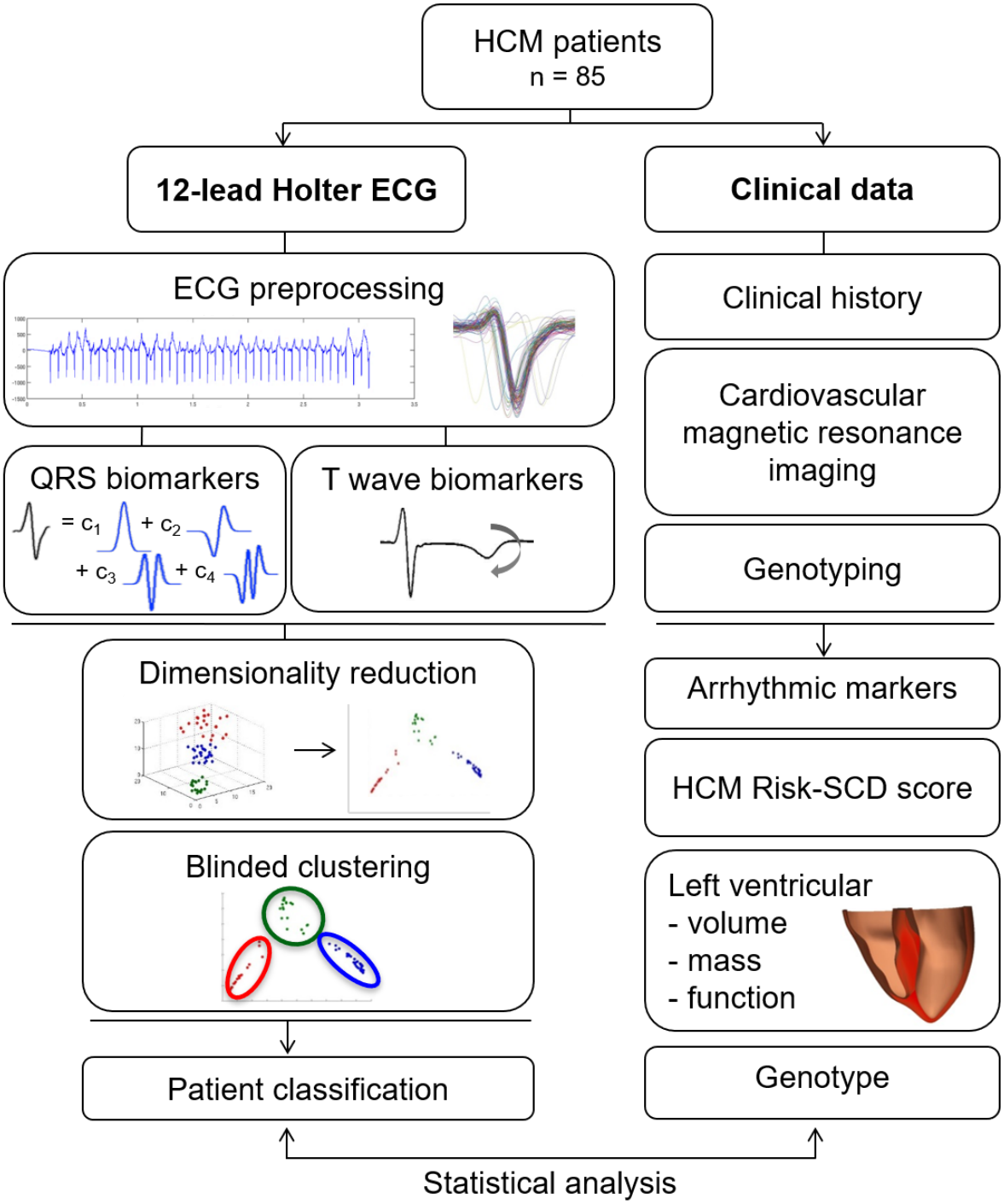


Figure 6.1 Summary of the methods applied for computational ECG phenotyping
The analysis and classification of ECGs using mathematical modelling and machine learning were performed by Dr Aurore Lyon. Their associations with clinical and cardiovascular magnetic resonance features, and all statistical analysis was performed by Dr Rina Ariga (Lyon et al., 2018).

computed in all 8 leads per participant. Average QRS and STT waveforms were then computed.

6.2.2. Extraction of QRS and T wave biomarkers

All biomarkers were calculated per lead: standard QRS biomarkers (QRS amplitude, duration and maximum slopes) and standard T wave biomarkers (T wave amplitude, ST segment displacement, QTc interval, JTc interval, T peak to T end interval and presence of T wave inversion; Figure 6.2).

- QRS amplitude, defined as the absolute value of the difference between maximum and minimum of the QRS complex values
- QRS width, defined as the time interval between the QRS onset and the QRS offset
- the maximum ascending/descending or descending/ascending slopes of the QRS defined as the first ascending and descending slopes depending on the QRS complex pattern
- the percentage of the S wave duration with respect to QRS duration
- STT segment amplitude, defined as the absolute value of the difference between maximum and minimum of the STT segment values
- STT segment elevation, defined as the difference between the beginning of the QRS complex and the beginning of the T wave
- QTc interval, defined as the duration between the beginning of the QRS and the end of the T wave, corrected with the Bazett's formula in each lead
- JTc interval, defined as the duration between the end of the QRS (J point) and the end of the T wave, corrected with the Bazett's formula in each lead

- T peak to T end interval, defined as the duration between the peak of the T wave and the end of the T wave in each lead

- T wave inversion, defined as a negative inflexion of at least 0.1mV in the mid to lateral precordial leads V3-6.

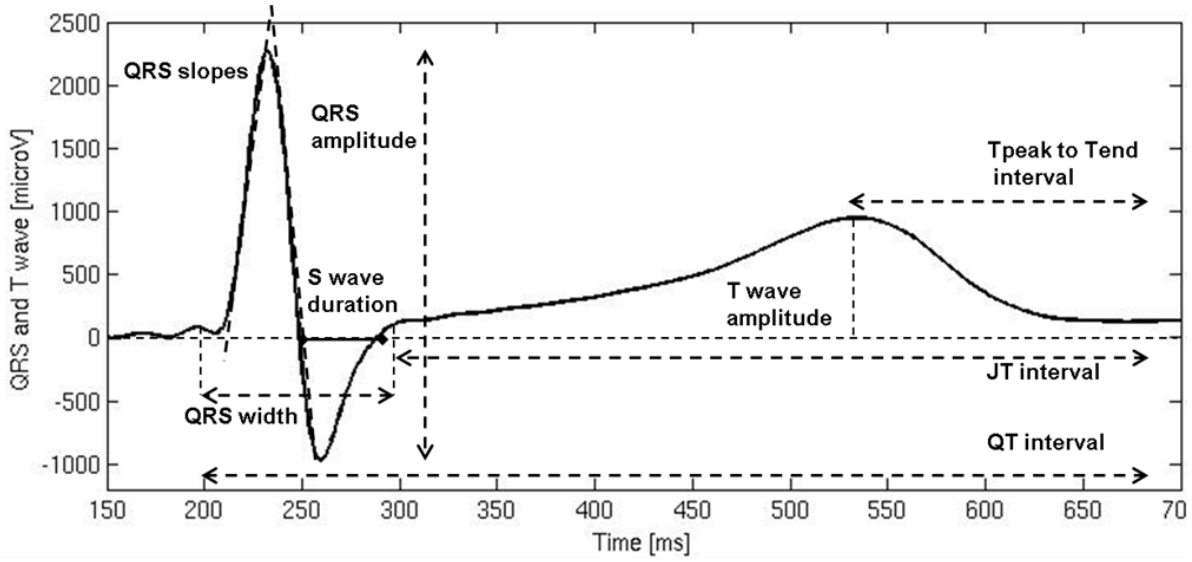


Figure 6.2 Standard ECG biomarkers from the QRS and T wave

6.2.3. Hermite transform

The QRS shape (morphology) was represented by a combination of Hermite functions, a set of mathematical functions with a well-established ability to provide a compact representation of the QRS complex (Laguna et al., 1996). The Hermite transform is well known in the literature for its ability to reconstruct the QRS complex. Three Hermite functions (defined in Equation 1 and illustrated in Figure 6.3) recovers 98% of the QRS energy in control subjects

(Sornmo et al., 1981). However, four Hermite functions were needed in HCM due to greater QRS heterogeneity.

$$\forall x \in \mathbb{R}, \forall n \in \mathbb{N}, \forall \sigma \in \mathbb{N}^*, \Psi_n(x,\sigma) = \left(\sigma 2^n n! \sqrt{\pi}\right)^{-\frac{1}{2}} e^{\frac{-x^2}{2\sigma^2}} H_n\left(\frac{x}{\sigma}\right) \quad \text{Equation 1}$$

where n is the order of the Hermite function Ψ and of the associated Hermite polynomial H, and σ the width parameter.

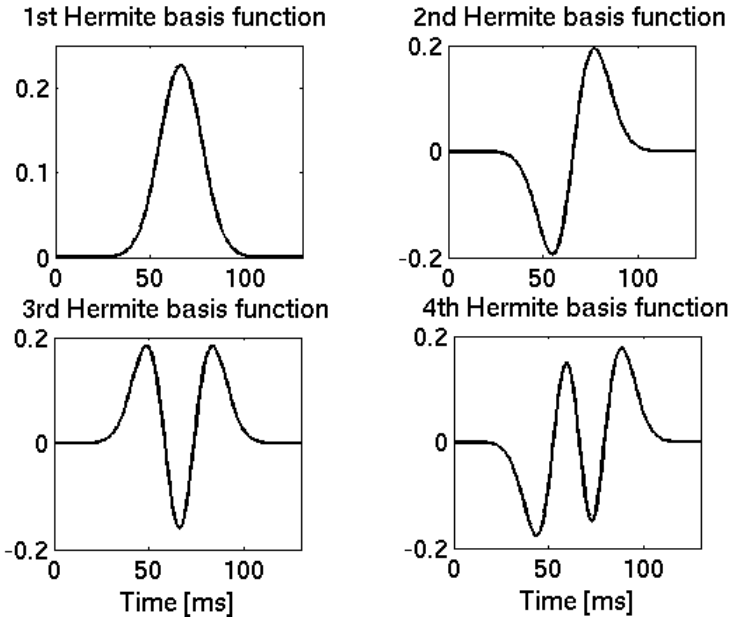


Figure 6.3 First four Hermite basis functions

This transform enables to denoise the signal and provides a more compact representation of the QRS complex (Laguna et al., 1996). In our implementation, QRS was expressed as a linear combination of the first four Hermite bases and a reconstruction error (Equation 2). The width of the Hermite functions was computed for each subject by minimising the fitting error

defined as the root mean square of the difference between the reconstructed and original QRS.

$$\forall t \in [1,2,\dots,T], \hat{x}(t) = \sum_{n=1}^{4} w_n \, b_n(t) + v(t) \qquad \text{Equation 2}$$

where $\hat{x}(t)$ is the reconstructed QRS signal, $b_n(t)$ the Hermite function of order n, t the time samples from T = 1 to 140ms, w_n the Hermite coefficients in the linear combination and $v(t)$ the reconstruction error.

Any particular QRS morphology such as an RSR' pattern can thus be generated as the sum of these scaled shapes (Figure 6.3). This resulted in five Hermite-based QRS biomarkers (referred to as morphological QRS biomarkers in the rest of the chapter): four coefficients of the Hermite basis and the fitting error.

6.2.4. Feature selection and dimensionality reduction for clustering

Each patient was represented by 40 values. This 40-dimensional feature vector of morphological QRS biomarkers comprised of the 5 Hermite-based biomarkers (4 Hermite coefficients and the fitting error) for each of the 8 leads. Using an unsupervised multi-cluster feature selection algorithm (Cai et al., 2010), redundant information was removed, and 7 significant features were identified as the best discriminators of the dataset. This technique aims at preserving the multi-cluster structure of the data and relies on spectral analysis technique combined to optimisation solving methods like L1-regularised least square. This is accomplished by introducing a penalty for adding extra terms into the regression.

The 7 features were reduced to two dimensions for visualisation using Laplacian eigenmaps dimensionality reduction by preserving the local geometrical properties, by computing the eigenvalues and eigenvectors of the graph Laplacian generalised eigenvector problem (Belkin and Niyogi, 2003) (Equation 3). This process reduced the number of variables under consideration and obtained the principal variables.

$$Ly = \lambda Dy \qquad \text{Equation 3}$$

with y and λ the eigenvectors and eigenvalues of the eigenvector problem, D a diagonal weight matrix computed by constructing the adjacency graph, W such that $D_{ii} = \sum_j W_{ji}$, and $L = D - W$ the Laplacian matrix.

A density-based clustering algorithm (DBSCAN (Ester et al., 1996)) was then applied on this low-dimensional representation of the dataset to extract subgroups. This algorithm identified clusters by maximising the density in each of the clusters. The minimum number of individuals in a cluster was set to $^{n}/_{25} = 3$, with $n = 85$ HCM patients. The distance between neighbouring individuals was evaluated using the Euclidean distance. Clustering analysis based only on QRS morphology was performed, and then repeated with the addition of T wave biomarkers. Clustering was performed by AL who was blinded to clinical data.

6.3. Results

6.3.1. Study population characteristics

The study population characteristics are summarised in Figure 6.1. HCM patients (n=85) had a more leftward QRS axis, larger QRS duration and amplitude, steeper QRS slopes and abnormal Q waves compared with controls (all $p<0.03$). They also showed lower T wave amplitude, T wave inversion, abnormal T wave axis, prolonged QTc and JTc intervals (all $p<0.003$).

Table 6.2 describes the clinical characteristics for the HCM patients. Patients were mainly asymptomatic (median NYHA functional class = 1) and were low risk for SCD (median HCM Risk-SCD score = 2.4%; median total risk factor = 1). Nineteen patients had an ICD implanted for primary prevention with a median follow-up of 3 years. Only 1 patient (5%) received an appropriate shock, which is in keeping with primary prevention discharge rates seen in a previous study (Maron et al., 2000b). Eleven percent of patients were G+LVH- and the majority had isolated septal hypertrophy (68%).

Table 6.1 Characteristics of healthy volunteers and HCM patients
[mean ± standard deviation, or number of participants (%)]

	Healthy volunteers (n=38)	**HCM patients** (n=85)	**p value**
Age, years	47 ± 15	45 ± 14	0.54
Male	25 (66)	58 (68)	0.84
Body mass index, kg/m^2	24 ± 4	26 ± 4	0.06
Systolic BP, mmHg	117 ± 14	118 ± 14	0.76
Diastolic BP, mmHg	70 ± 10	72 ± 12	0.33
CMR dimensions and function			
LV end-diastolic volume, ml	155 ± 35	154 ± 33	0.88
LV end-systolic volume, ml	50 ± 17	41 ± 16	**0.007**
LV ejection fraction, %	68 ± 5	74 ± 7	**0.00003**
LV mass index, g/m^2	54 ± 11	72 ± 25	**0.00002**
Maximal LV wall thickness, mm	11 ± 1	20 ± 6	**2×10^{-14}**
Left atrial diameter, mm	33 ± 7	39 ± 7	**0.00004**
Standard ECG features			
Heart rate, bpm	58 ± 11	58 ± 10	0.81
QRS axis, ^{o}	40 ± 34	13 ± 43	**0.0007**
QRS duration, ms	91 ± 9	98 ± 15	**0.02**
R wave amplitude	683 ± 200	764 ± 341	0.46
QRS amplitude, mV	1441 ± 414	1825 ± 652	**0.002**
QRS ascending slope	74 ± 22	89 ± 32	**0.025**
QRS descending slope	-118 ± 51	-150 ± 57	**0.001**
Pathological Q wave	0	20 (23)	**0.0004**
T wave axis, ^{o}	34 ± 17	69 ± 54	**0.0001**
Abnormal T wave axis	0	28 (35)	**9×10^{-6}**
T wave amplitude, mV	356 ± 141	170 ± 257	**0.0001**
T wave inversion	0	26 (30)	**0.00002**
Giant T wave inversion	0	6 (7)	0.18
T peak to T end interval, ms	81 ± 14	85 ± 18	0.16
ST segment displacement, mV	42 ± 45	26 ± 49	0.14
QTc interval, ms	411 ± 17	440 ± 27	**8×10^{-8}**
JTc interval, ms	300 ± 43	354 ± 99	**0.00003**

Table 6.2 Clinical and genotype characteristics of HCM patients
[number of patients (%)]

NYHA class, [median (range)]	1 (1-3)
NYHA III/IV	5 (6)
LVOT obstruction (gradient ≥30mmHg)	11 (13)
Implantable cardioverter-defibrillator	19 (22)
Appropriate ICD shocks	1
ICD follow-up, years [median (range)]	3 (0-12)
Hypertrophy morphology	
No LVH (G+LVH-)	9 (11)
Septal LVH	58 (68)
Apical LVH	4 (5)
Mixed septal & apical LVH	14 (16)
HCM Risk-SCD score, % [median (range)]	2.5 (0.8-11.0)
Conventional risk factors	
NSVT	23 (27)
Syncope	10 (12)
Family History SCD	17 (20)
Abnormal exercise BP response	7 (8)
Massive LVH ≥30mm	1 (1)
Total number of risk factors [median (range)]	1 (0-3)
0 Risk factors	34 (40)
1 Risk factor	45 (53)
≥ 2 Risk factors	6 (7)
Genotype	
Gene negative	27(32)
MYBPC3	33 (39)
MYH7	24 (28)
Troponin I	1 (1)

6.3.2. Clustering using QRS morphology only

Based on QRS morphology alone, three HCM groups were obtained (Figure 6.5, Panel A), with the main differences in first, second and third Hermite basis in lead II and lateral precordial leads (Figure 6.4; Figure 6.5, Panel B-D). Table 6.3 summarises the standard ECG features for the QRS-based groups.

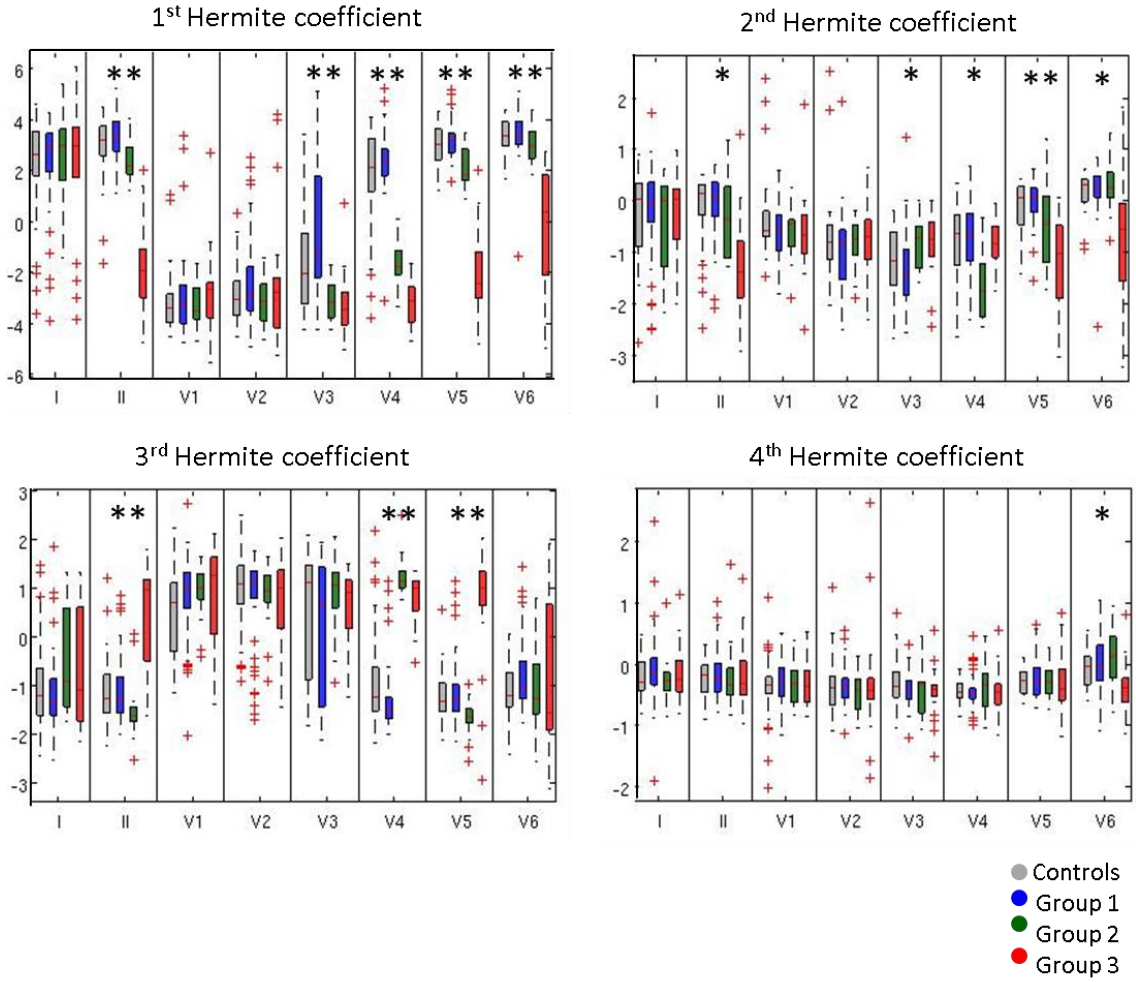


Figure 6.4 Comparison of the four Hermite coefficients in leads I-II, V1-6 for the three QRS-based HCM groups
Controls are shown for visual comparison but were not included in Kruskal-Wallis one-way analysis of variance. Mean, standard deviation and interquartile range; p-values are Bonferroni-corrected for multiple comparisons (*p-value<0.001, **p-value<1×10^{-6}) (Lyon et al., 2018).

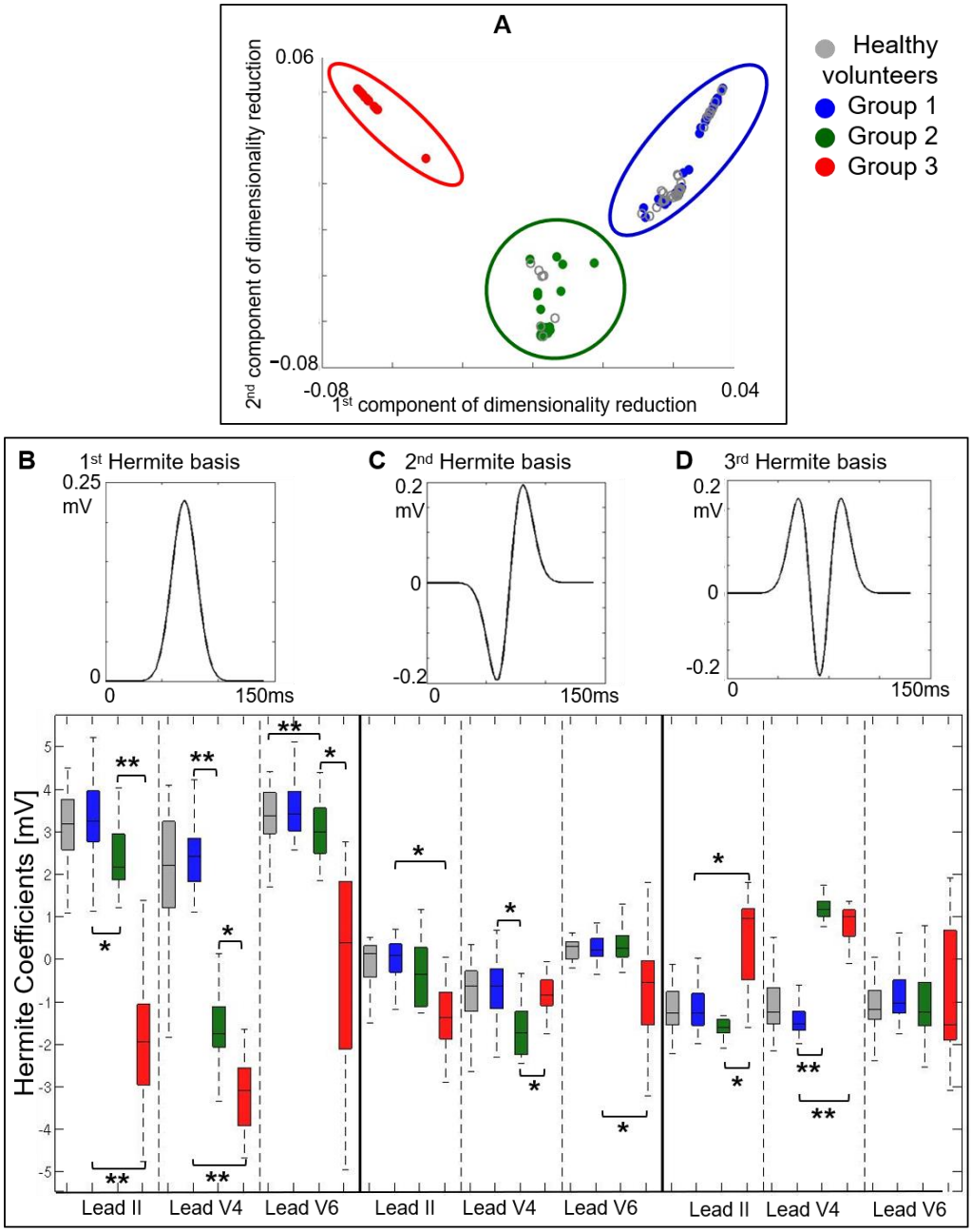


Figure 6.5 Clustering using QRS morphology alone identifies three HCM subgroups
The QRS morphology showed group differences in 3 features in lead II and the lateral precordial leads. (A) The three QRS-based HCM groups identified by cluster analysis using QRS morphological biomarkers alone are shown on the 2-dimensional space obtained by dimensionality reduction. (B–D) These QRS-based HCM groups show differences in the 1st, 2nd, and 3rd Hermite coefficients (mathematical functions representing the QRS shape: QRS morphological biomarkers) in leads II, V4 and V6. Healthy volunteers are shown for visual comparison but were not included in Kruskal–Wallis ANOVA (**$p < 1 \times 10^{-6}$, *$p < 0.001$) (Lyon et al., 2018).

Table 6.3 ECG and clinical features for QRS-based HCM groups
[mean ± standard deviation, median (range) or number of patients (%)]

	Group 1 (n=44)	**Group 2** (n=19)	**Group 3** (n=22)	**p value** (group comparison)
Age, years	47 ± 15	44 ± 12	43 ± 13	0.34
Male	30 (68)	12 (63)	16 (73)	0.79
Body mass index, kg/m^2	27 ± 5	25 ± 4	25 ± 4	0.16
Heart rate, bpm	58 ± 9	59 ± 13	55 ± 10	0.46
QRS axis, ^{o}	30 ± 33 *b*	29 ± 34 *c*	-37 ± 28	**1×10^{-11}**
QRS duration, ms	98 ± 17	96 ± 16	102 ± 13	0.13
QRS amplitude, mV	1876 ± 702	1807 ± 588	1737 ±613	0.88
QRS ascending slope	94 ± 34	92 ± 34	76 ± 23	0.10
QRS descending slope	-149 ± 58	-155 ± 60	-149 ± 56	0.95
Pathological Q waves	3 (7)*	8 (42)	9 (41)	**0.0003**
T wave axis, ^{o}	83 ± 60	49 ± 47	68 ± 41	0.15
Abnormal T axis	17 (41)	6 (33)	5 (25)	0.50
T amplitude, mV	107 ± 281	219 ±209	258 ±214	0.14
T wave inversion	20 (46)*	4 (21)	1 (5)	**0.001**
Giant T wave inversion	5 (11)	1 (5)	0	0.29
T peak to T end interval, ms	85 ± 19	86 ± 16	84 ± 19	1.00
ST displacement, mV	11 ± 48 *b*	38 ± 51	26 ± 49	**0.004**
QTc interval, ms	442 ± 25	429 ± 26	443 ± 29	0.29
JTc interval, ms	354 ± 71	342 ± 97	366±145	0.74
Lead V4				
R duration V4, ms	47 ± 11 *a,b*	38 ± 10	41 ± 17	**0.0001**
R amplitude V4, µv	1310 ± 706 *b*	1307 ± 648 *c*	551 ± 433	**0.00002**
S duration V4, ms	36 ± 17 *b*	41 ± 13	47 ± 19	**0.01**
S amplitude V4, µv	-568 ± 413 *a,b*	-1170 ± 570	-1270 ± 863	**0.00002**
Lead V6				
R duration V6, ms	54 ± 13 *b*	51 ± 14 *c*	31 ± 18	**0.000006**
R amplitude V6, µv	1290 ± 696 *b*	1227 ± 451 *c*	635 ± 455	**0.00008**
S duration V6, ms	17 ± 18 *b*	15 ± 17 *c*	35 ± 19	**0.0004**
S amplitude V6, µv	-118 ± 148 *b*	-122 ± 190 *c*	-501 ± 460	**0.00006**
HCM Risk-SCD score, %,	2.6 (1-11)	2.1 (1-6)	2.5 (1-9)	0.98
Conventional risk factors				
NSVT	14 (32)	4 (21)	5 (23)	0.69
Syncope	6 (14)	2 (11)	2 (9)	0.91
Family History SCD	7 (16)	5 (26)	5 (23)	0.60
Abnormal exercise BPR	5 (11)	0	2 (9)	0.44
Massive LVH ≥30mm	0	0	1 (5)	-

Cont.	**Group 1**	**Group 2**	**Group 3**	**p value**
Hypertrophy				
LV mass index, g/m^2	74 ± 28	63 ± 17	73 ± 26	0.30
Max LV wall, mm	19 ± 6	19 ± 5	21 ± 6	0.22
Hypertrophy morphology				
No LVH (G+LVH-)	8 (18)	1 (5)	0	
Septal LVH	23 (51)	16 (85)	20 (90)	
Apical LVH	2 (4)	1 (5)	1 (5)	
Mixed septal & apical LVH	12 (27)	1 (5)	1 (5)	
Other clinical features				
LV end-diastolic volume, ml	152 ± 28	155 ± 33	156 ± 41	0.87
LV end-systolic volume ml	40 ± 14	43 ± 14	41 ± 21	0.50
LV ejection fraction, %	74 ± 8	72 ± 8	74 ± 7	0.61
Left atrial diameter, mm	40 ± 7	37 ± 6	38 ± 8	0.25
LVOT gradient, mmHg	7.0 (4-111)	6.7 (2-110)	6.8 (3-92)	0.92
Genotype				
Gene positive	28 (64)	13 (68)	17 (77)	0.59

[a] Group 1 *vs* 2, [b] 1 *vs* 3, [c] 2 *vs* 3, p<0.05 on post hoc pairwise comparisons (p-values multiplied by 3 for Bonferroni adjustment of 3 tests).
* p<0.05 on post hoc contingency table analysis (p-values multiplied by 6 for Bonferroni adjustment of 3×2 combinations).

Group 1 was the largest with 52% of the patients and displayed normal QRS morphology (based on Hermite bases and normal QRS axis) (Figure 6.4, Figure 6.5). Group 2 (22% of patients) showed differences in V4 (in the first three Hermite bases) compared to controls and Group 1 but no difference in V6 (all post-hoc p<0.001). Thus, lead V4 in Group 2 displayed shorter R wave duration (2: 38 ms, 1: 47 ms; 2 *vs* 1, p=0.003) and deeper S waves (2: -1170 µv, 1: -568 µv; 2 *vs* 1, p=0.0003) compared to Group 1 (Table 6.3).

Group 3 (26% of patients) exhibited vast differences in lead II and V4-6 (in the first three Hermite bases) compared to the other HCM groups and controls (Figure 6.5, all post hoc

$p<6\times10^{-6}$). Differences in lead II were manifested as abnormally shifted QRS axis towards left axis deviation (LAD) (3: -37˚, 1: 30˚, 2: 29˚; 3 *vs* 1 and 3 *vs* 2, all post hoc $p<2\times10^{-7}$). In V4, the R wave duration was shorter than Group 1 and amplitude was shorter than Groups 1 and 2, S wave duration was longer than Group 1, and S amplitude was deeper than Group 1 (3 *vs* 1 and 3 *vs* 2, all post hoc $p<0.003$). In V6, R wave duration and amplitude were shorter, and S wave duration and amplitude larger than both the other groups (3 *vs* 1 and 3 *vs* 2, all post hoc $p<0.01$; Figure 3).

Although ECG features were significantly different between the QRS-based groups, clinical features and markers of arrhythmic risk were not (Table 6.3), suggesting that QRS biomarkers alone may not be useful for risk stratification.

6.3.3. Combined clustering with QRS morphology and T wave biomarkers identifies four HCM phenotypes

With the addition of T wave biomarkers to QRS morphology in the clustering analysis, four HCM groups were identified (Figure 6.6). T wave inversion was the principal T wave biomarker which subdivided Group 1 into two separate clusters: Group 1A with T wave inversion (n=21) and Group 1B without T wave inversion (n=24; Figure 6.7). Groups 2 and 3 remained as before. Table 4 summarises the standard ECG features for the four HCM groups. Group 1A had a more rightward T wave axis (1A: 156˚, 1B: 42˚, 2: 49˚, 3: 68˚; 1A *vs* 1B, 1A *vs* 2, 1A *vs* 3, all post hoc $p<2\times10^{-6}$) and the greatest number of patients with an abnormal T wave axis (17 patients;

post hoc $p=2\times10^{-6}$; Table 6.4). Group 1B had an absence of patients with pathological Q waves and abnormal T wave axes (all post hoc $p<0.01$).

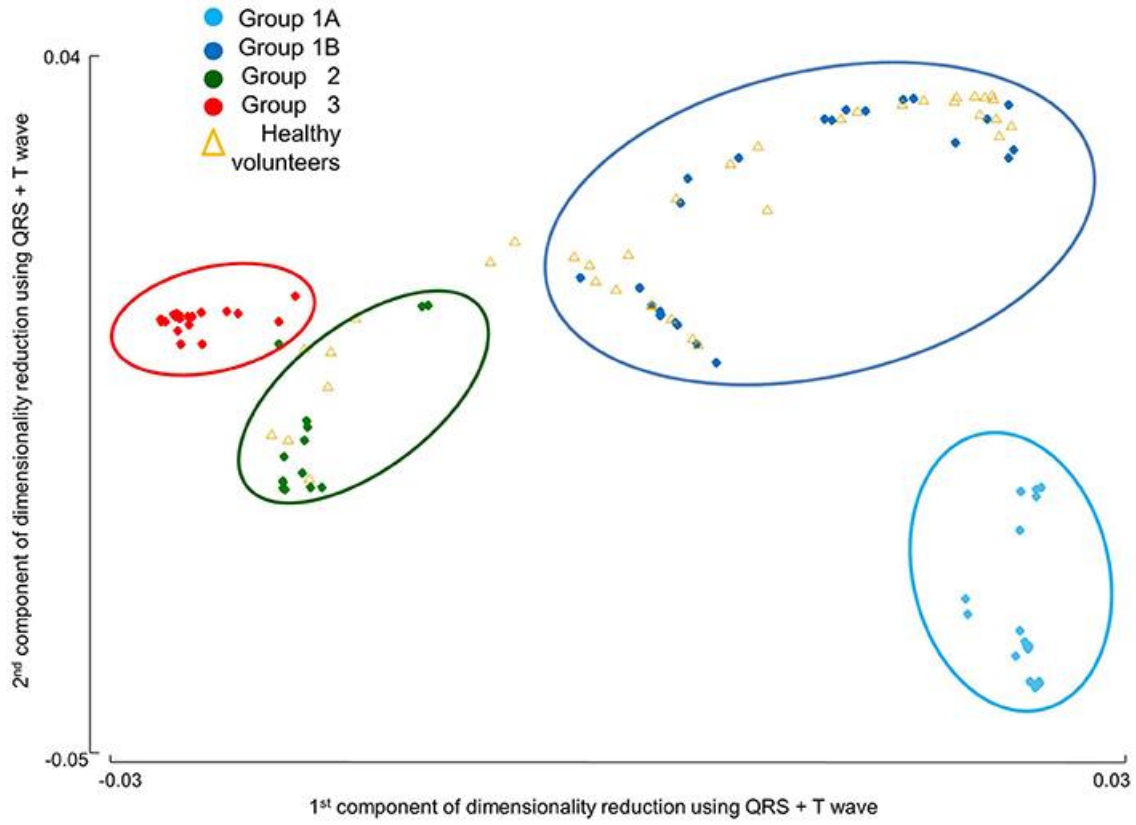


Figure 6.6 Four distinct HCM subgroups are identified based on QRS and T wave morphology
The four HCM groups identified by cluster analysis using both QRS and T wave morphology are shown on the 2-dimensional space obtained by dimensionality reduction (Lyon et al., 2018).

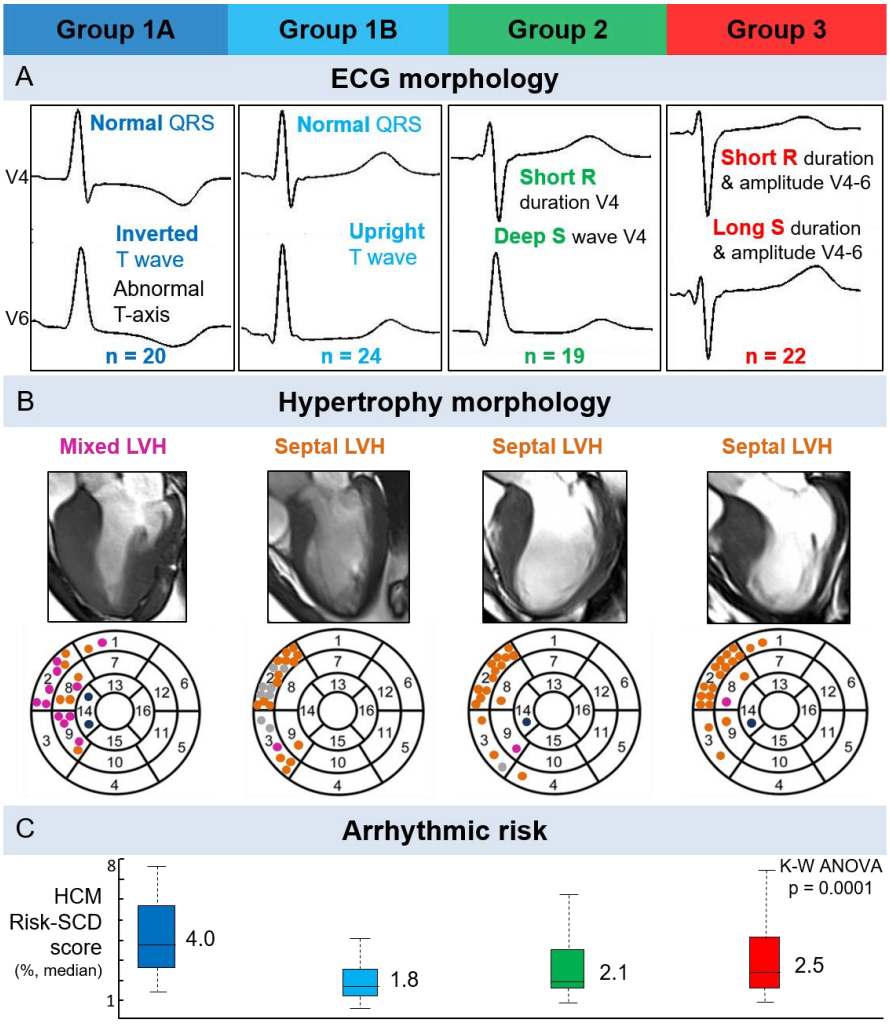


Figure 6.7 Four distinct ECG phenotypes in HCM exhibit differences in hypertrophy morphology and arrhythmic risk

(A) Representative ECG complexes for patients in each of the four groups, identified by combined clustering with QRS morphology and T wave biomarkers. Group 1A—normal QRS with inverted T wave (primary T wave inversion), Group 1B—normal QRS with upright T wave, Group 2—short R wave duration and deep S wave in V4, Group 3—left axis deviation, short R wave duration and amplitude, and long S wave duration and amplitude in V4 and V6. (B) Distribution of hypertrophy illustrated using a representative CMR for each group (top), and the segment of maximum left ventricular wall thickness for each patient (marked as a dot) in each group using the AHA 16-segment model. Group 1A had a predominance of patients with mixed septal and apical left ventricular hypertrophy (LVH; pink dots). Group 1B had the most gene positive patients with no hypertrophy (grey dots). Group 2 and 3 patients mainly had isolated septal hypertrophy (orange dots). Four patients had apical hypertrophy (navy dots). (C) HCM Risk-SCD score for each group. Patients with primary T wave inversion not secondary to QRS abnormalities (Group 1A), had the greatest HCM Risk-SCD score (Lyon et al., 2018).

Table 6.4 Characteristics of the four HCM phenotypes from combined QRS and T wave clustering

[mean ± standard deviation, median (range) or number of patients (%)]

	Group 1A (n=20)	**Group 1B** (n=24)	**Group 2** (n=19)	**Group 3** (n=22)	**p value** (group comparison)
Age, years	47 ± 12	48 ± 18	44 ± 12	43 ± 13	0.53
Male	15 (76)	15 (63)	12 (63)	16 (73)	0.78
Body mass index, kg/m^2	28 ± 6	26 ± 4	25 ± 4	25 ± 4	0.06
HCM Risk-SCD score, %	4.0 (2-11)^{a,b,c}	1.8 (1-4)	2 .1 (1-6)	2.5 (1-9)	**0.0001**
Conventional risk factors					
NSVT	11 (55)*	3 (13)	4 (21)	5 (23)	**0.016**
Syncope	2 (10)	4 (17)	2 (10)	2 (9)	0.88
Family History SCD	5 (254)	2 (8)	5 (26)	5 (23)	0.36
Abnormal exercise BPR	2 (10)	3 (12)	0	2 (9)	0.51
Massive LVH ≥30mm	0	0	0	1 (5)	-
Appropriate ICD shock	1	0	0	0	-
Hypertrophy					
LV mass index, g/m^2	90 ± 27 ^{a,b}	62 ± 23	63 ± 17	73 ± 26	**0.0003**
Max LV wall, mm	22 ± 4 ^{a}	16 ± 5	19 ± 5	21 ± 6	**0.002**
Hypertrophy morphology					**1×10^{-7}**
No LVH (G+LVH-)	0	8 (33)*	1 (5)	0	
Septal LVH	7 (35)*	15 (63)	16 (85)	20 (90)	
Apical LVH	2 (10)	0	1 (5)	1 (5)	
Mixed septal & apical LVH	11 (52)*	1 (4)	1 (5)	1 (5)	
Other clinical features					
LV EDV, ml	150 ± 26	154 ± 31	155 ± 33	156 ± 41	0.94
LV ESV, ml	35 ± 10	43 ± 15	43 ± 14	41 ± 21	0.26
LV ejection fraction, %	76 ± 7	72 ± 8	72 ± 8	74 ± 7	0.28
Left atrial diameter, mm	41 ± 5	39 ± 8	37 ± 6	38 ± 8	0.25
LVOT gradient, mmHg	6.5 (5-110)	7.2 (4-111)	6.7 (2-110)	6.8 (3-92)	0.81
Genotype					
Gene positive	9 (45)	19 (79)	13 (68)	17 (77)	0.08
Standard ECG features					
Heart rate, bpm	58 ± 10	58 ± 8	59 ± 13	58 ± 10	0.66
QRS axis, ^{o}	14 ± 30 ^{c}	44 ± 29 ^{e}	29 ± 34 ^{f}	-37 ± 28	**8×10^{-13}**
QRS duration, ms	94 ± 8	100 ± 21	96 ± 16	102 ± 13	0.23
QRS amplitude, mV	2006 ± 780	1762 ± 621	1807 ± 588	1737 ± 613	0.70
QRS ascending slope	93 ± 36	95 ± 33	92 ± 34	76 ± 23	0.19
QRS descending slope	-160 ± 60	-139 ± 56	-155 ± 60	-149 ± 56	0.47
Pathological Q waves	3 (14)	0 †	8 (38)	9 (43)	**0.0003**
T wave axis, ^{o}	156 ± 45 ^{a,b,c}	42 ± 27	49 ± 47	68 ± 41	**2×10^{-11}**
Abnormal T axis	17 (81) †	0 †	6 (33)	5 (25)	**7×10^{-8}**

cont.	Group 1A	Group 1B	Group 2	Group 3	p value
T amplitude, mV	-135 ± 202 [a,b,c]	308 ± 144	219 ± 209	257 ± 214	**9×10^{-8}**
T wave inversion	21 (100) [†]	0	4 (21)	1 (5)	**8×10^{-17}**
Giant T wave inversion	5 (24) [†]	0	1 (5)	0	**0.003**
T peak to T end, ms	91 ± 17	80 ± 20	86 ± 16	84 ± 19	0.19
ST segment displacement, mV	-13 ± 51 [a,b,c]	32 ± 33	38 ± 51	48 ± 38	**0.0001**
QTc interval, ms	452 ± 22	435 ± 26	429 ± 26	443 ± 29	0.05
JTc interval, ms	359 ± 47	349 ± 87	342 ± 97	366 ± 145	0.42

[a] Group 1A *vs* 1B, [b] 1A *vs* 2, [c] 1A *vs* 3, [d] 1B *vs* 2, [e] 1B *vs* 3, [f] 2 *vs* 3, p<0.05 on post hoc pairwise comparisons (p-values multiplied by 6 for Bonferroni adjustment of 6 tests).
*, † p<0.05 on post hoc contingency table analysis (p-values multiplied by 16 and 8 for Bonferroni adjustment of 4×4 and 4×2 combinations respectively).

6.3.4. Differences between the four HCM phenotypes in HCM Risk-SCD score, ventricular arrhythmia events and LV hypertrophy

Clinical and standard ECG features for each of the four HCM groups are shown in Table 6.4. There was no difference in age, gender or body mass index between the groups. Group 1A had the highest median HCM Risk-SCD score (1A: 4.0%, 1B: 1.8%, 2: 2.1%, 3: 2.5%; 1A *vs* 1B, 1A *vs* 2, 1A *vs* 3, all post hoc p≤0.02; Figure 6.7, panel C). There was a trend to increased NSVT in Group 1A (NSVT differed between the 4 phenotypes, p=0.016 but this was not significant when corrected for the three other risk factors also tested). Group 1A also contained the only ICD patient with an appropriate shock. Group 1B contained 8 of the 9 G+LVH- patients (Table 6.4, post-hoc p = 0.0003), of which 5 patients demonstrated ECG voltage criteria for LVH. Groups 2 and 3 patients had a lower HCM Risk-SCD score than Group 1A patients despite their abnormal QRS morphology (3: 2.5%, 2: 2.1%, 1A: 3.8%; 3 *vs* 1A, 2 *vs* 1A; post-hoc ≤ 0.02).

Group 1A exhibited a predominance of patients with mixed septal and apical hypertrophy (1A: 11 patients, 1B: 1 patient, 2: 1 patient, 3: 1 patient; post-hoc p = 4 × 10−6; Figure 6.7). Groups 1B, 2 and 3 had predominantly isolated septal hypertrophy (63, 85, and 90%, respectively).

6.3.5. Repeat combined QRS and T wave clustering with the exclusion of gene positive HCM with normal wall thickness (G+LVH-)

We considered G+LVH- patients within the HCM cohort to evaluate whether other structural and electrophysiological abnormalities in the absence of hypertrophy may yield ECG abnormalities. For example, 5 of the 9 G+LVH- patients displayed LVH on ECG voltage criteria. We removed the G+LVH- patients from the clustering analysis to investigate their influence on the phenotypic classification. The clustering algorithm yielded the same four remaining groups as with G+LVH-patients, with the same differences in QRS and T wave morphologies. Group 1A still exhibited a higher HCM Risk-SCD score compared to Group 1B and to Group 3 (post-hoc p = 0.006 and 0.04, respectively), and there was still a predominance of mixed septal and apical LVH in Group 1A (Table 6.5).

Table 6.5 Effect of excluding gene positive HCM with normal wall thickness on the four HCM phenotypes from combined QRS and T wave clustering
[mean ± standard deviation, median (range) or number of patients (%)]

	Group 1A (n=20)	Group 1B (n=17)	Group 2 (n=19)	Group 3 (n=20)	p value (group comparison)
HCM Risk-SCD score, %	3.4 (2-11) *a,b,c*	1.9 (1-4)	2.1 (1-6)	2.2 (1-9)	**0.004**
Hypertrophy					
LV mass index, g/m^2	90.1±27.3 *b*	69.8±23.1	67.0±18.1	71.4±26.2	**0.02**
Max LV wall, mm	22.0±4.1	19.5±3.6	19.4±4.9	21.2±5.8	0.24
Hypertrophy morphology					**4x10^{-5}**
Septal LVH	7 (35) *	16 (94)	17 (89)	18 (90)	
Apical LVH	2 (10)	0	1 (5)	1 (5)	
Mixed septal & apical LVH	11 (55) *	1(6)	1(5)	1(5)	

a Group 1A *vs* 1B, ***b*** 1A *vs* 2, ***c*** 1A *vs* 3, p<0.05 on post hoc pairwise comparisons
* p<0.05 on post hoc contingency table analysis

6.4. **Discussion**

This study is the first to use a machine learning approach to the ECG for the identification of phenotypes in a cohort of HCM patients. The main findings are that four HCM phenotypes are identified based on QRS morphology and T wave biomarkers analysed computationally using high fidelity ECGs, which show differences in HCM Risk-SCD score and the distribution of LV hypertrophy. Patients with normal QRS morphology and primary TWI not secondary to

QRS abnormalities (Group 1A) had the highest HCM Risk-SCD score and coexistence of septal and apical hypertrophy. Groups 2 and 3 with abnormalities in QRS morphology in V4 and V4-V6, respectively, had predominantly isolated septal hypertrophy. Since the ECG reflects ionic and structural abnormalities which are not captured by current measures within HCM risk stratification, the ECG-based classification proposed here may help to improve risk assessment. Our study shows the benefits of using machine learning methods to effectively dissect HCM heterogeneity and presents a step forward in improving individual patient management.

6.4.1. QRS morphology

We have quantitatively assessed the whole QRS shape (morphology) mathematically rather than describe discrete features. Cluster analysis with QRS morphology alone identified three groups with unique QRS features: normal QRS in Group 1, short R duration with deep S wave amplitude in V4 in Group 2 and left axis deviation, short R duration and amplitude in V4 with increased S duration and amplitude in both V4 and V6 in Group 3 (Figure 6.7). Although these QRS variations could not be accounted for by differences in hypertrophy, it is likely that fibrosis (Dumont et al., 2006) and disarray affects depolarisation by distorting and prolonging impulse propagation. CMR studies using tissue characterisation techniques such as late gadolinium enhancement (focal fibrosis), T1-mapping (diffuse fibrosis) and diffusion tensor imaging (disarray) are likely to provide further insight into the effects of structural remodelling on depolarisation and QRS patterns in HCM. Our analyses suggest that while QRS

features may be informative for diagnosis in HCM (Konno et al., 2004), categorising HCM groups on this basis showed no differences in association with known markers of risk.

6.4.2. T wave inversion

Lateral T wave inversion, a common repolarisation abnormality in HCM (Papadakis et al., 2009), was the critical T wave biomarker which when added to QRS morphology in the cluster analysis, identified four HCM groups with differences in clinical features. Group 1A patients had a higher HCM Risk-SCD score, a trend to increased NSVT, an appropriate shock and a predominance of mixed septal and apical pattern of hypertrophy.

TWI can be considered as primary or secondary abnormalities. Primary TWI occurs with altered heterogeneity in action potential duration or morphology without changes in depolarisation (normal QRS). Secondary TWI occurs with aberrant depolarisation (abnormal QRS) in the context of normal action potential characteristics. Thus, Group 1A patients with normal QRS have primary TWI. While TWI in Groups 2 and 3 with abnormal QRS represents secondary or combined primary and secondary TWI (Rautaharju et al., 2009). However only four patients in Group 2 and a single patient in Group 3 had TWI, while all 20 patients in Group 1A displayed TWI. TWI per se in HCM has been shown to increase SCD risk in some studies (Kuroda et al., 2002, Östman-Smith et al., 2009) but not in others (Maron et al., 1982, Sherrid et al., 2009). Our results provide a more specific characterisation of the influence of TWI in SCD risk, highlighting the importance of simultaneous normal QRS and TWI for increased risk. These results suggest that it is a primary TWI that increases SCD risk in HCM, rather than TWI

secondary to depolarisation abnormalities. A larger cohort is needed to confirm whether risk differs between patients with primary and secondary TWI.

TWI is caused by repolarisation abnormalities which are affected both by structural and ionic remodelling. In HCM, the overexpression of the L-type Ca^{2+} current, increased late sodium current and reduction of repolarisation currents lead to prolongation and heterogeneity in repolarisation (Coppini et al., 2013, Passini et al., 2016). T wave inversion may also be the result of ischaemia from microvascular dysfunction commonly seen in HCM (Petersen et al., 2007). Petersen et al. demonstrated that reduced endocardial perfusion was proportional to the magnitude of hypertrophy. Ischaemia may explain the T wave inversion seen in Group 1A patients as they had greater hypertrophy, which is also consistent with an increased sensitivity of T wave inversion in diagnosing HCM as LVH increases (Konno et al., 2004). However, Group 3 patients had a comparable magnitude of hypertrophy to Group 1A, yet there was no increased SCD risk, suggesting that additional factors may be implicated with increasing risk.

A further study has shown that patients with apical HCM and cavity obliteration had increased perfusion defects and NSVT rates as a result of ischaemia from extravascular compression of the coronary artery due to myocardial pressure during cavity obliteration (Matsubara et al., 2003). This may also be in keeping with Group 1A having the greatest number of patients with a mixed pattern of coexisting septal and apical hypertrophy which tend to show cavity obliteration and a worse prognosis (Yan et al., 2012); while Group 3 with 90% septal

hypertrophy, were at lower risk despite having similar wall thickness and mass index to 1A. Further imaging studies with novel perfusion assessment may improve our understanding of the mechanisms of ischaemia and in turn, the repolarisation abnormalities in HCM.

6.4.3. Low risk phenotypes

Patients in Group 1B (28%) with normal QRS and upright T waves were indistinguishable from controls based on ECG features both with and without the inclusion G+LVH- patients. These patients are likely to have less severe disease and better prognosis (McLeod et al., 2009). It is tempting to also speculate that HCM patients with hypertrophy in this group may have minimal fibrosis, disarray and ischaemia giving rise to relatively normal depolarisation and repolarisation. Finding the majority of G+LVH- patients (8 out 9 patients) in Group 1B showed that we can discriminate these inherently low risk patients solely by the ECG, despite 5 of these patients meeting ECG voltage criteria for LVH.

Despite the lack of hypertrophy, one G+LVH- patient was found in Group 2 which had QRS abnormalities in V4. This suggests that the ECG reflects the subtly abnormal myocardium which in this case was not hypertrophied but may have been affected by disarray or ionic remodelling. Although risk is thought to be significantly lower in G+LVH- than in HCM with hypertrophy, there are still a very small number of SCD in G+LVH- patients (Varnava et al., 2001a, Pasquale et al., 2012). Further studies are needed to assess whether computational ECG phenotyping may aid stratification in this particularly challenging low-risk group.

Group 3 on the other hand, had marked QRS abnormalities: LAD with QRS differences in V4 to V6. LAD is well-known to be associated with LVH but other factors such as a degree of left anterior fascicular block could also account for this leftward axis. Group 3 patients mainly had isolated septal hypertrophy, yet QRS abnormalities were seen in the lateral leads suggesting that remodelling may occur distal from the septum causing less uniform electrical propagation in the lateral leads. No genotype association was seen across any group, but our sample size may not have had adequate power to assess genotype-phenotype correlations.

6.4.4. Clinical implications

This study provides evidence that ECG phenotyping with advanced computational QRS morphology and T wave analysis is a powerful method of characterising HCM heterogeneity. Data suggest that HCM patients with a primary repolarisation abnormality as manifest by T wave inversion and abnormal T wave axis deviation but normal QRS are at greater risk of arrhythmia and SCD. This risk was associated with the extent of hypertrophy (greater number of segments involved in mixed septal and apical pattern of hypertrophy) rather than magnitude of hypertrophy (as measured by maximum wall thickness or mass index). A large-scale longitudinal study with cardiovascular end-point data will allow robust assessment of ECG phenotyping as an independent tool for accurate risk stratification. Studies involving computational image-based modelling and simulation are also needed to disentangle the relative contribution of structural, ischaemic and ionic factors which are likely to determine the heterogeneity in ECG biomarkers (Dutta et al., 2016). This improved understanding of HCM will eventually contribute to the development of new disease-modifying therapies.

6.4.5. Limitations

Our study makes associations with known risk factors, thus a large prospective long-term follow-up study such as the ongoing multicentre Hypertrophic Cardiomyopathy Registry (HCMR) (Kramer et al., 2015) will be needed to determine whether these findings will be an independent risk factor which improves current risk stratification for SCD.

ECG-based risk stratification must account for other factors that affect voltage amplitudes and lateral displacement of the LV such as age, gender, ethnicity and body habitus (Rautaharju et al., 1994, Rider et al., 2016). In our study, age, gender and body mass index were similar throughout the groups and 93% of patients were Caucasian. Large scale studies may require an ECG-adjustment factor for certain groups to improve accuracy as suggested in the setting of obesity (Rider et al., 2016). Limited accuracy of an ECG criterion can also result from variations in electrode placement especially in precordial electrodes . However, minimal changes in morphology were observed in leads V4-6. Therefore, criteria based on the lateral leads (which indeed demonstrated the greatest discrimination in HCM) would be robust to the inevitable variability of electrode site placement.

Our study used digital ECG data from 12-lead Holter recorders. The methods could equally be applied to standard resting 12-lead ECG which remains the most commonly used screening tool worldwide. However, for these novel computational methods to be successfully translated into clinical use, there needs to be a drive towards digital ECG acquisition rather than paper print-outs, which require manual digitisation before machine learning methods

can be applied. Future work will also need to assess whether the ECG morphology between ambulatory Holter ECG and standard supine ECG are comparable.

6.5. Conclusions

Four HCM phenotypes were identified based on QRS morphology and T wave biomarkers using a machine learning approach. Patients with primary TWI not secondary to QRS abnormalities had an increased HCM Risk-SCD score and an increased extent of hypertrophy with coexisting septal and apical hypertrophy. These results, and the nature of the underlying processes captured by the ECG, suggest that computational ECG phenotyping has the potential to be a novel and independent factor for risk stratification.

CHAPTER 7. **CONCLUSIONS AND FUTURE DIRECTIONS**

There is an unmet need to understand HCM heterogeneity and improve individual patient management. As we currently lack reliable methods to distinguish who will remain well with and who will be devastated by HCM complications. This thesis has pioneered diffusion tensor imaging and computational ECG phenotyping in HCM. These techniques have the potential to bring, for the first time, the underlying pathophysiology of HCM into the clinical arena of risk stratification.

7.1. **DT-CMR**

This work is currently the largest in vivo DT-CMR studies in HCM. DT-CMR is a non-invasive tool that permits us to measure myocardial microstructure in vivo – something previously only possible in post-mortem specimens. FA quantifies the directionality of water diffusion within each imaging voxel as its motion is impeded by myocytes and the surrounding interstitium. Thus, FA in a macroscopic imaging voxel is due to microscopic heterogeneity in myocyte alignment and the extent of interstitial expansion. In healthy controls, I demonstrated that diastolic FA showed high concordance with normal ventricular histology. A ring of high FA was seen in the mid-wall where myocytes are aligned in a single orientation (circumferentially), compared to the epicardium and endocardium where myocytes are progressively changing their orientation (helical arrangement).

I showed that diastolic FA was reduced in HCM compared to controls despite normal helix angle progression, and remained reduced after accounting for fibrosis which also contributes to low FA. Visually, this was consistent with published histology demonstrating that disarray and fibrosis (low FA – multiple orientations) invaded circumferentially-aligned mid-wall myocytes (high FA – single orientation). Reduced FA was associated with increased odds of ventricular arrhythmia in HCM patients independent of fibrosis and left ventricular hypertrophy. Diastolic FA may improve current risk stratification in HCM by including for the first time, an in vivo marker of disarray which is plausibly the most closely related feature to the risk of ventricular arrhythmias leading to sudden cardiac death.

DT-CMR acquisition times are still long, and full heart coverage remains a challenge. Future work is needed to shorten scan times by using novel acceleration techniques such as compressed sensing and multiband imaging. Improvements in SNR could be made by using CMR systems with increased gradient strength such as the 3T Prisma and spin-echo sequences which are insensitive to strain. Non-Gaussian models of diffusion require further evaluation as current DT-CMR is based on Gaussian diffusion. However, in vivo diffusion is not fully Gaussian (free) as it is hindered by intracellular and extracellular constituents and cannot be separated from other sources of water mobility, such as active transport, flow along pressure gradients, and changes in membrane permeability.

The origin of FA abnormalities – disarray versus fibrosis, cannot be determined directly. This work used multimodal CMR – LGE and ECV imaging, and segmental linear mixed-effects

modelling to account for the contribution of fibrosis to FA. However, pixel-by-pixel comparisons between diffusion and other CMR modalities may be possible if distortion correction from EPI imaging is included in every post-processing measurement. Alternatives to EPI imaging such as SSFP could also potentially decrease image distortion. Further technical development in post-processing automation is required to reduce analysis time and pave the way for a clinical work flow.

Although, I have shown a significant association of low FA with ventricular arrhythmia, there were patients with low FA and no evidence of ventricular arrhythmias. This partial discordance of FA with NSVT, a conventional risk factor, is a strength. FA may provide an independent insight into the underlying myocardium that clinical risk factors cannot. We now need to incorporate diastolic FA measurements into a large prospective multi-centre HCM study to assess the clinical utility of FA in predicting sudden cardiac death itself.

7.2. **ECG phenotyping**

ECG abnormalities in HCM are the signature of the underlying disease mechanisms such as disarray and ion channel remodelling. This work has shown for the first time, that computational modelling of ECG signals, unsupervised learning algorithms and cluster analysis can be employed to objectively identify distinct subgroups of HCM patients based on ECG morphology. The four ECG phenotypes demonstrated differences in risk of arrhythmia and hypertrophy patterns.

This work has led to high performance computer stimulations using personalised anatomical models by our group. These simulations produce biophysical models which can be altered at both the cellular and organ level including parameters such as ionic currents, purkinje fibre coupling, disarray and hypertrophy, to dissect the origin of these ECG phenotypes. Changing each parameter to varying extents to reproduce the ECG has revealed the distinct mechanisms causing these specific ECG patterns. Further work is now needed to see how this might translate towards individualised patient management and therapies.

Although the ECG is cheap and widely available, ECG phenotyping using machine learning will not be easily achievable due to the lack of digital ECGs. Most hospitals now have digital ECG machines, yet raw digital ECG files are discarded rather than archived, while the ECG is stored as a paper print-out or uploaded to a server as a PDF. Thus, ECG phenotyping using computational methods in the large prospective multicentre HCMR study will require tedious manual digitisation of scanned paper ECGs which were originally a digital dataset. Secondly, machine learning requires access to large clinical databases to provide separate training and testing datasets. >1000 datasets are required to prevent overfitting and make meaningful inferences which can then be generalised to a different cohort.

3-dimensional electrocardiographic imaging (ECGI) may better than a 12-lead ECG at characterising the electrical substrate due to better resolution at known locations relative to the heart. This method uses 256 body surface electrodes which are imaged using CMR or cardiac computed tomography, to provide data to reconstruct maps of epicardial

depolarisation and repolarisation. The next step would be to assess HCM patients with both DT-CMR and 3D ECG imaging to assess the relationship between electrophysiology and disarray at a much closer scale. Another potential direction would be to use the existing 24-Holter data to assess changes in beat to beat morphology or changes in heart rate.

7.3. Conclusion

FA is likely to represent disarray after accounting for fibrosis. We propose that diastolic FA is the first in vivo marker of disarray and a potential independent risk factor in HCM. Computational ECG phenotyping has identified distinct HCM phenotypes which are caused by distinct mechanisms. Computational ECG phenotyping is an important step to providing personalised medicine in this heterogenous disease and may guide targeted therapies. Ultimate progress in HCM risk stratification must include methods to quantify an individual's underlying arrhythmogenic substrate, potential triggers and understand the complex interplay between the two. Sudden cardiac death is so devastating particularly in the young that research must continue to pursue methods of individualising the propensity to ventricular arrhythmias in HCM.

REFERENCES

ABDULLAH, O. M., DRAKOS, S. G., DIAKOS, N. A., WEVER-PINZON, O., KFOURY, A. G., STEHLIK, J., SELZMAN, C. H., REID, B. B., BRUNISHOLZ, K. & VERMA, D. R. 2014. Characterization of diffuse fibrosis in the failing human heart via diffusion tensor imaging and quantitative histological validation. *NMR in Biomedicine,* 27**,** 1378-1386.

ADABAG, A. S., MARON, B. J., APPELBAUM, E., HARRIGAN, C. J., BUROS, J. L., GIBSON, C. M., LESSER, J. R., HANNA, C. A., UDELSON, J. E., MANNING, W. J. & MARON, M. S. 2008. Occurrence and Frequency of Arrhythmias in Hypertrophic Cardiomyopathy in Relation to Delayed Enhancement on Cardiovascular Magnetic Resonance. *Journal of the American College of Cardiology,* 51**,** 1369-1374.

ALETRAS, A. H., TILAK, G. S., HSU, L.-Y. & ARAI, A. E. 2011. Heterogeneity of intramural function in hypertrophic cardiomyopathy: mechanistic insights from MRI late gadolinium enhancement and high-resolution DENSE strain maps. *Circulation: Cardiovascular Imaging***,** CIRCIMAGING. 110.958751.

ALFONSO, F., FRENNEAUX, M. P. & MCKENNA, W. J. 1989. Clinical sustained uniform ventricular tachycardia in hypertrophic cardiomyopathy: association with left ventricular apical aneurysm. *Heart,* 61**,** 178-181.

ANDERSON, K., SUTTON, M. S. J. & LIE, J. 1979. Histopathological types of cardiac fibrosis in myocardial disease. *The Journal of pathology,* 128**,** 79-85.

ANDERSON, R. H., HO, S. Y., REDMANN, K., SANCHEZ-QUINTANA, D. & LUNKENHEIMER, P. P. 2005. The anatomical arrangement of the myocardial cells making up the ventricular mass. *European journal of cardio-thoracic surgery,* 28**,** 517-525.

ASHRAFIAN, H., MCKENNA, W. J. & WATKINS, H. 2011. Disease pathways and novel therapeutic targets in hypertrophic cardiomyopathy. *Circulation research,* 109**,** 86-96.

AUTHORS/TASK FORCE, M., ELLIOTT, P. M., ANASTASAKIS, A., BORGER, M. A., BORGGREFE, M., CECCHI, F., CHARRON, P., HAGEGE, A. A., LAFONT, A., LIMONGELLI, G., MAHRHOLDT, H., MCKENNA, W. J., MOGENSEN, J., NIHOYANNOPOULOS, P., NISTRI, S., PIEPER, P. G., PIESKE, B., RAPEZZI, C., RUTTEN, F. H., TILLMANNS, C., WATKINS, H., ADDITIONAL, C., O'MAHONY, C., GUIDELINES, E. S. C. C. F. P., ZAMORANO, J. L., ACHENBACH, S., BAUMGARTNER, H., BAX, J. J., BUENO, H., DEAN, V., DEATON, C., EROL, Ç., FAGARD, R., FERRARI, R., HASDAI, D., HOES, A. W., KIRCHHOF, P., KNUUTI, J., KOLH, P., LANCELLOTTI, P., LINHART, A., NIHOYANNOPOULOS, P., PIEPOLI, M. F., PONIKOWSKI, P., SIRNES, P. A., TAMARGO, J. L., TENDERA, M., TORBICKI, A., WIJNS, W., WINDECKER, S., DOCUMENT, R., HASDAI, D., PONIKOWSKI, P., ACHENBACH, S., ALFONSO, F., BASSO, C., CARDIM, N. M., GIMENO, J. R., HEYMANS, S., HOLM, P. J., KEREN, A., KIRCHHOF, P., KOLH, P., LIONIS, C., MUNERETTO, C., PRIORI, S., SALVADOR, M. J., WOLPERT, C., ZAMORANO, J. L., FRICK, M., ALIYEV, F., KOMISSAROVA, S., MAIRESSE, G., SMAJIĆ, E., VELCHEV, V., ANTONIADES, L., LINHART, A., BUNDGAARD, H., HELIÖ, T., LEENHARDT, A., KATUS, H. A., EFTHYMIADIS, G., SEPP, R., THOR GUNNARSSON, G., CARASSO, S., KERIMKULOVA, A., KAMZOLA, G., SKOURI, H., ELDIRSI, G., KAVOLIUNIENE, A., FELICE, T., MICHELS, M., HERMANN HAUGAA, K., LENARCZYK,

R., BRITO, D., APETREI, E., BOKHERIA, L., LOVIC, D., HATALA, R., GARCIA PAVÍA, P., et al. 2014. 2014 ESC Guidelines on diagnosis and management of hypertrophic cardiomyopathyThe Task Force for the Diagnosis and Management of Hypertrophic Cardiomyopathy of the European Society of Cardiology (ESC). *European Heart Journal,* 35**,** 2733-2779.

BARMPOUTIS, A., VEMURI, B. C., SHEPHERD, T. M. & FORDER, J. R. 2007. Tensor splines for interpolation and approximation of DT-MRI with applications to segmentation of isolated rat hippocampi. *IEEE transactions on medical imaging,* 26**,** 1537-1546.

BASSER, P. J., MATTIELLO, J. & LEBIHAN, D. 1994. Estimation of the effective self-diffusion tensor from the NMR spin echo. *Journal of Magnetic Resonance, Series B,* 103**,** 247-254.

BASSO, C., THIENE, G., CORRADO, D., BUJA, G., MELACINI, P. & NAVA, A. 2000. Hypertrophic cardiomyopathy and sudden death in the young: pathologic evidence of myocardial ischemia. *Human pathology,* 31**,** 988-998.

BECKER, A. E. & CARUSO, G. 1982. Myocardial disarray. A critical review. *Br Heart J,* 47**,** 527-38.

BELKIN, M. & NIYOGI, P. 2003. Laplacian eigenmaps for dimensionality reduction and data representation. *Neural computation,* 15**,** 1373-1396.

BENSON, A. P., GILBERT, S. H., LI, P., NEWTON, S. M. & HOLDEN, A. V. 2008. Reconstruction and Quantification of Diffusion Tensor Imaging-Derived Cardiac Fibre and Sheet Structure in Ventricular Regions used in Studies of Excitation Propagation. *Mathematical Modelling of Natural Phenomena,* 3**,** 101-130.

BEUCKELMANN, D. J., NÄBAUER, M. & ERDMANN, E. 1992. Intracellular calcium handling in isolated ventricular myocytes from patients with terminal heart failure. *Circulation,* 85**,** 1046-1055.

BIERNACKA, A. & FRANGOGIANNIS, N. G. 2011. Aging and cardiac fibrosis. *Aging and disease,* 2**,** 158.

BULLER, V. G., VAN DER GEEST, R. J., KOOL, M. D., VAN DER WALL, E. E., DE ROOS, A. & REIBER, J. H. 1997. Assessment of regional left ventricular wall parameters from short axis magnetic resonance imaging using a three-dimensional extension to the improved centerline method. *Investigative radiology,* 32**,** 529-539.

CAI, D., ZHANG, C. & HE, X. Unsupervised feature selection for multi-cluster data. Proceedings of the 16th ACM SIGKDD international conference on Knowledge discovery and data mining, 2010. ACM, 333-342.

CALLOT, V., BENNETT, E., DECKING, U. K., BALABAN, R. S. & WEN, H. 2003. In vivo study of microcirculation in canine myocardium using the IVIM method. *Magnetic resonance in medicine,* 50**,** 531-540.

CAPTUR, G., LOPES, L., PATEL, V., LI, C., BASSETT, P., SYRRIS, P., SADO, D. M., MAESTRINI, V., MOHUN, T. J. & MCKENNA, W. J. 2014. Abnormal cardiac formation in hypertrophic cardiomyopathy-fractal analysis of trabeculae and preclinical gene expression. *Circulation: Genomic and Precision Medicine***,** CIRCGENETICS. 113.000362.

CAULFIELD, J. & BORG, T. 1979. The collagen network of the heart. *Laboratory investigation; a journal of technical methods and pathology,* 40**,** 364-372.

CAVALERA, M., WANG, J. & FRANGOGIANNIS, N. G. 2014. Obesity, metabolic dysfunction, and cardiac fibrosis: pathophysiological pathways, molecular mechanisms, and therapeutic opportunities. *Translational Research,* 164**,** 323-335.

CECCHI, F., OLIVOTTO, I., MONTEREGGI, A., SANTORO, G., DOLARA, A. & MARON, B. J. 1995. Hypertrophic cardiomyopathy in Tuscany: clinical course and outcome in an unselected regional population. *Journal of the American College of Cardiology,* 26**,** 1529-1536.

CHABINIOK, R., WANG, V. Y., HADJICHARALAMBOUS, M., ASNER, L., LEE, J., SERMESANT, M., KUHL, E., YOUNG, A. A., MOIREAU, P. & NASH, M. P. 2016. Multiphysics and multiscale modelling, data–model fusion and integration of organ physiology in the clinic: ventricular cardiac mechanics. *Interface focus,* 6**,** 20150083.

CHARRON, P., CARRIER, L., DUBOURG, O., TESSON, F., DESNOS, M., RICHARD, P., BONNE, G., GUICHENEY, P., HAINQUE, B. & BOUHOUR, J. 1997. Penetrance of familial hypertrophic cardiomyopathy. *Genetic counseling (Geneva, Switzerland),* 8**,** 107-114.

COPPINI, R., FERRANTINI, C., YAO, L., FAN, P., DEL LUNGO, M., STILLITANO, F., SARTIANI, L., TOSI, B., SUFFREDINI, S., TESI, C., YACOUB, M., OLIVOTTO, I., BELARDINELLI, L., POGGESI, C., CERBAI, E. & MUGELLI, A. 2012. Late Sodium Current Inhibition Reverses Electro-Mechanical Dysfunction in Human Hypertrophic Cardiomyopathy. *Circulation*.

COPPINI, R., FERRANTINI, C., YAO, L., FAN, P., DEL LUNGO, M., STILLITANO, F., SARTIANI, L., TOSI, B., SUFFREDINI, S., TESI, C., YACOUB, M., OLIVOTTO, I., BELARDINELLI, L., POGGESI, C., CERBAI, E. & MUGELLI, A. 2013. Late Sodium Current Inhibition Reverses

Electromechanical Dysfunction in Human Hypertrophic Cardiomyopathy. *Circulation,* 127**,** 575-584.

DAVIES, M. 1984. The current status of myocardial disarray in hypertrophic cardiomyopathy. *British heart journal,* 51**,** 361.

DAVIES, M. & MCKENNA, W. 1995. Hypertrophic cardiomyopathy—pathology and pathogenesis. *Histopathology,* 26**,** 493-500.

DE BAKKER, J., VAN CAPELLE, F., JANSE, M. J., TASSERON, S., VERMEULEN, J. T., DE JONGE, N. & LAHPOR, J. R. 1993. Slow conduction in the infarcted human heart.'Zigzag'course of activation. *Circulation,* 88**,** 915-926.

DE BAKKER, J. M., VAN CAPELLE, F. J., JANSE, M. J., TASSERON, S., VERMEULEN, J. T., DE JONGE, N. & LAHPOR, J. R. 1996. Fractionated electrograms in dilated cardiomyopathy: origin and relation to abnormal conduction. *Journal of the American College of Cardiology,* 27**,** 1071-1078.

DE CHAZAL, P., O'DWYER, M. & REILLY, R. B. 2004. Automatic classification of heartbeats using ECG morphology and heartbeat interval features. *IEEE transactions on biomedical engineering,* 51**,** 1196-1206.

DIBB, R., QI, Y. & LIU, C. 2015. Magnetic susceptibility anisotropy of myocardium imaged by cardiovascular magnetic resonance reflects the anisotropy of myocardial filament α-helix polypeptide bonds. *Journal of Cardiovascular Magnetic Resonance,* 17**,** 60.

DOU, J., REESE, T. G., TSENG, W. Y. & WEDEEN, V. J. 2002. Cardiac diffusion MRI without motion effects. *Magn Reson Med,* 48**,** 105-14.

DOU, J., TSENG, W. Y., REESE, T. G. & WEDEEN, V. J. 2003. Combined diffusion and strain MRI reveals structure and function of human myocardial laminar sheets in vivo. *Magn Reson Med,* 50**,** 107-13.

DUMONT, C. A., MONSERRAT, L., SOLER, R., RODRÍGUEZ, E., FERNANDEZ, X., PETEIRO, J., BOUZAS, A., BOUZAS, B. & CASTRO-BEIRAS, A. 2006. Interpretation of electrocardiographic abnormalities in hypertrophic cardiomyopathy with cardiac magnetic resonance. *European Heart Journal,* 27**,** 1725-1731.

DUTTA, S., MINCHOLÉ, A., ZACUR, E., QUINN, T. A., TAGGART, P. & RODRIGUEZ, B. 2016. Early afterdepolarizations promote transmural reentry in ischemic human ventricles with reduced repolarization reserve. *Progress in biophysics and molecular biology,* 120**,** 236-248.

EDELMAN, R. R., GAA, J., WEDEEN, V. J., LOH, E., HARE, J. M., PRASAD, P. & LI, W. 1994. In vivo measurement of water diffusion in the human heart. *Magn Reson Med,* 32**,** 423-8.

EFTHIMIADIS, G. K., PAGOURELIAS, E. D., PARCHARIDOU, D., GOSSIOS, T., KAMPERIDIS, V., THEOFILOGIANNAKOS, E. K., PAPPA, Z., MEDITSKOU, S., HADJIMILTIADES, S. & PLIAKOS, C. 2013. Clinical characteristics and natural history of hypertrophic cardiomyopathy with midventricular obstruction. *Circulation Journal,* 77**,** 2366-2374.

ELLIOTT, P. & MCKENNA, W. J. 2004. Hypertrophic cardiomyopathy. *The Lancet,* 363**,** 1881-1891.

ELLIOTT, P. M., GIMENO, J. R., TOMÉ, M. T., SHAH, J., WARD, D., THAMAN, R., MOGENSEN, J. & MCKENNA, W. J. 2006. Left ventricular outflow tract obstruction and sudden death

risk in patients with hypertrophic cardiomyopathy. *European heart journal,* 27**,** 1933-1941.

ELLIOTT, P. M., POLONIECKI, J., DICKIE, S., SHARMA, S., MONSERRAT, L., VARNAVA, A., MAHON, N. G. & MCKENNA, W. J. 2000. Sudden death in hypertrophic cardiomyopathy: identification of high risk patients. *Journal of the American College of Cardiology,* 36**,** 2212-2218.

ESTER, M., KRIEGEL, H.-P., SANDER, J. & XU, X. A density-based algorithm for discovering clusters in large spatial databases with noise. Kdd, 1996. 226-231.

FEMENÍA, F., ARCE, M., VAN GRIEKEN, J., TRUCCO, E., MONT, L., ABELLO, M., MERINO, J. L., RIVERO-AYERZA, M., GORENEK, B. & RODRIGUEZ, C. 2013. Fragmented QRS as a predictor of arrhythmic events in patients with hypertrophic obstructive cardiomyopathy. *Journal of Interventional Cardiac Electrophysiology,* 38**,** 159-165.

FERRANS, V. J., MORROW, A. G. & ROBERTS, W. C. 1972. Myocardial ultrastructure in idiopathic hypertrophic subaortic stenosis: a study of operatively excised left ventricular outflow tract muscle in 14 patients. *Circulation,* 45**,** 769-792.

FERREIRA, P. F., KILNER, P. J., MCGILL, L.-A., NIELLES-VALLESPIN, S., SCOTT, A. D., HO, S. Y., MCCARTHY, K. P., HABA, M. M., ISMAIL, T. F. & GATEHOUSE, P. D. 2014. In vivo cardiovascular magnetic resonance diffusion tensor imaging shows evidence of abnormal myocardial laminar orientations and mobility in hypertrophic cardiomyopathy. *Journal of Cardiovascular Magnetic Resonance,* 16**,** 87.

FERREIRA, P. F., NIELLES-VALLESPIN, S., SCOTT, A. D., SILVA, R., KILNER, P. J., ENNIS, D. B., AUGER, D. A., SUEVER, J. D., ZHONG, X. & SPOTTISWOODE, B. S. 2018. Evaluation of

the impact of strain correction on the orientation of cardiac diffusion tensors with in vivo and ex vivo porcine hearts. *Magnetic resonance in medicine,* 79**,** 2205-2215.

FRANCIA, P., SANTINI, D., MUSUMECI, B., SEMPRINI, L., ADDUCI, C., PAGANNONE, E., PROIETTI, G. & VOLPE, M. 2014. Clinical Impact of Nonsustained Ventricular Tachycardia Recorded by the Implantable Cardioverter-Defibrillator in Patients with Hypertrophic Cardiomyopathy. *Journal of cardiovascular electrophysiology,* 25**,** 1180-1187.

FROELING, M., STRIJKERS, G. J., NEDERVEEN, A. J., CHAMULEAU, S. A. & LUIJTEN, P. R. 2014. Diffusion tensor MRI of the heart–in vivo imaging of myocardial fiber architecture. *Current Cardiovascular Imaging Reports,* 7**,** 9276.

GALLICHAN, D., ANDERSSON, J. L., JENKINSON, M., ROBSON, M. D. & MILLER, K. L. 2010. Reducing distortions in diffusion-weighted echo planar imaging with a dual-echo blip-reversed sequence. *Magnetic resonance in medicine,* 64**,** 382-390.

GARRIDO, L., WEDEEN, V. J., KWONG, K. K., SPENCER, U. M. & KANTOR, H. L. 1994. Anisotropy of water diffusion in the myocardium of the rat. *Circ Res,* 74**,** 789-93.

GEERTS, L., BOVENDEERD, P., NICOLAY, K. & ARTS, T. 2002. Characterization of the normal cardiac myofiber field in goat measured with MR-diffusion tensor imaging. *Am J Physiol Heart Circ Physiol,* 283**,** H139-45.

GERSH, B. J., MARON, B. J., BONOW, R. O., DEARANI, J. A., FIFER, M. A., LINK, M. S., NAIDU, S. S., NISHIMURA, R. A., OMMEN, S. R. & RAKOWSKI, H. 2011. 2011 ACCF/AHA guideline for the diagnosis and treatment of hypertrophic cardiomyopathy: a report of the American College of Cardiology Foundation/American Heart Association Task Force on

Practice Guidelines. *The Journal of thoracic and cardiovascular surgery,* 142**,** e153-e203.

GIMENO, J. R., MONSERRAT, L., PÉREZ-SÁNCHEZ, I., MARÍN, F., CABALLERO, L., HERMIDA-PRIETO, M., CASTRO, A. & VALDÉS, M. 2009. Hypertrophic cardiomyopathy. A study of the troponin-T gene in 127 Spanish families. *Revista Española de Cardiología (English Edition),* 62**,** 1473-1477.

GREENBAUM, R., HO, S. Y., GIBSON, D., BECKER, A. & ANDERSON, R. 1981. Left ventricular fibre architecture in man. *British heart journal,* 45**,** 248-263.

GUIZAR-SICAIROS, M., THURMAN, S. T. & FIENUP, J. R. 2008. Efficient subpixel image registration algorithms. *Optics letters,* 33**,** 156-158.

GUTTMANN, O. P., RAHMAN, M. S., O'MAHONY, C., ANASTASAKIS, A. & ELLIOTT, P. M. 2014. Atrial fibrillation and thromboembolism in patients with hypertrophic cardiomyopathy: systematic review. *Heart,* 100**,** 465-472.

HALES, P. W., SCHNEIDER, J. E., BURTON, R. A., WRIGHT, B. J., BOLLENSDORFF, C. & KOHL, P. 2012. Histo-anatomical structure of the living isolated rat heart in two contraction states assessed by diffusion tensor MRI. *Progress in biophysics and molecular biology,* 110**,** 319-330.

HARRINGTON, K. B., RODRIGUEZ, F., CHENG, A., LANGER, F., ASHIKAGA, H., DAUGHTERS, G. T., CRISCIONE, J. C., INGELS, N. B. & MILLER, D. C. 2005. Direct measurement of transmural laminar architecture in the anterolateral wall of the ovine left ventricle: new implications for wall thickening mechanics. *American Journal of Physiology-Heart and Circulatory Physiology,* 288**,** H1324-H1330.

HARRIS, K. M., SPIRITO, P., MARON, M. S., ZENOVICH, A. G., FORMISANO, F., LESSER, J. R., MACKEY-BOJACK, S., MANNING, W. J., UDELSON, J. E. & MARON, B. J. 2006. Prevalence, clinical profile, and significance of left ventricular remodeling in the end-stage phase of hypertrophic cardiomyopathy. *Circulation,* 114**,** 216-225.

HO, S. Y. 2009. Anatomy and myoarchitecture of the left ventricular wall in normal and in disease. *European Journal of Echocardiography,* 10**,** iii3-iii7.

HOLMES, A. A., SCOLLAN, D. F. & WINSLOW, R. L. 2000. Direct histological validation of diffusion tensor MRI in formaldehyde-fixed myocardium. *Magn Reson Med,* 44**,** 157-61.

HOSHINO, T., FUJIWARA, H., KAWAI, C. & HAMASHIMA, Y. 1983. Myocardial fiber diameter and regional distribution in the ventricular wall of normal adult hearts, hypertensive hearts and hearts with hypertrophic cardiomyopathy. *Circulation,* 67**,** 1109-1116.

HSU, E. W., BUCKLEY, D. L., BUI, J. D., BLACKBAND, S. J. & FORDER, J. R. 2001. Two-component diffusion tensor MRI of isolated perfused hearts. *Magnetic resonance in medicine,* 45**,** 1039-1045.

HSU, E. W., MUZIKANT, A. L., MATULEVICIUS, S. A., PENLAND, R. C. & HENRIQUEZ, C. S. 1998. Magnetic resonance myocardial fiber-orientation mapping with direct histological correlation. *Am J Physiol,* 274**,** H1627-34.

HUGHES, S. 2004. The pathology of hypertrophic cardiomyopathy. *Histopathology,* 44**,** 412-427.

JONES, D. K. & BASSER, P. J. 2004. “Squashing peanuts and smashing pumpkins”: how noise distorts diffusion-weighted MR data. *Magnetic Resonance in Medicine: An Official Journal of the International Society for Magnetic Resonance in Medicine,* 52**,** 979-993.

JONES, D. K., HORSFIELD, M. A. & SIMMONS, A. 1999. Optimal strategies for measuring diffusion in anisotropic systems by magnetic resonance imaging. *Magnetic Resonance in Medicine: An Official Journal of the International Society for Magnetic Resonance in Medicine,* 42**,** 515-525.

KANG, K.-W., JANARDHAN, A. H., JUNG, K. T., LEE, H. S., LEE, M.-H. & HWANG, H. J. 2014. Fragmented QRS as a candidate marker for high-risk assessment in hypertrophic cardiomyopathy. *Heart Rhythm,* 11**,** 1433-1440.

KARAMITSOS, T. D., HUDSMITH, L. E., SELVANAYAGAM, J. B., NEUBAUER, S. & FRANCIS, J. M. 2007. Operator induced variability in left ventricular measurements with cardiovascular magnetic resonance is improved after training. *Journal of Cardiovascular Magnetic Resonance,* 9**,** 777-783.

KAWARAI, H., KAJIMOTO, K., MINAMI, Y., HAGIWARA, N. & KASANUKI, H. 2011. Risk of sudden death in end-stage hypertrophic cardiomyopathy. *Journal of cardiac failure,* 17**,** 459-464.

KELLMAN, P., ARAI, A. E., MCVEIGH, E. R. & ALETRAS, A. H. 2002. Phase-sensitive inversion recovery for detecting myocardial infarction using gadolinium-delayed hyperenhancement. *Magnetic Resonance in Medicine,* 47**,** 372-383.

KINGSLEY, P. B. 2006. Introduction to diffusion tensor imaging mathematics: Part III. Tensor calculation, noise, simulations, and optimization. *Concepts in Magnetic Resonance Part A,* 28**,** 155-179.

KOFFLARD, M. J., TEN CATE, F. J., VAN DER LEE, C. & VAN DOMBURG, R. T. 2003. Hypertrophic cardiomyopathy in a large community-based population: clinical outcome and identification of risk factors for sudden cardiac death and clinical deterioration. *Journal of the American College of Cardiology,* 41**,** 987-993.

KONNO, T., SHIMIZU, M., INO, H., YAMAGUCHI, M., TERAI, H., UCHIYAMA, K., OE, K., MABUCHI, T., KANEDA, T. & MABUCHI, H. 2004. Diagnostic value of abnormal Q waves for identification of preclinical carriers of hypertrophic cardiomyopathy based on a molecular genetic diagnosis. *European Heart Journal,* 25**,** 246-251.

KRAMER, C. M., APPELBAUM, E., DESAI, M. Y., DESVIGNE-NICKENS, P., DIMARCO, J. P., FRIEDRICH, M. G., GELLER, N., HECKLER, S., HO, C. Y. & JEROSCH-HEROLD, M. 2015. Hypertrophic Cardiomyopathy Registry: The rationale and design of an international, observational study of hypertrophic cardiomyopathy. *American heart journal,* 170**,** 223-230.

KUMAR, R. G. & KUMARASWAMY, Y. 2012. Investigating cardiac arrhythmia in ECG using random forest classification. *International Journal of Computer Applications,* 37**,** 31-34.

KUNG, G. L., NGUYEN, T. C., ITOH, A., SKARE, S., INGELS, N. B., JR., MILLER, D. C. & ENNIS, D. B. The presence of two local myocardial sheet populations confirmed by diffusion tensor MRI and histological validation. *J Magn Reson Imaging,* 34**,** 1080-91.

KURIBAYASHI, T. & ROBERTS, W. C. 1992. Myocardial disarray at junction of ventricular septum and left and right ventricular free walls in hypertrophic cardiomyopathy. *The American journal of cardiology,* 70**,** 1333-1340.

KURODA, N., OHNISHI, Y., YOSHIDA, A., KIMURA, A. & YOKOYAMA, M. 2002. Clinical significance of T-wave alternans in hypertrophic cardiomyopathy. *Circulation journal,* 66**,** 457-462.

LAGUNA, P., JANÉ, R., OLMOS, S., THAKOR, N. V., RIX, H. & CAMINAL, P. 1996. Adaptive estimation of QRS complex wave features of ECG signal by the Hermite model. *Medical and Biological Engineering and computing,* 34**,** 58-68.

LAKDAWALA, N. K., THUNE, J. J., MARON, B. J., CIRINO, A. L., HAVNDRUP, O., BUNDGAARD, H., CHRISTIANSEN, M., CARLSEN, C. M., DORVAL, J.-F. & KWONG, R. Y. 2011. Electrocardiographic features of sarcomere mutation carriers with and without clinically overt hypertrophic cardiomyopathy. *The American journal of cardiology,* 108**,** 1606-1613.

LE BIHAN, D., BRETON, E., LALLEMAND, D., AUBIN, M., VIGNAUD, J. & LAVAL-JEANTET, M. 1988. Separation of diffusion and perfusion in intravoxel incoherent motion MR imaging. *Radiology,* 168**,** 497-505.

LE BIHAN, D., BRETON, E., LALLEMAND, D., GRENIER, P., CABANIS, E. & LAVAL-JEANTET, M. 1986. MR imaging of intravoxel incoherent motions: application to diffusion and perfusion in neurologic disorders. *Radiology,* 161**,** 401-407.

LEGRICE, I. J., SMAILL, B. H., CHAI, L. Z., EDGAR, S. G., GAVIN, J. B. & HUNTER, P. J. 1995. Laminar structure of the heart: ventricular myocyte arrangement and connective

tissue architecture in the dog. *American Journal of Physiology - Heart and Circulatory Physiology,* 269**,** H571-H582.

LIM, K.-K., MARON, B. J. & KNIGHT, B. P. 2009. Successful catheter ablation of hemodynamically unstable monomorphic ventricular tachycardia in a patient with hypertrophic cardiomyopathy and apical aneurysm. *Journal of cardiovascular electrophysiology,* 20**,** 445-447.

LLAMEDO, M. & MARTÍNEZ, J. P. 2011. Heartbeat classification using feature selection driven by database generalization criteria. *IEEE Transactions on Biomedical Engineering,* 58**,** 616-625.

LOHEZIC, M., TEH, I., BOLLENSDORFF, C., PEYRONNET, R., HALES, P. W., GRAU, V., KOHL, P. & SCHNEIDER, J. E. 2014. Interrogation of living myocardium in multiple static deformation states with diffusion tensor and diffusion spectrum imaging. *Progress in biophysics and molecular biology,* 115**,** 213-225.

LYON, A., ARIGA, R., MINCHOLÉ, A., MAHMOD, M., ORMONDROYD, E., LAGUNA, P., DE FREITAS, N., NEUBAUER, S., WATKINS, H. & RODRIGUEZ, B. 2018. Distinct ECG phenotypes identified in hypertrophic cardiomyopathy using machine learning associate with arrhythmic risk markers. *Frontiers in physiology,* 9**,** 213.

MACFARLANE, P., DEVINE, B., LATIF, S., MCLAUGHLIN, S., SHOAT, D. & WATTS, M. 1990. Methodology of ECG interpretation in the Glasgow program. *Methods of information in medicine,* 29**,** 354-361.

MANTICA, M., DELLA BELLA, P. & ARENA, V. 1997. Hypertrophic cardiomyopathy with apical aneurysm: a case of catheter and surgical therapy of sustained monomorphic ventricular tachycardia. *Heart,* 77**,** 481-483.

MARON, B. J. 2002. Hypertrophic cardiomyopathy: a systematic review. *JAMA,* 287**,** 1308-20.

MARON, B. J., ANAN, T. J. & ROBERTS, W. C. 1981a. Quantitative Analysis of the Distribution of Cardiac Muscle Cell Disorganization in the Left Ventricular. *Circulation,* 63.

MARON, B. J., CASEY, S. A., CHAN, R. H., GARBERICH, R. F., ROWIN, E. J. & MARON, M. S. 2015. Independent assessment of the European Society of Cardiology sudden death risk model for hypertrophic cardiomyopathy. *American Journal of Cardiology,* 116**,** 757-764.

MARON, B. J., FERRANS, V. J., HENRY, W. L., CLARK, C. E., REDWOOD, D. R., ROBERTS, W. C., MORROW, A. G. & EPSTEIN, S. E. 1974. Differences in distribution of myocardial abnormalities in patients with obstructive and nonobstructive asymmetric septal hypertrophy (ASH): light and electron microscopic findings. *Circulation,* 50**,** 436-446.

MARON, B. J., GARDIN, J. M., FLACK, J. M., GIDDING, S. S., KUROSAKI, T. T. & BILD, D. E. 1995. Prevalence of hypertrophic cardiomyopathy in a general population of young adults. Echocardiographic analysis of 4111 subjects in the CARDIA Study. Coronary Artery Risk Development in (Young) Adults. *Circulation,* 92**,** 785-9.

MARON, B. J., MARON, M. S. & SEMSARIAN, C. 2012a. Double or compound sarcomere mutations in hypertrophic cardiomyopathy: a potential link to sudden death in the absence of conventional risk factors. *Heart Rhythm,* 9**,** 57-63.

MARON, B. J., MCKENNA, W. J., DANIELSON, G. K., KAPPENBERGER, L. J., KUHN, H. J., SEIDMAN, C. E., SHAH, P. M., SPENCER, W. H., SPIRITO, P. & TEN CATE, F. J. 2003. American College of Cardiology/European Society of Cardiology clinical expert consensus document on hypertrophic cardiomyopathy: a report of the American College of Cardiology foundation task force on clinical expert consensus documents and the European Society of Cardiology committee for practice guidelines. *Journal of the American College of Cardiology,* 42**,** 1687-1713.

MARON, B. J., OLIVOTTO, I., SPIRITO, P., CASEY, S. A., BELLONE, P., GOHMAN, T. E., GRAHAM, K. J., BURTON, D. A. & CECCHI, F. 2000a. Epidemiology of hypertrophic cardiomyopathy–related death. *Circulation,* 102**,** 858-864.

MARON, B. J., OLIVOTTO, I., SPIRITO, P., CASEY, S. A., BELLONE, P., GOHMAN, T. E., GRAHAM, K. J., BURTON, D. A. & CECCHI, F. 2000b. Epidemiology of hypertrophic cardiomyopathy–related death: revisited in a large non–referral-based patient population. *Circulation,* 102**,** 858-864.

MARON, B. J. & ROBERTS, W. C. 1979. Quantitative analysis of cardiac muscle cell disorganization in the ventricular septum of patients with hypertrophic cardiomyopathy. *Circulation,* 59**,** 689-706.

MARON, B. J., ROBERTS, W. C. & EPSTEIN, S. E. 1982. Sudden death in hypertrophic cardiomyopathy: a profile of 78 patients. *Circulation,* 65**,** 1388-1394.

MARON, B. J., ROWIN, E. J., CASEY, S. A., HAAS, T. S., CHAN, R. H., UDELSON, J. E., GARBERICH, R. F., LESSER, J. R., APPELBAUM, E. & MANNING, W. J. 2012b. Risk stratification and

outcome of patients with hypertrophic cardiomyopathy over 60 years of age. *Circulation*, CIRCULATIONAHA. 112.136085.

MARON, B. J., SAVAGE, D. D., WOLFSON, J. K. & EPSTEIN, S. E. 1981b. Prognostic significance of 24 hour ambulatory electrocardiographic monitoring in patients with hypertrophic cardiomyopathy: a prospective study. *The American journal of cardiology,* 48**,** 252-257.

MARON, B. J., SHEN, W.-K., LINK, M. S., EPSTEIN, A. E., ALMQUIST, A. K., DAUBERT, J. P., BARDY, G. H., FAVALE, S., REA, R. F. & BORIANI, G. 2000c. Efficacy of implantable cardioverter–defibrillators for the prevention of sudden death in patients with hypertrophic cardiomyopathy. *New England Journal of Medicine,* 342**,** 365-373.

MARON, B. J., SHIRANI, J., POLIAC, L. C., MATHENGE, R., ROBERTS, W. C. & MUELLER, F. O. 1996. Sudden death in young competitive athletes: clinical, demographic, and pathological profiles. *Jama,* 276**,** 199-204.

MARON, B. J., SPIRITO, P., SHEN, W. & ET AL. 2007. Implantable cardioverter-defibrillators and prevention of sudden cardiac death in hypertrophic cardiomyopathy. *JAMA,* 298**,** 405-412.

MARON, B. J., WOLFSON, J. K., CIRÓ, E. & SPIRITO, P. 1983. Relation of electrocardiographic abnormalities and patterns of left ventricular hypertrophy identified by 2-dimensional echocardiography in patients with hypertrophic cardiomyopathy. *american Journal of Cardiology,* 51**,** 189-194.

MARON, B. J., WOLFSON, J. K., EPSTEIN, S. E. & ROBERTS, W. C. 1986. Intramural ("small vessel") coronary artery disease in hypertrophic cardiomyopathy. *Journal of the American College of Cardiology,* 8**,** 545-557.

MARON, B. J., WOLFSON, J. K. & ROBERTS, W. C. 1992. Relation between extent of cardiac muscle cell disorganization and left ventricular wall thickness in hypertrophic cardiomyopathy. *The American journal of cardiology,* 70**,** 785-790.

MARON, M. S. 2013. Contrast-Enhanced CMR in HCM. JACC: Cardiovascular Imaging.

MARON, M. S., OLIVOTTO, I., MARON, B. J., PRASAD, S. K., CECCHI, F., UDELSON, J. E. & CAMICI, P. G. 2009. The case for myocardial ischemia in hypertrophic cardiomyopathy. *J Am Coll Cardiol,* 54**,** 866-75.

MARTINEZ, J. P., ALMEIDA, R., OLMOS, S., ROCHA, A. P. & LAGUNA, P. 2004. A wavelet-based ECG delineator: evaluation on standard databases. *Biomedical Engineering, IEEE Transactions on,* 51**,** 570-581.

MASUDA, H., YAMAUCHI, M., YOSHIDA, M., TAKAHASHI, M., NANJO, H., ASARI, Y. & SUGITA, A. 2005. Side-to-side linking of myocardial cells in hypertrophic cardiomyopathy: Whole heart microscopic observation with tangential sections. *Pathology international,* 55**,** 677-687.

MATSUBARA, K., NAKAMURA, T., KURIBAYASHI, T., AZUMA, A. & NAKAGAWA, M. 2003. Sustained cavity obliteration and apical aneurysm formation in apical hypertrophic cardiomyopathy. *Journal of the American College of Cardiology,* 42**,** 288-295.

MCCLYMONT, D., TEH, I., CARRUTH, E., OMENS, J., MCCULLOCH, A., WHITTINGTON, H. J., KOHL, P., GRAU, V. & SCHNEIDER, J. E. 2017a. Evaluation of non-Gaussian diffusion in cardiac MRI. *Magnetic resonance in medicine,* 78**,** 1174-1186.

MCCLYMONT, D., TEH, I. & SCHNEIDER, J. E. 2017b. The impact of signal-to-noise ratio, diffusion-weighted directions and image resolution in cardiac diffusion tensor imaging–insights from the ex-vivo rat heart. *Journal of Cardiovascular Magnetic Resonance,* 19**,** 90.

MCGILL, L.-A., ISMAIL, T., NIELLES-VALLESPIN, S., FERREIRA, P., SCOTT, A., ROUGHTON, M., KILNER, P., HO, S. Y., MCCARTHY, K., GATEHOUSE, P., DE SILVA, R., SPEIER, P., FEIWEIER, T., MEKKAOUI, C., SOSNOVIK, D., PRASAD, S., FIRMIN, D. & PENNELL, D. 2012. Reproducibility of in-vivo diffusion tensor cardiovascular magnetic resonance in hypertrophic cardiomyopathy. *Journal of Cardiovascular Magnetic Resonance,* 14**,** 86.

MCGILL, L.-A., SCOTT, A. D., FERREIRA, P. F., NIELLES-VALLESPIN, S., ISMAIL, T., KILNER, P. J., GATEHOUSE, P. D., DE SILVA, R., PRASAD, S. K. & GIANNAKIDIS, A. 2015a. Heterogeneity of fractional anisotropy and mean diffusivity measurements by in vivo diffusion tensor imaging in normal human hearts. *PloS one,* 10**,** e0132360.

MCGILL, L., FERREIRA, P., SCOTT, A., NIELLES-VALLESPIN, S., GIANNAKIDIS, A., KILNER, P., GATEHOUSE, P., DE SILVA, R., FIRMIN, D. & PENNELL, D. 2015b. Relationship between cardiac diffusion tensor imaging parameters and anthropometrics in healthy volunteers. *Journal of Cardiovascular Magnetic Resonance,* 18**,** 2.

MCKENNA, W. J., ENGLAND, D., DOI, Y. L., DEANFIELD, J. E., OAKLEY, C. & GOODWIN, J. F. 1981. Arrhythmia in hypertrophic cardiomyopathy. I: Influence on prognosis. *British Heart Journal,* 46**,** 168-172.

MCLEOD, C. J., ACKERMAN, M. J., NISHIMURA, R. A., TAJIK, A. J., GERSH, B. J. & OMMEN, S. R. 2009. Outcome of patients with hypertrophic cardiomyopathy and a normal electrocardiogram. *Journal of the american College of Cardiology,* 54**,** 229-233.

MELACINI, P., BASSO, C., ANGELINI, A., CALORE, C., BOBBO, F., TOKAJUK, B., BELLINI, N., SMANIOTTO, G., ZUCCHETTO, M. & ILICETO, S. 2010. Clinicopathological profiles of progressive heart failure in hypertrophic cardiomyopathy. *European heart journal,* 31**,** 2111-2123.

MICHELS, M., SOLIMAN, O. I., PHEFFERKORN, J., HOEDEMAEKERS, Y. M., KOFFLARD, M. J., DOOIJES, D., MAJOOR-KRAKAUER, D. & TEN CATE, F. J. 2009. Disease penetrance and risk stratification for sudden cardiac death in asymptomatic hypertrophic cardiomyopathy mutation carriers. *European heart journal,* 30**,** 2593-2598.

MINAMI, Y., KAJIMOTO, K., TERAJIMA, Y., YASHIRO, B., OKAYAMA, D., HARUKI, S., NAKAJIMA, T., KAWASHIRO, N., KAWANA, M. & HAGIWARA, N. 2011. Clinical implications of midventricular obstruction in patients with hypertrophic cardiomyopathy. *Journal of the American College of Cardiology,* 57**,** 2346-2355.

MOODY, G. B. & MARK, R. G. 2001. The impact of the MIT-BIH arrhythmia database. *IEEE Engineering in Medicine and Biology Magazine,* 20**,** 45-50.

MOON, J. C., REED, E., SHEPPARD, M. N., ELKINGTON, A. G., HO, S., BURKE, M., PETROU, M. & PENNELL, D. J. 2004. The histologic basis of late gadolinium enhancement

cardiovascular magnetic resonance in hypertrophic cardiomyopathy. *Journal of the American College of Cardiology,* 43**,** 2260-2264.

MORAVSKY, G., OFEK, E., RAKOWSKI, H., BUTANY, J., WILLIAMS, L., RALPH-EDWARDS, A., WINTERSPERGER, B. J. & CREAN, A. 2013. Myocardial fibrosis in hypertrophic cardiomyopathy: accurate reflection of histopathological findings by CMR. *JACC: Cardiovascular Imaging,* 6**,** 587-596.

MUSUMECI, M. B., SPIRITO, P., CAUTI, F. M. & AUTORE, C. 2011. High risk for sudden death identified by electrocardiographic loop recording in a patient with hypertrophic cardiomyopathy without major risk factors. *The American journal of cardiology,* 107**,** 1558-1560.

NAGY, Z., LINDSTRÖM, K., WESTERBERG, H., SKARE, S., ANDERSSON, J., HALLBERG, B., LILJA, A., FLODMARK, O., LAGERCRANTZ, H. & KLINGBERG, T. 2005. Diffusion tensor imaging on teenagers, born at term with moderate hypoxic-ischemic encephalopathy. *Pediatric research,* 58**,** 936.

NASIRI, J. A., NAGHIBZADEH, M., YAZDI, H. S. & NAGHIBZADEH, B. ECG arrhythmia classification with support vector machines and genetic algorithm. Computer Modeling and Simulation, 2009. EMS'09. Third UKSim European Symposium on, 2009. IEEE, 187-192.

NICOD, P., POLIKAR, R. & PETERSON, K. L. 1988. Hypertrophic cardiomyopathy and sudden death. *New England Journal of Medicine,* 318**,** 1255-1257.

NIELLES-VALLESPIN, S., KHALIQUE, Z., FERREIRA, P. F., DE SILVA, R., SCOTT, A. D., KILNER, P., MCGILL, L.-A., GIANNAKIDIS, A., GATEHOUSE, P. D. & ENNIS, D. 2017. Assessment of

myocardial microstructural dynamics by in vivo diffusion tensor cardiac magnetic resonance. *Journal of the American College of Cardiology,* 69**,** 661-676.

NIELLES-VALLESPIN, S., MEKKAOUI, C., GATEHOUSE, P., REESE, T. G., KEEGAN, J., FERREIRA, P. F., COLLINS, S., SPEIER, P., FEIWEIER, T., DE SILVA, R., JACKOWSKI, M. P., PENNELL, D. J., SOSNOVIK, D. E. & FIRMIN, D. 2013. In vivo diffusion tensor MRI of the human heart: Reproducibility of breath-hold and navigator-based approaches. *Magnetic Resonance in Medicine,* 70**,** 454-465.

NIELLES-VALLESPIN, S., MEKKAOUI, C., GATEHOUSE, P., REESE, T. G., KEEGAN, J., FERREIRA, P. F., COLLINS, S., SPEIER, P., FEIWEIER, T. & DE SILVA, R. 2014. Erratum to In vivo diffusion tensor MRI of the human heart: Reproducibility of breath-hold and navigator based approaches (Magn Reson Med 2013; 70: 454–465). *Magnetic Resonance in Medicine,* 72**,** 599-599.

NOORDEN, S. V., OLSEN, E. & PEARSE, A. 1971. Hypertrophic obstructive cardiomyopathy, a histological, histochemical, and ultrastructural study of biopsy material. *Cardiovascular Research,* 5**,** 118-131.

O'HANLON, R., GRASSO, A., ROUGHTON, M., MOON, J. C., CLARK, S., WAGE, R., WEBB, J., KULKARNI, M., DAWSON, D., SULAIBEEKH, L., CHANDRASEKARAN, B., BUCCIARELLI-DUCCI, C., PASQUALE, F., COWIE, M. R., MCKENNA, W. J., SHEPPARD, M. N., ELLIOTT, P. M., PENNELL, D. J. & PRASAD, S. K. Prognostic significance of myocardial fibrosis in hypertrophic cardiomyopathy. *J Am Coll Cardiol,* 56**,** 867-74.

O'MAHONY, C., JICHI, F., PAVLOU, M., MONSERRAT, L., ANASTASAKIS, A., RAPEZZI, C., BIAGINI, E., GIMENO, J. R., LIMONGELLI, G., MCKENNA, W. J., OMAR, R. Z., ELLIOTT, P. M. & FOR

THE HYPERTROPHIC CARDIOMYOPATHY OUTCOMES, I. 2014. A novel clinical risk prediction model for sudden cardiac death in hypertrophic cardiomyopathy (HCM Risk-SCD). *European Heart Journal,* 35**,** 2010-2020.

O'MAHONY, C., TOME-ESTEBAN, M., LAMBIASE, P. D., PANTAZIS, A., DICKIE, S., MCKENNA, W. J. & ELLIOTT, P. M. 2013. A validation study of the 2003 American College of Cardiology/European Society of Cardiology and 2011 American College of Cardiology Foundation/American Heart Association risk stratification and treatment algorithms for sudden cardiac death in patients with hypertrophic cardiomyopathy. *Heart,* 99**,** 534-541.

OBERMEYER, Z. & EMANUEL, E. J. 2016. Predicting the future—big data, machine learning, and clinical medicine. *The New England journal of medicine,* 375**,** 1216.

OLIVETTI, G., CIGOLA, E., MAESTRI, R., CORRADI, D., LAGRASTA, C., GAMBERT, S. R. & ANVERSA, P. 1996. Aging, cardiac hypertrophy and ischemic cardiomyopathy do not affect the proportion of mononucleated and multinucleated myocytes in the human heart. *Journal of molecular and cellular cardiology,* 28**,** 1463-1477.

OLIVOTTO, I., CAMICI, P. G., MERLINI, P. A., RAPEZZI, C., PATTEN, M., CLIMENT, V., SINAGRA, G., TOMBERLI, B., MARIN, F. & EHLERMANN, P. 2018. Efficacy of Ranolazine in Patients With Symptomatic Hypertrophic Cardiomyopathy: The RESTYLE-HCM Randomized, Double-Blind, Placebo-Controlled Study. *Circulation: Heart Failure,* 11**,** e004124.

OLIVOTTO, I., CECCHI, F., POGGESI, C. & YACOUB, M. H. 2012. Patterns of disease progression in hypertrophic cardiomyopathy: an individualized approach to clinical staging. *Circulation: Heart Failure,* 5**,** 535-546.

OPIE, L. H. 2004. *Heart physiology: from cell to circulation*, Lippincott Williams & Wilkins.

ÖSTMAN-SMITH, I., WISTEN, A., NYLANDER, E., BRATT, E.-L., GRANELLI, A. D.-W., OULHAJ, A. & LJUNGSTRÖM, E. 2009. Electrocardiographic amplitudes: a new risk factor for sudden death in hypertrophic cardiomyopathy. *European heart journal,* 31**,** 439-449.

PAPADAKIS, M., BASAVARAJAIAH, S., RAWLINS, J., EDWARDS, C., MAKAN, J., FIROOZI, S., CARBY, L. & SHARMA, S. 2009. Prevalence and significance of T-wave inversions in predominantly Caucasian adolescent athletes. *European heart journal,* 30**,** 1728-1735.

PASQUALE, F., SYRRIS, P., KASKI, J. P., MOGENSEN, J., MCKENNA, W. J. & ELLIOTT, P. 2012. Long-term outcomes in hypertrophic cardiomyopathy caused by mutations in the cardiac troponin T gene. *Circulation: Genomic and Precision Medicine,* 5**,** 10-17.

PASSINI, E., MINCHOLÉ, A., COPPINI, R., CERBAI, E., RODRIGUEZ, B., SEVERI, S. & BUENO-OROVIO, A. 2016. Mechanisms of pro-arrhythmic abnormalities in ventricular repolarisation and anti-arrhythmic therapies in human hypertrophic cardiomyopathy. *Journal of molecular and cellular cardiology,* 96**,** 72-81.

PETERSEN, S. E., JEROSCH-HEROLD, M., HUDSMITH, L. E., ROBSON, M. D., FRANCIS, J. M., DOLL, H. A., SELVANAYAGAM, J. B., NEUBAUER, S. & WATKINS, H. 2007. Evidence for microvascular dysfunction in hypertrophic cardiomyopathy: new insights from multiparametric magnetic resonance imaging. *Circulation,* 115**,** 2418-25.

PETERSEN, S. E., SELVANAYAGAM, J. B., WIESMANN, F., ROBSON, M. D., FRANCIS, J. M., ANDERSON, R. H., WATKINS, H. & NEUBAUER, S. 2005. Left ventricular non-compaction: insights from cardiovascular magnetic resonance imaging. *Journal of the American College of Cardiology,* 46**,** 101-105.

PETTIGREW, J. B. 1864. XIV. On the arrangement of the muscular fibres in the ventricles of the vertebrate heart, with physiological remarks. *Philosophical Transactions of the Royal Society of London,* 154**,** 445-500.

PIECHNIK, S. K., FERREIRA, V. M., DALL'ARMELLINA, E., COCHLIN, L. E., GREISER, A., NEUBAUER, S. & ROBSON, M. D. 2010. Shortened Modified Look-Locker Inversion recovery (ShMOLLI) for clinical myocardial T1-mapping at 1.5 and 3 T within a 9 heartbeat breathhold. *Journal of cardiovascular magnetic resonance,* 12**,** 69.

POPE, A. J., SANDS, G. B., SMAILL, B. H. & LEGRICE, I. J. 2008. Three-dimensional transmural organization of perimysial collagen in the heart. *American Journal of Physiology-Heart and Circulatory Physiology,* 295**,** H1243-H1252.

PRIORI, S. G., ALIOT, E., BLOMSTROM-LUNDQVIST, C., BOSSAERT, L., BREITHARDT, G., BRUGADA, P., CAMM, A. J., CAPPATO, R., COBBE, S. M. & DI MARIO, C. 2001. Task force on sudden cardiac death of the European Society of Cardiology. *European heart journal,* 22**,** 1374-1450.

RAUTAHARJU, P. M., SURAWICZ, B. & GETTES, L. S. 2009. AHA/ACCF/HRS recommendations for the standardization and interpretation of the electrocardiogram: part IV: the ST segment, T and U waves, and the QT interval a scientific statement from the American Heart Association Electrocardiography and Arrhythmias Committee, Council on Clinical Cardiology; the American College of Cardiology Foundation; and the Heart Rhythm Society Endorsed by the International Society for Computerized Electrocardiology. *Journal of the American College of Cardiology,* 53**,** 982-991.

RAUTAHARJU, P. M., ZHOU, S. H. & CALHOUN, H. P. 1994. Ethnic differences in ECG amplitudes in North American white, black, and Hispanic men and women: effect of obesity and age. *Journal of electrocardiology,* 27**,** 20-31.

REESE, T. G., WEDEEN, V. J. & WEISSKOFF, R. M. 1996. Measuring diffusion in the presence of material strain. *Journal of Magnetic Resonance, Series B,* 112**,** 253-258.

REESE, T. G., WEISSKOFF, R. M., SMITH, R. N., ROSEN, B. R., DINSMORE, R. E. & WEDEEN, V. J. 1995. Imaging myocardial fiber architecture in vivo with magnetic resonance. *Magn Reson Med,* 34**,** 786-91.

RIDER, O. J., NTUSI, N., BULL, S. C., NETHONONDA, R., FERREIRA, V., HOLLOWAY, C. J., HOLDSWORTH, D., MAHMOD, M., RAYNER, J. J. & BANERJEE, R. 2016. Improvements in ECG accuracy for diagnosis of left ventricular hypertrophy in obesity. *Heart***,** heartjnl-2015-309201.

RODRIGUEZ, L., SMEETS, J. L., TIMMERMANS, C., BLOMMAERT, D., DANTZIG, J. M., MUINCK, E. & WELLENS, H. J. 1997. Radiofrequency catheter ablation of sustained monomorphic ventricular tachycardia in hypertrophic cardiomyopathy. *Journal of cardiovascular electrophysiology,* 8**,** 803-806.

SANCHEZ-QUINTANA, D., CLIMENT, V., HO, S. & ANDERSON, R. 1999. Myoarchitecture and connective tissue in hearts with tricuspid atresia. *Heart,* 81**,** 182-191.

SANDS, G. B., GERNEKE, D. A., HOOKS, D. A., GREEN, C. R., SMAILL, B. H. & LEGRICE, I. J. 2005. Automated imaging of extended tissue volumes using confocal microscopy. *Microscopy research and technique,* 67**,** 227-239.

SATOH, H., MATOH, F., SHIRAKI, K., SAITOH, T., ODAGIRI, K., SAOTOME, M., URUSHIDA, T., KATOH, H., TAKEHARA, Y., SAKAHARA, H. & HAYASHI, H. 2009. Delayed Enhancement on Cardiac Magnetic Resonance and Clinical, Morphological, and Electrocardiographical Features in Hypertrophic Cardiomyopathy. *Journal of Cardiac Failure,* 15**,** 419-427.

SAUMAREZ, R., CAMM, A., PANAGOS, A., GILL, J., STEWART, J., DE BELDER, M., SIMPSON, I. & MCKENNA, W. 1992. Ventricular fibrillation in hypertrophic cardiomyopathy is associated with increased fractionation of paced right ventricular electrograms. *Circulation,* 86**,** 467-474.

SAUMAREZ, R. C. 1994. Electrophysiological investigation of patients with hypertrophic cardiomyopathy. Evidence that slowed intraventricular conduction is associated with an increased risk of sudden death. *Br Heart J,* 72**,** S19-23.

SAUMAREZ, R. C., PYTKOWSKI, M., STERLINSKI, M., BOURKE, J. P., CLAGUE, J. R., COBBE, S. M., CONNELLY, D. T., GRIFFITH, M. J., MCKEOWN, P. P. & MCLEOD, K. 2008. Paced ventricular electrogram fractionation predicts sudden cardiac death in hypertrophic cardiomyopathy. *European heart journal,* 29**,** 1653-1661.

SAVAGE, D. D., SEIDES, S. F., CLARK, C. E., HENRY, W. L., MARON, B. J., ROBINSON, F. C. & EPSTEIN, S. E. 1978. Electrocardiographic findings in patients with obstructive and nonobstructive hypertrophic cardiomyopathy. *Circulation,* 58**,** 402-408.

SCHILLER, N. B., SHAH, P. M., CRAWFORD, M., DEMARIA, A., DEVEREUX, R., FEIGENBAUM, H., GUTGESELL, H., REICHEK, N., SAHN, D. & SCHNITTGER, I. 1989. Recommendations for

quantitation of the left ventricle by two-dimensional echocardiography. *Journal of the American Society of Echocardiography,* 2**,** 358-367.

SCHINKEL, A., VRIESENDORP, P. A., SIJBRANDS, E., JORDAENS, L. J., FOLKERT, J. & MICHELS, M. 2012. Outcome and complications after implantable cardioverter defibrillator therapy in hypertrophic cardiomyopathy. *Circ Heart Fail,* 5**,** 552-559.

SCIRICA, B. M., MORROW, D. A., HOD, H., MURPHY, S. A., BELARDINELLI, L., HEDGEPETH, C. M., MOLHOEK, P., VERHEUGT, F. W., GERSH, B. J. & MCCABE, C. H. 2007. Effect of ranolazine, an antianginal agent with novel electrophysiological properties, on the incidence of arrhythmias in patients with non–ST-segment–elevation acute coronary syndrome: results from the Metabolic Efficiency with Ranolazine for Less Ischemia in Non–ST-Elevation Acute Coronary Syndrome–Thrombolysis in Myocardial Infarction 36 (MERLIN-TIMI 36) randomized controlled trial. *Circulation,* 116**,** 1647-1652.

SCOLLAN, D. F., HOLMES, A., WINSLOW, R. & FORDER, J. 1998. Histological validation of myocardial microstructure obtained from diffusion tensor magnetic resonance imaging. *Am J Physiol,* 275**,** H2308-18.

SCOTT, A. D., FERREIRA, P. F., NIELLES-VALLESPIN, S., GATEHOUSE, P., MCGILL, L. A., KILNER, P., PENNELL, D. J. & FIRMIN, D. N. 2015. Optimal diffusion weighting for in vivo cardiac diffusion tensor imaging. *Magnetic resonance in medicine,* 74**,** 420-430.

SCOTT, A. D., NIELLES-VALLESPIN, S., FERREIRA, P. F., MCGILL, L. A., PENNELL, D. J. & FIRMIN, D. N. 2016. The effects of noise in cardiac diffusion tensor imaging and the benefits of averaging complex data. *NMR in Biomedicine,* 29**,** 588-599.

SEIDMAN, J. & SEIDMAN, C. 2001. The genetic basis for cardiomyopathy: from mutation identification to mechanistic paradigms. *Cell,* 104**,** 557-567.

SEMSARIAN, C., INGLES, J., MARON, M. S. & MARON, B. J. 2015. New perspectives on the prevalence of hypertrophic cardiomyopathy. *Journal of the American College of Cardiology,* 65**,** 1249-1254.

SEPP, R., SEVERS, N. J. & GOURDIE, R. G. 1996. Altered patterns of cardiac intercellular junction distribution in hypertrophic cardiomyopathy. *Heart,* 76**,** 412-417.

SHEPPARD, M. 2000. Hypertrophic cardiomyopathy. *Current Diagnostic Pathology,* 6**,** 251-260.

SHERRID, M. V., COTIGA, D., HART, D., EHLERT, F., HAAS, T. S., SHEN, W.-K., LINK, M. S., ESTES III, N. M., EPSTEIN, A. E. & SEMSARIAN, C. 2009. Relation of 12-lead electrocardiogram patterns to implanted defibrillator-terminated ventricular tachyarrhythmias in hypertrophic cardiomyopathy. *The American journal of cardiology,* 104**,** 1722-1726.

SHIRANI, J., PICK, R., ROBERTS, W. C. & MARON, B. J. 2000. Morphology and significance of the left ventricular collagen network in young patients with hypertrophic cardiomyopathy and sudden cardiac death. *Journal of the American College of Cardiology,* 35**,** 36-44.

SODICKSON, D. K., GRISWOLD, M. A., JAKOB, P. M., EDELMAN, R. R. & MANNING, W. J. 1999. Signal-to-noise ratio and signal-to-noise efficiency in SMASH imaging. *Magnetic Resonance in Medicine: An Official Journal of the International Society for Magnetic Resonance in Medicine,* 41**,** 1009-1022.

SORAJJA, P., OMMEN, S. R., NISHIMURA, R. A., GERSH, B. J., BERGER, P. B. & TAJIK, A. J. 2003. Adverse prognosis of patients with hypertrophic cardiomyopathy who have epicardial coronary artery disease. *Circulation,* 108**,** 2342-2348.

SORNMO, L., BORJESSON, P. O., NYGARDS, M.-E. & PAHLM, O. 1981. A method for evaluation of QRS shape features using a mathematical model for the ECG. *IEEE Transactions on Biomedical Engineering***,** 713-717.

SÖRNMO, L. & LAGUNA, P. 2005. *Bioelectrical signal processing in cardiac and neurological applications*, Academic Press.

SPIRITO, P., BELLONE, P., HARRIS, K. M., BERNABÒ, P., BRUZZI, P. & MARON, B. J. 2000. Magnitude of left ventricular hypertrophy and risk of sudden death in hypertrophic cardiomyopathy. *New England Journal of Medicine,* 342**,** 1778-1785.

SPIRITO, P., RAPEZZI, C., AUTORE, C., BRUZZI, P., BELLONE, P., ORTOLANI, P., FRAGOLA, P. V., CHIARELLA, F., ZONI-BERISSO, M. & BRANZI, A. 1994. Prognosis of asymptomatic patients with hypertrophic cardiomyopathy and nonsustained ventricular tachycardia. *Circulation,* 90**,** 2743-2747.

SPOTNITZ, H. M., SPOTNITZ, W. D., COTTRELL, T. S., SPIRO, D. & SONNENBLICK, E. H. 1974. Cellular basis for volume related wall thickness changes in the rat left ventricle. *Journal of molecular and cellular cardiology,* 6**,** 323-331.

STEJSKAL, E. O. & TANNER, J. E. 1965. Spin diffusion measurements: spin echoes in the presence of a time-dependent field gradient. *The journal of chemical physics,* 42**,** 288-292.

STOECK, C. T., KALINOWSKA, A., VON DEUSTER, C., HARMER, J., CHAN, R. W., NIEMANN, M., MANKA, R., ATKINSON, D., SOSNOVIK, D. E. & MEKKAOUI, C. 2014. Dual-phase cardiac diffusion tensor imaging with strain correction. *PLoS One,* 9**,** e107159.

STREETER, D. D., SPOTNITZ, H. M., PATEL, D. P., ROSS, J. & SONNENBLICK, E. H. 1969. Fiber orientation in the canine left ventricle during diastole and systole. *Circulation research,* 24**,** 339-347.

SYSKA, P., PRZYBYLSKI, A., CHOJNOWSKA, L., LEWANDOWSKI, M., STERLIŃSKI, M., MACIĄG, A., GEPNER, K., PYTKOWSKI, M., KOWALIK, I., MĄCZYŃSKA-MAZURUK, R., RUZYŁŁO, W. & SZWED, H. 2010. Implantable Cardioverter-Defibrillator in Patients With Hypertrophic Cardiomyopathy: Efficacy and Complications of the Therapy in Long-Term Follow-up. *Journal of Cardiovascular Electrophysiology,* 21**,** 883-889.

SZCZEPANKIEWICZ, F., LASIČ, S., VAN WESTEN, D., SUNDGREN, P. C., ENGLUND, E., WESTIN, C.-F., STÅHLBERG, F., LÄTT, J., TOPGAARD, D. & NILSSON, M. 2015. Quantification of microscopic diffusion anisotropy disentangles effects of orientation dispersion from microstructure: applications in healthy volunteers and in brain tumors. *NeuroImage,* 104**,** 241-252.

TEARE, D. 1958. Asymmetrical hypertrophy of the heart in young adults. *British heart journal,* 20**,** 1.

TEH, I., BURTON, R. A., MCCLYMONT, D., CAPEL, R. A., ASTON, D., KOHL, P. & SCHNEIDER, J. E. 2016. Mapping cardiac microstructure of rabbit heart in different mechanical states by high resolution diffusion tensor imaging: A proof-of-principle study. *Progress in biophysics and molecular biology,* 121**,** 85-96.

THOMSON, H. L., MORRIS-THURGOOD, J., ATHERTON, J. & FRENNEAUX, M. 1998. Reduced cardiopulmonary baroreflex sensitivity in patients with hypertrophic cardiomyopathy. *Journal of the American College of Cardiology,* 31**,** 1377-1382.

TOFTS, P. S., LLOYD, D., CLARK, C. A., BARKER, G. J., PARKER, G. J. M., MCCONVILLE, P., BALDOCK, C. & POPE, J. M. 2000. Test liquids for quantitative MRI measurements of self-diffusion coefficient in vivo. *Magnetic Resonance in Medicine,* 43**,** 368-374.

TSENG, W. Y., DOU, J., REESE, T. G. & WEDEEN, V. J. 2006. Imaging myocardial fiber disarray and intramural strain hypokinesis in hypertrophic cardiomyopathy with MRI. *J Magn Reson Imaging,* 23**,** 1-8.

TSENG, W. Y., REESE, T. G., WEISSKOFF, R. M. & WEDEEN, V. J. 1999. Cardiac diffusion tensor MRI in vivo without strain correction. *Magn Reson Med,* 42**,** 393-403.

TSENG, W. Y., WEDEEN, V. J., REESE, T. G., SMITH, R. N. & HALPERN, E. F. 2003. Diffusion tensor MRI of myocardial fibers and sheets: correspondence with visible cut-face texture. *J Magn Reson Imaging,* 17**,** 31-42.

TUNNICLIFFE, E., SCOTT, A., FERREIRA, P., ARIGA, R., MCGILL, L.-A., NIELLES-VALLESPIN, S., NEUBAUER, S., PENNELL, D., ROBSON, M. & FIRMIN, D. 2014. Intercentre reproducibility of cardiac apparent diffusion coefficient and fractional anisotropy in healthy volunteers. *Journal of Cardiovascular Magnetic Resonance,* 16**,** 31.

UNVERFERTH, D. V., BAKER, P. B., PEARCE, L. I., LAUTMAN, J. & ROBERTS, W. C. 1987. Regional myocyte hypertrophy and increased interstitial myocardial fibrosis in hypertrophic cardiomyopathy. *American Journal of Cardiology,* 59**,** 932-936.

VALDERRÁBANO, M., CHEN, P.-S. & LIN, S.-F. 2003. Spatial distribution of phase singularities in ventricular fibrillation. *Circulation,* 108**,** 354-359.

VAN DER BEL-KAHN, J. 1977. Muscle fiber disarray in common heart diseases. *Am J Cardiol,* 40**,** 355-64.

VARNAVA, A., ELLIOTT, P., SHARMA, S., MCKENNA, W. & DAVIES, M. 2000. Hypertrophic cardiomyopathy: the interrelation of disarray, fibrosis, and small vessel disease. *Heart,* 84**,** 476-482.

VARNAVA, A. M., ELLIOTT, P. M., BABOONIAN, C., DAVISON, F., DAVIES, M. J. & MCKENNA, W. J. 2001a. Hypertrophic cardiomyopathy: histopathological features of sudden death in cardiac troponin T disease. *Circulation,* 104**,** 1380-1384.

VARNAVA, A. M., ELLIOTT, P. M., MAHON, N., DAVIES, M. J. & MCKENNA, W. J. 2001b. Relation between myocyte disarray and outcome in hypertrophic cardiomyopathy. *Am J Cardiol,* 88**,** 275-9.

WATANABE, T., KUSACHI, S., YAMANISHI, A., KUMASHIRO, H., NUNOYAMA, H., SANO, I., NAKAHAMA, M., MURAKAMI, T., NAITO, I. & NINOMIYA, Y. 1998. Localization of type IV collagen α chain in the myocardium of dilated and hypertrophic cardiomyopathy. *Japanese heart journal,* 39**,** 753-762.

WATKINS, H., ASHRAFIAN, H. & REDWOOD, C. 2011. Inherited cardiomyopathies. *N Engl J Med,* 364**,** 1643-56.

WHITE, S. K., SADO, D. M., FONTANA, M., BANYPERSAD, S. M., MAESTRINI, V., FLETT, A. S., PIECHNIK, S. K., ROBSON, M. D., HAUSENLOY, D. J. & SHEIKH, A. M. 2013. T1 mapping

for myocardial extracellular volume measurement by CMR: bolus only versus primed infusion technique. *JACC: Cardiovascular Imaging,* 6**,** 955-962.

WHITTAKER, P., ROMANO, T., SILVER, M. D. & BOUGHNER, D. R. 1989. An improved method for detecting and quantifying cardiac muscle disarray in hypertrophic cardiomyopathy. *American heart journal,* 118**,** 341-346.

WU, M. T., SU, M. Y., HUANG, Y. L., CHIOU, K. R., YANG, P., PAN, H. B., REESE, T. G., WEDEEN, V. J. & TSENG, W. Y. 2009. Sequential changes of myocardial microstructure in patients postmyocardial infarction by diffusion-tensor cardiac MR: correlation with left ventricular structure and function. *Circ Cardiovasc Imaging,* 2**,** 32-40, 6 p following 40.

WU, M. T., TSENG, W. Y., SU, M. Y., LIU, C. P., CHIOU, K. R., WEDEEN, V. J., REESE, T. G. & YANG, C. F. 2006. Diffusion tensor magnetic resonance imaging mapping the fiber architecture remodeling in human myocardium after infarction: correlation with viability and wall motion. *Circulation,* 114**,** 1036-45.

YAN, L., WANG, Z., XU, Z., LI, Y., TAO, Y. & FAN, C. 2012. Two hundred eight patients with apical hypertrophic cardiomyopathy in China: clinical feature, prognosis, and comparison of pure and mixed forms. *Clinical cardiology,* 35**,** 101-106.

INDEX OF FIGURES

FIGURE 1.1 MACROSCOPIC FINDINGS OF HYPERTROPHIC CARDIOMYOPATHY 2

FIGURE 1.2 CARDIOVASCULAR MAGNETIC RESONANCE IMAGING IN HCM 3

FIGURE 1.3 2011 ACC/AHA GUIDELINES FOR ICD IMPLANTATION IN HCM (GERSH ET AL., 2011) 5

FIGURE 1.4 2014 ESC GUIDELINES FOR ICD IMPLANTATION IN HCM (AUTHORS/TASK FORCE ET AL., 2014) 6

FIGURE 1.5 HISTOLOGY OF MYOCYTE DISARRAY 10

FIGURE 1.6 MOLECULAR DIFFUSION 13

FIGURE 1.7 THE DIFFUSION TENSOR ELLIPSOID 15

FIGURE 1.8 THE DIFFUSION TENSOR MATRIX 15

FIGURE 1.9 THE EIGENSYSTEM 16

FIGURE 1.10 FRACTIONAL ANISOTROPY 18

FIGURE 1.11 HELIX ANGLE FROM DT-CMR AND HISTOLOGY DATA 19

FIGURE 1.12 TRACTOGRAPHY 20

FIGURE 1.13 HELIX ANGLE AND SHEETLET ANGLE 21

FIGURE 1.14 MYOLAMINAR SHEET DYNAMICS 22

FIGURE 1.15 STEJSKAL-TANNER PULSED GRADIENT SPIN ECHO DIFFUSION SEQUENCE 23

FIGURE 1.16 STIMULATED ECHO ACQUISITION MODE (STEAM) 26

FIGURE 1.17 DIFFUSIVITY, FRACTIONAL ANISOTROPY, HELIX ANGLES AND SHEETLET ANGLES WITH AND WITHOUT STRAIN CORRECTION 28

FIGURE 1.18 TIME CURVES OF RADIAL STRAIN, DIFFUSION AND FA IN A GEL PHANTOM 28

FIGURE 1.19 WHITE MATTER TRACTOGRAPHY 29

FIGURE 1.20 DIFFUSION SIGNAL DECAY AS A FUNCTION OF B-VALUE IN THE MYOCARDIUM 31

FIGURE 1.21 DIMENSIONALITY REDUCTION 35

FIGURE 1.22 FEATURE EXTRACTION 36

FIGURE 1.23 CLUSTERING ANALYSIS 37

FIGURE 2.1 THE STEAM DT-CMR SEQUENCE USED 41
FIGURE 2.2 DT-CMR ACQUISITION 43
FIGURE 2.3 COMPARISON OF PREVIOUSLY PUBLISHED ADC AND FA VALUES IN HEALTHY CONTROLS 45
FIGURE 2.4 BLAND-ALTMAN PLOTS TO COMPARE ADC AND FA OBTAINED BY EACH CENTRE INDEPENDENTLY 46
FIGURE 2.5 DT-CMR ARTEFACT DUE TO BREATHING 47
FIGURE 2.6 DT-CMR ARTEFACT DUE TO GRADUAL LOSS OF BREATH-HOLDING 47
FIGURE 2.7 DT-CMR ARTEFACT DUE TO MARKED SINUS ARRHYTHMIA 48
FIGURE 2.8 DT-CMR ARTEFACT DUE TO BRADYCARDIA 49
FIGURE 2.9 MANUAL SEGMENTATION OF THE FIRST DT-CMR REFERENCE IMAGE 50
FIGURE 2.10 MANUAL REJECTION OF CORRUPTED DT-CMR IMAGES 51
FIGURE 2.11 FIBRE AND SHEETLET ANGLE DEFINITIONS 52
FIGURE 2.12 HELIX ANGLE FROM DT-CMR AND HISTOLOGY DATA WITH LINEAR FIT FOR HELIX ANGLE GRADIENT CALCULATION 53
FIGURE 2.13 CENTRELINE METHOD TO MEASURE MAXIMAL SEGMENTAL LV WALL THICKNESS 57
FIGURE 2.14 THE 16-SEGMENT LEFT VENTRICULAR MODEL 57
FIGURE 2.15 EXTRACELLULAR VOLUME (ECV) FROM NATIVE AND POST-CONTRAST T1 MAPS 59
FIGURE 3.1 HELIX ANGLES (LEFT) AND SHEETLET ANGLES (RIGHT) FROM EX VIVO DT-CMR 63
FIGURE 3.2 MYOCYTE AND SHEETLET ORIENTATION CORRESPOND TO THE PRIMARY AND SECONDARY EIGENVECTORS OF THE DIFFUSION TENSOR 64
FIGURE 3.3 PETTIGREW'S ANATOMICAL DISSECTIONS OF THE HEART 65
FIGURE 3.4 MULTISCALE CARDIAC ANATOMY 66
FIGURE 3.5 STREETER'S MEASUREMENTS OF TRANSMURAL PROGRESSION IN FIBRE ANGLE 67
FIGURE 3.6 LV ARCHITECTURE OF THE BASAL, MID AND APICAL SHORT-AXIS VENTRICULAR SECTIONS 68
FIGURE 3.7 THE PROPOSED TRANSMURAL HETEROGENEITY OF FRACTIONAL ANISOTROPY 69
FIGURE 3.8 THE PROPOSED EFFECT OF MYOCYTE ORIENTATION ON FRACTIONAL ANISOTROPY 70
FIGURE 3.9 STANDARD AND HIGH-RESOLUTION DT-CMR MAPS 72
FIGURE 3.10 DIASTOLIC DT-CMR IMAGES AND ADC, FA, HELIX AND SHEETLET ANGLE MAPS 74

FIGURE 3.11 SYSTOLIC DT-CMR IMAGES AND ADC, FA, HELIX AND SHEETLET ANGLE MAPS 75
FIGURE 3.12 POOR QUALITY DATA FROM THE APICAL SLICE DUE TO INCONSISTENT BREATH-HOLDING AT THE END OF THE SCAN 77
FIGURE 3.13 SLICE POSITION OF THE DIASTOLIC DT-CMR SHORT-AXIS VENTRICULAR SLICES 78
FIGURE 3.14 MEAN DIASTOLIC FA AND HELIX ANGLE FROM EPI- TO ENDOCARDIUM IN MID SLICE 79
FIGURE 3.15 SLICE MEAN FA ACROSS ALL CONTROLS MAPPED TO NORMALISED LV CO-ORDINATES 80
FIGURE 3.16 SEGMENTAL VARIATION OF FRACTIONAL ANISOTROPY (A) AND SNR (B) IN THE MID-VENTRICULAR SLICE 81
FIGURE 3.17 SEGMENTAL COMPARISON OF FRACTIONAL ANISOTROPY (A) AND SNR (B) BETWEEN THE DIASTOLIC BASAL AND MID SLICE 84
FIGURE 3.18 MID (A) AND BASAL (B) DIASTOLIC SLICE COMPARISON OF FA AND SNR MAPS 85
FIGURE 4.1 PHOTOMICROGRAPH OF MYOCYTES FROM A NORMAL (LEFT) AND HCM (RIGHT) LV 92
FIGURE 4.2 MYOCARDIAL ARCHITECTURE IN THE MID-VENTRICULAR SLICE IN A NORMAL AND HCM HEART. 93
FIGURE 4.3 HISTOLOGICAL MAP OF DISARRAY IN A SEPTAL SECTION IN HCM (LEFT) AND PERCENTAGE AREA OF DISARRAY IN HCM AND CONTROLS (RIGHT) 95
FIGURE 4.4 MYOCYTE ORIENTATION DISTRIBUTIONS FROM 3 NORMAL (TOP ROW) AND 3 HCM HEARTS (BOTTOM ROW) 95
FIGURE 4.5 DIASTOLIC FA WAS REDUCED IN HCM COMPARED TO CONTROLS 102
FIGURE 4.6 SEGMENTAL VARIATION BY SLICE AND GROUP OF FA AND SNR 103
FIGURE 4.7 DT-CMR MAPS IN AN HCM PATIENT FROM BOTH PHASES 105
FIGURE 4.8 MID-VENTRICULAR MEAN FA ACROSS ALL SUBJECTS BY GROUP MAPPED TO NORMALISED LV CO-ORDINATES 106
FIGURE 4.9 MAXIMUM LV WALL THICKNESS AT END-DIASTOLE BY MID-VENTRICULAR SEGMENT 107
FIGURE 4.10 MEAN DIASTOLIC SNR AND FA FROM EPI- TO ENDOCARDIUM IN MID SLICE IN HCM (RED) AND CONTROL (BLUE) 107
FIGURE 4.11 MEAN FA OF THE MAXIMALLY THICKENED SEGMENT HAD REDUCED FA COMPARED TO THE INFEROLATERAL SEGMENT IN HCM 108
FIGURE 4.12 DIFFERENCES BETWEEN REGIONS OF INTEREST BY SEGMENTING ALONGSIDE CINE 110
FIGURE 4.13 BLAND-ALTMAN PLOT SHOWING EXCELLENT INTER-OBSERVER REPRODUCIBILITY OF MID-VENTRICULAR SLICE MEAN FA 110
FIGURE 4.14 TENSOR VISUALISATION IN THE MID DIASTOLIC SLICE OF A HEALTHY CONTROL AND HCM PATIENT 111

FIGURE 5.1 THE SUPPORTING FIBROCOLLAGENOUS NETWORK AROUND MYOCYTES 118

FIGURE 5.2 MACROSCOPIC VIEW OF THE THREE-DIMENSIONAL ORGANISATION OF VENTRICULAR MYOCARDIUM 120

FIGURE 5.3 FRACTIONAL ANISOTROPY (FA) CALCULATED FROM THE DIFFUSION TENSOR 122

FIGURE 5.4 MULTIMODAL IMAGING OF DISARRAY USING DIFFUSION TENSOR CARDIAC MAGNETIC RESONANCE, LATE GADOLINIUM ENHANCEMENT AND EXTRACELLULAR VOLUME MAPPING 126

FIGURE 5.5 MEAN SHEETLET ANGLE IN SEGMENT OF MAXIMUM WALL THICKNESS 127

FIGURE 5.6 REDUCED FA IN HCM EVEN AFTER ADJUSTMENT FOR FIBROSIS 128

FIGURE 5.7 REDUCED FA IN HCM WITH VENTRICULAR ARRHYTHMIAS 131

FIGURE 5.8 A TREND TO INCREASED ECV BUT NOT HYPERTROPHY IN HCM WITH VENTRICULAR ARRHYTHMIA 131

FIGURE 6.1 SUMMARY OF THE METHODS APPLIED FOR COMPUTATIONAL ECG PHENOTYPING 139

FIGURE 6.2 STANDARD ECG BIOMARKERS FROM THE QRS AND T WAVE 141

FIGURE 6.3 FIRST FOUR HERMITE BASIS FUNCTIONS 142

FIGURE 6.4 COMPARISON OF THE FOUR HERMITE COEFFICIENTS IN LEADS I-II, V1-6 FOR THE THREE QRS-BASED HCM GROUPS .. 148

FIGURE 6.5 CLUSTERING USING QRS MORPHOLOGY ALONE IDENTIFIES THREE HCM SUBGROUPS 149

FIGURE 6.6 FOUR DISTINCT HCM SUBGROUPS ARE IDENTIFIED BASED ON QRS AND T WAVE MORPHOLOGY 153

FIGURE 6.7 FOUR DISTINCT ECG PHENOTYPES IN HCM EXHIBIT DIFFERENCES IN HYPERTROPHY MORPHOLOGY AND ARRHYTHMIC RISK 154

INDEX OF TABLES

TABLE 2.1 PHANTOM VALIDATION OF DT-CMR STEAM SEQUENCE 44

TABLE 2.2 COMPARISON OF PREVIOUSLY PUBLISHED ADC AND FA VALUES 46

TABLE 3.1 DT-CMR PARAMETERS BY SLICE IN HEALTHY CONTROLS. 76

TABLE 3.2 INTERCENTRE REPRODUCIBILITY REFERENCE VALUES FOR MID-VENTRICULAR SLICE 78

TABLE 3.3 DIASTOLIC MID-VENTRICULAR DT-CMR PARAMETERS BY SEGMENT IN HEALTHY CONTROLS 82

TABLE 4.1 CLINICAL AND IMAGING CHARACTERISTICS BY GROUP 99

TABLE 4.2 DT-CMR PARAMETERS IN DIASTOLE BY SLICE 101

TABLE 5.1 CHARACTERISTICS OF HCM PATIENTS WITH AND WITHOUT VENTRICULAR ARRHYTHMIA 130

TABLE 6.1 CHARACTERISTICS OF HEALTHY VOLUNTEERS AND HCM PATIENTS 146

TABLE 6.2 CLINICAL AND GENOTYPE CHARACTERISTICS OF HCM PATIENTS 147

TABLE 6.3 ECG AND CLINICAL FEATURES FOR QRS-BASED HCM GROUPS 150

TABLE 6.4 CHARACTERISTICS OF THE FOUR HCM PHENOTYPES FROM COMBINED QRS AND T WAVE CLUSTERING 155

TABLE 6.5 EFFECT OF EXCLUDING GENE POSITIVE HCM WITH NORMAL WALL THICKNESS ON THE FOUR HCM PHENOTYPES FROM COMBINED QRS AND T WAVE CLUSTERING 158